Investigation of the film growth and physical properties of thin molecular layers of the spin crossover compound Fe(HB(tz)3)2

Alin-Ciprian Bas

Université Fédérale
Toulouse Midi-Pyrénées

THÈSE

En vue de l'obtention du

DOCTORAT DE L'UNIVERSITÉ DE TOULOUSE

Délivré par l'Université Toulouse 3 - Paul Sabatier

Présentée et soutenue par

ALIN-CIPRIAN BAS

Le 20 février 2019

Etude de la croissance et des propriétés physiques des couches minces moléculaires du composé Fe(HB(tz)3)2 à transition de spin

Ecole doctorale : **SDM - SCIENCES DE LA MATIERE - Toulouse**

Spécialité : **Physique**

Unité de recherche :
LCC - Laboratoire de Chimie de Coordination

Thèse dirigée par
Gabor MOLNAR et Christophe THIBAULT

Jury

Mme Petra Ágota SZILÁGYI, Rapporteur
Mme Zoia VOITENKO, Rapporteur
M. Philippe DEMONT, Examinateur
M. José SÁNCHEZ COSTA, Examinateur
M. Gabor MOLNAR, Directeur de thèse
M. Christophe THIBAULT, Co-directeur de thèse

Acknowledgments

Contents

General Introduction

The recent progress in the nanoscale synthesis and organization of molecular spin crossover (SCO) materials allowed the elaboration of a variety of molecular nano-objects (nanoparticles, thin films, nanopatterns, nanoscale assemblies, etc.) exhibiting SCO properties. These new nanometer-sized materials offer the appealing possibility to exploit their switchable (bistability) properties at the nanometric scale and open the way for the integration and implementation of SCO in various applications (optical memories/switches, sensors, electronic junctions or mechanical actuators) [1-3]. Despite the considerable progress accomplished in this research field in the past decade, numerous challenges remain to be addressed. Notably, it appears crucial to enlarge considerably the portfolio of SCO complexes displaying robust, near room temperature switching properties. Turning these compounds into high quality nanomaterials calls also for rigorous material science studies along with fundamental understanding of the role of surface/interface properties on the desired functionality. In addition, critical studies will be necessary to explore the possibilities of their integration, function and reliability in 'real world' devices. Of particular importance would be to clarify if the robustness of the SCO phenomenon and the scalability of the processing methods can meet the stringent requirements for commercial applications. In this context, this thesis work describes the growth and physical properties of nanometric thin films of the SCO compound $Fe(HB(tz)_3)_2$ (tz = 1,2,4-triazol-1-yl). Following a brief introduction on the SCO phenomenon and SCO films in Chapter 1, we describe in Chapter 2 the vacuum deposition of this compound by thermal evaporation and we show that a straightforward solvent vapor annealing process allows for obtaining unprecedented robust, high quality, thin films exhibiting SCO near room temperature. Chapter 3 is devoted to the deep investigation of the SCO properties, including the reversibility of the SCO over numerous switching cycles as well as its thermal, environmental and processing stability. A specific attention is placed also on the careful investigation of finite size effects when reducing the thickness of the films. Chapter 4 describes the properties of hybrid luminescent – SCO films consisting of a combination of $Fe(HB(tz)_3)_2$ and $Ir(ppy)_3$ (ppy = 2-phenylpyridine) molecules either in binary or multilayer films. The luminescence modulation by the SCO in these films provides a first step towards high-resolution, near-field optical detection of the SCO phenomenon and, as a consequence, the local variation of temperature. Finally, in Chapter 5 we discuss the use of atomic force microscopy in the high spatial resolution imaging of the SCO in films of $Fe(HB(tz)_3)_2$ with particular emphasis on the quantitative measurements of mechanical properties.

Chapter 1. Introduction

In this chapter, we will first briefly discuss the basic aspects of molecular spin crossover phenomenon, including the electronic and thermodynamical aspects as well as the different stimuli, which can induce the SCO. The second part of the chapter summarizes the state of the art of the fabrication and characterization of SCO films.

1.1 Introduction to the Spin Crossover Phenomenon

The spin transition phenomenon was observed for the first time in 1931 by Cambi and co-workers who identified a strange magnetic behavior in a series of Fe (III) complexes based on tri-dithiocarbamate ligand [4]. They noticed a reversible conversion of the spin state as a result of temperature variation [5]. Until the mid-50s, they did not discuss about spin transition but "anomalous" magnetic behavior. In 1956, the notion of spin equilibrium behavior was evoked by Griffith [6]. In 1964, Baker and Bobonich demonstrated the first spin transition in the solid state on the $[Fe(phen)_2(NCS)_2]$ (phen=1,10-phenanthroline) complex based on Fe (II) [7]. In the same year, Ewald et al., [8] introduced the notion of "spin-crossover", as part of the ligand field theory, according to the Tanabe-Sugano diagrams in which appears the crossing of the energy curves of the electronic states as a function of the energy of the ligand field for octahedral $d^4 – d^7$ transition metal complexes. They established that a change in the spin state of the complexes is possible when the ligand field energy and energy of electron pairing in the orbitals d are comparable. Until now, this vision of the phenomenon has not been changed and can be found in different articles and textbook.

The spin transition phenomenon can occur in compounds with metal ions belonging to the first series of transition metals and more particularly having electronic configurations $3d^4$ to $3d^7$ as in compounds of Fe (III), Fe (II), Co (II) and less frequently in Co (III), Cr (II), Mn (II) and Mn (III). However, the majority of the studied complexes have an iron(II) central ion [9]. For this reason, in the following the general principles, which govern the spin transition, will be discussed for Fe (II).

1.1.1 Crystal Field Theory

In 1929, the physicist Hans Bethe proposed the crystal field theory [10]. This theory can be used to understand the origin of the spin transition phenomenon. In this theory, the interaction between the metal center and the ligands is considered mainly electrostatic. The metal ion is

positively charged, while the ligands have a negative charge. The ligand charge distribution determine the symmetry of the external electrostatic field who will act on the transition metal and cause the degeneration [11]. This model is relatively simple and allows a qualitative approach and a first explanation to the spin transition phenomenon.

If we take the example of the free Fe (II) ion, where the electronic energy levels of the five 3d orbitals are degenerated. If the iron (II) ion is placed in a perfect octahedral geometry field Oh, formed by six negatively charged ligands, then the six 3d electrons of the metal center undergo repulsive forces from the ligands.

For an easier understanding of the crystal field theory, we have to understand the description of the five degenerate d- orbitals (see figure 1.1):

- d_{xy}: the lobes are located between the x and the y axes;
- d_{xz}: the lobes are located between the x and the z axes;
- d_{yz}: the lobes are located between the y and the z axes;
- $d_{x^2-y^2}$: the lobes are located on the x and y axes;
- d_{z^2}: there are two lobes on the z axes and there is a donut shape ring that is on the *xy* plane around the other two lobes.

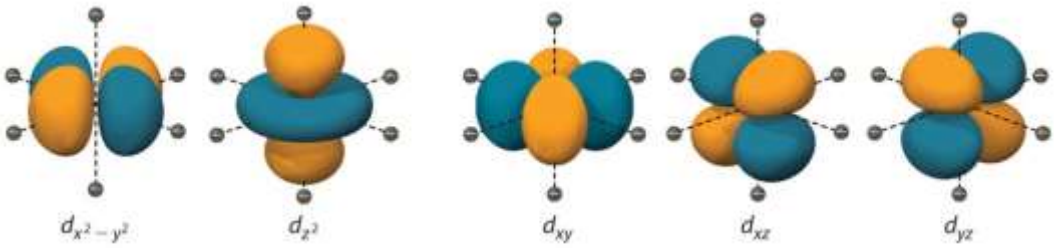

Figure 1.1: Schematic representation of the 3*d* orbitals in an octahedral complex.

According to the crystal field theory, the population of d orbitals will be governed by the minimization of electrostatic energy. The effect of an octahedral field causes the energy levels of the degenerated d orbitals (in the case of the free ion) to break up into two energy levels: a first low energy level t_{2g} comprising three non-bonding degenerated orbitals: (d_{xy}, d_{yz}, d_{xz}) and a second higher energy level e_g composed of two anti-bonding degenerated orbitals (d_{z^2}, $d_{x^2-y^2}$) as shown in Figure 1.2. The energy gap between these two levels t_{2g} and e_g noted here with Δ_o is determined by the strength of the ligand field (also called the crystal field splitting energy) which is 10Dq. Dq is a semi-empirical parameter associated with crystal field strength that depends on the charge distribution of the metal ion and the metal-ligand distance (r) as:

($\Delta \approx 1/r^n$ with n =5- 6) [11].

It is possible to decompose the energy of the t_{2g} and e_g levels into two contributions: a spherical field which has the effect and elevate the energy of the electronic levels of the free ion of an $E_{spherical}$ value and a contribution associated with the lowering of the symmetry and thus the partial lifting of degeneracy.

$$E_{e_g} = E_{free} + \Delta E_{spherical} + \frac{6}{10} \times 10Dq$$
$$E_{t_{2g}} = E_{free} + \Delta E_{spherical} - \frac{4}{10} \times 10Dq \quad (1.1)$$

where the E_{free} is the energy of the free Fe^{II} ion.

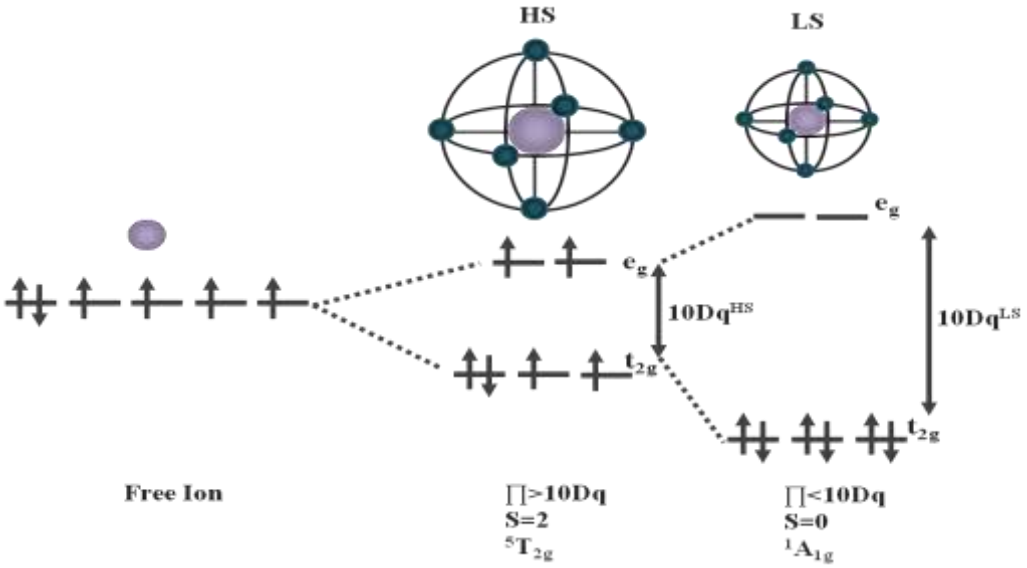

Figure 1.2: Separation of the 3d orbitals of an Fe(II) ion in an octahedral environment induced by the ligand field strength 10Dq.

In addition to this energy, the electron-electron repulsion, also called the spin pairing energy Π has to be taken into account. Depending on the intensity of the ligand field, the 6 electrons of the Fe (II) ion can be divided in two different ways (see figure above). Within the molecule, two main effects compete. In the first case, the electrons tend to occupy the orbitals d according to Hund's rule do to the exchange term. In the second case, they tend to fill the t_{2g} level, of lower energy. As a result of this competition, it is possible to define two fundamental states with different distribution for the six d electrons depending on the magnitude of 10Dq and Π (see Figure 1.2):

- When *Π > 10Dq* (weak crystalline field), the electrons will occupy the five d orbitals according to Hund's rule, with maximum spin multiplicity as for the free ion (2S+1=5). In the case of Fe (II), the total spin is S =2, and this paramagnetic ground state is denominated *high spin state (HS)*, represented by the spectroscopic term $^5T_{2g}$.
- When *Π < 10Dq* (strong crystalline field), the electrons occupy the lowest energy level t_{2g}, in violation of Hund's rule and maximizing the number of paired electrons, with minimum spin multiplicity (2S+1=1). In the case of Fe (II), the total spin is S = 0, and this diamagnetic state is called *low spin state (LS)*, represented by the spectroscopic term $^1A_{1g}$.

The energy difference between the LS and HS states is determined mainly by the strength of the ligand field around the Fe (II) ion. The strength of the ligand field is a function of the nature of the ligand and the distance (d) between the transition metal and the ligand. In the case of neutral ligand, the ligand field is descripted by the following equation:

$$\Delta_o = 10Dq(d) \approx \frac{\mu}{d^6} \tag{1.2}$$

The ratio of the ligand field strengths between two spin states can be described by the following equation:

$$\frac{10Dq^{LS}}{10Dq^{HS}} = \left(\frac{r_{HS}}{r_{LS}}\right)^n \approx 1.75 \tag{1.3}$$

where r_{LS} and r_{HS} are respectively the average metal-ligand distances in the LS and HS states and n = 5 – 6. In the LS state, the metal-ligand distance is in the order of $r_{LS} \approx 2.0$ Å. In the HS state, the metal-ligand distance is greater than the LS state and is therefore of the order of $r_{HS} \approx$ 2.2 Å (see Figure 1.3).

The origin of these two spin states (LS and HS) can be predicted by Tanabe Sugano diagrams [12, 13]. For example, the diagram in Figure 1.4, show how the electronic states of the free Fe(II) ion are divided into ground and excited states under the influence of the ligand field strength in units of the Racah parameter (electronic repulsion B).

The small difference in energy between a LS and HS configuration explains the limited number of spin transition compounds compared to the vast 'library' of Fe (II) coordination complexes. This also explains that a small change of the nature of the compound, as the modification of the ligand, anion or solvent disrupts completely, in some cases, the physical properties (magnetic, vibrational, optical, electrical and structural) of the complex.

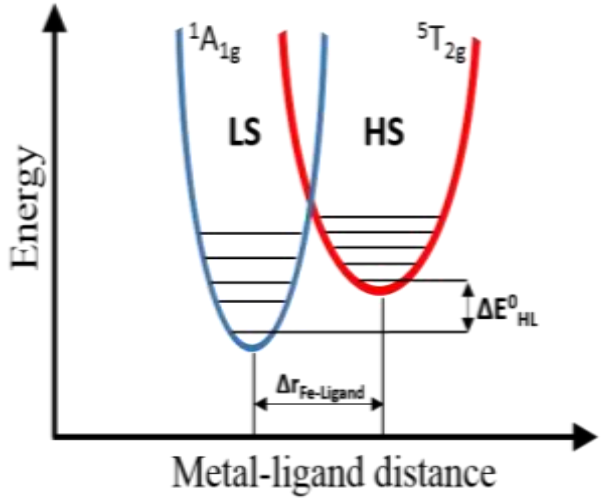

Figure 1.3: Simplified configurational diagram of two molecular spin states (HS and LS).

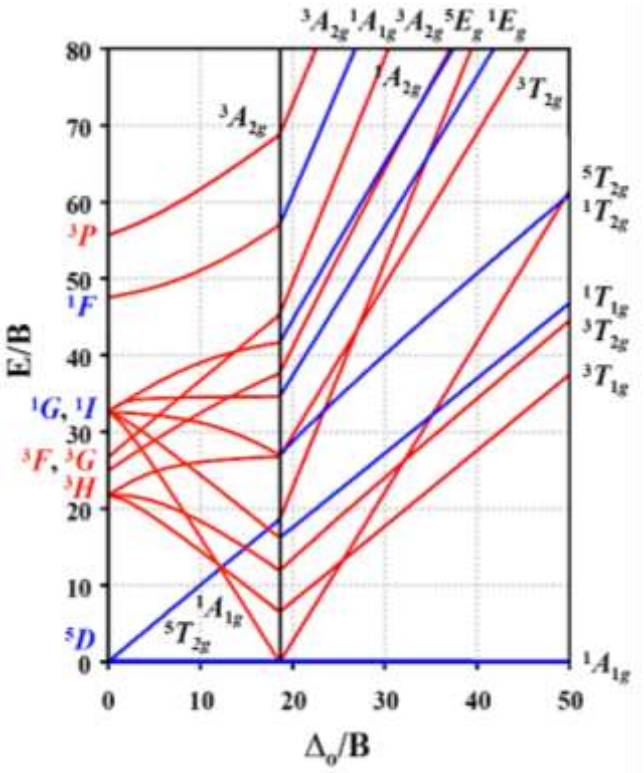

Figure 1.4: Tanabe-Sugano diagram for a transition metal ion with six d electrons in a octahedral ligand field symmetry.

Based on the diagrams in Figure 1.3 and Figure 1.4, because 10 Dq depends on the metal-ligand bond length and as Π varies only slightly with temperature, the energy difference between the HS and LS states ($\Delta E^0_{HL} = E^0_{HS} - E^0_{LS}$) was estimated by A. Hauser as a function of $10Dq^{HS}$ or $10Dq^{LS}$ for octahedral Fe(II) complexes as illustrated in Figure 1.5, where 3 regimes can be observed:

- For $10Dq^{HS}$ < 10000 cm^{-1} and ΔE^0_{HL} < 0. In this case, the HS state is the quantum mechanical ground state and is thermodynamically stable at all temperatures.
- For $10Dq^{LS}$ > 23000 cm^{-1}, ΔE^0_{HL} > 2000 cm^{-1}. In this case, the LS state is the quantum mechanical ground state and remains thermodynamically stable for very high temperatures.
- In the range $10Dq^{HS}$ = 11000 ÷ 12500 cm^{-1}, $10Dq^{LS}$ = 19000 ÷ 22000 cm-1 and $^0_{HL}$ = 0 ÷ 2000 cm^{-1} the phenomenon of thermo-induced spin transition may occur.

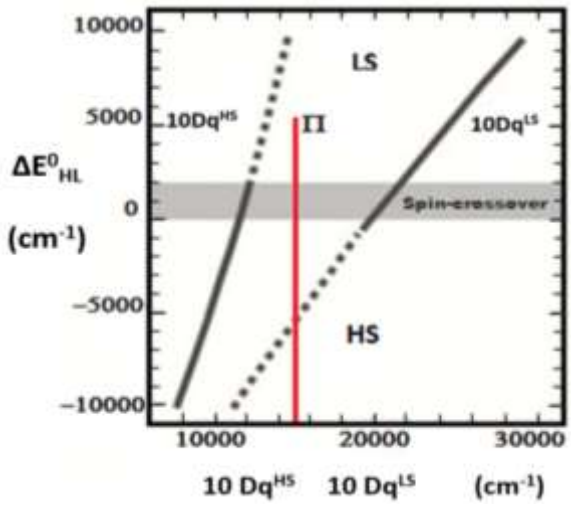

Figure 1.5: Stability regions of the LS and HS states as a function of 10Dq for octahedral Fe(II) complexes [11].

1.1.2 Thermodynamic aspects of the spin transition

The classical thermodynamic approach can describe the spin transition phenomenon as an equilibrium between two phases (LS and HS). For that, we consider a system constituted by a set of isolated molecules (without interaction). Under usual temperature and pressure conditions, the relevant thermodynamical function for this system is the Gibbs free energy, G. At constant pressure, the difference of Gibbs free enthalpy between the HS and LS states ($\Delta G = \Delta G_{HS} - \Delta G_{LS}$) is written as follows [14, 15]:

$$\Delta G = \Delta H - T\Delta S \tag{1.4}$$

where ΔH and ΔS correspond to the enthalpy ($H_{HS} - H_{LS}$) and entropy ($S_{HS} - S_{LS}$) variations during the LS → HS transition. When the proportions of molecules in the HS and LS states are equal, the equilibrium temperature $T_{1/2}$, defined by $\Delta G = 0$, is written as:

$$T_{1/2} = \frac{\Delta H}{\Delta S} \tag{1.5}$$

where ΔH and ΔS must be of the same sign since $T_{1/2}$, given in Kelvin (K), is always positive.

Using the equation 1.5, it is possible to summarize the spin transition as follows:

- If $T < T_{1/2}$, then $\Delta H > T\Delta S$, the enthalpy term dominates and the thermodynamic ground state is the LS state ($G_{LS} < G_{HS}$);
- If $T > T_{1/2}$, then $\Delta H < T\Delta S$, the entropic term dominates and the thermodynamic ground state is the HS state ($G_{LS} > G_{HS}$);
- If $T = T_{1/2}$, then $\Delta H = T\Delta S$, the enthalpy and entropy variations are equal and the two spin states are present in the same proportion ($G_{LS} = G_{HS}$).

The variation of entropy can be estimated by taking into account the electronic, vibrational, configurational, rotational and translational contributions. These last two terms can be excluded if we consider the complex in the solid state. Moreover, in the absence of orientation disorder, the configurational term is also excluded. The entropy change is then composed of two primary contributions, one electronic (ΔS_{el}) and the other vibrational (ΔS_{vib}):

$$\Delta S = \Delta S_{el} + \Delta S_{vib} + \cancel{\Delta S_{rot}} + \cancel{\Delta S_{transl}} + \cancel{\Delta S_{conf}} \quad (1.6)$$

ΔS_{el} is the sum of contributions due to changes in spin state and orbital moment:

$$\Delta S_{el} = \Delta S_{el}^{spin} + \Delta S_{el}^{orb} \quad (1.7)$$

where:

$$\Delta S_{el}^{spin} = R \ln(2S_{HS} + 1/2S_{LS} + 1) \quad (1.8)$$

$$\Delta S_{el}^{orb} = R \ln(2L_{HS} + 1/2L_{LS} + 1) \quad (1.9)$$

R represent the ideal gas constant [$R = 8.314$ J K^{-1} mol^{-1}].

Thereby, in the case of an Fe(II) complex, for a transition from the LS state ($^1A_1$) to the HS state ($^5T_2$),the two electronic contributions are calculated as follows:

$$\Delta S_{el}^{spin} = R \ln(5) = 13.38 \text{ J } K^{-1} \text{ mol}^{-1} \quad (1.10)$$

$$\Delta S_{el}^{orb} = R \ln(3) = 9.13 \text{ J } K^{-1} \text{ mol}^{-1} \quad (1.11)$$

However, the symmetry around the metal ion is actually lower, the orbital degeneration is generally raised and ΔS_{el}^{orb} becomes negligible. Therefore $\Delta S_{el} \approx \Delta S_{el}^{spin} = 13.38$ J K^{-1} mol^{-1}. Calorimetric measurements performed on compounds based on Fe(II) typically give a variation

of ΔS between 40 - 60 J K^{-1} mol^{-1} [16, 17]. We notice that these experimental values are much higher than 13.38 J $K^{-1}mol^{-1}$ corresponding to the variation of the entropy of electronic origin. The remaining contribution comes from the variations of the molecular vibration frequencies. Much of the difference in vibrational entropy is attributed to the difference of the intramolecular vibration modes (ΔS_{vib}^{intra}) between the HS and LS state, due to the elongation of the metal-ligands distances. The contribution of the vibrational entropy in the spin transition was initially demonstrated by Sorai and Seki [18] and observed by Raman spectroscopy in 2000 by Bousseksou et al. [19]. However, a material in the solid state has non-negligible intermolecular bonds, which gives rise to intermolecular vibrations. These vibrations are dependent on the spin state, imply a variation of entropy ΔS_{vib}^{inter} and modify the variation of total entropy.

1.1.3 Temperature induced spin crossover

The spin transition can be triggered by different stimuli such as temperature variation, pressure, light irradiation, magnetic field, or gas/vapor adsorption [1, 20, 21], but the most usual way to induce spin transition is by temperature variation.

In a diluted SCO system, the intermolecular interactions can be neglected hence the change of the spin state of the system can be described as a sum of the conversions of isolated molecules. In this case, the spin state change follows Boltzmann distribution. On the other hand, in the case of a bulk solid the intermolecular interactions and the crystal packing of the material will play an important role. When a molecule switches from the LS to the HS state there is an increase of volume of the molecule that will change the energy of the other molecules in the solid due to elastic stress and strain. In addition, this increase in volume is associated with a decrease of the intermolecular forces of the material that is translated in an increase of its compressibility. These elastic mechanisms are denoted globally as the cooperativity of the SCO material.

By convention, a thermal spin transition curve is represented by the fraction of molecules in the HS state (n_{HS}) depending on the temperature. In the example of a material with a spin transition composed of N molecules, at a given temperature and pressure, there will be N_{HS} molecules in the HS and N_{LS} =N – N_{HS} in the LS state. The high-spin fraction n_{HS} is defined as follows:

$$n_{HS} = \frac{N_{HS}}{N_{HS} + N_{LS}} = \frac{N_{HS}}{N} \tag{1.12}$$

A spin transition curve plotted in this manner $n_{HS} = f(T)$, can provide a lot of information according to its shape. Figure 1.6 shows the most frequently observed cases in spin transition materials. The main source of the diversity of the spin crossover curves is the degree of cooperativity between the molecules, which is determined by the lattice properties and the way that metal-ligand deformations are propagated through the solid. In general, gradual spin conversions (Figure 1.6a) are characteristic of materials where interactions between metal centers are weak. Each metal center then undergoes the change of spin state independently of its neighbors.

In 1964, for the first time, a first-order spin transition was observed in the solid state by Baker and Bobonich for the compound [$Fe(phen)_2 (NCS)_2$] [7]. Three years later, in 1967, this observation was confirmed by Koenig and Madeja [22]. The abrupt transition is represented in figure 1.6b. This behavior was attributed to the intermolecular interactions and the notion of cooperative system was introduced [23, 24]. In very cooperative systems, we notice the appearance of a phase transition of the first order accompanied by a hysteresis cycle, represented in Figure 1.6c. This category of transitions are characterized by two "*transition temperatures*": one for the heating mode $T^{\uparrow}_{1/2}$ (representing the transition temperature from the LS to the HS state), and another for the cooling mode $T^{\downarrow}_{1/2}$ (transition temperature from the HS to the LS state). For the occurrence of hysteresis in a spin transition curve, two main factors are responsible: first, the transition can be accompanied with a structural phase change in the lattice, and the second case, the intramolecular structural changes which take place upon the transition may be transmitted to the neighboring molecules due to strong elastic interactions between them [9]. This memory effect was observed for the first time by König and Richter in 1976 for the [$Fe(4,7\text{-}(CH_3)_2\text{-}phen)_2(NCS)_2$] compounds [25].

The spin transition can also occur in several steps (figure 1.6d). The first 2-step transition was reported by Zelentsov for the case of a Fe (III) complex of 2-brommo-salicylaldehyde-thiosemicarbazone [26]. These transitions are not common and may occur for different reasons. It may be linked simply to the existence of different crystallographic positions of metal ions in the crystal. However, this phenomenon can also exist in mono- or polynuclear systems where the environment of each metal ion is identical. In this case, the transition of one of the metals causes local distortions and makes the transition of the neighbor metal less favorable [27]. Such preferential formation of HS/LS pairs was associated with the competition of short- and long-range interactions [28, 29].

Incomplete transitions were also reported (figure 1.6e). This may correspond to the appearance of a residual HS fraction at low temperature and/or a residual LS fraction at high temperature [8]. The occurrence of this kind of transition may be related to several causes. First, this phenomenon may appear due to a kinetic effect at very low temperatures when molecules in the HS state are trapped or "freeze" by a quenching effect. This effect is frequently seen around liquid nitrogen temperature [30]. Another cause is related to the existence of defects in the lattice able to prevent locally the formation of LS species (HS fraction) or HS species (LS fraction).

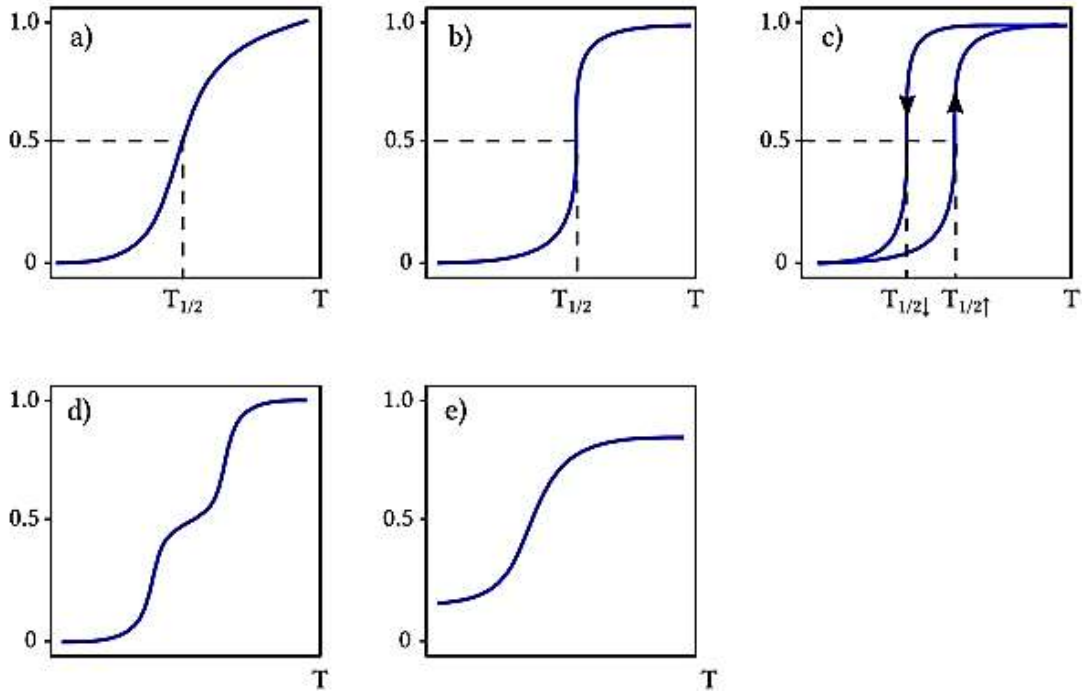

Figure 1.6: Principle types of the thermal SCO responses plotting the high spin fraction (n_{HS}) as a function of temperature. a) gradual spin conversion, b) abrupt spin transition, c) spin transition with hysteresis, d) double step spin transition and e) incomplete spin transition. [30]

The link between cooperativity and crystal structure is evident but remains extremely difficult to quantify. Intermolecular contacts between spin centers can conduct to strong cooperativity. These interactions could occur through strong or weak hydrogen bonds, from π-π stacking, or simply from Van der Waals forces. Cooperativity is also transmitted mechanically in a molecular crystal, between molecules with a high degree of surface contact. Large structural differences between the HS and LS states can lead to strong cooperativity, as long as the lattice is sufficiently flexible to adapt these changes [31]. The hysteresis loop confers the system a bistability which can be exploited in different applications such as memory devices, molecular switches, sensors, or displays.

1.1.4 Pressure induced spin crossover

Another external stimulus that can trigger or modify the spin transition is the application of an external pressure [32]. High-pressure spectroscopic studies of Drickamer, Ferraro and Evans starting in the sixties have already addressed the SCO phenomenon using Mössbauer, UV-Vis and IR spectroscopies associated with either piston-cylinder or anvil-type pressure cells. High-pressure investigations using a plethora of different pressure cells and detection methods were then continued by many teams. They reported that in the case of Fe(II) compounds, under the action of external pressure, the spin transition is shifted to higher temperatures by ca. 15-20 K/kbar. The pressure applied to the sample stabilizes the LS state of smaller volume and increases the transition temperature [33, 34]. By applying a 'moderate' pressure in the range of 0 - 1 GPa, the potential wells suffer only a relative vertical displacement, and the gap between the LS and HS states increases by $p\Delta V$, where ΔV is the volume difference between the two spin states (Figure 1.7). Nevertheless, applying pressure to a spin transition compound can have other effects as well, such as the modification of the electronic structure, the modification of the crystallographic structure or both at the same time. In general, the application of pressure tends to smear out the hysteresis, but in a few cases, a stable or increasing hysteresis width was also reported.

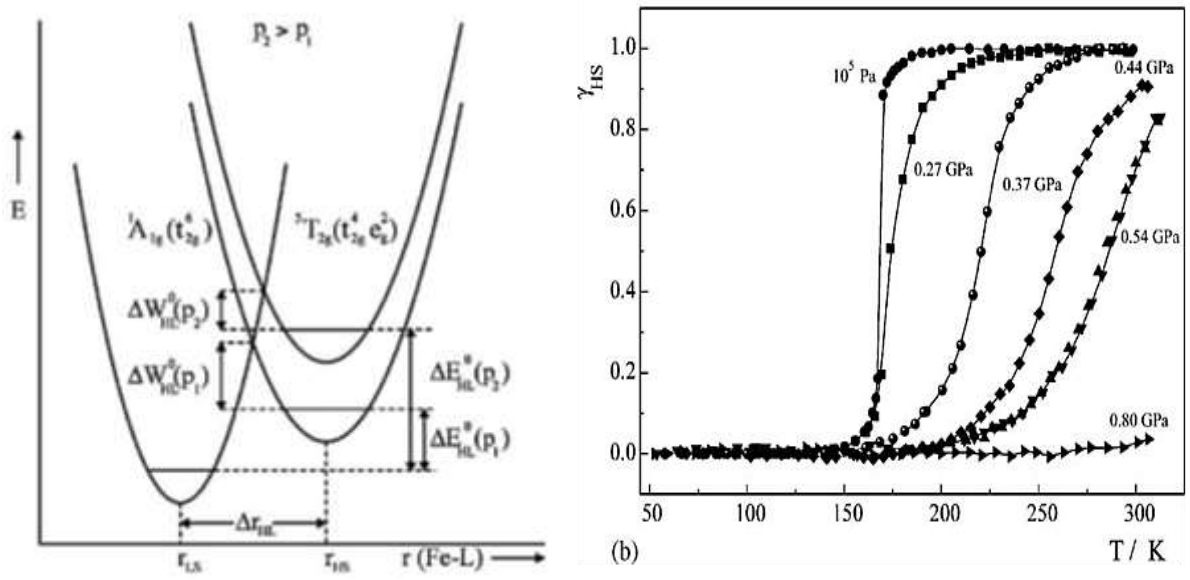

Figure 1.7: (left) Schematic representation of pressure effect on the LS and HS potential wells of Fe(II) compounds [9]. (right) High spin fraction vs. temperature for the compound $[CrI_2(depe)_2]$ at different hydrostatic pressures [35].

1.1.5 Light-induced spin state change

The spin transition can be induced by light (UV, visible or near IR) in two mains ways: by direct effect on the ion at low temperature (LIESST effect: "*Light Induced Excited Spin State Trapping*") or indirectly through a coordinated ligand (LD-LISC: "*Ligand-Driven Light-Induced Spin Changes*").

Light irradiation effect on SCO compounds was reported for the first time in 1982 by McGarvey and Lawthers [36]. They reported the use of a pulsed laser to perturb the equilibrium between singlet (^{1}A) and quintuplet (^{5}T) states in several Fe (II) complexes SCO in solution. Subsequently, in 1984, the LIESST effect was discovered in the solid state by Decurtins et al. [37]. This solid state effect corresponds to the quantitative trapping of compounds in a metastable HS state by optical pumping at cryogenic temperature (typically below 50 K), in other words, when the relaxation HS → LS, fast at high temperature, is slowed down. They discovered that a light excitation at 530 nm transforms the LS state of the compound $[Fe(ptz)_6](BF_4)_2$ into a metastable HS state whose lifetime at 20 K is greater than a week. The reverse phenomenon (reverse LIESST) was soon demonstrated by Hauser in 1986 on the same compound and corresponds to the switch from the metastable HS state to the LS state by irradiation in the near infrared (λ =820 nm) [38]. The Jablonski diagram (see Figure 1.10) illustrates the LIESST and reverse LIESST effects with vertical transitions and relaxation processes.

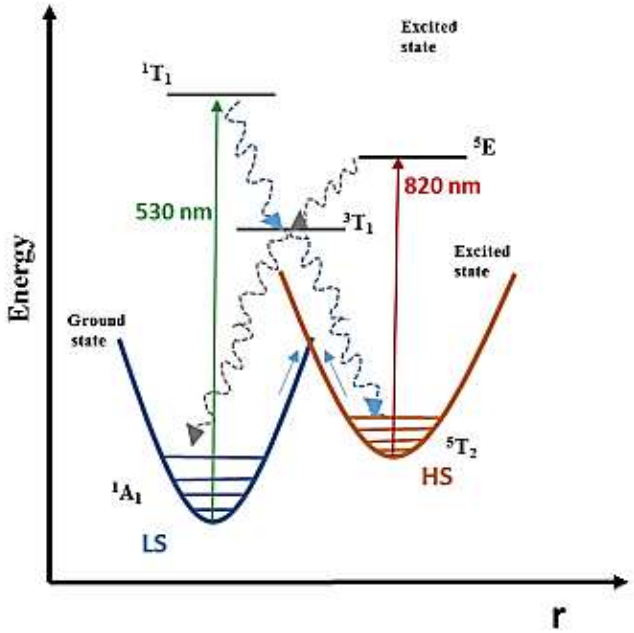

Figure 1.10: Jablonski diagram showing LIESST and reverse LIESST effects: case of the $[Fe(ptz)_6](BF4)_2$ complex [39].

The light induced switching process initially involves a transition from ground state $^1A_1$ to excited state $^1T_1$ which has a short life (< 1ps) [40] and suffers a relaxation into the metastable HS state $^5T_2$. If the temperature is low enough, the system remains trapped in this state due to the energy barrier between the HS and LS states. This phenomenon has been observed for a large number of Fe(II) complexes [41] and it is much less common in the case of Fe(III) [42]. The phenomenon of reverse-LIESST involves irradiating the absorption band of the HS state with a λ = 820 nm wavelength thus populating ^5E state (transition between the $^5T_2$ and ^5E levels). From this state the system can relax to the $^1A_1$ (LS) state.

Ligand-driven light-induced spin change (LD-LISC) was reported first by Zarembowitch et al., in 1992 in order to obtain photo-switchable compounds at higher temperatures than those of the LIESST effect [43]. These studies consist of introducing photo-isomeric ligands in the complex [44]. By irradiation with a wavelength corresponding to the isomerization of the ligand, the ligand field strength and the spin transition behavior change [45, 46]. For example, the [Fe(trans-stpy)$_4$(NCS)$_2$] compound has a gradual spin crossover centered around 180 K while the compound [Fe(cis-stpy)$_4$(NCS)$_2$] remains in the HS state down to 10 K. This difference in magnetic property is attributed to a stronger ligand field in the case of *trans* ligand relative to the *cis* ligand (see Figure 1.11). The LD-LISC effect offers potential applications in the storage of information at room temperature.

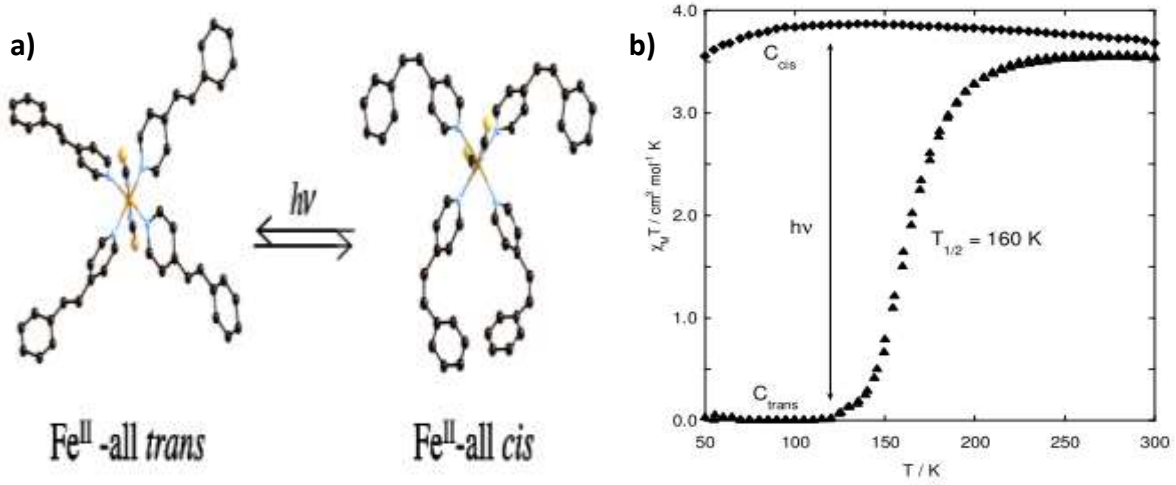

Figure 1.11: a) The crystallographic structure for compound [Fe(trans-stpy)$_4$(NCS)$_2$] and [Fe(cis-stpy)$_4$(NCS)$_2$]. [47] b) Temperature dependence of χ_MT for compound [Fe(stpy)$_4$(NCS)$_2$] in the cis and trans forms [48].

1.2 Spin crossover thin films

Spin crossover compounds present adjustable properties under external stimuli, such as color, magnetic susceptibility, electrical conductivity, dielectric constant and mechanical properties [49-54]. The combination of all these properties gives to this category of materials the status of potential candidate in various areas of technology such as information storage devices, sensors, actuators, displays [52-57] and more recently in hybrid electronics [58], spintronics and optoelectronics [59].

For these applications, the key step that researchers want to overcome today in nanotechnology is related to the size reduction while maintaining crystallinity and the degree of cooperativity in spin-transition materials. Hence, in the last 10 years considerable effort has been made to reach the nanometer scale with SCO compounds [1]. The development of SCO materials at the nanoscale was achieved through several approaches: the synthesis of nanoparticles and nanocomposites or the elaboration of continuous and/or patterned thin films with nanometric thickness. Keeping in mind the potential applications, in this thesis, we will focus on the elaboration and investigation of thin films displaying SCO above room temperature. Before describing our results, in the following sub-chapters, we summarize the main approaches reported in the literature for the fabrication and characterization of SCO films.

1.2.1 Fabrication methods of SCO thin films

Various synthesis variants have been exploited to grow SCO films in a thickness range from the sub-monolayer to several micrometers. A common problem is the elaboration of homogeneous thin films as typically a variety of inhomogeneous thin deposits are obtained. Besides the morphology of the films, another typical issue is the modification/degradation of the SCO properties of the films.

1.2.1.1 Langmuir-Blodgett technique

The first approach used for the elaboration of thin films of spin crossover complexes was the Langmuir-Blodgett technique [60]. This method consists in forming a monolayer of compound on the surface of an aqueous solution through the presence of amphiphilic molecules. By immersion of a solid substrate (see Figure 1.12), it is possible to obtain a film with a monolayer thickness. If several consecutive cycles are applied the final thickness will correspond to the sum of the monolayers.

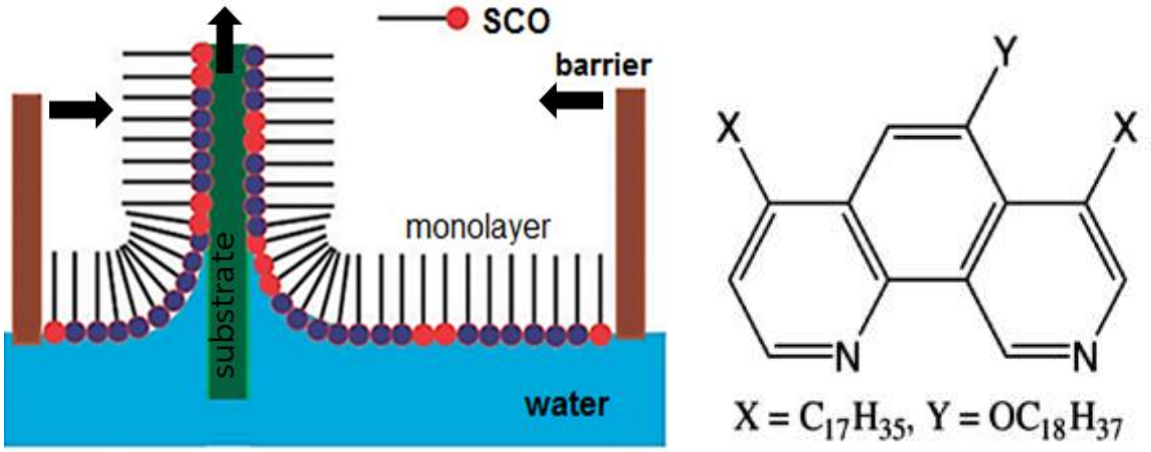

Figure 1.12: Schematic diagram of Langmuir-Blodgett films preparation and schematic view of the phenanthroline ligand modified by hydrophobic chains.

The first fabrication of thin films of SCO compounds using Langmuir-Blodgett method was reported in 1998 by Soyer et al. [61]. This film was developed using an amphiphilic iron (II) complex [$Fe^{II}L_2(NCS)_2$, with L a substituted bipyridine]. The LB technique can provide very good homogeneity and thickness control of the order of one monolayer, but as a disadvantage requires the presence of specific amphiphilic functional groups in the SCO, and is therefore materials-dependent.

1.2.1.2 Spin coating

Spin coating is one of the most commonly used methods in laboratories to grow uniform thin films with calibrated thickness (ranging from a few nanometers to a few microns). This method involves depositing a small amount of solution (coating material) on the center of a rotating substrate (Figure 1.13). The rotation is continued until the solution is homogeneously distributed on the substrate by centrifugal force. Usually, the applied solvent is volatile and simultaneously evaporates. The final thickness of the film depends on the following factors: nature of the solvent, viscosity of the solution, substrate, temperature and the selected deposition parameters (rotational speed, acceleration and time). This method it was used for the first time in 2002 by Bousseksou et al., [62] who deposited by spin-coating a complex mixture of formula [Fe(4R-trz)$_3$]A_2 with polyvinylacetate (PVA) in acetonitrile. In 2007, Matsuda and Tajima have demonstrated the ease of using this method to produce a homogeneous thin film of the complex [Fe(dpp)$_2$](BF_4)$_2$(dpp = 2,6-di(pyrozollyl)pyridine) on a glass substrate. They obtained a thin film with thicknesses of 30 nm and an average roughness close to 3 nm [63]. In the next year, the same team uses this spin coated compound and they succeeded to incorporate it into the

light emitter layer of an organic luminescent device - OLED [59, 64]. In 2010, Tissot and co-workers [65] have "spin-coated" a polymeric silica gel containing the complex of $[Fe((mepy)_3tren)](PF_6)_2$. In this case the spin-coating method triggers the precipitation of nanoparticles of the complex in the polymer matrix. In our team, Félix et al. have used the spin coating method to fabricate nanometric layers of $[Fe(hptrz)_3]$-$(OTs)_2$ (hptrz = 4-heptyl-1,2,4-triazole and OTs = tosylate) on glass substrate and demonstrated that the plasmon resonance can be used to detect de SCO phenomenon in this type of thin films [66]. Also in our team, Quintero et al., elaborated good quality thin films of $[Fe(hptrz)_3](OTs)_2$ doped with acride orange [67]. They demonstrate that the spin state change can be followed through luminescence measurements even in films with thickness below 100 nm (Figure 1.14).

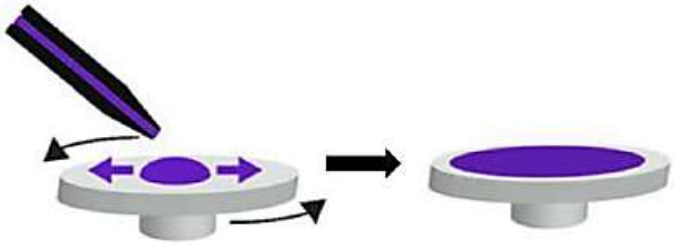

Figure 1.13: Schematic diagram of making a thin film by spin coating

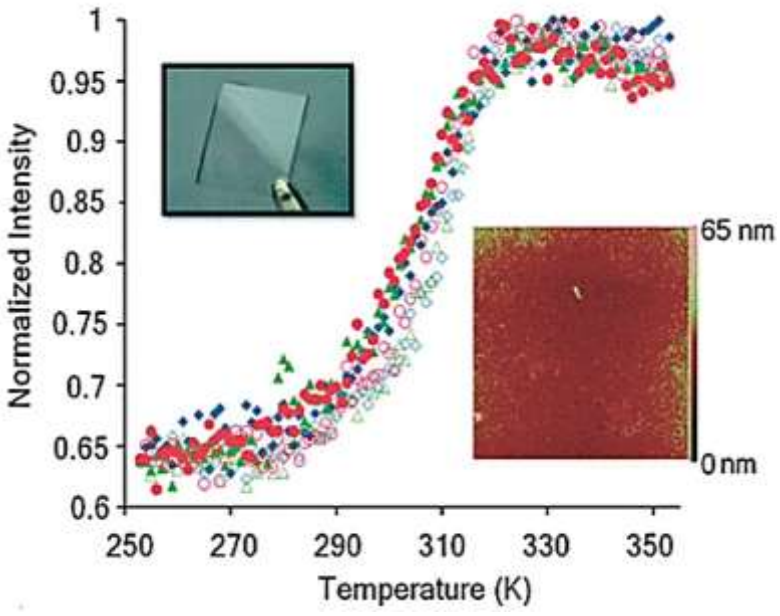

Figure 1.14: Normalized thermal variation of the luminescence intensity at 550 nm with an excitation at 450 nm in a spin coated thin film (85 nm) of $[Fe(hptrz)_3](OTs)_2$ doped with acride orange during three consecutive thermal cycles (dT/dt = 2 K min^{-1}; open and closed symbols for heating and cooling modes, respectively). Insets: photograph of a spin coated SCO thin film on a 1 cm^2 quartz substrate and AFM image (34 × 34 μm^2) of its surface [67].

1.2.1.3 Drop casting

Drop casting is a very simple method for fabricating thin films. The process consists of the deposition of a drop of a solution (mixture of compounds) on a substrate and then the solvent is evaporated in a controlled environment. The critical points are the saturating vapor pressure of the solvent and the evaporation temperature which can accelerate or slow down the evaporation of the solvent. This method suffers from the intrinsic production of non-homogeneous thin films because the solute tends to accumulate to the boundaries of the drop (coffee-stain effect) [68]. The drop casting technique is often used therefore for preliminary tests (to obtain relatively thick deposits) or when the homogeneity of the deposit is not critical.

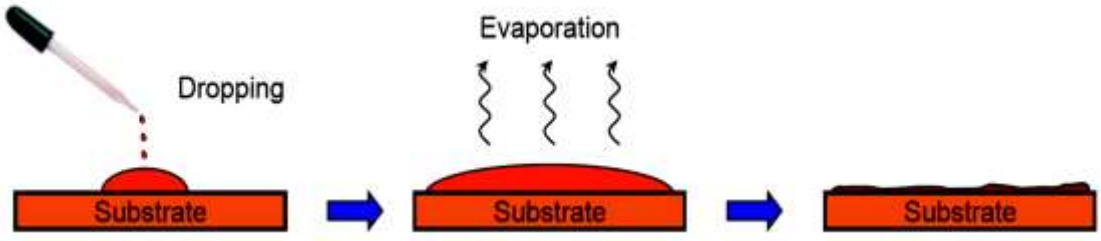

Figure 1.15: Schematic diagram of making a thin film by drop casting

In 2001, Y. Galyametdinov et al.,[69] developed a drop cast film which contains SCO compounds embedded in liquid crystals (LCs). This material was based on a Fe(III) complex combining both LC and SCO properties. In this case, the spin transition and liquid crystal properties did not operate in the same temperature range. The compound has a gradual spin transition between 300 K and 80 K, while the appearance of the smectic phase occurs around 400 K. In 2006, Seredyuk et al. [70] have reported the design and successful synthesis of SCO liquid crystals operating around the room temperature. This was possible by using a triazole ligand functionalized by aromatic/alkyl chains [3,5-dialkoxy-N-4H-1,2,4-triazol-4-ylbenzamide ligands with $Fe(4\text{-}MeC_6H_4\text{-}SO_3)_2$ salt], resulting in a polymer complex with the formula $[Fe(Cn\text{-}trz)_3](4\text{-}Me\text{-}C_6H_4SO_3)\cdot H_2O$. The SCO behavior occurs in this case in the temperature range where the material shows a discotic columnar mesophase. In the same year, Kuroiwa and co-workers, reported a new class of SCO compounds able to form thin films by casting, using ligands functionalized with lipophilic groups [71]. The SCO properties of lipophilic, supramolecular Fe(II)-1,2,4-triazole complexes were investigated in chloroform and cast films. The obtained film showed a reversible abrupt spin-crossover accompanied by thermal hysteresis. The observed bistability was related to dynamic structural transformations between lamellar and hexagonal structures.

1.2.1.4 Sequential surface assembly

The sequential assembly makes it possible to obtain films of nanometric thicknesses and controllable compositions by immersion of a substrate in a series of different chemical solutions containing the reagents. In other words it consists of the direct synthesis of the SCO complex on the surface of different substrates (see figure 1.16). This approach needs a set-up similar to dip-coating.

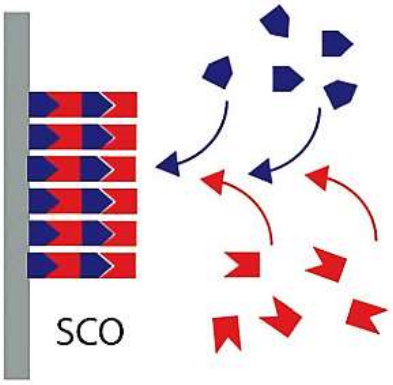

Figure 1.16: Schematic diagram of making a thin film by the sequential assembly method.

In 2003, Nakamoto et al. synthesized films of the $[Fe^{II}(H\text{-}trz)_3]_n$ complex by using an ion-exchange resin (Nafion) as counter anion [72]. The SCO complex film preparation consisted in immersing the Nafion substrate in an aqueous solution of $FeSO_4$ followed by an immersion in a methanol solution of 1,2,4-triazole (see Figure. 1.17). They reported that the thin films exhibit a spin crossover phenomenon at about 260 K and the existence of one-dimensional chain structure of $[Fe^{II}(H\text{-}trz)_3]_n$ on Nafion was proved by means of EXAFS. Using the same method, Hajime et al., reported the synthesis of Fe(1,8-diaminosarcophagine) which preserve the SCO phenomenon as in the bulk and capable of working as a sensor for protons [73].

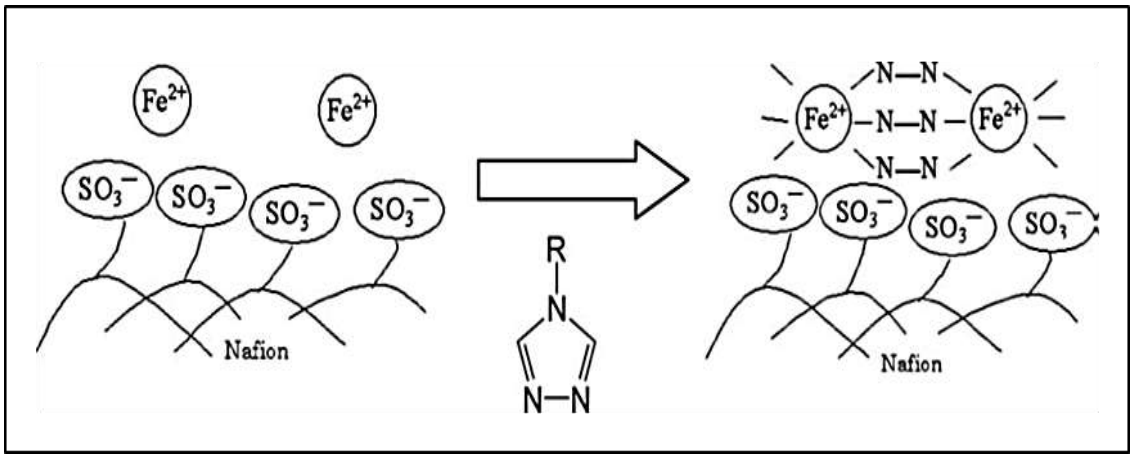

Figure 1.17: Schematic film preparation process of Fe^{II}(R-trz)-Nafion (N-N is the R-trz ligand) [72].

Films of three-dimensional (3D) coordination networks can be also made by sequential assembly via successive adsorption reactions involving the formation of coordination bonds within a layer, but also between the different layers constituting the 3D networks. Our group was interested in this perspective and in 2006, Cobo et al. reported the fabrication of thin films using the sequential assembly of three dimensional SCO coordination polymers [Fe(pyrazine){M(CN)$_4$}] (M=Ni, Pd, or Pt) via coordination reactions [74]. A gold-coated silicon substrate was first functionalized with a disulfide-based anchoring layer to ensure a quasi-epitaxy between the surface and the material to be deposited. Then, the process comprises a number of deposition cycles, each cycle corresponding to the assembly of the iron center, the tetracyanometalate unit and the pyrazine ligand (see Figure 1.18). It should be noted that in this case, all the reactions were conducted at low temperature (- 60 °C) to reduce the desorption rate of the coordinated species. The multilayers obtained revealed a hysteresis loop with a width of 25 K centered around 310 K. This approach has been extended to novel coordination polymers displaying thermal, guest and light-induced SCO phenomena [75-77].

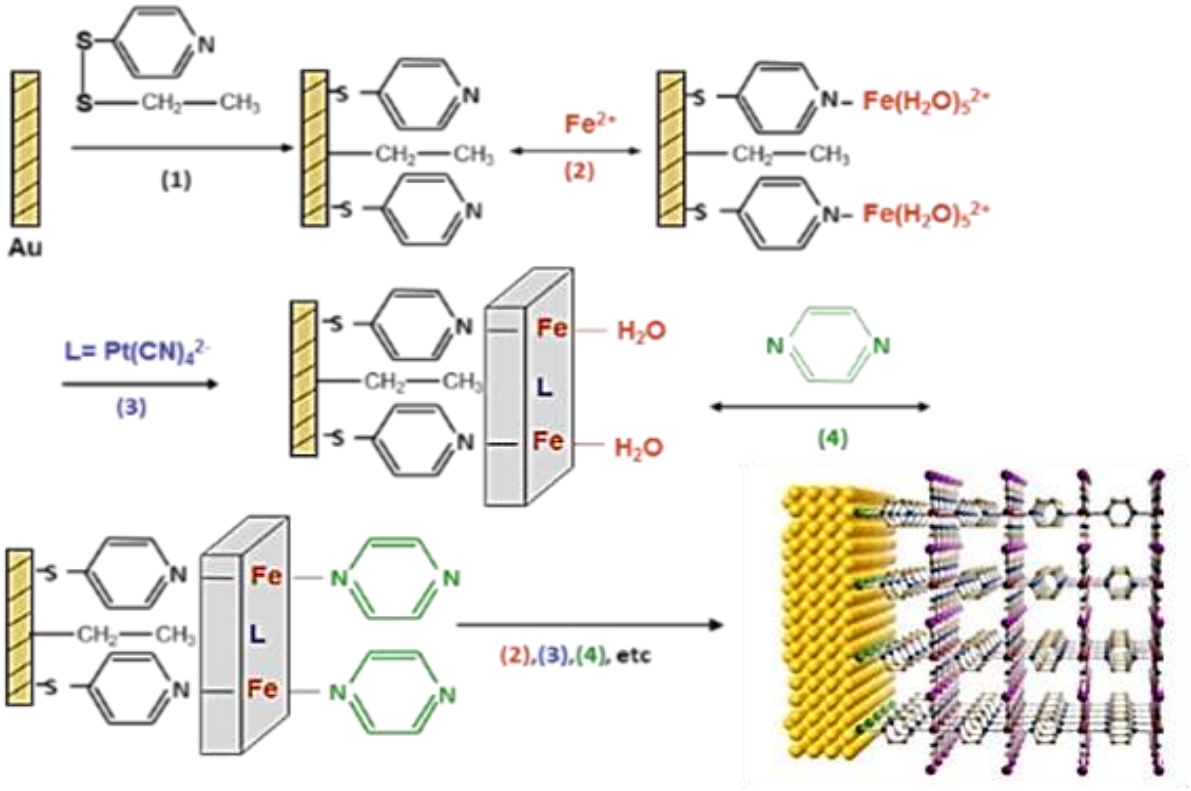

Figure 1.18: Film preparation process (layer by layer) of the compound [Fe(pyrazine){Pt(CN)$_4$}] by the successive adsorption of metal ions and ligands.

1.2.1.5 Micro and nanopatterning of films

To fabricate nanoscale objects, one may use two major approaches: top-down or bottom-up. In the former case, one starts with a (relatively) large object, which is cut it into smaller pieces until it is nanosized. Vice-versa the bottom-up fabrication consists of building a nano-object from atoms and/or molecules. In the SCO field different top down approaches, including lithographic and non-lithographic methods (lift-off processes, micro-contact printing, shadow masks, etc.) have been explored to generate distinct patterns of SCO films [78].

In 2007, for the first time, our group reported a process for nano and microscale assembly of the 3D spin-crossover coordination polymer [Fe(pyrazine){Pt(CN)$_4$}] by using a combination of top-down (lift-off) and bottom-up (multilayer sequential assembly) methods [79]. At first, a gold-coated silicon surface was covered by a conventional polymethylmethacrylate (PMMA) EBL resist, in which square-shaped patterns of different size and density have been written by a focused electron beam. Then the spin crossover complexes were deposited both in the openings of the resist as well as on top of the PMMA. Finally, the patterns were transferred by lifting off the PMMA. Remarkably, regular patterns of [Fe(pyrazine){Pt(CN)$_4$}] could be formed on the surfaces down to 50 nm lateral sizes, which display SCO properties.

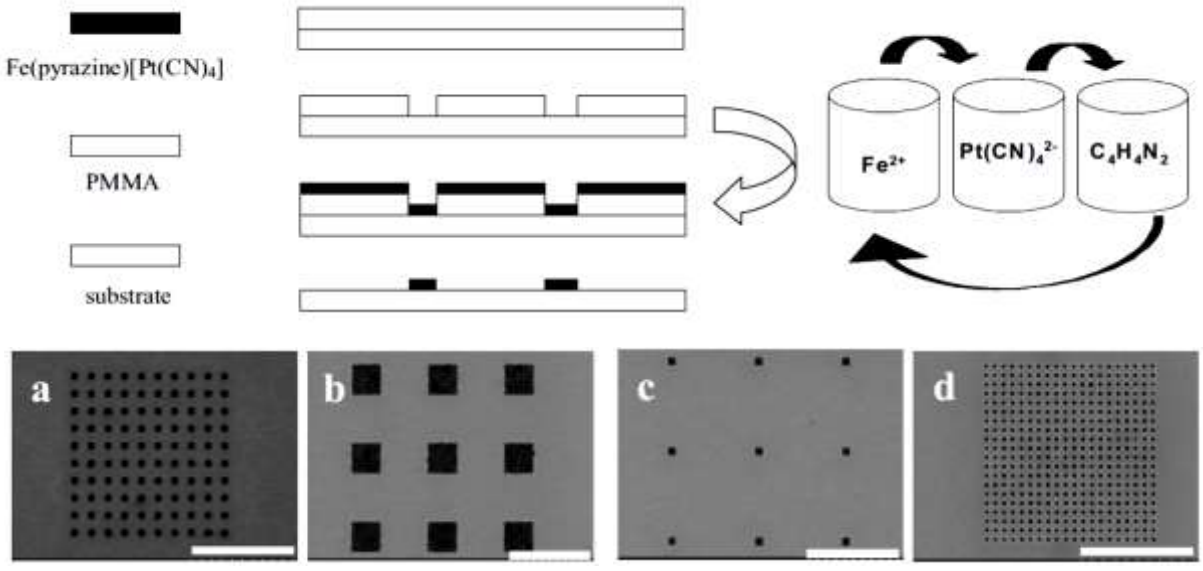

Figure 1.19: Schematic procedure for the patterning of [Fe(pyrazine){Pt(CN)$_4$}] (top) and SEM images of patterns of [Fe(pyrazine){Pt(CN)$_4$}] (bottom) [79].

1.2.1.6 Thermal evaporation

One of the most desirable configuration of SCO materials for the development of nano-devices would be homogeneous thin films whose thickness can be adjusted with nanometric precision. Vacuum deposition of materials by thermal evaporation seems to be one of the best techniques to achieve such controlled, high quality, clean and homogeneous films (see Figure 1.20).

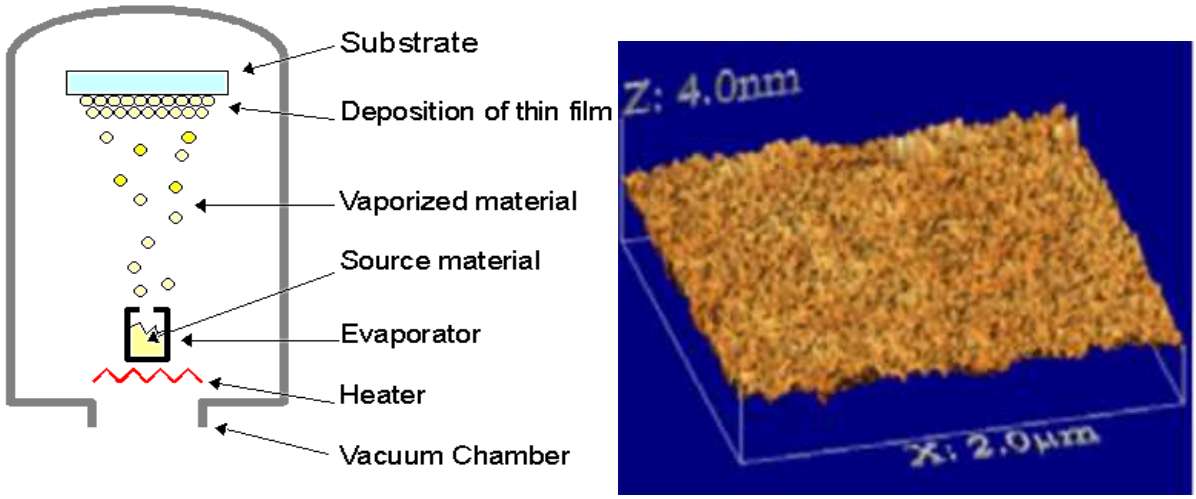

Figure 1.20: Schematic representation of vacuum sublimation and AFM image of a vacuum evaporated film of $Fe(phen)_2(NCS)_2$ [58].

However, only a very limited number of spin crossover compounds can be deposited by this technique. From the existing literature, to our knowledge, up to now only 10 evaporable SCO complexes have been investigated to this purpose, including mainly the ferrous pyrazolylborate complexes, $[Fe(HB(pz)_3)_2]$(pz=pyrazolyl),[80] $[Fe((3,5\text{-}(CH_3)_2pz)_3BH)_2]$, [81] $[Fe(H_2B(pz)_2)_2(L)]$ with L = 2,2'-bipyridine 4 or 1,10-phenanthroline (phen), [82, 83] and the derivatives of the latter with L = 4-methyl-phen, 5-chloro-phen, 4,7-dichloro-phen, 4,7-dimethyl-phen, [84] and 3,4,7,8-tetramethyl-phen, [85] as well as the complexes $Fe^{II}(phen)_2(NCS)_2$ [58, 86] and $[Fe^{II}(NCS)_2L]$ (L = 1-{6-[1,1-di(pyridin-2-yl)ethyl]-pyridin-2-yl}-N,N-dimethylmethanne) [87].

These compounds allowed remarkable developments in the last six years for the investigation of the SCO phenomenon in single molecules and/or in ultra-thin films. In particular, a series of scanning tunneling microscopy (STM) investigations [88-93] provided convincing evidence for the possibility to detect and manipulate the spin-state of individual molecules on surfaces opening new exciting perspectives for the fields of molecular electronics and spintronics. As it can be expected [94] the subject of the interaction between the molecules

and the substrate surface has proven to be of particular importance and therefore, this issue has been addressed by different X-ray and UV-spectroscopic techniques [81, 87, 95-103]. Besides the fields of molecular electronics, evaporable SCO molecules are also of great interest for the possibility of their "faultless" integration into various nanoscale devices. This was demonstrated for micro-electromechanical (MEMS) [104] and electronic [80, 105, 106] devices but one can also predict their preferential use in a range of photonic applications requiring high quality films [107].

Unfortunately, the spin transition temperature of the evaporable SCO compounds reported up to now falls far below room temperature, except for **[**$Fe(HB(pz)_3)_2$], which shows, however, an extremely gradual spin conversion [108]. In addition, not all of the compounds could be obtained as high quality crystalline films. For example, films of 1,10-phenanthroline (phen) are smooth and continuous, but are also amorphous and exhibit a very gradual SCO in contrast to the bulk compound [83]. In order to facilitate the integration of SCO materials into 'real-world' applications there is still a strong need for evaporable complexes, which can form high quality films with SCO at technologically relevant temperatures. In order to be sublimated, these compounds should meet several requirements. First, they should be neutral, have low molecular weight, thermally stable and should not contain other molecules, such as solvents and other guests, in the lattice. All these features must be combined with the presence of a reproducible and reversible SCO behavior above room temperature, which is maintained also by the films.

Considering all these aspects, we examined the 'forgotten' SCO complex [$Fe(HB(tz)_3)_2$] (tz = triazolyl). The synthesis of this compound was pioneered by Trofimenko *et al.* [109] already in 1967 and it was investigated by the groups of Janiak and Miller later on [110-113]. Recently, our group has reinvestigated the bulk compound [114]. In particular, we could obtain single crystal X-ray structural data in the low spin (LS) and high spin (HS) forms and we have shown that the abrupt spin transition around 333 K is isostructural and very robust over successive thermal cycling. In addition, the possibility to form films by vacuum sublimation, which we used to purify the complex, was also evidenced. In the next chapter, we will present more in detail the properties of this sublimable SCO complex.

1.2.2 Characterization methods of spin crossover thin films

SCO complexes undergo drastic variations in their crystallographic structure, but also in terms of electronic, magnetic, vibrational, and optical properties. The detection of the spin transition can be realized therefore by a variety of methods as a function of the different controllable external parameters (temperature, light irradiation, pressure, etc.). For the characterization of bulk SCO materials, the most common techniques are magnetic susceptibility measurements, Mössbauer spectroscopy, X-ray diffraction, UV-Vis optical absorption/reflectance measurements, vibrational spectroscopy (FTIR and Raman) and calorimetry. In the following we will highlight those, which are best suited for the characterization of SCO films and discuss emerging methods (refractive index sensing, scanning probe microscopies and X-ray spectroscopies), which are better adapted for the study of very thin films.

Magnetic susceptibility measurements are probably the most used in history to characterize the SCO materials [115, 116]. In general, superconducting quantum interference device (SQUID) magnetometers are used and the change between the HS and LS states is put in evidence by the variation of the magnetic susceptibility (χ_M) of the SCO compound as a function of temperature ($\chi_M(T)$). For a paramagnetic material, the product $\chi_M T$ is constant at any temperature, according to the Curie law. Therefore, this representation allows us to find the transition temperature of a SCO compound. The magnetic susceptibility χ_M for a spin crossover compound is determined by the temperature dependence of the contribution χ_{HS} and χ_{LS}, according with the following equation:

$$\chi_M(T) = \gamma_{HS}(T)\chi_{HS} + (1-\gamma_{HS}(T))\chi_{LS} \quad (1.15)$$

If we know the susceptibilities of the pure HS and LS states, the HS mole fraction can be easily determined and represented as a function of T to obtain the spin transition curve. However, most often we represent χT vs. T (when χ_{HS} and χ_{LS} are not known or determined imprecisely). Magnetometry has been used to investigate SCO films (see for example Figure 1.21), but this technique meets severe sensibility limitations for films below a few hundred nm thickness. To increase the detection limit often the films are deposited on flexible substrates (e.g. Kapton), which is then rolled on in order to be able to introduce a higher quantity of materials into the magnetometer.

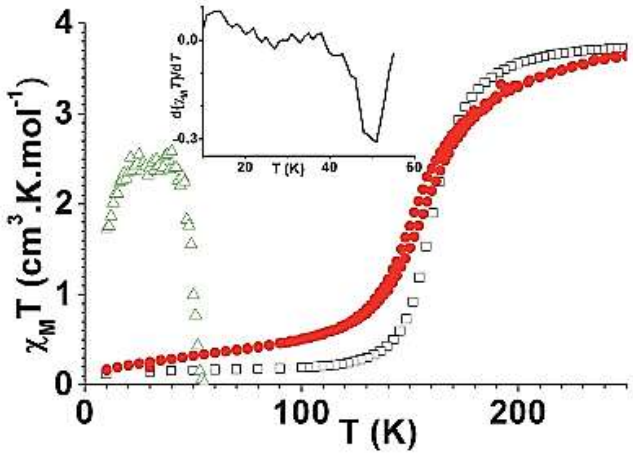

Figure 1.21: Temperature dependence of χT for [Fe(H_2Bpz)$_2$(bipy)]: bulk at 1 T (black squares), thin film at 1 T on Kapton (red filled circles), and after irradiation at 5 T (green triangles) [83].

Crystallographic measurements such as X-ray diffraction techniques can be used to obtain the structural evolution of crystalline solids upon the SCO by measuring the unit cell parameters, the elongation of the metal-ligand distances and also the deformations of the angles between bonds [117]. Both single crystal and powder X- ray diffraction techniques can yield detailed structural insights into the SCO phenomenon and have been extensively exploited within the field. Unfortunately, X-ray diffraction measurements of nanometric thin films using conventional methods generally produces a week signal from the film and an intense signal from the substrate. One of the ways to avoid/reduce this problem is to perform measurements with a fixed grazing angle of incidence, popularly known as GIXRD. In this diffraction geometry, only crystal planes parallel to the substrate can be observed. This allows probing the crystallinity and crystal structure as well as to determine the orientation of the film (if any). As an example Figure 1.22 shows the angle-dependent GIXRD study of the SCO complex [Fe(qnal)$_2$] [118].

Vibrational spectroscopic measurements, including both infrared absorption and Raman spectroscopies, are frequently used to characterize SCO complexes since the bond strength between the SCO metal and its ligands change significantly from one spin state to the other. Therefore, there will be vibrational modes characteristic of each spin state, which can be easily recognized due to the corresponding peak position and intensity change. Currently, these methods have been extended and coupled to optical microscopes in order to perform localized micro-Raman and micro-IR spectroscopies, which constitute the preferred means for the

investigation of micro and nano-scale samples. Figure 1.23 shows a typical investigation wherein thermal and light induced SCO was demonstrated in a film of the complex {Fe(azpy)[Pd(CN)$_4$]} by Raman spectroscopy [75]. Yet, often the spectroscopic signals are rather weak and further work towards signal enhancement using SERS (surface-enhanced Raman spectroscopy) or PMIRAS (Phase Modulation Infrared Reflection Absorption Spectroscopy) will be necessary.

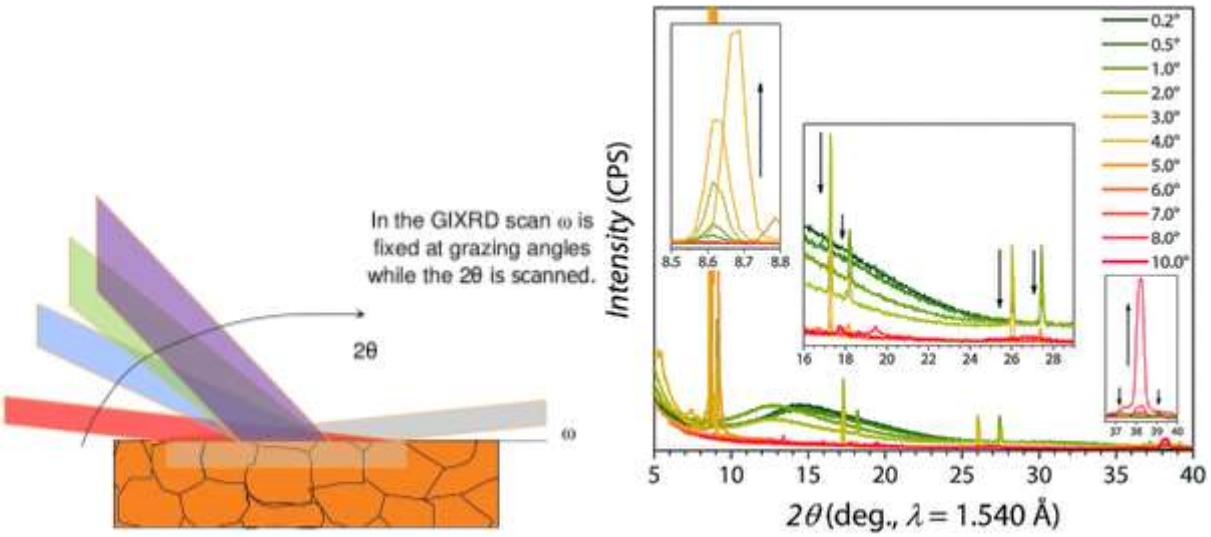

Figure 1.22: (Left) Principle of the GIXRD experiment. (Right) GIXRD pattern (5–40 2θ) of the SCO film [Fe(qnal)$_2$] at different incident angles (see legend). Insets show the principal diffraction peak (left), the higher-order peaks (middle), and the peak of the gold surface (right) in detail. Arrows indicate the intensity change upon incident angle increase [118].

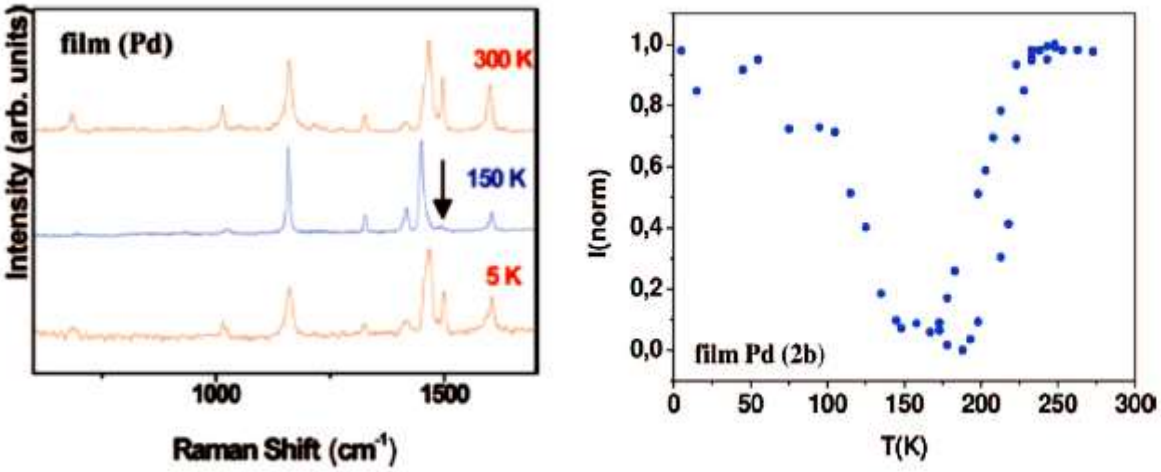

Figure 1.23: Raman spectra of a thin film of {Fe(azpy)[Pd(CN)$_4$]} at selected temperatures and normalized temperature dependence of the Raman marker peak at 1497 cm^{-1} revealing successive thermal (HS to LS) and light induced (LS to HS) spin transitions upon cooling [75].

Optical reflectivity/absorption measurements are based on changes in the electronic absorption properties of materials during spin transition [11, 119]. For obvious reasons, different electronic absorption bands appear in the HS and LS electronic states in the UV-Vis-NIR spectral ranges when considering ligand field (LF) or metal-ligand charge transfer (MLCT or LMCT) transitions. On the other hand, intra-ligand (IL) transitions might not be much affected by the SCO. (N.B. Less frequently MMCT and ILCT transition may also occur in SCO complexes.) In general, the HS state of iron (II) complexes is usually less colored compared to that of the LS state, which allows for the straightforward monitoring of the SCO phenomenon by optical reflectivity and absorption spectroscopies. However, in thin films these color changes cannot be always detected – in particular in the case of weak LF transitions, hence MLCT transitions (occurring often in the UV range) are preferentially monitored (see for example Figure 1.24).

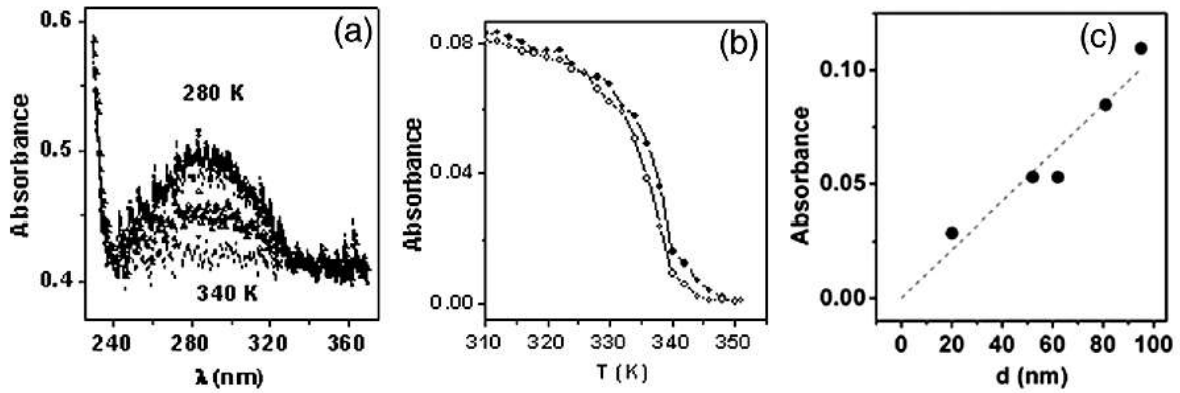

Figure 1.24: (a) Selected temperature-dependent absorption spectra of an 80-nm thin film of the compound $[Fe(hptrz)_3](OTs)_2$ in the UV spectral region. (b) Temperature dependence of the absorbance of the same film at 285 nm. (c) Variation of the absorbance at 285 nm as a function of the film thickness allowing to deduce an absorption coefficient of ca. 10000 cm^{-1} [120].

Refractive index sensing is an emerging approach to detect the spin transition in nanometric thin films. Indeed, SCO materials exhibit important changes of the refractive index through the whole UV–vis–IR spectral ranges due primarily to the important density change accompanying the spin state. As mentioned before, the unit cell expansion ($\Delta V/V$) upon the SCO varies typically between 1 and 10 %, depending on the nature of the compound. As a consequence of this significant density change, we expect a change of the real part of the refractive index upon SCO in the range between $\Delta n = 0.01 - 0.1$. Various approaches, including simple specular reflectivity measurements and more complex ellipsometry [121], SPR (surface plasmon

resonance – see Figure 1.25) spectroscopy [66] and optical diffraction [121] have been successfully employed to follow the spin state changes in very thin SCO films (down to a few nm thickness).

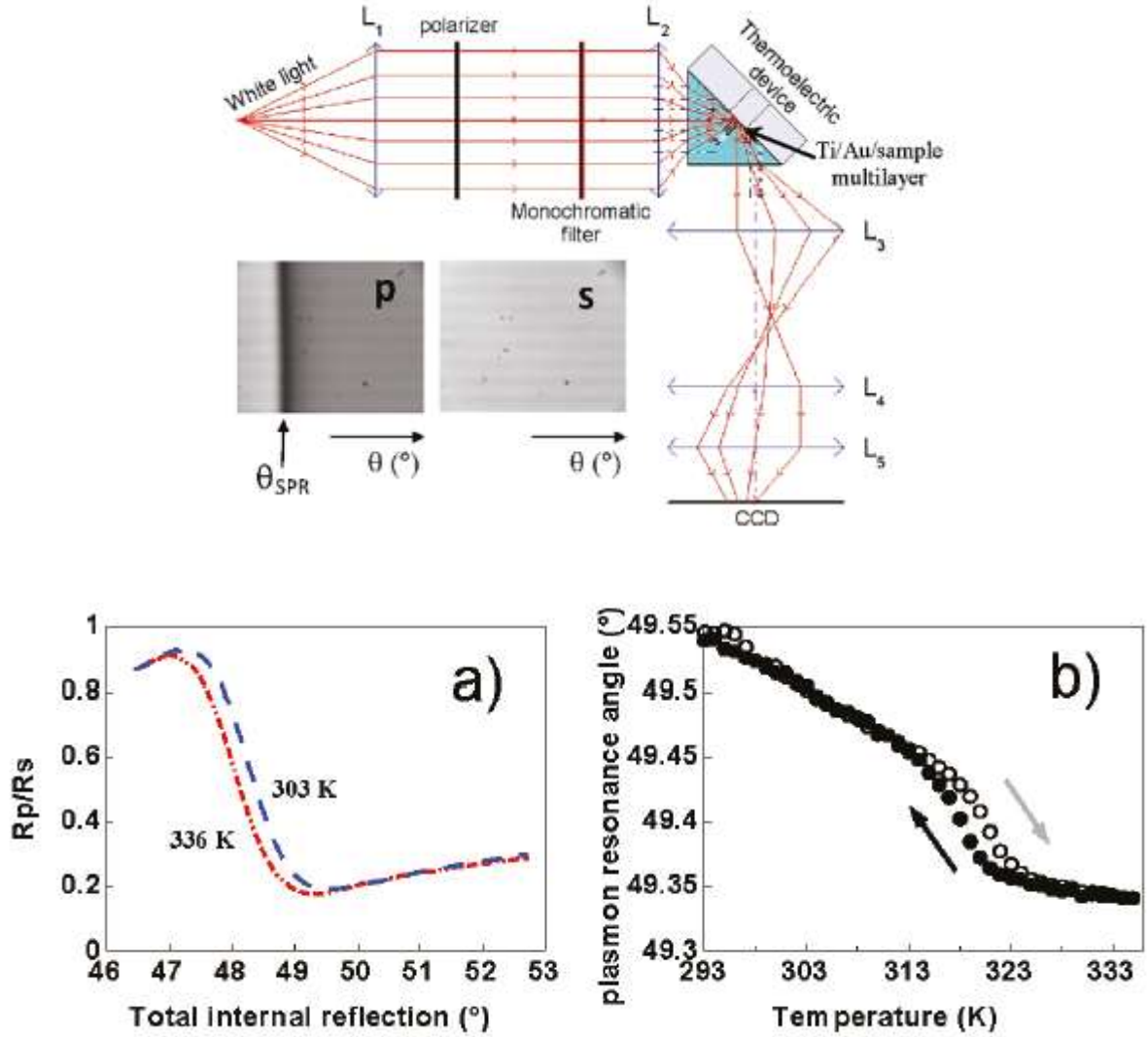

Figure 1.25: Upper panel: SPR setup developed at the LCC-CNRS. Lower panel: (a) Angle-dependent reflectance spectra of a glass/Ti (5 nm)/Au (45 nm)/[Fe(hptrz)3](OTs)2 (30 nm) multilayer at 303K (LS state) and 336 K (HS state) (λ = 660 nm). (b) Temperature dependence of the plasmon resonance angle (reflectance minima) of the multilayer in the heating and cooling modes (dT/dt = 2 K/min) [66].

The previously mentioned SCO film characterization techniques are usually accessible locally in research laboratories. On the other hand, **X-ray spectroscopies** are mostly accessible at synchrotron light sources. X-ray spectroscopy encompasses a range of techniques where spectroscopic information is gained from a process in which a core hole is created by an X-ray photon. Such techniques can provide unique insight into the electronic and molecular structure, often combined with element-, spin-, orbital-, and orientational sensitivity and are particularly

well adapted for investigating SCO films down to the sub-monolayer thickness [122]. The most common of these techniques is X-ray absorption spectroscopy (XAS) with its variants: X-ray absorption near edge structure (XANES) and extended X-ray absorption fine structure (EXAFS), which have proven their utility in determining the spin state and the local structure around the absorbing SCO metal ion, respectively (see Figure 1.26 for an example). Another important technique is XPS (X-ray photoelectron spectroscopy), which is based on the emission of electrons from atoms induced by absorption of X-ray photons. The XPS spectra characterizes the electron binding energy and allows thus to determine (among other informations) the oxidation and spin state of SCO materials. Owing to the short mean free path of electrons in condensed matter, XPS is particularly well suited for the measurement of films with thicknesses of up to a few nanometers.

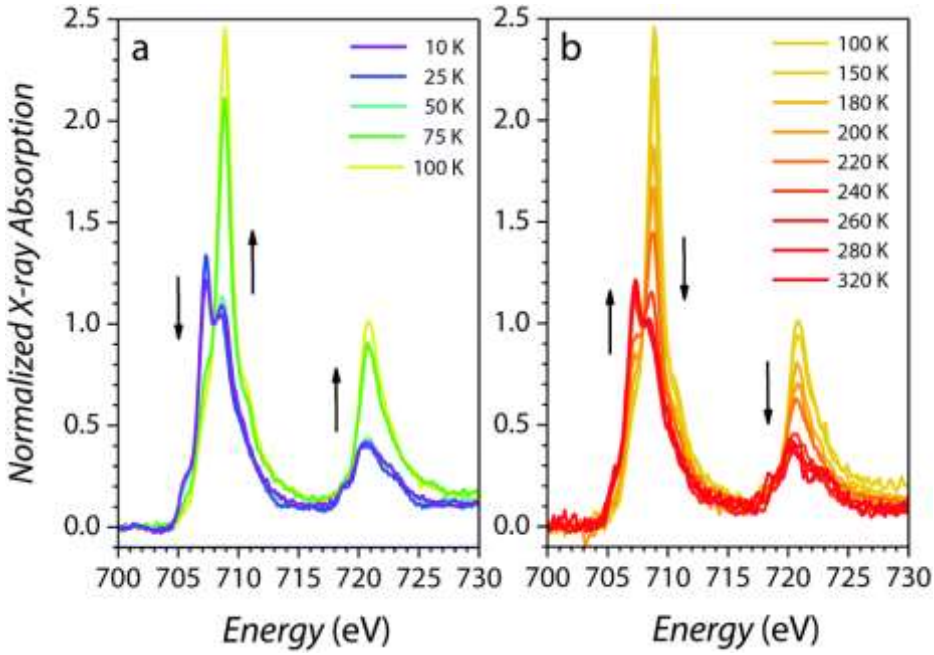

Figure 1.26: Temperature dependent XAS spectra of the SCO film [Fe(qnal)$_2$] revealing both X-ray induced (a) and temperature induced (b) spin state changes [118].

Scanning probe microscopy (SPM) refers to a family of surface analysis methods, which use a nanometric probe ("SPM tip") in interaction with a sample surface and a scanner, which allows to control with nanometric precision the position of the probe with respect to the surface, both laterally and vertically. Beyond their surface imaging capabilities they provide also access to various material properties, such as surface charge and electro-magnetic field distributions, elastic moduli, thermal conductivity, etc. In the SCO field, until now, most of the published SPM results have been obtained using Scanning Tunneling Microscopy (STM), which probes

the local electronic structure of a surface with atomic resolution. This technique provided in the past few years a number of exciting results – such as the role of molecule – substrate interaction on the SCO properties (see Figure 1.27 for an example).

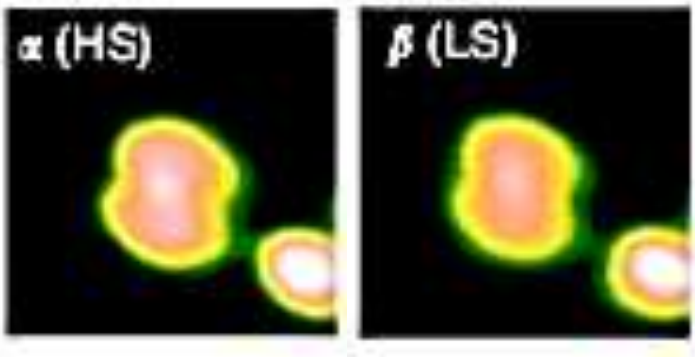

Figure 1.27: STM topographic images of a single $Fe(phen)_2(NCS)_2$ molecule in the HS and LS states. Molecules were deposited on a $Cu_2N/Cu(100)$ substrate. Each image is 3.7 × 3.7 nm^2 large [91].

However, STM can be used only to investigate the properties of isolated SCO molecules as well as molecules in ultrathin films consisting of only one or two layers. In this respect, atomic force microscopy (AFM) appears a more promising approach for the investigation of SCO films consisting of more than a few layers. In this thesis, we will focus therefore on the use of AFM approaches (see chapter 5). Variable temperature AFM has been previously used in our team to investigate a few SCO materials. Single crystals of the SCO complex $\{Fe(pyrazine)[Pt(CN)_4]\}$ have been imaged simultaneously by AFM (topography scans) and near-field scanning optical microscopy (NSOM) across the first-order thermal spin transition with sub-micrometer spatial resolution [123]. It was shown that the spin transition is accompanied by both reversible and irreversible (fatigue) changes of the surface topography of the crystals. The hysteresis associated with the spin transition could be reproduced both from the AFM topographic features and from the NSOM data (Figure 1.28).

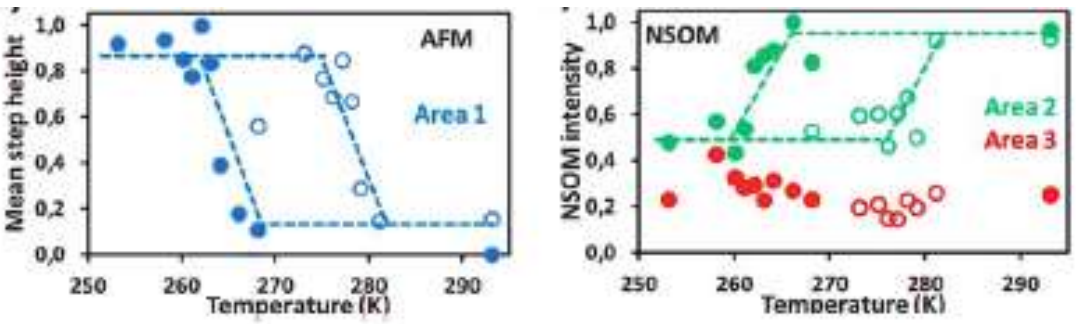

Figure 1.28: (left) Temperature dependence of the AFM topography (step height) and NSOM intensity on a selected surface area of a single crystal of $\{Fe(pyrazine)[Pt(CN)_4]\}$ around the spin transition [123].

NSOM was also used to detect the spin transition in nanocrystalline films of the SCO complex $[Fe(Htrz)_2(trz)]BF_4$ (Htrz = 1,2,4-triazole and trz = 1,2,4-triazolato) and we suggested that this approach may open up perspectives for micro- and nano-thermometry measurements with sub-wavelength spatial resolution [124]. Variable temperature AFM topography measurements on the same film revealed drastic changes of the surface topography upon the thermal spin transition, including both reversible and irreversible changes (Figure 1.29) [125]. These changes were correlated with the SCO behavior of this sample and it was suggested that the well-known shift of the spin transition temperature between the first and second heating cycles might arise due to microstructural changes in the sample. Interestingly, a slow recovery of the 'irreversible' morphology changes was also observed on a time scale of several weeks.

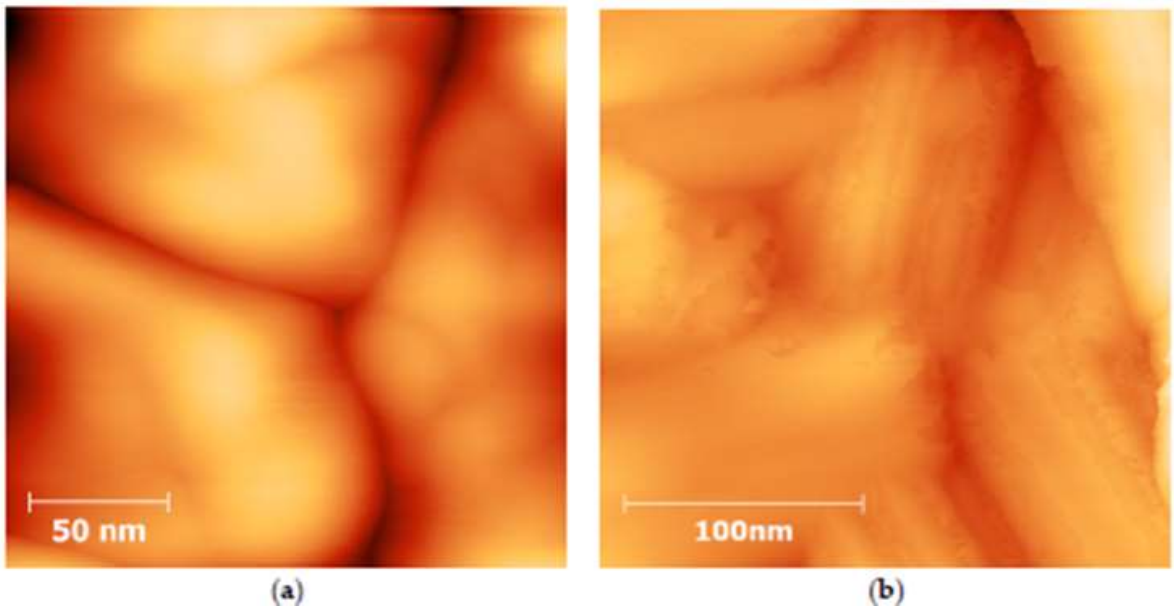

Figure 1.29: High resolution AFM topography images obtained (a) on a fresh film of $[Fe(Htrz)_2(trz)]BF_4$ and (b) after eight spin state switching cycles [125].

While the $[Fe(Htrz)_2(trz)]BF_4$ films exhibited a very significant microstructural reorganization during the spin transition, films of the related iron-triazole complex $[Fe(hptrz)_3](OTs)_2$ (hptrz = 4-heptyl-1,2,4-triazole, OTs = tosylate) displayed no discernible surface topography changes between the HS and LS forms [126]. On the other hand, the quantitative nano-mechanical analysis of these films allowed to evidence a decrease of the Young's modulus by ca. 25-30 % when going from the LS (1.7 GPa) to the HS (1.3 GPa) state – in line with the well-known softening of metal-ligand bonds in the HS state (Figure 1.30). These measurements provide thus scope for high-resolution quantitative imaging of the spin transition in thin molecular layers.

Nevertheless, several serious experimental challenges have been also evidenced during these experiments. In particular, it was shown that the geometry of the AFM probe changes continuously during the scans making any quantitative analysis difficult. In addition, whenever the temperature of the sample and the probe is different heat exchange may occur, leading to erroneous temperature readings - up to several tens of degrees [127].

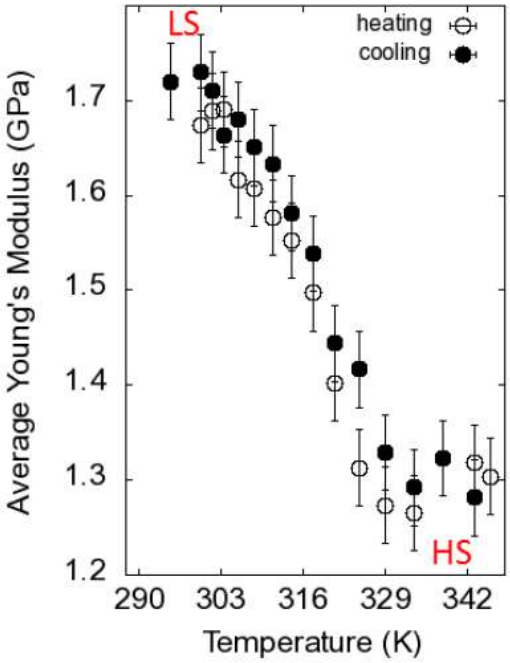

Figure 1.30: Temperature dependence of the Young's modulus of a 40 nm thick film of $[Fe(hptrz)_3](OTs)_2$ in the heating and cooling modes determined by AFM [126].

Chapter 2. Elaboration of thin films of $[Fe(HB(tz)_3)_2]$

Outside the field of spin-transition materials, the technique of vacuum evaporation is widely used for the manufacture of thin films of controllable thicknesses by playing on the temperature, the duration of deposition and the vacuum reached in the sublimator chamber. Moreover, this technique can be easily integrated into the processes used in the electronics industry. In this chapter we discuss the growth of high-quality films of the $[Fe(HB(tz)_3)_2]$ SCO complex by thermal evaporation and we show these films exhibit a fully reversible spin transition above room temperature in ambient air upon repeated thermal cycling.

2.1 Pristine thermally evaporated thin films

We are interested in the $[Fe(HB(tz)_3)_2]$ complex, which contains poly(azolylborate) ligands of the scorpionate type (hydrotris triazolylborate $HB(tz)_3$). This mononuclear complex is neutral and low weight, which makes it a good candidate for sublimation.

The solvent-free crystals of $[Fe(HB(tz)_3)_2]$ crystallize in an orthorhombic space group Pbca with half a complex molecule in the asymmetric unit; the second half being generated by the symmetry operation 1-x,1−y, 1−z [114] (see Figure 2.1) [114].

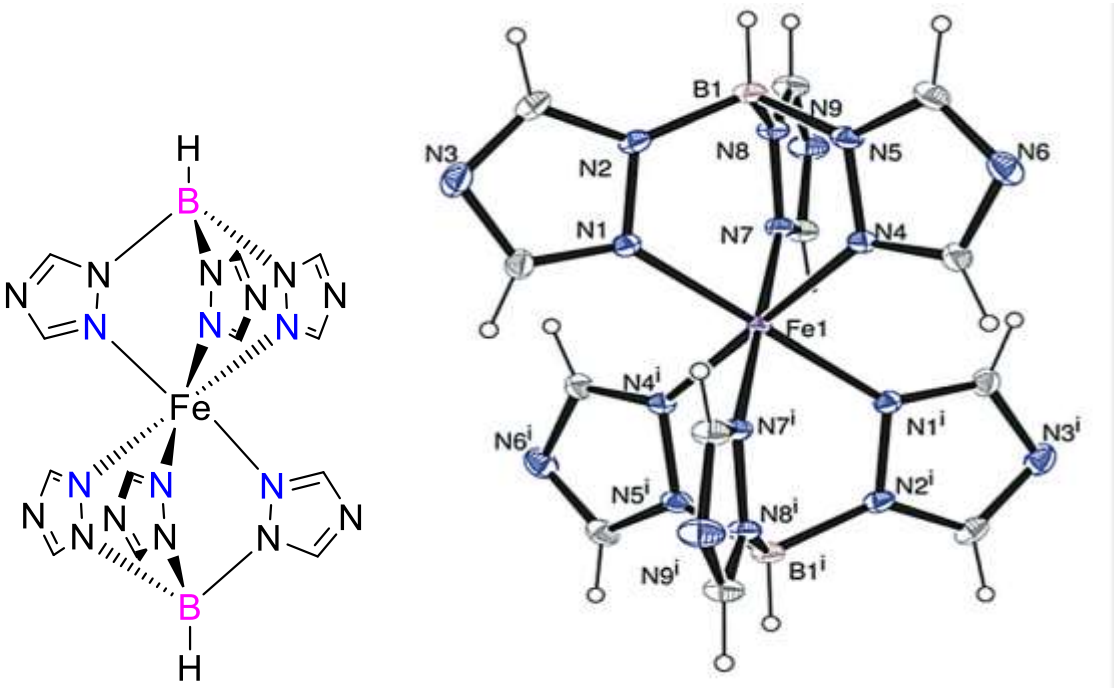

Figure 2.1: Schematic drawing and structural view of the complex $[Fe(HB(tz)_3)_2]$.

Magnetic susceptibility measurements performed on powder samples revealed spin transition temperatures of $T_{1/2}^{\downarrow}$ = 332 K for the cooling mode and $T_{1/2}^{\uparrow}$ = 334 K for the heating mode, indicating thus a narrow hysteresis loop of ca. 2 K width (Figure 2.2). This (isostructural) spin transition is accompanied by a nearly isotropic change of the Fe^{II}–N bond lengths (8.3 ± 0.5 %) and a highly anisotropic unit cell volume change (4.6 %). The very high cooperativity of the spin transition in this compound (Γ =5700 ± 50 J mol^{-1}) is rather unusual in mononuclear SCO compounds. This property can be related to the dense crystal packing and relatively high stiffness of the lattice (Debye temperature θ_D =198 ± 2 K), which involves numerous C–H···N hydrogen contacts between each molecule with fourteen neighboring molecules [114].

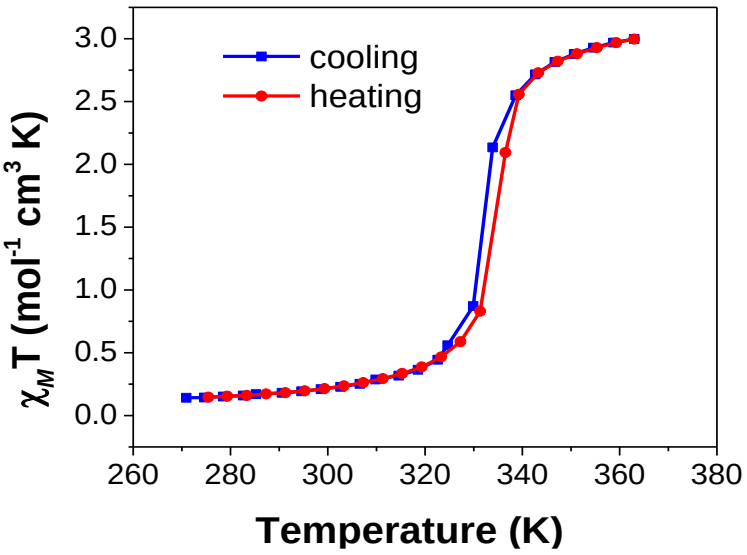

Figure 2.2: Temperature dependence of molar magnetic susceptibility of the powder of $[Fe(HB(tz)_3)_2]$ in the heating and cooling modes.

Reagents and solvents used in this study are commercially available. The solvent-free microcrystalline powder of $[Fe(HB(tz)_3)_2]$ was synthesized and obtained in our group by Sylvain Rat as described in ref [114]. Thin films were grown by thermal evaporation in a PREVAC thermal deposition system (see Figure 2.3) at a base pressure of ca. 2 x 10^{-7} mbar. The bulk powder was first purified by sublimation and then evaporated at 250 °C at a rate 0.03 Å/s. The evaporation rate and film thickness were monitored *in-situ* by a quartz crystal microbalance. The films were deposited onto fused silica, crystalline silicon (100) and polycrystalline gold (15 nm thickness) substrates, which were cleaned with acetone and isopropanol to remove contaminants. The final control of the film thickness was carried out by AFM.

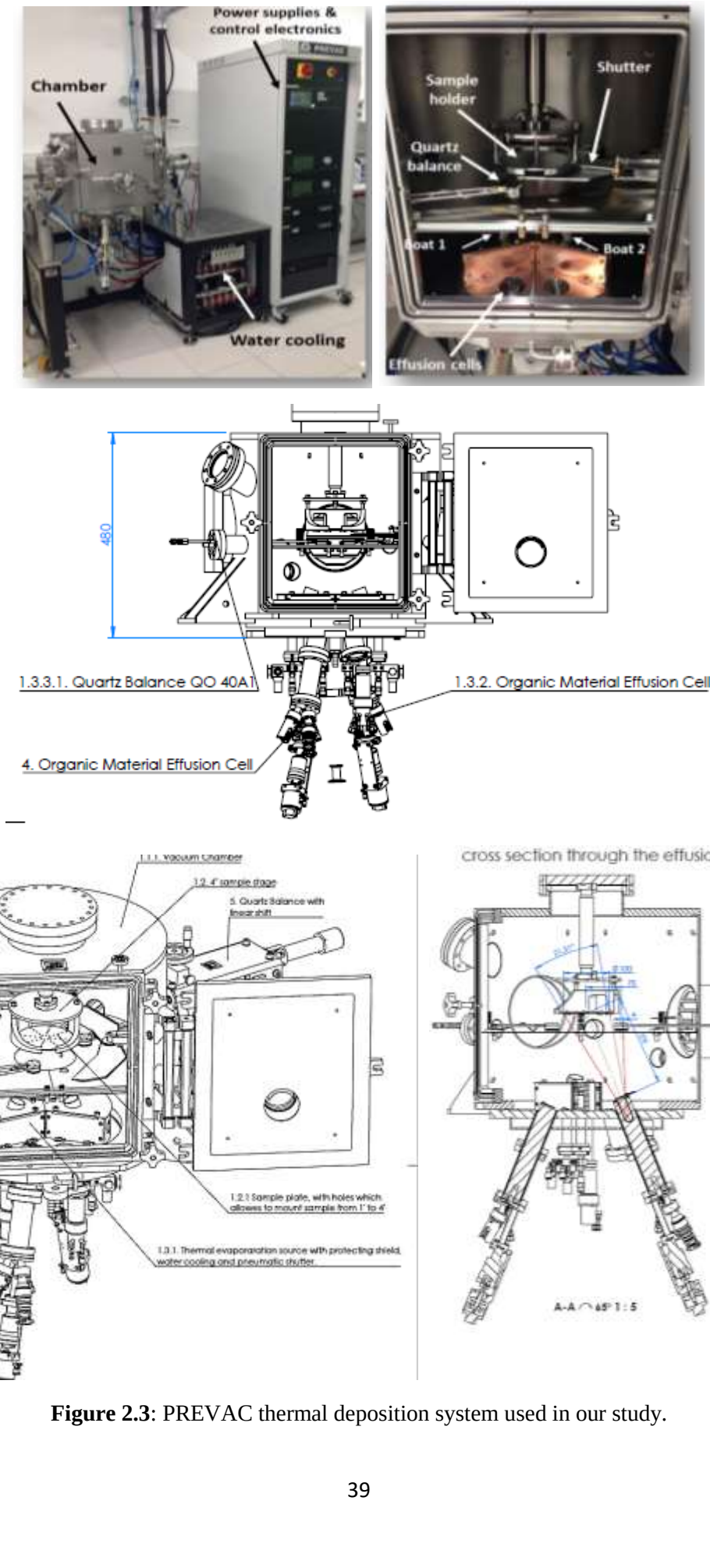

Figure 2.3: PREVAC thermal deposition system used in our study.

AFM topography measurements were done using a Cypher-ES microscope (Oxford Instruments) in amplitude-modulation mode at room temperature using OMCLAC160TS-R3 (Olympus) probes. The AFM analysis of the as-deposited film showed that the resulting films are smooth and continuous, but also rather heterogeneous in terms of morphology and roughness (see Figure 2.4). For example, the characterization of a film of ca. 1 cm^2 surface area and 75 nm thickness revealed different regions with roughness ranging between ca. 0.5 and 5 nm.

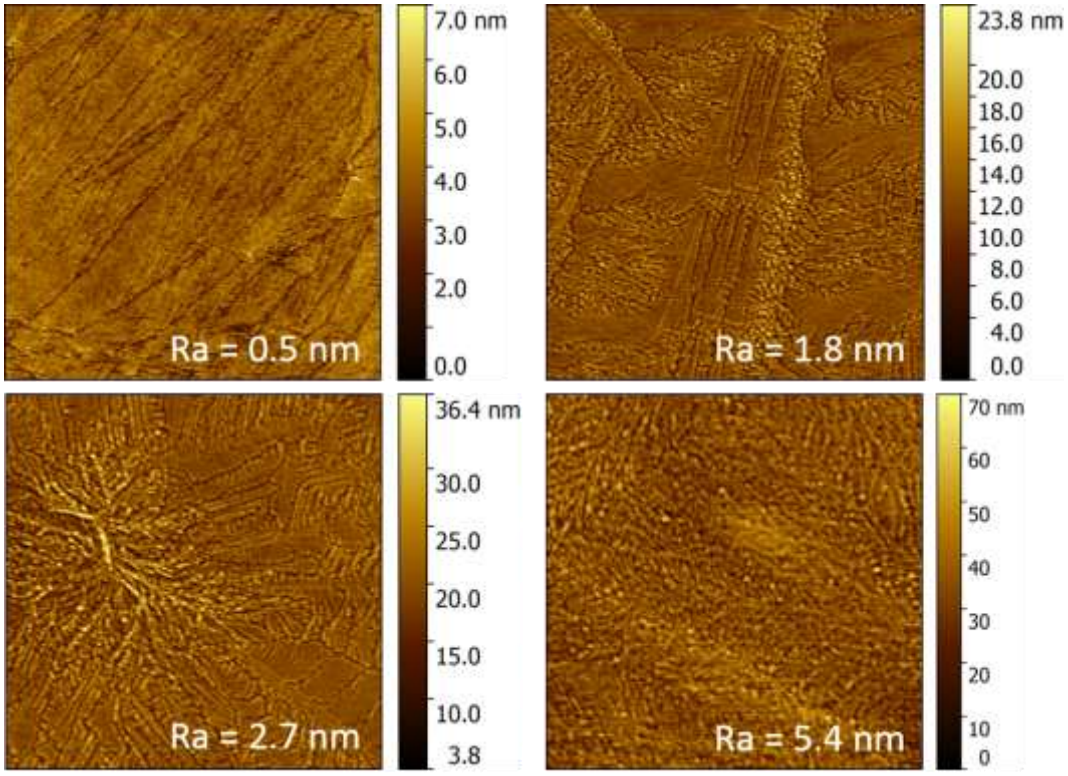

Figure 2.4: AFM topography images of a pristine thermally evaporated film (75 nm thickness) of $[Fe(HB(tz)_3)_2]$. Image sizes are 10 × 10 μm^2.

The spin transition in these films was followed by UV spectroscopy. Films were deposited on fused silica substrates in order to follow the thermal variation of the spin state of the complex by temperature dependent optical absorbance measurements. We have found that the films are transparent in the visible range independently of the temperature, while they exhibit a pronounced absorbance change associated with the SCO in the UV (see Figure 2.5). Temperature dependent absorbance spectra of the thin films were collected at wavelengths between 250 and 800 nm using a Cary 50 (Agilent Technologies) spectrophotometer and a Linkam FTIR-600 liquid nitrogen cryostat

(equipped with fused silica windows) (see Figure A2.1.1 in Annexes). The sample chamber was purged by dry nitrogen and spectra were acquired in the 293-393 K range with 1 K/min rate. The UV absorbance change at 317 nm for a 75 nm thick pristine film along four heating-cooling cycles is represented in Figure 2.6. The abrupt spin transition, similar to that obtained for the bulk powder, is apparent around 337 K. However, contrary to the powder sample, the spin transition in the pristine films is poorly reproducible: both the absorbance values and the shape of the curves change from cycle to cycle.

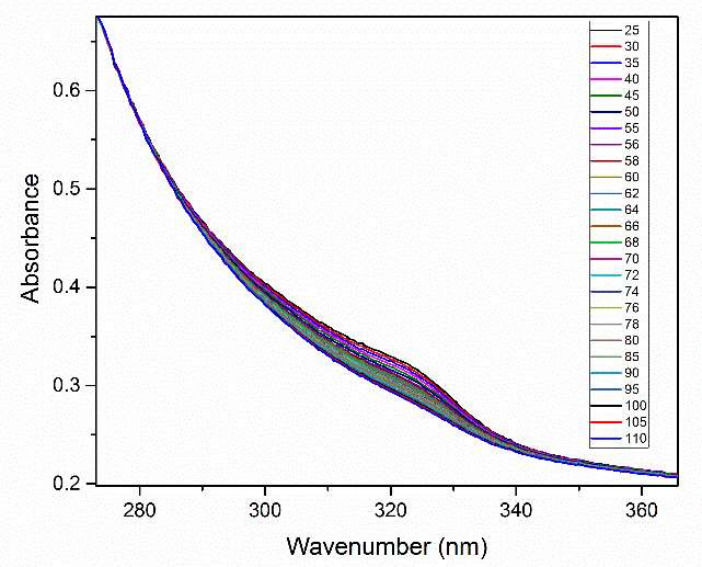

Figure 2.5: Variable temperature (in °C) UV absorbance spectra of a 30 nm thick pristine evaporated film of $[Fe(HB(tz)_3)_2]$ deposited on a fused silica substrate.

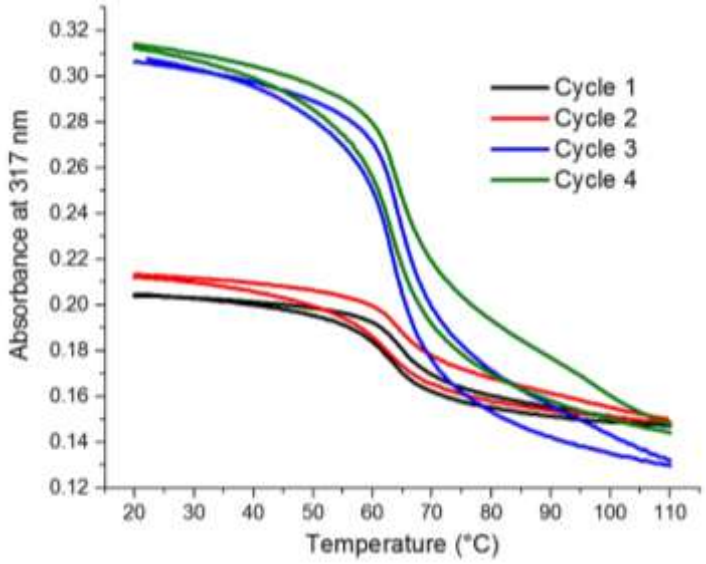

Figure 2.6: Absorbance (λ = 317 nm) of a 75 nm thick pristine film of $[Fe(HB(tz)_3)_2]$ along four heating-cooling cycles.

In order to unveil the origin of this lack of stability, the films were further characterized by X-ray diffraction (Figure 2.7). The grazing incidence X-ray diffraction (GIXRD) experiments were carried out in a PANalytical X'Pert PRO MPD system using Cu-Kα radiation (45 kV and 40 mA) with a parallel-beam configuration. The incident beam optics consisted of a mirror with a 1/32° divergence slit. A parallel plate collimator (0.18°) and Soller slits (0.04°) were mounted on the path of the diffracted beam. An X'Celerator detector in receiving slit mode was used for X-ray collection. Sample temperature was controlled using a Peltier stage. The results in Figure 2.7 highlight that the freshly prepared films are amorphous. On the other hand, by prolonging the storage time (days/weeks) in ambient air, several peaks appear in the XRD pattern, i.e. the films evolve to a polycrystalline form. We have not carried out a detailed study of this ageing phenomenon, but we observed it repeatedly for different film thicknesses (see Figure 2.8). The amorphous nature of the films can probably explain the lack of appreciable spin transition in the as-prepared samples, while the structural change observed upon prolonged storage may account for the evolving SCO behavior (in time and also from one cycle to another).

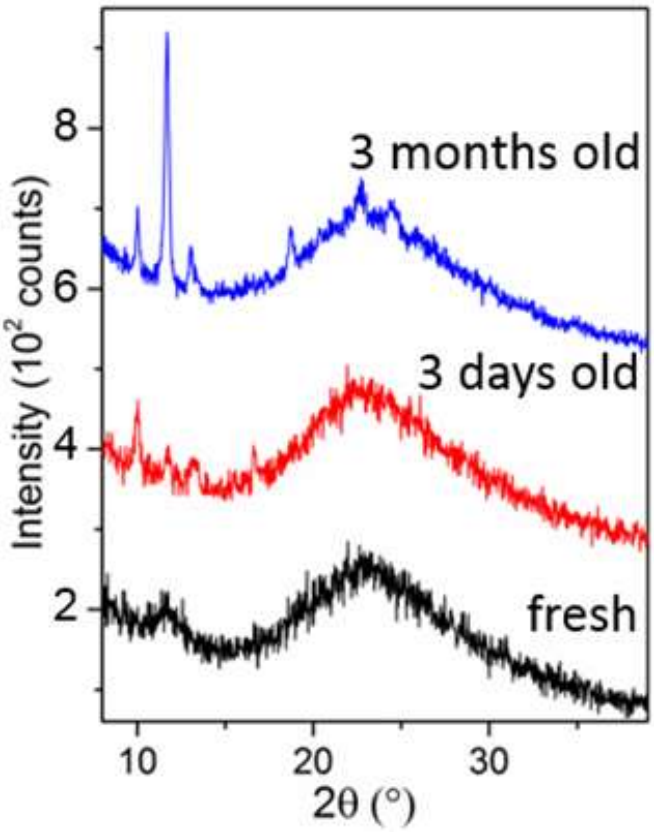

Figure 2.7: Evolution of the GIXRD pattern for different storage times is ambient air for a film of $[Fe(HB(tz)_3)_2]$ with thickness of ca. 80 nm.

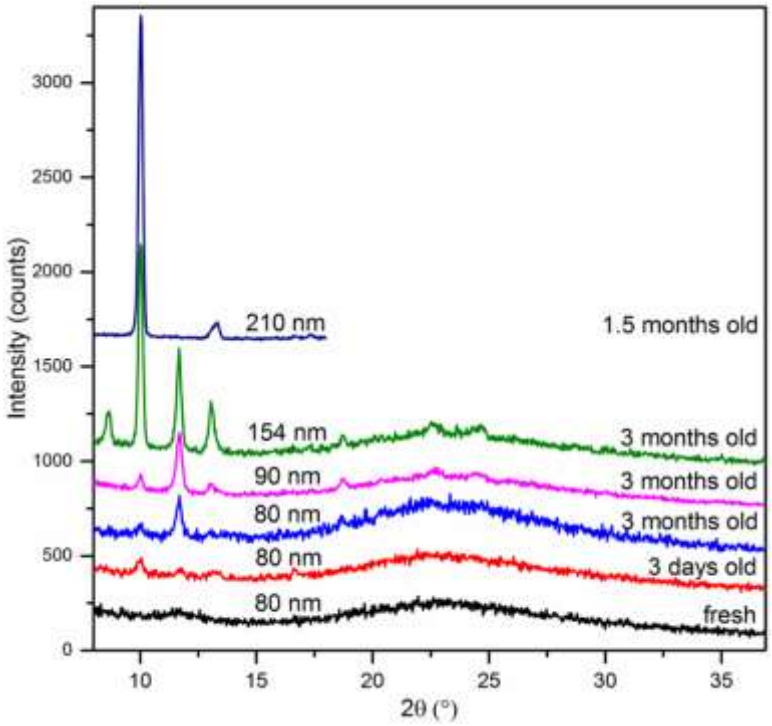

Figure 2.8: XRD patterns of pristine films of $[Fe(HB(tz)_3)_2]$ with different thicknesses and storage times.

2.2 Crystallization by solvent vapour annealing

2.2.1 Water vapour annealing

In order to obtain stable films with reproducible SCO behavior, we tried to convert the amorphous films to the crystalline form. To this aim thermal and solvent-vapour annealing are the most frequently used methods in the literature [128]. In our case we tried different methods, but we could not find any appropriate condition for thermally-induced crystallization (see Figure 2.9). Freshly evaporated films were annealed at three different temperatures: 160, 220 and 280 °C for 15 s on a hot plate. After this protocol we noticed that annealing at 280 °C led to a complete film destruction, while films annealed at 160 °C showed inhomogeneous morphology as evidenced by optical imaging. Films annealed at 220 °C show better crystallinity, but also a heterogeneous structure on the whole surface of the sample with a significant roughness ($R_a \approx 29$ nm) and they become hazy when observed by naked eye. Compared to humidity treated films, in the UV-Vis spectra of annealed films, the absorbance values are not proportional to the film thickness and the baseline tends to increase due to light scattering.

On the other hand, the fact that the films undergo a slow crystallization in ambient air suggested that water vapour (which is a moderate solvent for our SCO compound) might be used to accelerate this process. Indeed, the exposure of our fresh films to humid air (ca. 75÷80 %) at room temperature led to their very efficient and fast crystallization. This spectacular process was followed *in-situ* by AFM, optical absorption and Raman measurements. The AFM image in Figure 2.10a shows the topography of a freshly evaporated film revealing a very low roughness (R_a = 0.45 nm). Then, we added a water drop (*ca.* 20 µL) into the AFM chamber and we acquired immediately another topography scan. As shown in Figure 2.10b, at the timescale of the measurements (ca. 2÷3 min) the film experienced a dramatic morphological transformation: the initially rather featureless surface of the film evolved into a nano-crystalline morphology displaying well-defined grain boundaries and a higher roughness (R_a = 6÷7 nm).

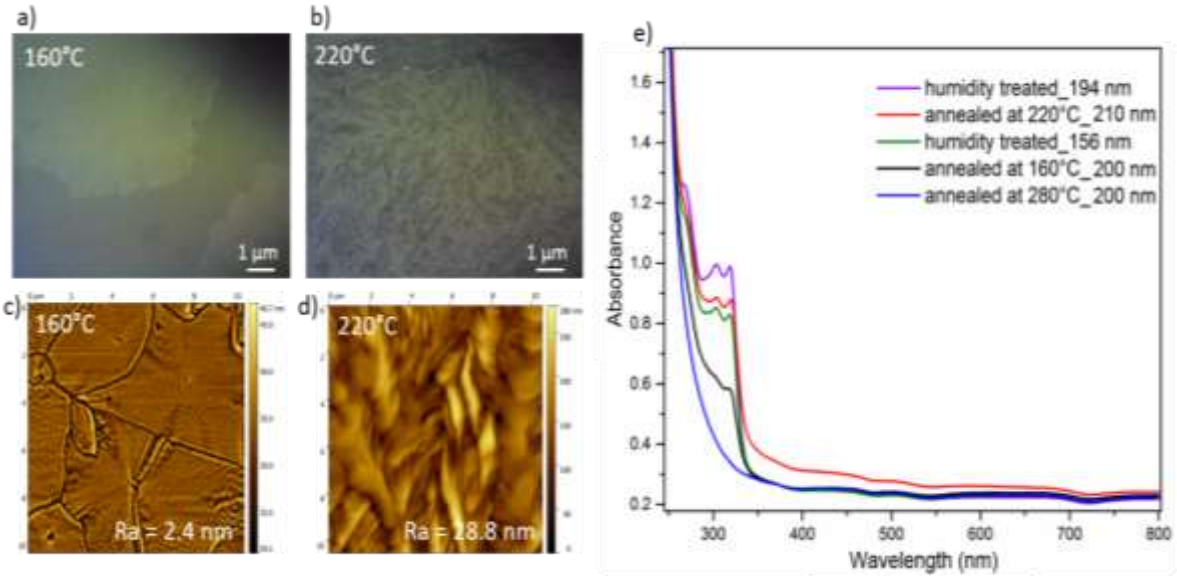

Figure 2.9: Film annealing at high-temperature. Optical images of [Fe(HB(tz)$_3$)$_2$] films annealed at 160 °C (a) and 220 °C (b). AFM images of films annealed at 160 °C (c) and 220 °C (d). UV-Vis absorbance spectra of annealed films (at 160, 220 and 280 °C) and humidity treated films (e).

Interestingly, the addition of a water drop to another sample with the same thickness (150 nm), which was previously exposed to ambient air for 2 hours, did not induce any obvious change in the surface morphology (see Figure 2.10c,d). This means that 'irreversible' changes occur in the films in ambient air and the humidity treatment must be carried out on freshly prepared films in order to achieve a high degree of crystallinity. It is important to mention that the surface morphology depicted in Figure 2.10b does not represent the final stage of crystallization, as the humidity in the AFM chamber was not high enough for a complete transformation. Indeed,

when the solvent annealing was carried out in a dedicated chamber for 75÷80 % relative humidity (see Figure A2.2.1 in Annexes) we could obtain extremely well reproducible film morphologies with roughness (R_a) below 2.5 nm (150 nm thickness). Perhaps even more importantly, in contrast to the pristine samples, these crystalline films cover uniformly the whole substrate surface and their morphology was found stable on storage in ambient air for several months (this topic will be detailed in the next chapter of this thesis). On the other hand, solvent annealing did not change considerably the film thickness (see Figure A2.2.2 in Annexes).

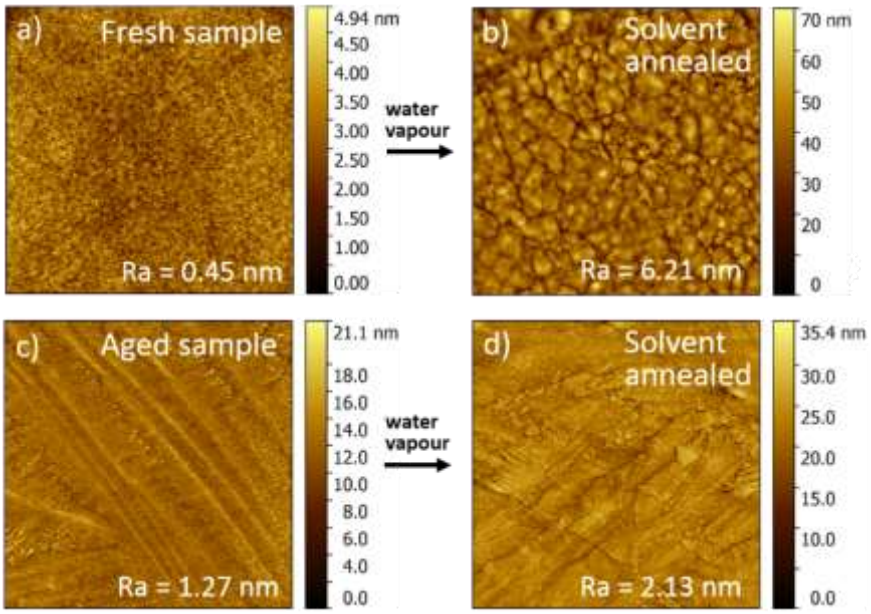

Figure 2.10: AFM imaging of the crystallization of a film of $[Fe(HB(tz)_3)_2]$ of 150 nm thickness. AFM topography of a fresh sample before (a) and after (b) exposure to humidity. (c-d) The effect of the same treatment on another film, which was stored previously in ambient air. Image sizes are 10 × 10 μm^2.

The increase of the UV absorbance upon exposure to humidity can be used to follow the crystallization process. For fully crystalline films we found that the absorbance at $\lambda = 317$ nm is closely proportional to the film thickness (see Figure 2.11). Hence it is possible to establish the efficiency of the annealing process from a simple room temperature absorption spectrum (provided the film thickness is known). As an example, Figure 2.12 shows the UV absorbance of two 90 nm thick films, either stored in ambient air or annealed in 80 % humidity, revealing a crystallinity of ca. 49% and 100% respectively. Samples showing a complete and homogenous crystallization could be achieved with thicknesses ranging from ca. 20 to 200 nm.

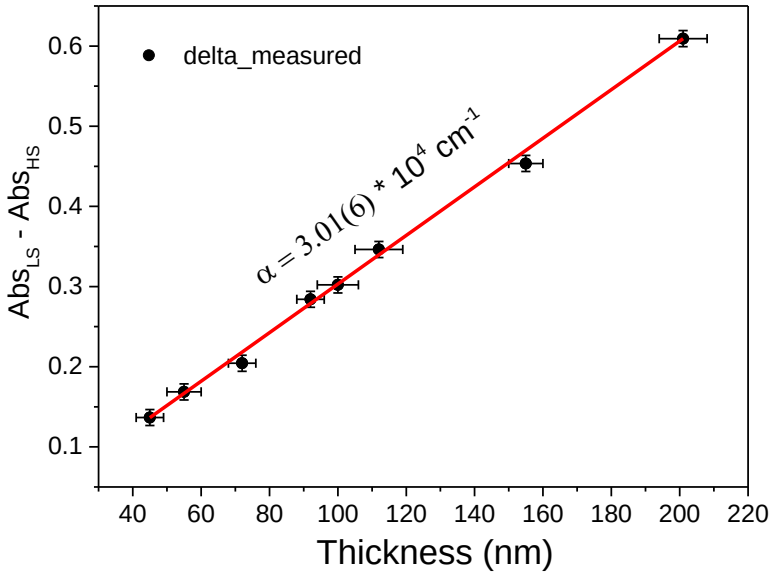

Figure 2.11: Evaluation of the degree of crystallinity and the completeness of the spin transition in $[Fe(HB(tz)_3)_2]$ films. The graph shows the variation in absorbance between the LS and HS states (Abs_{LS}-Abs_{HS}) at 317 nm for various film thicknesses determined by AFM. The black squares correspond to the experimentally measured values, while the red line corresponds to the theoretically expected values for a fully complete spin transition. This evaluation is based on the assumption that the 194 nm film displays a complete spin transition, which was inferred from the temperature dependent Raman analysis of this film. The slope of the fitted line gives an absorption coefficient of ca. 30100 cm^{-1}.

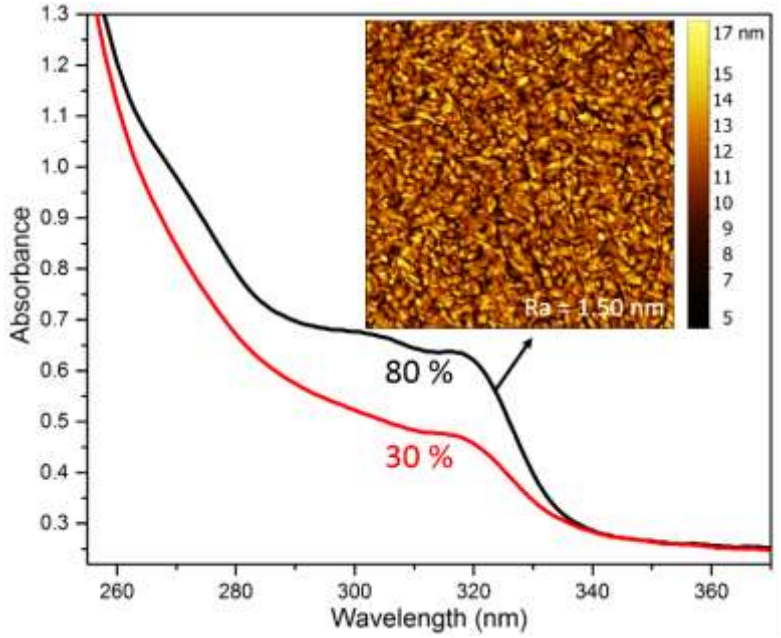

Figure 2.12: Absorption spectra acquired at 293 K for 90 nm thick films of $[Fe(HB(tz)_3)_2]$ stored either in 30 % (ambient air) or in 80 % relative humidity. The inset shows the AFM image of the humidity treated film (image size is 10 × 10 μm^2).

Thicker films crystallized only partially, most probably only in the proximity of the surface layers (leaving the underlying ones in amorphous/semi-crystalline form), while films with a thickness below ca. 20 nm formed a more-or less discontinuous layer of grains. Figure 2.13 shows characteristic AFM and TEM images as well as a photograph of a 70 nm thick film on a glass substrate.

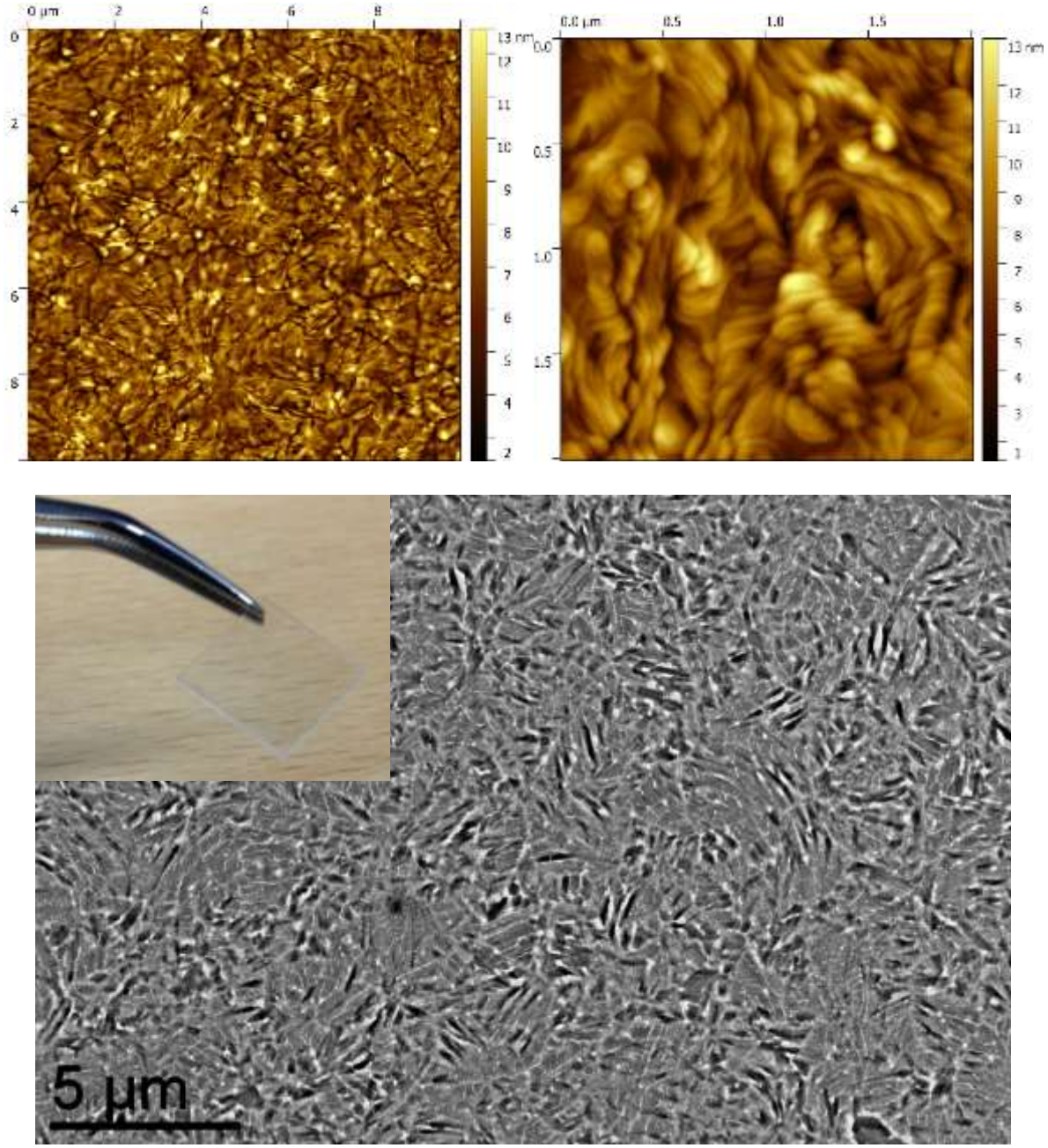

Figure 2.13: Characteristic AFM and TEM images of water annealed films of $[Fe(HB(tz)_3)_2]$ (70 nm thickness). A photograph of a film deposited on a glass substrate is also shown.

These films are smooth, continuous and not observable by naked eye, neither by low magnification optical microscope – confirming their high quality. Interestingly, we remark both in the AFM and TEM images rather particular spherulitic film morphologies, which indicate radial film growth associated with a lamellar organization, but we have not investigated in more detail this complex phenomenon.

We have analyzed the transformation of thin films from the amorphous to the crystalline form using Raman spectroscopy. Figure 2.14 shows the spectra of a film before, during and after the treatment and presents three different spectral footprints.

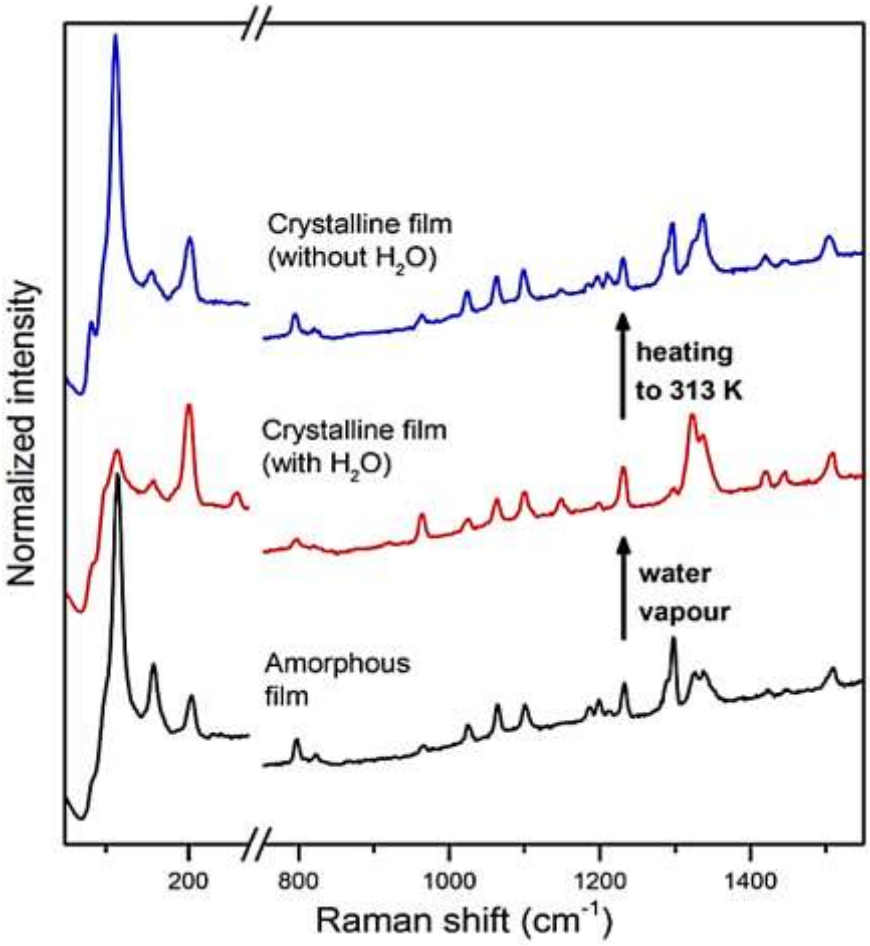

Figure 2.14: Raman spectra of a thin film (138 nm thickness) of $[Fe(HB(tz)_3)_2]$ at three stages of its synthesis: the pristine amorphous film, hydrated crystalline film (after humidity treatment) and the final dehydrated crystalline film (after heating to 313 K).

A first spectral modification occurs upon exposure to water vapour, which we thus attribute to the crystallization process. Then, a slight heating of the film to *ca.* 313 K allowed us to obtain a spectrum, which remained stable and reproducible upon thermal cycling as well as on storage in ambient air. Since this latter spectrum corresponds closely to the spectrum of the powder of

the complex [114], we can attribute this second spectral change to the loss of water. Interestingly, the Raman spectrum of the film in its stable form (dehydrated crystalline) matches more closely the spectrum of oriented single crystals of our SCO compound than that of the polycrystalline powder [114]. This finding indicates that the crystalline films are possibly also oriented. To further investigate the crystallinity and texture of the films we acquired XRD data for humidity treated films. As shown in Figure 2.15 the diffraction pattern of the films consists of a single peak at 2θ = 10.02° indicating a preferential crystallographic orientation. (*N. B.* The very broad peak around 2θ = 20° ÷ 25° is typical for amorphous fused silica substrates)[81]. The peak intensity approximately scales with the film thicknesses.

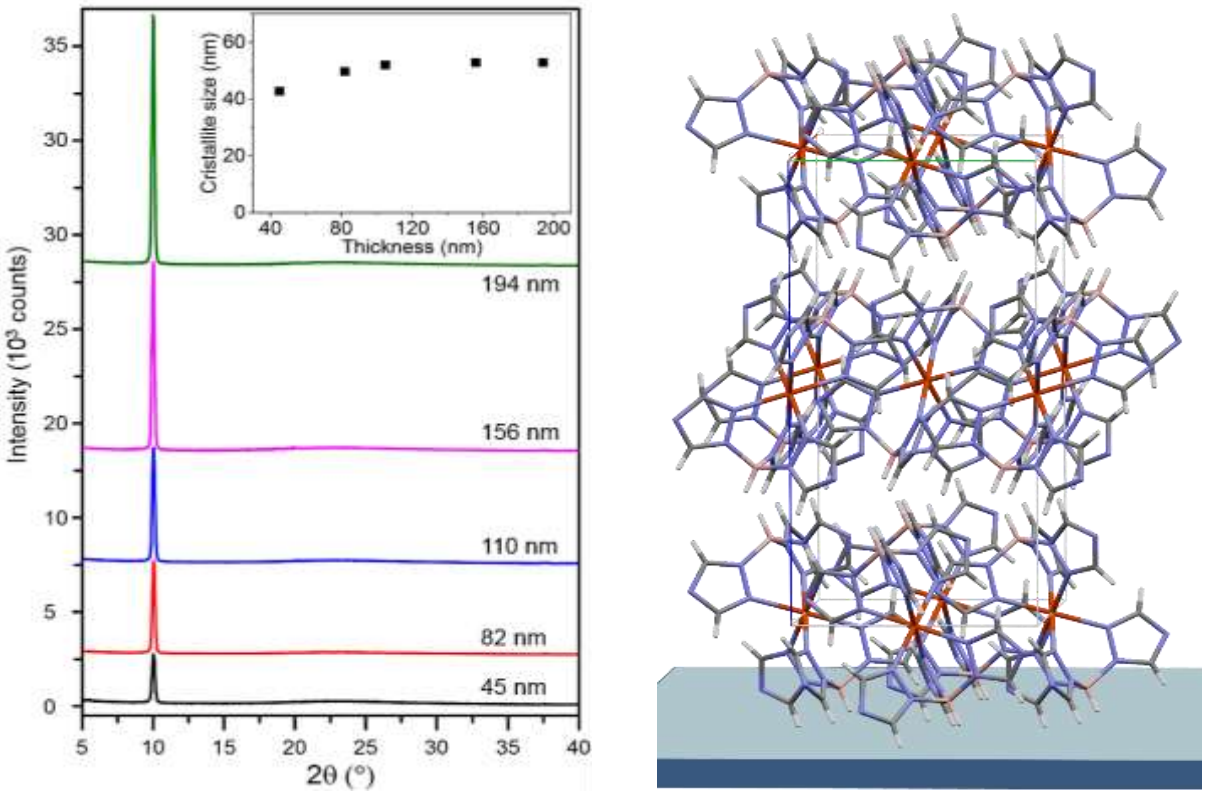

Figure 2.15: XRD patterns of crystalline thin films of $[Fe(HB(tz)_3)_2]$ for various thicknesses. The inset shows the size of the crystalline domains as a function of the film thickness. The structure of the oriented film is also depicted.

This diffraction pattern of the crystalline films can be compared with that of the bulk powder, which exhibits a peak at 2θ = 10.11° corresponding to the 002 reflection (see Figure 2.16). This peak assignment is clearly substantiated by the brusque shift of this diffraction peak from 2θ =10.02° (LS state) to 9.43° (HS state) during the SCO – closely matching the behavior of the bulk sample (see Figure 2.16). It should be noted also that no other *00l* diffraction peaks have significant intensity in the simulated powder XRD

data of [Fe(HB(tz)$_3$)$_2$] complex [114]. We can thus conclude that the crystalline domains in the films grow preferentially with their orthorhombic *c*-axis normal to the substrate surface. This finding was repeatedly observed for different film thickness and for different substrates, such as glass, polymer, single crystalline silicon and polycrystalline gold substrates (see Figure 2.17).

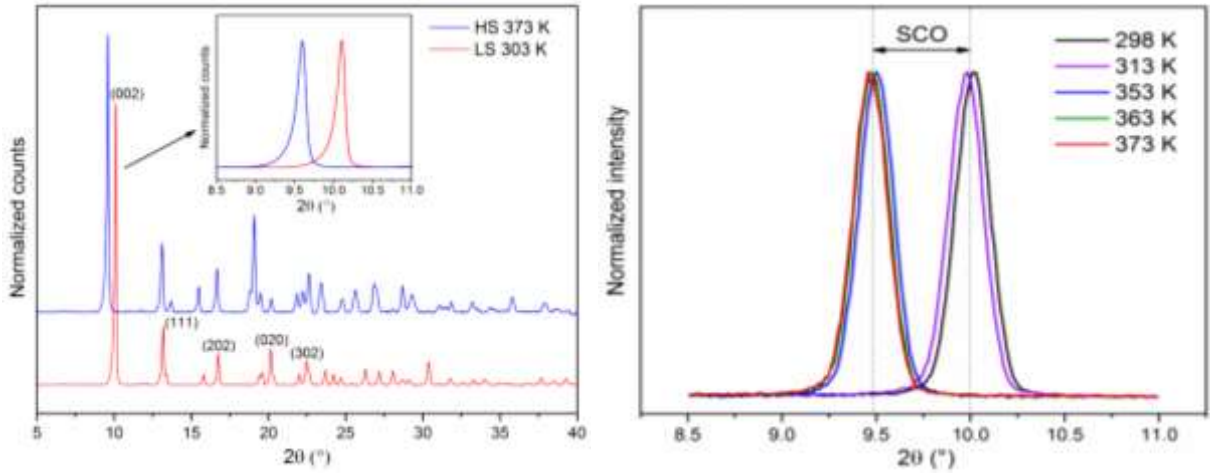

Figure 2.16: (left panel) PXRD patterns of the bulk powder of [Fe(HB(tz)$_3$)$_2$] in the LS and HS states. The peak corresponding to the (002) reflection shifts from 2θ = 10.11° at 303 K to 9.59° at 373 K. (right panel) GIXRD patterns of a 194 nm crystalline film at different temperatures.

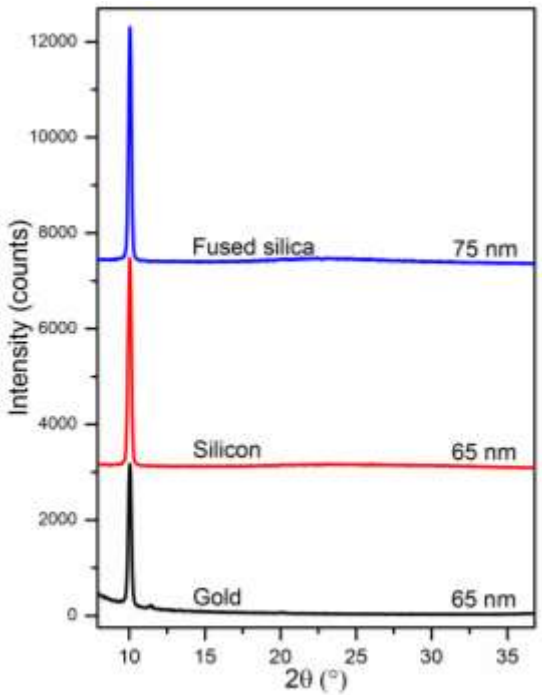

Figure 2.17: XRD patterns of solvent annealed films of [Fe(HB(tz)$_3$)$_2$] on different substrates (fused silica, single crystalline silicon and polycrystalline gold).

It is interesting to note that single crystals of $[Fe(HB(tz)_3)_2]$ tend also to grow naturally with large *00l* facets suggesting these facets have relatively low surface energy. It is worth to mention also that the LS to HS spin transition in this compound leads to a very significant strain (ca. +5.6 %) along the orthorhombic *c*-axis, while in the other directions the changes are smaller or even opposite (*a*-axis: -2.3 %, *b*-axis: +1.0 %) [114]. Neglecting other possible contributions (e.g. micro-strain) one can estimate the mean size of the ordered (crystalline) domains, which is directly linked to the peak broadening in the XRD diffraction patterns through the Scherrer equation [129]:

$$\tau = \frac{K\lambda}{\beta \cos\theta} \tag{2.1}$$

where τ is the mean size of the ordered (crystallite) domains, K is a dimensionless shape factor with a value close to the unity, λ is the X-ray wavelength, β is the line broadening at half the maximum intensity (FWHM) after subtracting the instrumental line broadening (in radians) and θ is the Bragg angle.

As shown in the inset of Figure 2.15 the size of crystalline domains (along the c-axis) remains quite similar (from 43 to 53 nm) for film thicknesses between *ca.* 45 and 200 nm. One may note that the Scherrer analysis of the bulk powder led to *ca.* 80-100 nm crystalline domain sizes [114].

2.2.2 Spin crossover properties of crystalline films

We will now focus on the spin transition properties of recrystallized films. To follow the spin transition in a quantitative manner, variable temperature optical absorption measurements were performed over four heating-cooling cycles between 293 K and 393 K with a rate of 1K/min. Figure 2.18 shows the absorbance spectra of a 90 nm thick crystalline film at different temperatures in the UV region. The intense absorption bands between 260 and 340 nm exhibit three maxima around 272, 305 and 317 nm at 293 K (see inset in Figure 2.18a). The absorption coefficients associated with these peaks are *ca.* 10^4 cm^{-1} indicating these are strongly allowed charge transfer transitions. These absorption bands are bleached upon increasing the temperature to 393 K, which we can obviously assign to the SCO phenomenon. Indeed the plot of the absorbance at 317 nm as a function of the temperature (Figure 2.18b) reveals an abrupt change around 338 K with a small hysteresis, which is virtually the same as the one observed for the bulk powder [114]. (N. B. The spin transition in the crystalline films was also confirmed by magnetic measurements. See Figure A2.2.3 in the Annexes).

Since the spin transition is virtually complete in both directions (see Figure 2.11 for details) and the absorbance at 317 nm is directly proportional to the LS fraction (n_{LS}) the plot in Figure 2.18b can be considered as a quantitative spin transition curve (n_{LS} *vs.* T). It is interesting to note that during the first heating the transition temperature ($T_{1/2}^{\uparrow}$ = 339.8 K) is slightly higher than in the successive cycles, which is the well-known "*run-in*" phenomenon [130]. However, beyond the first heating the transition temperatures ($T_{1/2}^{\uparrow}$ = 338.1 K and $T_{1/2}^{\downarrow}$ = 337.6 K) become perfectly reproducible, which can be well appreciated from the derivatives of the transition curves in the inset of Figure 2.18b.

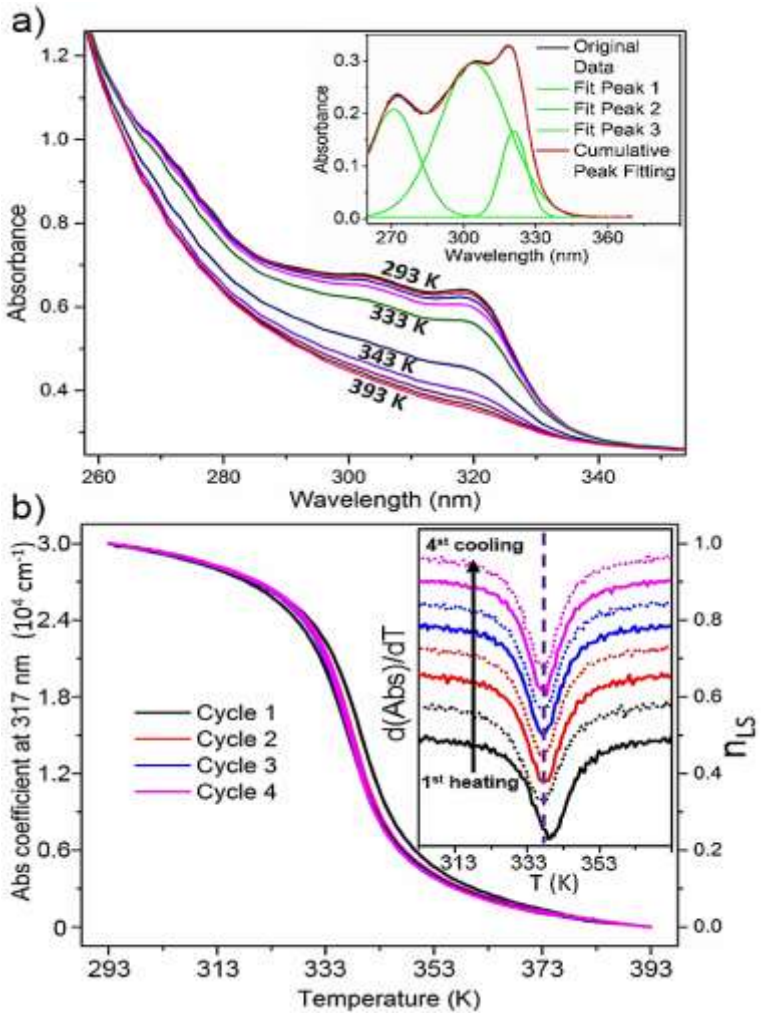

Figure 2.18: (a) Absorbance spectra of a 90 nm crystalline film of $[Fe(HB(tz)_3)_2]$ acquired at different temperatures on heating. The inset shows peak fitting of the baseline subtracted spectrum at 293 K. (b) Temperature dependence of the absorbance at 317 nm along four thermal cycles recorded at 1 K/min scan rate. The inset shows the derivatives of the transition curves.

This SCO behavior observed for the 90 nm thick film was perfectly reproduced for all other crystalline films with different thicknesses (see Figure 2.19) and, at first sight, no remarkable

size effect has been observed. (As we will discuss in Chapter 3, a careful investigation allowed us to reveal a slight, but very well-defined size effect in these films.) In order to further investigate the SCO behavior, temperature dependent Raman spectra were also acquired (Figure 2.20, see also Figure A2.2.4). During the spin transition, the Raman spectra of the films undergo characteristic changes in intensity and frequency in agreement with the spectra of the bulk powder [114]. In particular, one can observe the increase in intensity of representative HS peaks around 1407, 1046, 123 and 102 cm^{-1}, while the LS markers around 1420 and 113 cm^{-1} loose in intensity. Raman spectra enable also the observation of the coexistence of the LS and HS states at 338 K and confirm the completeness of the spin transition.

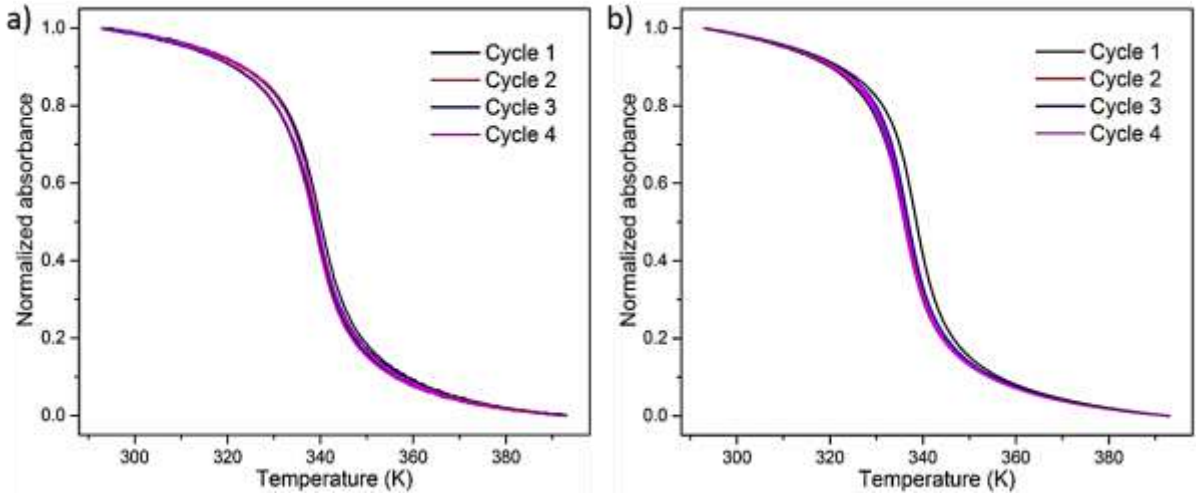

Figure 2.19: Temperature dependence of the absorbance at 317 nm along four heating-cooling cycles recorded at 1 K/min scan rate for films of $[Fe(HB(tz)_3)_2]$ with thickness of 45 nm (a) and 194 nm (b).

We have also investigated the SCO properties of thicker films. In order to achieve crystalline films with thicknesses above ca. 200 nm it appears necessary to do the film growth in two steps. First, we prepared a freshly evaporated film with thickness of ca. 185 nm and then exposed to controlled air humidity of 75-80 % for 10 min in order to achieve a good crystallinity. In the next step, a second 185 nm thick film of the SCO complex $[Fe(HB(tz)_3)_2]$ was deposited by vacuum thermal evaporation on top of the existing film. Then, the freshly prepared second layer was exposed to the 'standard' humidity treatment (the same as the previous one). Finally, a third layer with a thickness of ca. 185 nm was subsequently deposited, but this time without exposing the new layer to a humidity treatment. At each step, the film was analyzed by variable temperature UV absorption spectroscopy (see Figure 2.21 for the room temperature spectra and Figure 2.22 for the full study of the final film). From these results, we can conclude that by preparing a first well-crystallized layer with thickness below 200 nm it is possible to achieve

the regrowth of next layers to obtain thicker crystalline films. It appears that the humidity treatment is necessary only for the first layer.

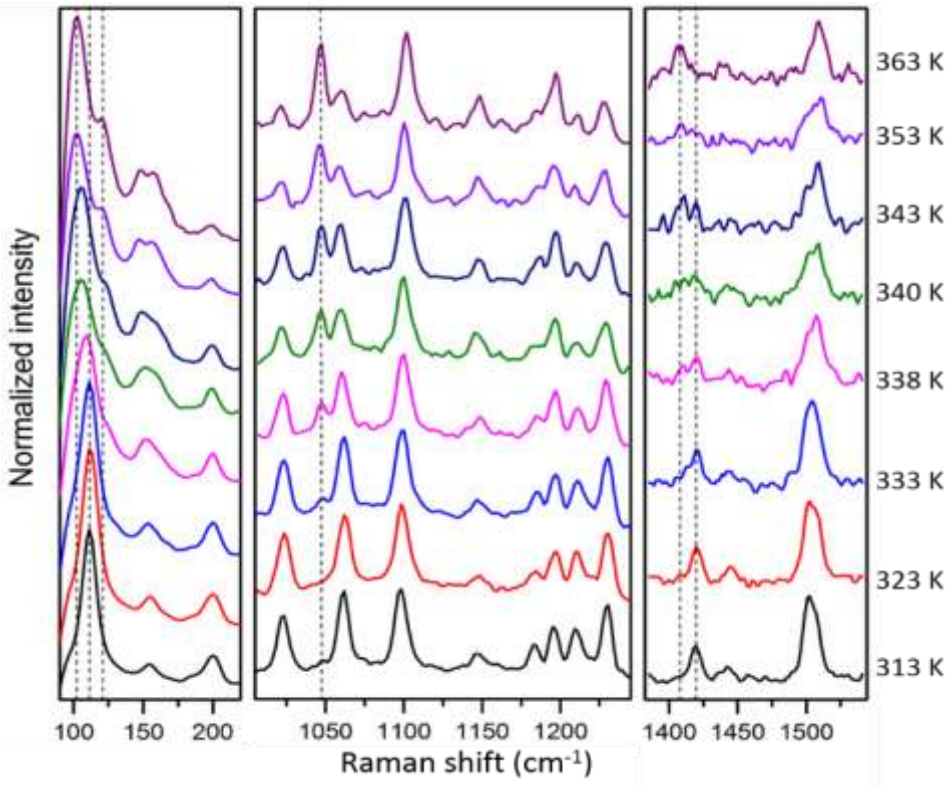

Figure 2.20: Raman spectra of a 194 nm thick crystalline film of $[Fe(HB(tz)_3)_2]$ acquired at different temperatures in the heating mode.

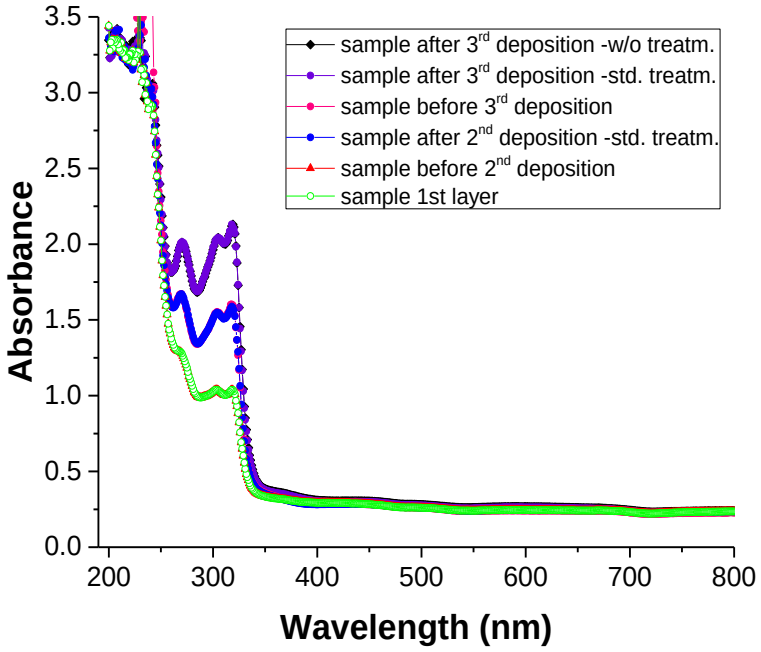

Figure 2.21: Absorbance spectra acquired at 293 K following the subsequent deposition of 3 layers of $[Fe(HB(tz)_3)_2]$ with ca. 3×185 nm thickness. Only the first two layers were annealed in humidity.

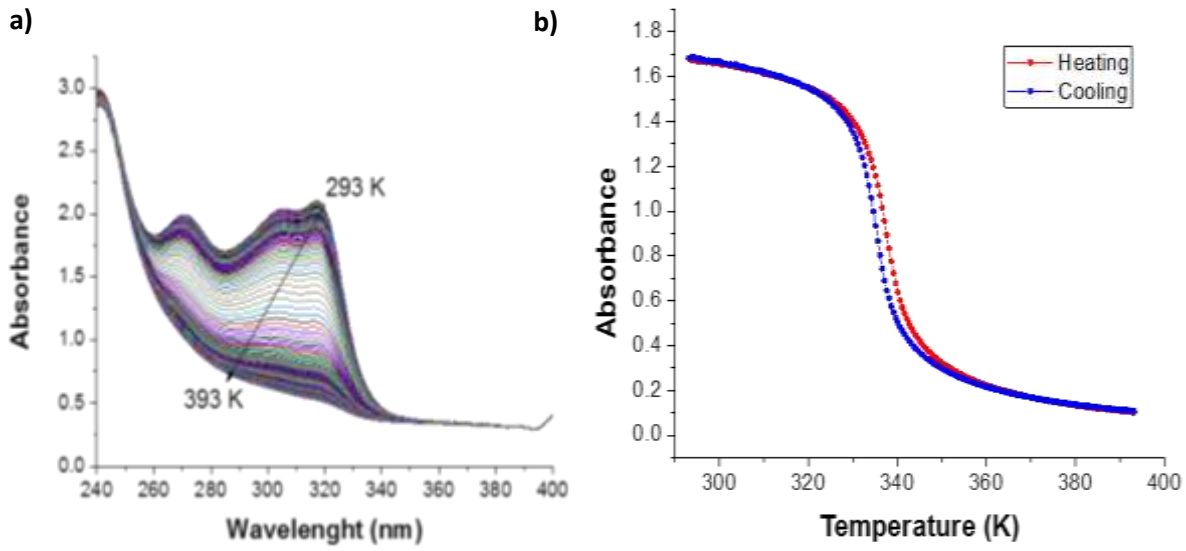

Figure 2.22: a) Variable temperature absorbance spectra and b) Temperature dependence of the absorbance along the first heating–cooling cycle recorded at 1 K min^{-1} scan rate for the 3-layer film.

2.2.3 In-situ investigation of the crystallization in controlled humidity

The crystallization process upon water exposure was further investigated by *in-situ* UV-VIS absorbance measurements using a dedicated environmental chamber with simultaneous humidity and temperature control. For *in-situ* absorbance measurements, the heating-cooling stage was connected to a Linkam RH95 humidity controller (see Figure A2.2.5 in Annexes), which allows for a fine control of the humidity around the sample between 5 and 90 % RH. (N.B. Due to the fast kinetics of the annealing process we were unable to conduct *in-situ* AFM and GIXRD measurements.) For *in-situ* spectroscopy, a freshly evaporated film of $[Fe(HB(tz)_3)_2]$ with thickness of ca.100 nm was placed in a temperature controlled chamber, wherein the relative humidity was changed from 40 to 80 % while measuring the absorbance of the film at a sampling rate of 10 Hz. Figure 2.23 displays the absorbance change at 318 nm together with the variation of RH for a fixed temperature of 298 K. The striking observation here is the very abrupt change in absorbance at a relative humidity value of *ca.* 72 %. In a short period of *ca.* 8 s, the absorbance of the film increases sharply from 0.27 to 0.40. Before this increase the absorbance change is slow, while after the jump the absorbance of the film remains constant for any value of RH, *i.e.* the effect is irreversible. This result was repeatedly observed on fresh films (see Figure A2.2.6 in Annexes) and indicates that the crystallization of the film during the water vapor annealing occurs by the simultaneous nucleation of a large number of seeds, which then form small, densely packed crystals. The crystalline state reached at the end

of the process is extremely stable in air even for repeated thermal cycling. It is worth noting that the humidity treatment results in a solvated film, but the water molecules are desorbed in ambient air *below* the spin transition temperature and they have therefore no effect on the SCO properties [114].

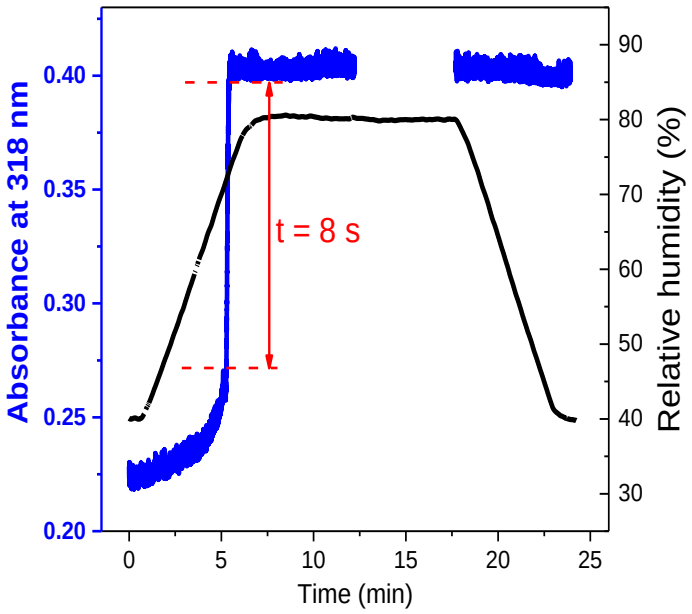

Figure 2.23: Absorbance change (baseline corrected) at 318 nm of a $[Fe(HB(tz)_3)_2]$ thin film as a function of time (blue curve) for increasing and decreasing values of relative humidity (black curve) at a fixed temperature of 298 K. (Note that between ca. 12.5 and 17.5 min no absorbance data were acquired.)

Obviously, the water vapor annealing process is influenced by many parameters such as temperature, fluctuations of RH and exposure time. Regarding this last parameter, we observed that the films remain stable during longer exposure (2 h) to humidity. As already mentioned before, we also noticed that keeping the films in ambient air before water vapor treatment leads to an irreversible evolution ('aging') of the films towards an ill-defined, semi-crystalline state. Figure 2.24a depicts the results of water vapor annealing of three similar films with *ca.* 100 nm thickness, which were exposed to an ambient humidity of *ca.* 57 % for 2 min, 15 min and 2.5 hours before the SVA treatment. One can notice that the film exposed for 2.5 hours displayed a high initial absorbance and did not show any further increase of absorbance with increased relative humidity. This film then revealed different properties compared to the 'freshly treated' samples. Notably, the 10.01° XRD peak intensity of the film exposed to ambient air for 2.5 h is four times less than the peak intensity of the film with only 2 min exposure to ambient air (see Figure 2.24b and **Table 2.1**).

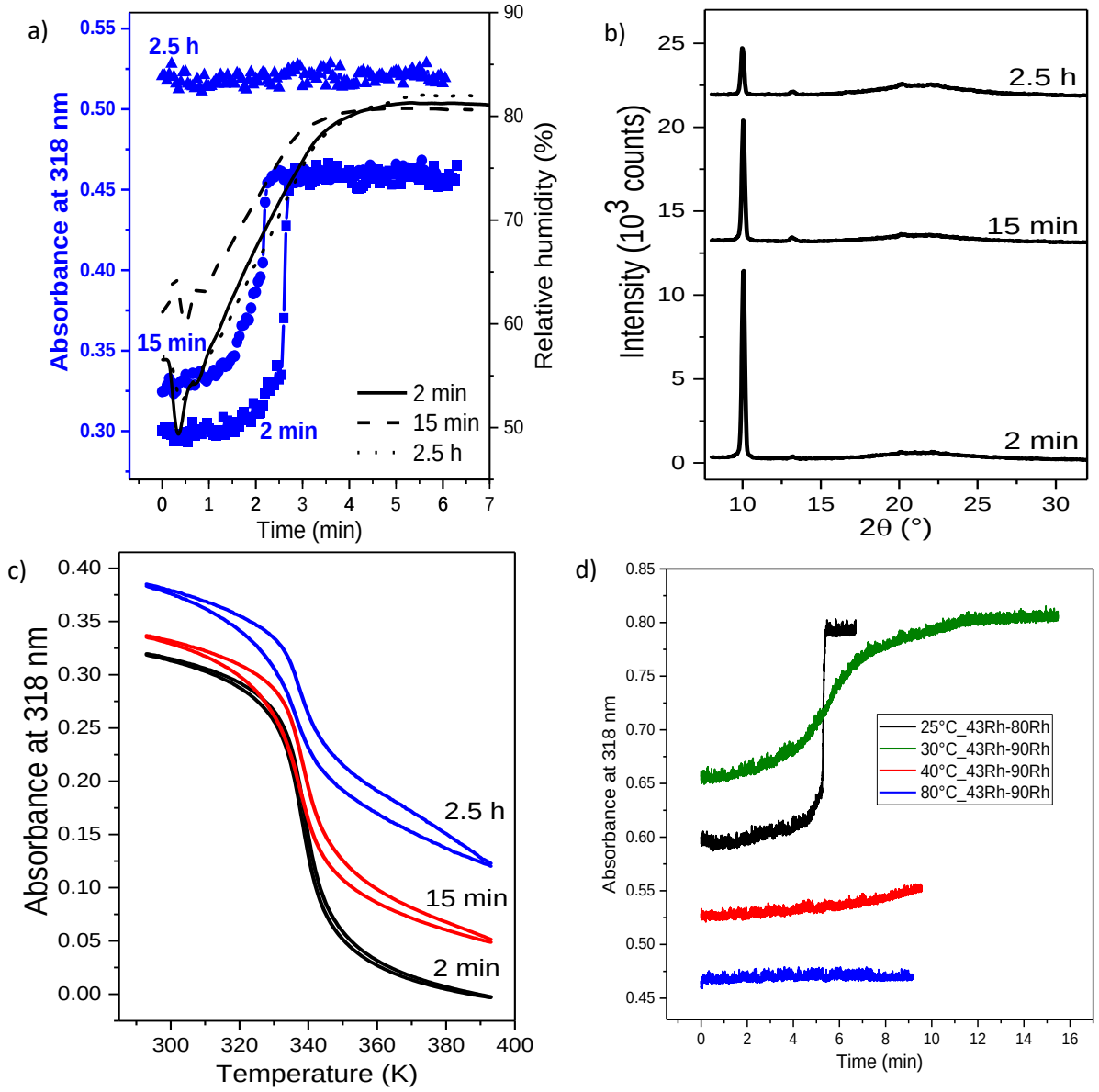

Figure 2.24: (a) Absorbance change (λ = 318 nm; baseline corrected) on increasing relative humidity values, (b) XRD patterns and (c) temperature dependence of the absorbance along the second heating–cooling cycle (λ = 318 nm, dT/dt = 1 K min^{-1}; baseline corrected) for three [Fe(HB(tz)$_3$)$_2$] thin films stored in air for 2 min, 15 min and 2.5 hours before water vapor annealing. (d) Effect of temperature on the humidity annealing of [Fe(HB(tz)$_3$)$_2$] thin films (scans between 43% and 90 % RH).

In addition, the relative intensity of other diffraction peaks became more pronounced, indicating that in ambient air, the film evolves in an irreversible manner towards a less crystalline state and less oriented texture. In line with this observation, the spin transition became less complete and less abrupt for prolonged 'aging' in ambient air (Figure 2.24c). In addition, the shape of the SCO curves displays an unusual hysteresis over the entire heating-cooling cycle, which indicates continuous sample evolution.

We have also investigated the effect of solvent annealing temperature and it turned out that increasing the temperature of the substrate during the water vapor annealing led to decreasing efficiency. At 303 K, the crystallization was still observed, although more gradually. At higher temperatures, however, no absorbance change was detected even for RH 90% indicating less efficient interaction with the water molecules (see Figure 2.24d).

We can thus conclude that water vapor annealing (RH > 72 %) applied to freshly evaporated [$Fe(HB(tz)_3)_2$] films provides a simple, yet very efficient means to achieve an abrupt and complete SCO transition with a high environmental stability, while the slow 'aging' of the films at lower relative humidity (i.e. in ambient air) leads to less stable, less oriented, semi-crystalline films displaying incomplete and broad spin transitions.

Table 2.1. Properties of [$Fe(HB(tz)_3)_2$] films stored in air for different times before humidity treatment.

Aging time	$T_{1/2}$ (K)	ΔT (K)	Abs_{LS}-Abs_{HS}	I_{002} (counts)	Abs_{400nm} (baseline corrected)
2 min	339.2	0.9	0.32	11200	0.09
15 min	339.0	2.4	0.29	7200	0.14
2.5 h	339.5	3.8	0.26	2800	0.20

2.2.4 Annealing in different solvents

Solvent vapor annealing (SVA), which consists of exposing a film to a solvent vapor at (or near) room temperature, has recently become an increasingly popular 'mild' method to control thin film morphology and crystallinity. Considering that one can use various solvents with different solubility parameters and vapor pressure, SVA represents a highly versatile approach. In particular, the effects of solvent vapors on block copolymer films,[128, 131-133] organic semiconductors films [134-138] and compounds of pharmaceutical interest [139,140] have been described formerly. However, the effects of solvent vapors on SCO films were previously not much explored [141]. The effects of SVA mainly depend on the properties of applied solvents [134, 135, 137]. Solvent molecules interact with the surface of a material and, depending on solvent-material affinity, film permeability, morphology, exposure time and temperature, the solvent can diffuse into it or condense on the surface and dissolve molecules. In either case, the 'softening' of the material then enables movement and/or rearrangement of molecules.

In order to deepen our understanding of this process, we systematically examined the crystallinity, morphology and SCO characteristics of thin films of [$Fe(HB(tz)_3)_2$] after their exposure to the vapors of five different solvents: diethyl ether, acetone, dichloromethane, ethanol and water. [$Fe(HB(tz)_3)_2$] films were characterized by means of grazing incidence X-

ray diffraction (GIXRD), atomic force microscopy (AFM) and variable-temperature ultraviolet-visible (UV-Vis) absorption techniques.

The films were deposited onto fused silica substrates, which were cleaned with acetone and isopropanol to remove contaminants. After film deposition, the substrates with $[Fe(HB(tz)_3)_2]$ thin films were immediately placed in a sealed vial of 60 ml along with an open vial containing 10 ml of a given solvent. This led to a saturated solvent atmosphere in the large vial while direct contact between the film and the liquid was avoided. Except otherwise stated, annealing was carried out at room temperature for 10 min. Identical vials were used for each experiment thus leading to different saturated vapor pressures for the different solvents.

The solubility of $[Fe(HB(tz)_3)_2]$ is rather low in common solvents. Among those used in our study, diethyl ether, acetone and ethanol can be considered as non-solvents, while water and dichloromethane are "poor solvents" (*ca.* 1 mg/mL at 298 K). We have chosen these solvents with different polarities, vapor pressures and hydrogen-bonding abilities to enable meaningful comparisons. **Table 2.2** gathers some commonly used quantitative parameters describing these properties. In particular, the Hansen solubility parameters characterize the cohesive energy density of the substance, decomposed for dispersive interactions (δ_d), polar interactions (δ_p) and hydrogen bonding contributions (δ_H). The vapor pressure (P_v), boiling point (T_b) and surface tension (γ) are also related to the cohesive forces between the solvent molecules, while the Gutmann donor number (*DN*) is used to quantify the Lewis basicity of solvents.

First, we analyzed by GIXRD the crystalline structure of the five solvent-exposed $[Fe(HB(tz)_3)_2]$ films of ca. 200 nm thickness. In the diffraction geometry used, only crystal planes parallel to the substrate can be observed. This allows probing the crystallinity (and crystal structure) and determination of the preferred crystal orientation. Figure 2.25 shows the diffraction patterns of the solvent annealed films as well as that of the freshly evaporated film. One may notice that the initial featureless diffraction pattern of the amorphous, pristine film drastically changes after exposure to the different solvents. Remarkably, the diffraction pattern of each solvent annealed film is dominated by a single, intense and narrow peak at a 2θ value of 10.01°. In other words, water is not the only solvent, which recrystallizes the films. However, one may notice that the film treated with CH_2Cl_2 exhibits significantly weaker diffraction intensity at 10.01° in comparison with the films exposed to other solvents. In addition, the XRD pattern of the dichloromethane-exposed film exhibits other diffraction peaks with relatively high intensities (with respect to the main peak). These results denote that the crystallinity and ordering of the dichloromethane-annealed films is lower when compared to other samples.

Table 2.2. Solvent properties [142]: Hansen solubility parameters (dispersive, polar and H-bonding) in units of MPa, vapor pressure (at 20 °C) in units of kPa, boiling point (at 1 atm) in units of °C, surface tension (at 20 °C in air) in units of mN/m and Gutmann donor numbers in units of kcal/mol.

Solvent	δ_d	δ_p	δ_H	P_v	T_b	γ	DN
Water	15.5	16.0	42.3	3.17	100	72.8	18
Ethanol	15.8	8.8	19.4	5.95	78.3	22.1	32
Diethyl ether	14.5	2.9	4.6	58.7	34.6	17.1	19.2
Dichloromethane	17.0	7.3	7.1	57.3	39.8	26.5	1
Acetone	15.5	10.4	7.0	30.6	56.3	25.2	17

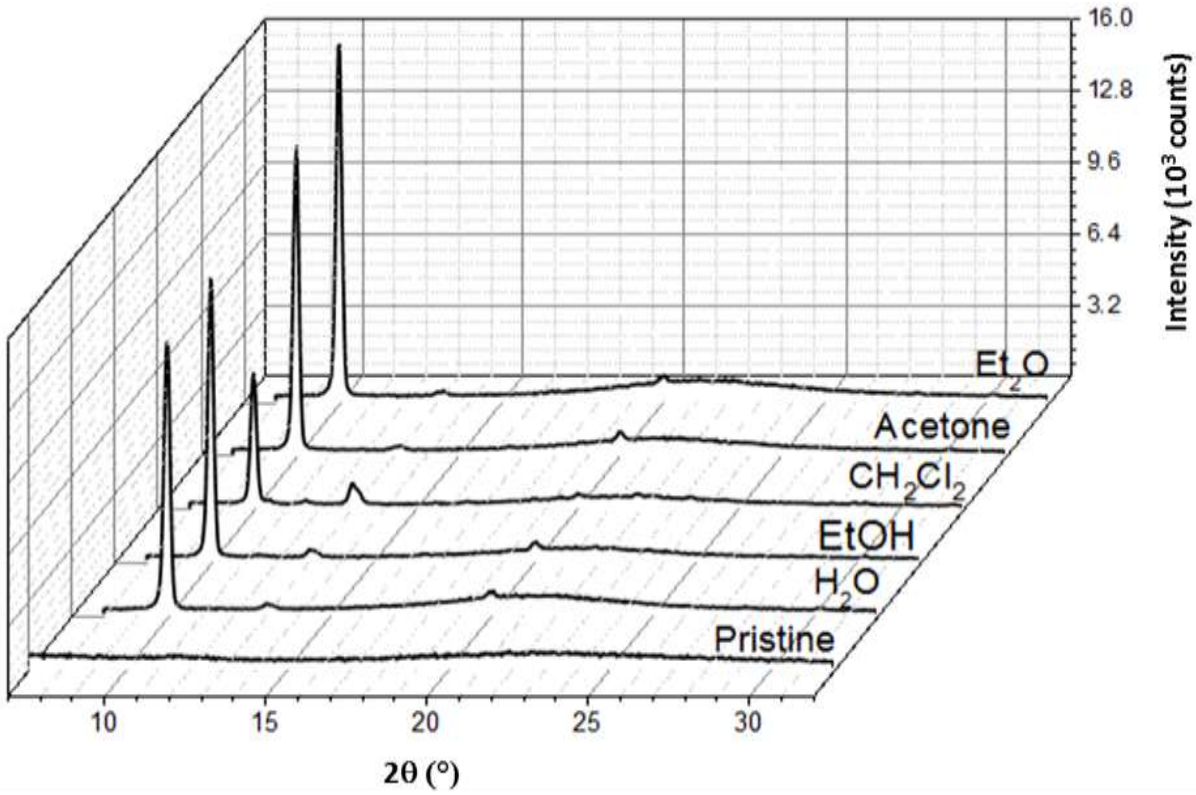

Figure 2.25: XRD patterns of $[Fe(HB(tz)_3)_2]$ thin films exposed to different solvents. The diffractogram of a pristine film is also shown. (*N.B.* The broad peak around 2θ = 15°÷27° is typical for amorphous fused silica substrates used in this study [81]).

To investigate how the different crystallinity of the films alter the SCO properties, we performed variable temperature optical absorption measurements over two heating – cooling cycles between 293 K and 393 K. Figure 2.26a shows selected UV absorbance spectra of the SCO thin films annealed with different solvents. The intense absorption bands between 260 and

340 nm are bleached upon increasing the temperature from 293 to 393 K, which can be explained by the SCO phenomenon. Figure 2.26b displays the absorbance (at 318 nm) as a function of temperature for the different solvent-treated films.

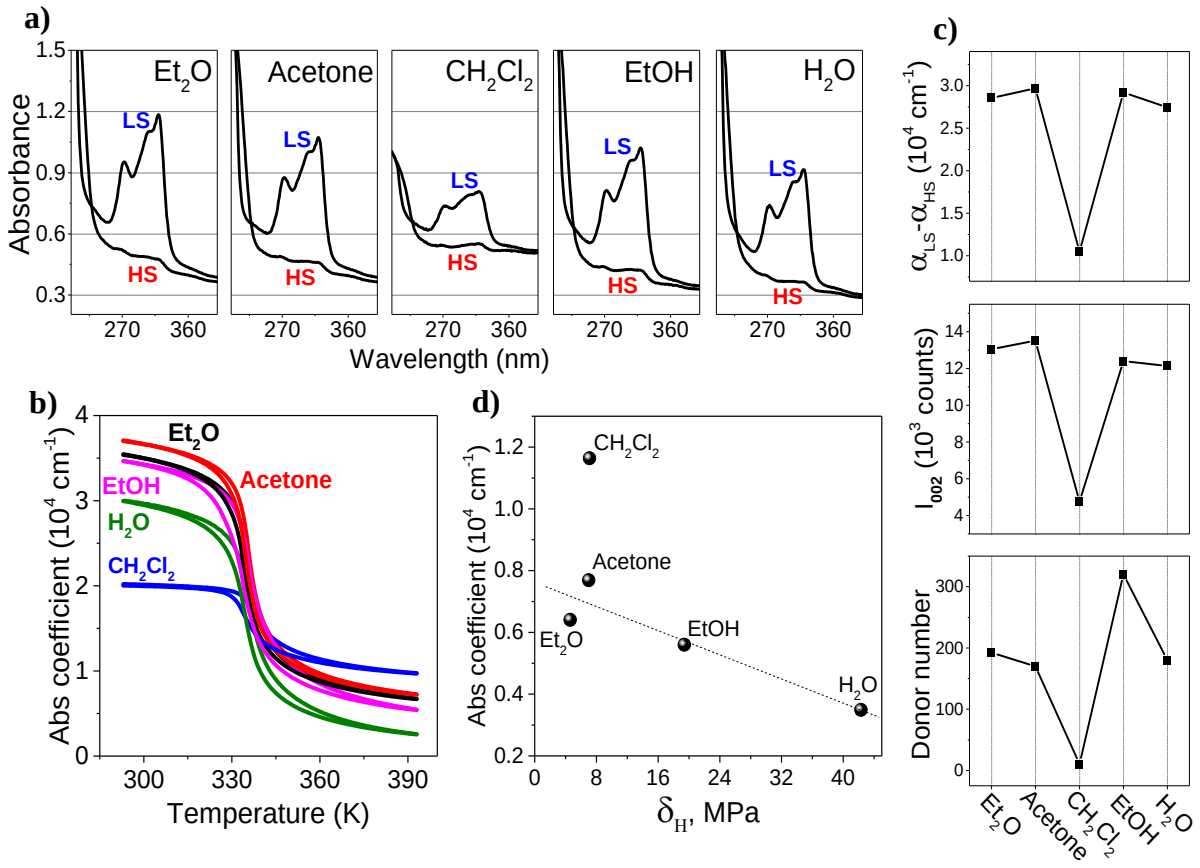

Figure 2.26: (a) Absorbance spectra acquired at 293 K (LS) and 393 K (HS) in the heating mode for [Fe(HB(tz)$_3$)$_2$] films annealed with different solvents. (b) Temperature dependence of the absorbance coefficient at 318 nm (baseline corrected) along the second heating–cooling cycle recorded at 1 K min^{-1} scan rate for different solvent treated samples. (c) Absorbance coefficient change at the spin transition (λ = 318 nm), intensity of the *002* XRD peak (thickness normalized) and solvent donor number for different solvent treated samples. (d) Absorbance coefficient at 400 nm (baseline corrected) as a function of the Hansen solubility parameter δ_H.

One may note that all films exhibit a rather abrupt spin transition with similar transition temperatures ($T_{1/2}$ ≈ 336 K) and small hysteresis widths (ΔT ≈ 2 K) (see also Table 2.3). However, the shape and intensity of the absorption spectra of the CH_2Cl_2-treated sample is different from the others and therefore the absorbance change upon the spin transition is drastically reduced in this sample indicating an incomplete SCO (*ca.* 36 %). In addition, the absorbance change between the LS and HS states (Abs_{LS}- Abs_{HS}) and intensity of the XRD peak

at 2θ = 10.01° (I_{002}) are correlated for the different samples (see Figure 2.26c and Table 2.3). These findings suggest that the lower degree of crystallinity and ordering could be the primary cause for the very incomplete spin transition in the CH_2Cl_2 vapor annealed sample.

Table 2.3. Properties of solvent annealed films: spin transition temperature, hysteresis width, absorbance coefficient change upon the spin transition (at 318 nm), intensity of the *002* XRD peak (thickness normalized), UV-Vis absorption coefficient at 400 nm (baseline corrected).

Solvent	$T_{1/2}$ (K)	ΔT (K)	α_{LS}-α_{HS} (10^4 cm^{-1})	I_{002} (counts)	α_{400nm} (10^4 cm^{-1})
Diethyl ether	335.6	1.6	2.85	13000	0.64
Acetone	336.0	1.3	2.97	13500	0.77
Dichloro-methane	338.9	3.5	1.05	4740	1.16
Ethanol	335.7	3.1	2.92	12400	0.56
Water	336.0	2.2	2.74	12100	0.35

When comparing the properties of the different solvents used (see Table 2.2 and Figure 2.26c), it appears that the poor crystallinity of the sample treated with dichloromethane and consequently its inferior SCO properties might be related to its low donor number, *i.e.* its low ability to accept hydrogen bonds, in comparison with the four other solvents used in our study. We can thus suggest that the SVA treatment of films of $[Fe(HB(tz)_3)_2]$ is more efficient when the SCO molecules can form hydrogen bonds with the solvent molecules. Since $[Fe(HB(tz)_3)_2]$ is much less soluble in diethyl ether/acetone/ethanol than in dichloromethane, the most plausible mechanism of SVA in the present case would be solvent diffusion into the film causing intermolecular hydrogen bonds to break. Then, the higher mobility of the SCO molecules can allow the pristine metastable film to evolve into a thermodynamically more favorable crystalline state.

Another interesting observation one can make about the absorption spectra in Figure 2.26a-b of the different solvent treated samples is their substantially different spectral baseline (see also Table 2.3). This finding denotes that the light scattering intensity of the films strongly differs, indicating that the morphology of the films must be different. To further investigate this aspect, we examined the surface morphology of different solvent-exposed $[Fe(HB(tz)_3)_2]$ films using optical microscopy and AFM. Figure 2.27 shows the optical and AFM topography images of the thin films after exposure to the solvents. The water-exposed $[Fe(HB(tz)_3)_2]$ film is

characterized by a smooth and continuous morphology, while the other samples appear more irregular. At first glance, the AFM topography images suggest that CH_2Cl_2 as well as EtOH treated films are smooth, characterized by low values of arithmetic average roughness R_a. However, in this case the small area AFM topography analysis is not representative as optical images show the presence of some large-scale aggregates/crystals in these samples as well.

Interestingly, the light scattering intensity (i.e. the baseline of the absorbance spectra) is correlated with the Hansen solubility parameter δ_H of the solvents (Figure 2.26d), denoting that the surface roughness decreases when δ_H increases. (*N.B.* The case of CH_2Cl_2 deviates from this trend, but we believe the deviation occurs due to its different crystallinity.) The solubility parameters of solvents have already been reported to be correlated with the changes in crystallinity and morphology of various organic films when exposed to the solvents [134, 135, 139, 140, 143]. In our case we can suggest that during SVA, water condenses on the smooth and amorphous surface of the pristine film. Since the solubility of $[Fe(HB(tz)_3)_2]$ in water is not very high, fast supersaturation occurs and a large number of crystallization seeds form simultaneously, leading to densely packed, small crystallites and thus a smooth surface morphology. For the other solvents, larger crystals form, which indicates different film growth mechanism(s) involving possibly no surface condensation and less nucleation seeds.

Overall, we can conclude that the water vapor annealing gives the most efficient recrystallization procedure, offering the best control on film morphology, crystallinity and SCO properties.

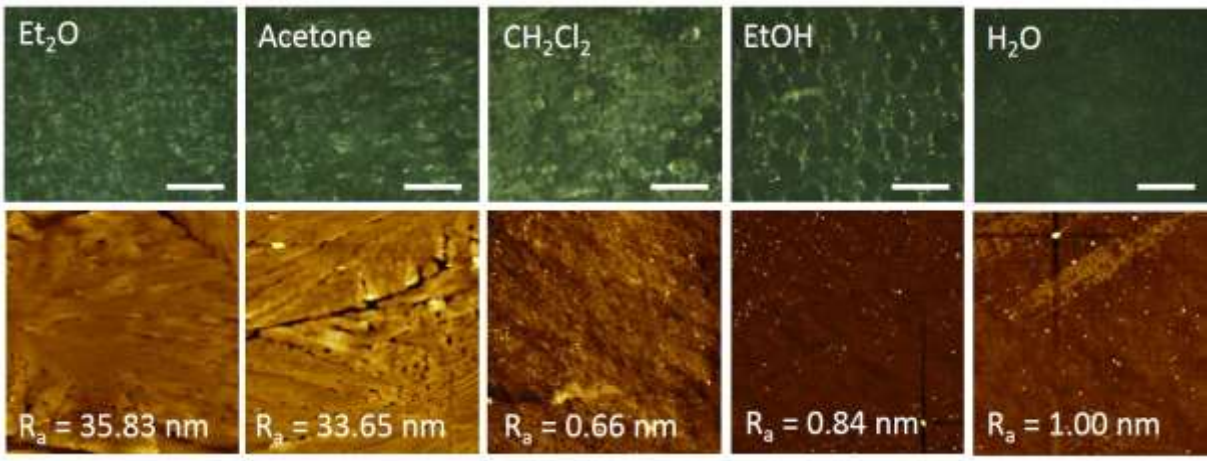

Figure 2.27: Optical microscopy (*top panel*) and AFM surface topography (*bottom panel*) characterization of the different solvent vapor annealed $[Fe(HB(tz)_3)_2]$ films. Scale bar in optical images: 500 µm; AFM image size: 30×30 μm^2.

2.3 Conclusions

High quality thin films of the spin crossover complex $[Fe(HB(tz)_3)_2]$ have been successfully deposited by high-vacuum thermal evaporation on different substrate materials with an accurate control of the film thickness. The as-deposited amorphous films could be fully recrystallized using solvent-vapour annealing. To this aim, five different solvents were tested: diethyl ether, acetone, dichloromethane, ethanol and water. Grazing incidence X-ray diffraction and UV spectrophotometry showed that the EtO_2, $(CH_3)_2CO$, EtOH and H_2O treated films feature highly oriented crystalline structure - with the orthorhombic *c*-axis normal to the substrate - and an abrupt spin transition at *ca.* 336 K. CH_2Cl_2 vapor annealed films are less crystalline and do not exhibit a complete spin transition. On the other hand, AFM analysis showed that water is the only solvent, which provides a smooth, homogenous and continuous film morphology (down to *ca.* 20 nm thickness). Based on these findings we suggested that the key parameters responsible for film crystallinity and for the control of film morphology could be the hydrogen bonding ability of the solvents as well as their solubility parameters.

The recrystallization process in water was more deeply studied by UV absorption measurements with *in situ* humidity control. This analysis showed that the crystallization in approx. 75-80 % relative humidity air at room temperature is complete within a few seconds above a threshold humidity value (~100 % crystallinity for thicknesses below *ca.* 200 nm). A subsequent slight thermal annealing at 313 K led to very robust, dehydrated crystalline films. The Raman spectrum of these films is comparable with that of the bulk $[Fe(HB(tz)_3)_2]$ sample. The detailed temperature dependent UV absorption and Raman spectroscopic study demonstrated that the crystalline films display a cooperative, complete and tightly reproducible spin transition above room temperature, similar to the bulk material. All these properties make the humidity annealed films of $[Fe(HB(tz)_3)_2]$ a very attractive candidate for integration in nanoscale photonic, actuating and electronic devices.

On the whole, we found that solvent vapor annealing provides a simple and fast, yet very powerful method to control crystallinity, texture, morphology, spin crossover properties and environmental stability of thin films of $[Fe(HB(tz)_3)_2]$. We believe this approach will be increasingly important for the engineering of various SCO films.

Chapter 3. Spin transition properties of $[Fe(HB(tz)_3)_2]$ films

In this chapter we present a deep investigation of the spin crossover properties of the $[Fe(HB(tz)_3)_2]$ films whose fabrication was detailed in Chapter 2. We were particularly interested about the stability of the SCO in these films (towards thermal cycling, storage and processing conditions, etc.) as well as about the possible size dependence of the spin transition.

3.1 SCO and its stability

The ability to process homogeneous, reproducible and stable thin films is a fundamental requirement for any application of functional materials, especially in the case of SCO systems, whose behavior is critically related to the local environment. Furthermore, stability and reversibility are also mandatory prerequisites for physical properties studies, such as the scanning probe microscopy investigations we discuss in Chapter 5. The thin films of $[Fe(HB(tz)_3)_2]$ described in Chapter 2 appear as promising samples in terms of stability. As was mentioned before, using a very rigorous protocol during deposition and post-deposition it is possible to obtain films with very high purity and tight thickness control. In the next sub-sections we discuss the results we obtained during the investigation of stability of the spin transition in this film under the action of different factors such as: temperature, switching cycles, storage time and processing conditions.

3.1.1 Thermal stability

From a technological point of view, the highest processing temperature that the sample can withstand is a particularly important information. To investigate this issue we prepared by thermal evaporation on fused silica substrate a $[Fe(HB(tz)_3)_2]$ film of *ca*. 125 nm thickness. Prior the thermal stability study, we performed on this thin film variable temperature optical absorption measurements over four heating – cooling cycles between 293 K and 393 K, which revealed stable SCO properties, similar to what we have seen previously in Chapter 2 (see Figure A3.1.1 in Annexes). In the next step, we have carried out a series of heating-cooling cycles such a way that the heating range was increased in each successive cycle by 10 K. The sample temperature in these measurements was controlled using a Linkam THMS600 liquid nitrogen cryostat and measurements were performed at 4 K min^{-1} in dry nitrogen atmosphere while monitoring the UV absorbance of the film at 317 nm. After each cycle temperature, a UV-vis absorption spectrum was recorded at room temperature. Figure 3.1a shows these spectra, while Figure 3.1b represent the evolution of the (room T) absorbance at 317 nm as a function of the annealing temperature. As we have seen before, at room temperature (LS state)

the films exhibit intense absorption bands in the UV range between 250 and 340 nm. These absorption bands remain unchanged even after annealing the films at temperatures as high as 230 °C. For annealing temperatures above ca. 260 °C the absorbance disappears. Since this temperature corresponds to the sublimation temperature, we can conclude that no major degradation of the films takes place before the film is evaporated. Most importantly for us, the spin transition properties of the film have been perfectly reproducible for annealing temperatures up to 230 °C – which can be clearly inferred from the thermal SCO curves displayed in Figure 3.2.

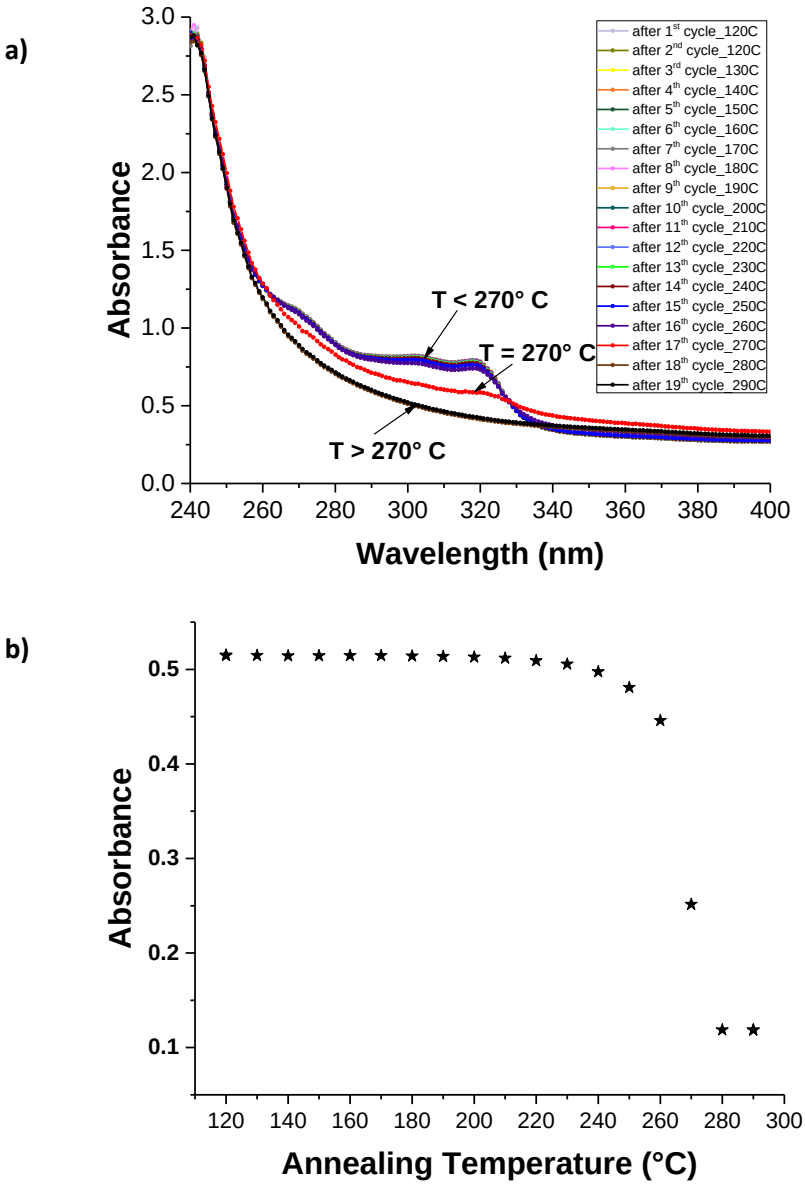

Figure 3.1: a) UV absorbance spectra of a 125 nm thick film of $[Fe(HB(tz)_3)_2]$ acquired at room temperature after the sample was annealed successively at temperatures between 120 °C and 290 °C. b) Evolution of the room temperature absorbance of the film at 317 nm as a function of the annealing temperature.

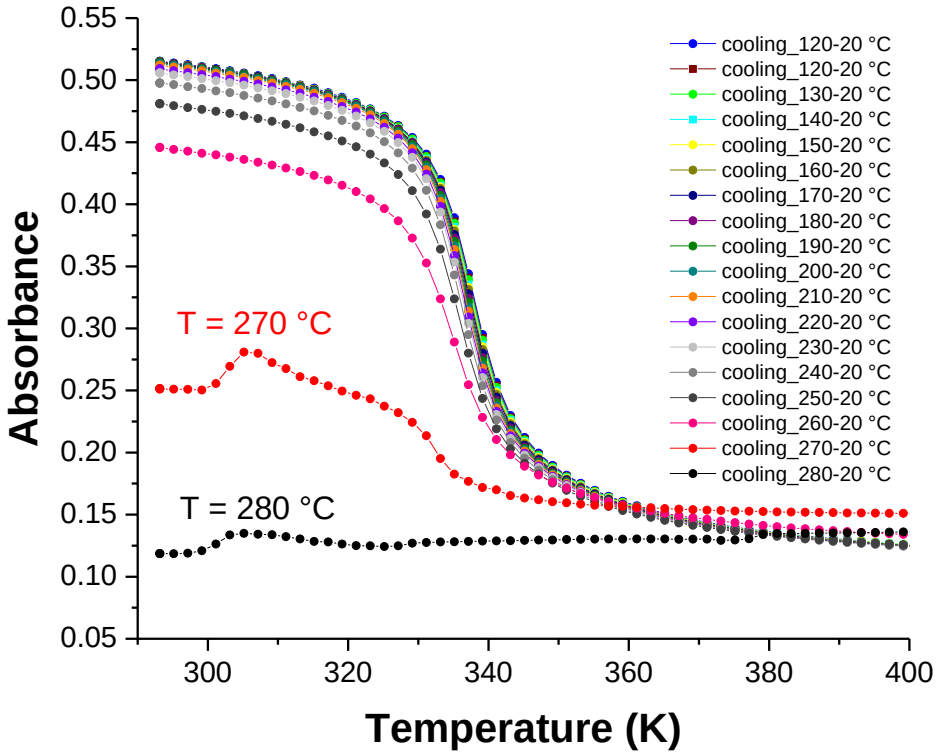

Figure 3.2: Temperature dependence of the absorbance spectra along seventeen cooling cycles recorded at 4 K/min scan rate for a 125 nm thick film of $[Fe(HB(tz)_3)_2]$. For each cycle, the heating range was extended by a step of 10 K.

3.1.2 Long term environmental stability

Another important concern is the stability of the films upon extended periods of storage in ambient air. In order to examine this question several crystalline thin films with different thicknesses from different batches have been stored in ambient air for a year and their properties have been regularly inspected. The first proofs for the stability of the films was obtained by tracking the room temperature optical absorption in the UV spectral region (See Figure 3.3 and Figure A3.1.2.1 in the Annexes for further examples), which allowed us to demonstrate the invariance of the LS absorption bands over a period of 59 weeks, and also by AFM microscopy, which allowed to show that the film morphology is also stable (Figure 3.4). For the sample analyzed in Figure 3.3 we have also carried out temperature dependent UV absorbance measurements after a long period of storage. Figure 3.5 compares the thermal spin transition properties of the freshly prepared sample with that of the same sample following 59 weeks of ageing in air. Remarkably, the temperature of the transition, the shape of the transition curve and the completeness of the SCO remain virtually unaltered (within the experimental accuracy)

over this period of more than 1 year. We notice a slight vertical upshift of the whole transition curve, which may be attributed either to an increased light scattering of the films or, most likely, due to slight differences in the experimental conditions (e.g. position of the cryostat vs. the light beam of the spectrophotometer, etc.). It should be noted that the ensemble of the results regarding the environmental stability were obtained with relatively thick films (in the 50- 200 nm range) and it is possible that for very thin films (< 10- 20 nm) the temporal evolution of the SCO properties is more pronounced. Indeed, preliminary XPS results on our films (provided by Bruno Domenichini from the University of Dijon) indicate that upon a long period of storage in ambient air (months scale) the surface of the films becomes oxidized as the presence of Fe^{III} is detected (Figure 3.6).

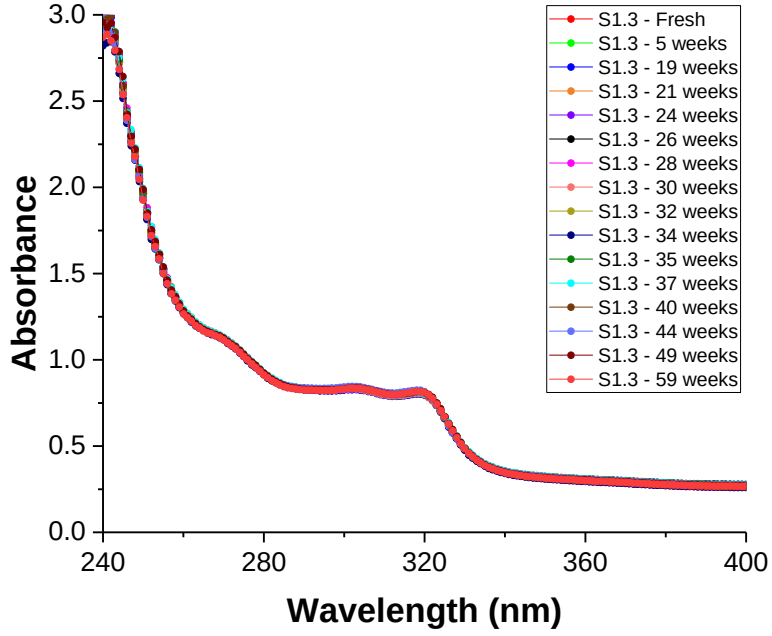

Figure 3.3: Absorbance spectra of a 175 nm thick crystalline film of $[Fe(HB(tz)_3)_2]$ acquired at 293 K regularly along a period of 59 weeks of storage in ambient air.

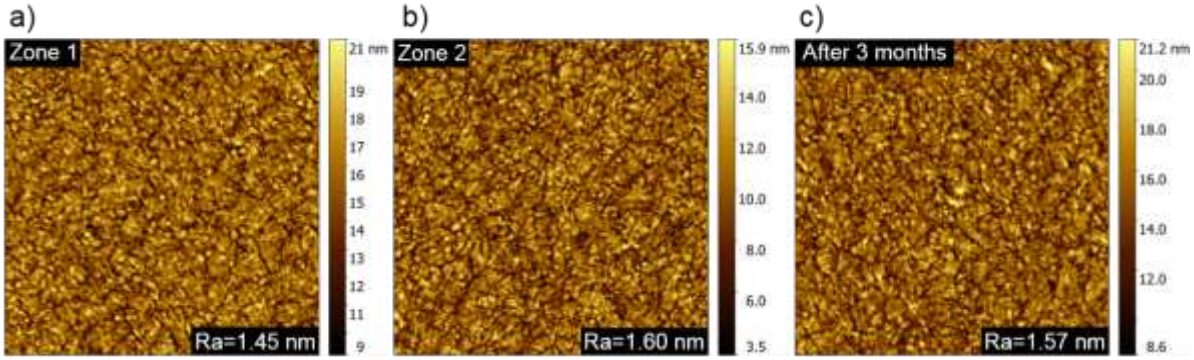

Figure 3.4: Selected AFM topography images of crystalline films of $[Fe(HB(tz)_3)_2]$: (a)-(b) two different zones of a 90 nm film; (c) the same film after 3 months of storage in ambient air;

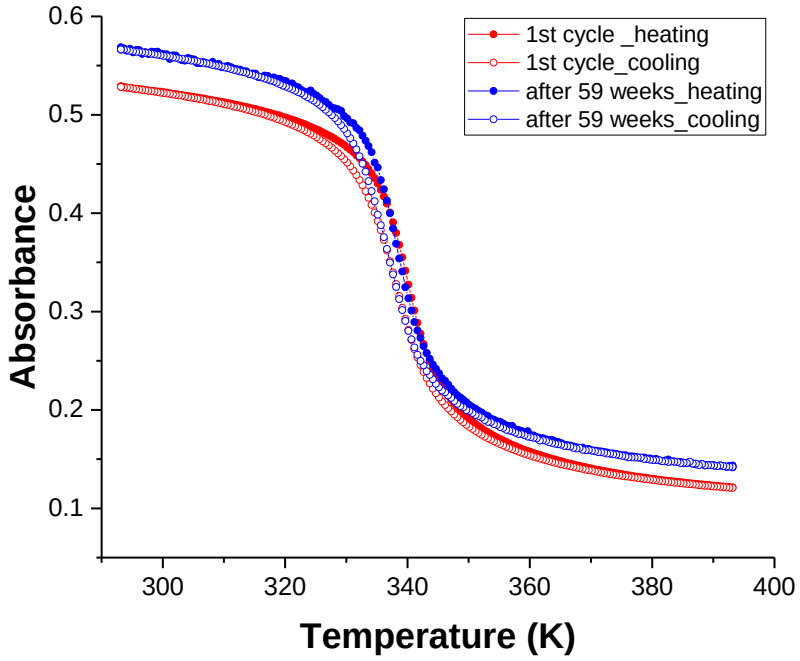

Figure 3.5: Temperature dependence of the absorbance spectra of a 175 nm thick crystalline film of $[Fe(HB(tz)_3)_2]$ recorded at 1 K/min scan rate following immediately the film preparation and after 59 weeks of storage in ambient air.

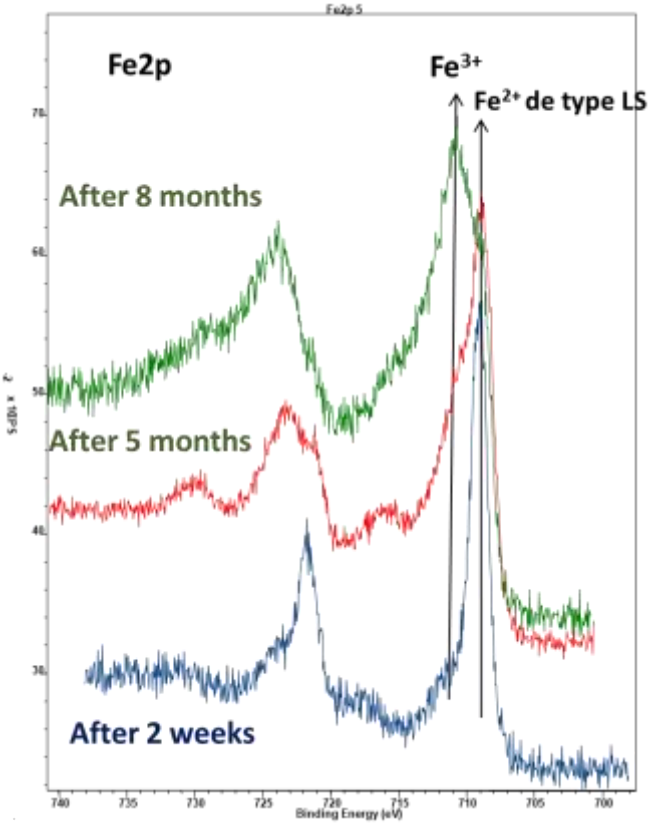

Figure 3.6: XPS spectra (Fe2p) of $[Fe(HB(tz)_3)_2]$ recorded at 293 K after different storage times.

3.1.3 Processing stability

In order to be able to integrate $[Fe(HB(tz)_3)_2]$ films into different devices one must be able to deposit the films on various surfaces and, in many cases, it is also necessary to deposit further layers on top of the SCO film. As we have already seen in chapter 2 the crystallinity and SCO properties of our films do not seem to be influenced considerably by the underlying substrate. We used polycrystalline aluminium and gold, single crystalline silicon, glass ITO, cellulose, polymer, etc. substrates – in each case comparable results. Some further examples for different substrates will be also presented in Chapters 4 and 5 with the same conclusion. We attribute this invariance of the properties of the film on the nature of the underlying substrate to the fact that the films are submitted to a post-deposition water vapor annealing treatment (recrystallization), which involves crystallization starting from the top of the film and which presumably overwhelms any eventual effect of the substrate.

On the other hand, we have observed more substantial effects when depositing different materials on top of the $[Fe(HB(tz)_3)_2]$ film. Indeed, any deposition process is associated with different physico-chemical influences, such as heating, exposure to various radiations and/or to solvents, which can negatively affect the underlying film. Notably, we tried to deposit an SiOx layer over a film of $[Fe(HB(tz)_3)_2]$ using plasma-enhanced chemical vapor deposition (PECVD). As it can be observed in Figure 3.7 during the process the SCO film suffered serious damages – in some cases even film delamination occurred – which we attribute to the presence of highly reactive ionized gaseous species in the processing plasma (e.g. SiH_4, NO_2, H_2, etc.).

Figure 3.7: Optical microscopy images of the surface of a $[Fe(HB(tz)_3)_2]$ film before (left) and after (middle) the deposition of a layer of SiOx by PECVD. A witness surface (substrate only) is also shown after PECVD deposition (right).

We could obtain significantly more promising results for metal deposition. Notably, we deposited a 100 nm thick Al film by vacuum thermal evaporation with a rate of 10 Å s^{-1} on films of $[Fe(HB(tz)_3)_2]$ with different thicknesses (100 and 200 nm) on ITO/glass substrates.

During the evaporation of the Al film, the samples were cooled by water to prevent the perforation of the SCO layer. Figure 3.8 shows scanning electron microscopy (SEM) analyses on the cross-sections of these multilayers following focused ion beam (FIB) milling. We can observe regular arrangements without noticeable degradations/perforations. More importantly, the spin transition properties of the films were preserved after the deposition of the aluminum layer, which we could infer from variable temperature optical reflectivity measurements (through the transparent substrate) shown in Figure 3.8. It is fair to note, however, that deposition of gold and cobalt layers on the SCO field gave less satisfactory results and led to damages in the SCO film.

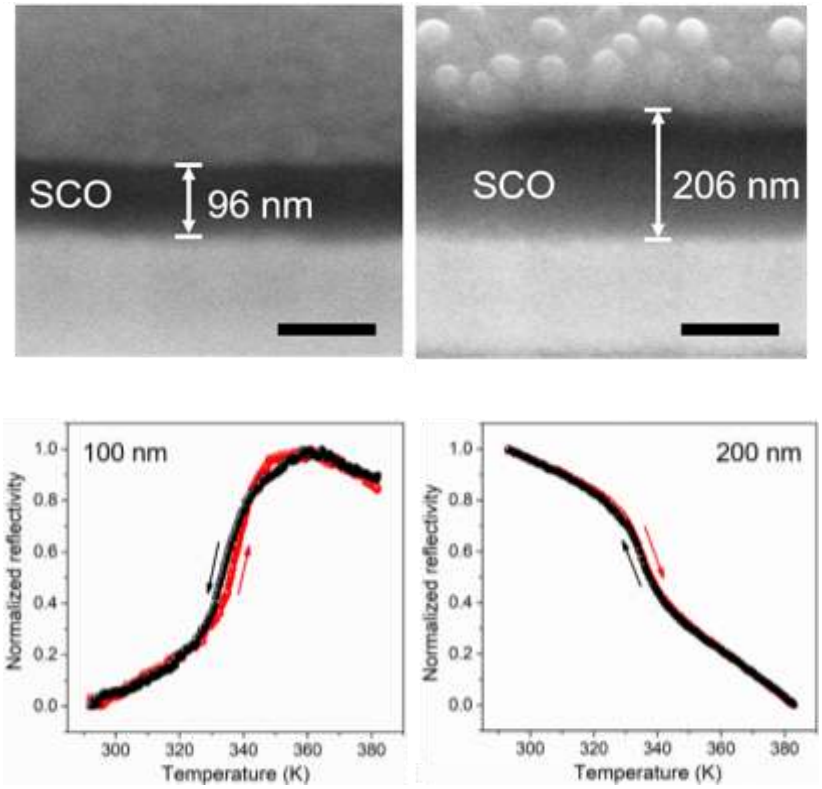

Figure 3.8: (Top panel) SEM images of FIB milled cross-sections of glass/ITO/[Fe(HB(tz)$_3$)$_2$]/Al stacks for two different SCO thicknesses. (Bottom panel) variable temperature optical reflectivity of the same glass/ITO/[Fe(HB(tz)$_3$)$_2$]/Al stacks.

Towards the processing of our films we have also deposited a ca. 1 μm thick layer of a photolithographic resist (SU8) on top of a 140 nm thick [Fe(HB(tz)$_3$)$_2$] film by spray coating the acetone solution of the resist. After the spray coating process, the sample was exposed to UV-irradiation and heated in two steps to 363 K (2 min) and 423 K (3 min) to achieve the cross-linking of the resist. Finally, variable temperature UV absorption spectroscopy was used to analyze the effect of the SU8 layer on the SCO properties. As shown in Figure 3.9 the deposition

of the SU8 layer only slightly altered the spin transition properties including a ca. 2-3 K downshift of the transition temperature and a slight reduction of the completeness of the spin transition.

Overall, we can conclude that we succeeded to deposit both conducting metallic and optically transparent dielectric layers on top of the $[Fe(HB(tz)_3)_2]$ opening up possibilities for the integration of these films into various devices. Further work will be necessary to fabricate high quality multilayers with other technologically interesting materials and to achieve micro- and nanoscale patterning of the different parts of the multilayers.

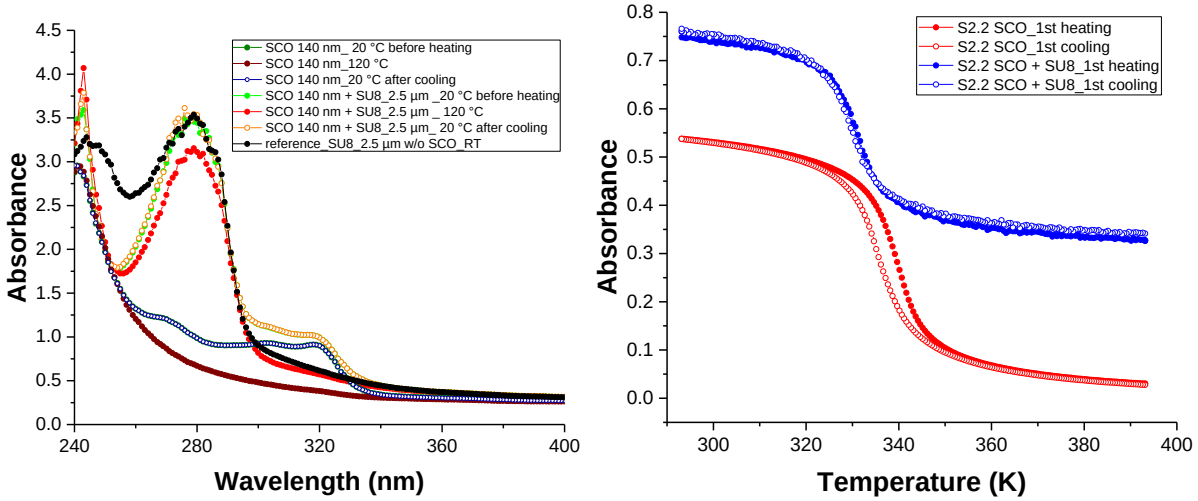

Figure 3.9: (Left panel) Optical absorbance spectra of a140 nm thick $[Fe(HB(tz)_3)_2]$ film in the HS (120 °C) and LS (20 °C) states, before and after spray coating with SU8. (Right panel) Spin transition curves before (red) and after (blue) SU8 coating.

3.1.4 Switching stability

Most crucially, the robustness of the spin transition must be determined for our SCO thin film, i.e. we have to investigate if it can withstand multiple thermal cycling. Usually, in the literature, the SCO is induced thermally for different samples and the transition curve is recorded over only a few heating-cooling cycles. Yet, even for a small number of thermal cycles, depending on the compound, the spin transition behavior may change or even disappear due to various phenomena, which include the loss or uptake of solvent molecules, mechanical fatigue or irreversible structural changes.

To our best knowledge, fatigability tests have been performed up to now only on the $[Fe(Htrz)_2(trz)](BF_4)$ SCO compound. Gural'skiy and coworkers reported a first proof of this stability using a bilayer actuator device (built using an SCO/PMMA composite) which was

actuated by applying current over more than 300 actuating cycles with no observed fatigue of the actuator [144]. Nagy et al., investigated a cellulose composites of the same SCO compound for its reversible thermochromic properties and reported that the color change was detected even after 1000 thermal cycles [145]. Lefter and coworkers have analyzed the thermal stability of the SCO compound $[Fe(Htrz)_2(trz)](BF_4)$ over a series of 3000 consecutive thermal cycles in ambient air by means of optical reflectivity measurements [146]. They reported that the sample still presents a hysteretic behavior even after 3000 thermal cycles, but the hysteresis width decreased from 40 K to 28 K temperatures (see Figure 3.10). A crystallographic study of Grosjean et al. [147] was carried out on sub-micrometer-size particles of $[Fe(Htrz)_2(trz)](BF_4)$. The particles were submitted to 50 thermal cycles and the evolution of their crystal structure and microstructure was followed in situ by means of powder X-ray diffraction (PXRD). It turned out that the unit cell, in particular parameter a, is slightly modified during the first few cycles, but remains well reproducible afterwards. It was thus suggested that the initial "run-in" of the SCO properties during the first heating occurs not due to solvent loss as it was previously suggested, but as a result of a small ordering of the lattice. On the other hand, the authors pointed out a significant structural fatigability reflected by a continuous and highly anisotropic decrease of the coherent domain size along the crystallographic b direction (i.e., along the Fe-triazole chains) over successive thermal cycles. In agreement with the XRD analysis, Manrique et al. has revealed by variable temperature AFM topography measurements both reversible and irreversible morphological changes of this sample upon thermal cycling [125].

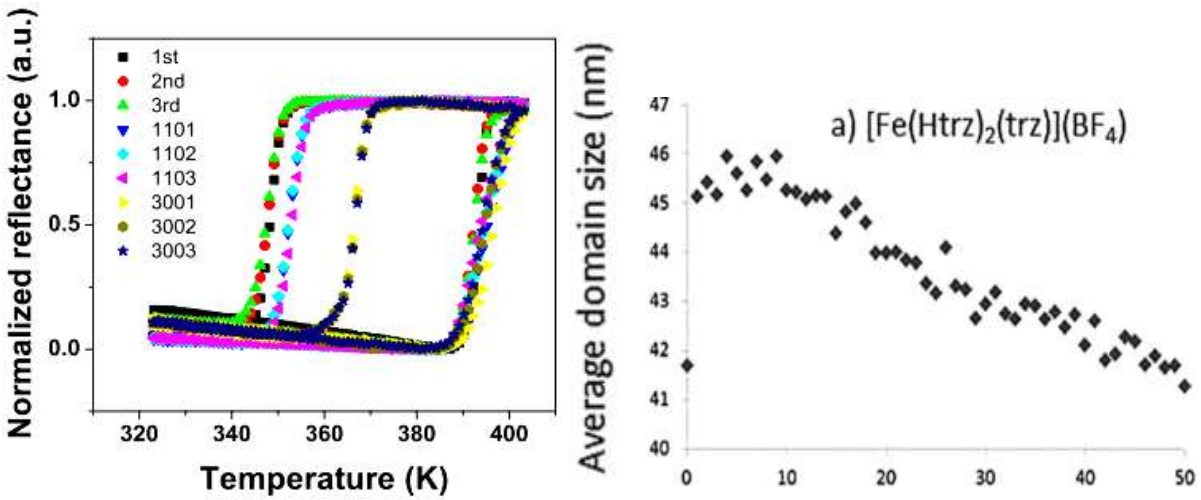

Figure 3.10: (Left panel) Thermal SCO hysteresis of $[Fe(Htrz)_2(trz)](BF_4)$ before and after 1100 and 3000 consecutive cycling.[146] (Right panel) Evolution of the average crystallographic domain size in $[Fe(Htrz)_2(trz)](BF_4)$ particles over 50 thermal cycles [147].

In order to investigate the switching stability (LS↔HS state) of the $[Fe(HB(tz)_3)_2]$ films, we performed two experiments. First, a series of ca. 10000 consecutive thermal cycles were imposed to a film deposited on a glass substrate and the quantitative spin transition curves have been recorded before and after the cycling by means of variable temperature optical absorption. Then, we have also deposited a film on a gold microwire, which we used as a fast microheater in order to submit the SCO film to a large number of thermal cycles (ca. 1 million). In this case the SCO was followed by variable temperature optical reflectance measurements.

For the first experiment, the film was placed on a temperature controlled Peltier stage (Linkam PE94 - see Figure 3.11) and cycled between 55 °C and 75 °C (in order to ensure a full LS - HS - LS conversion) with a rate of 20 °C/min while recording the time – temperature profiles.

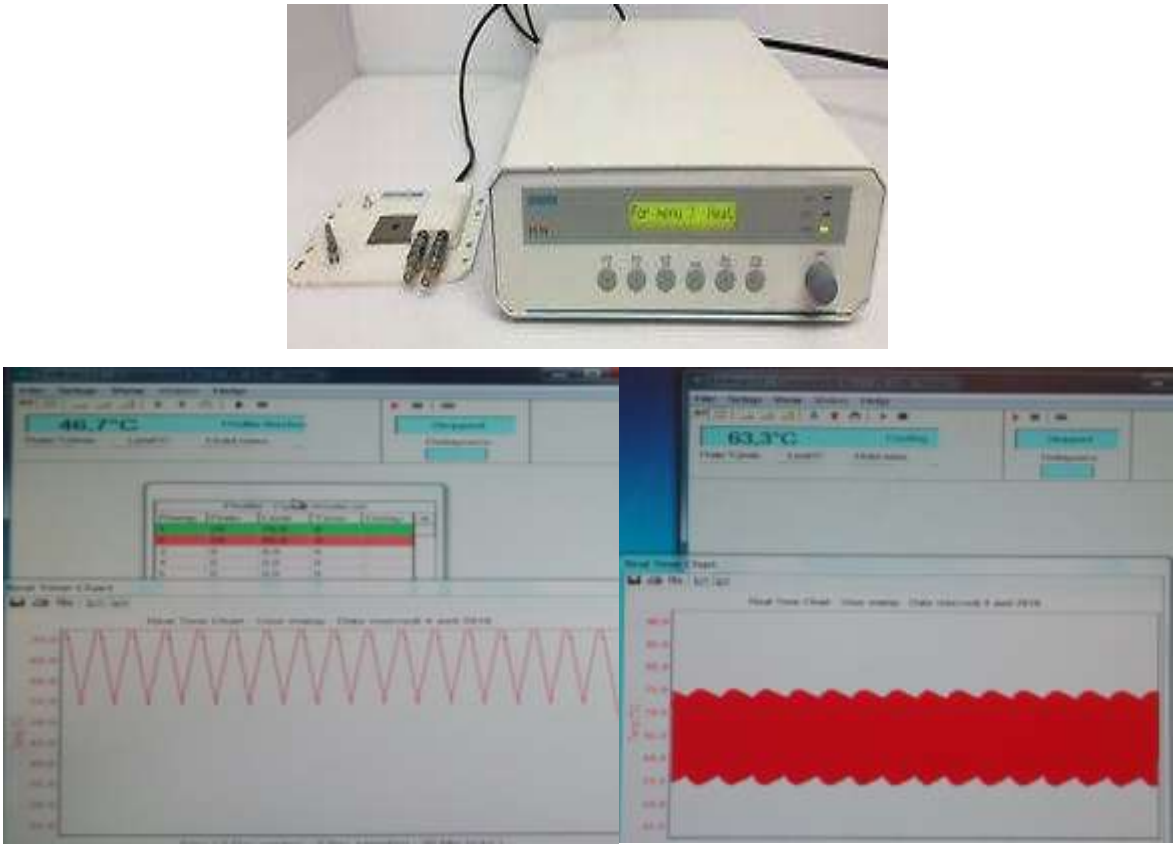

Figure 3.11: Photo of the Peltier stage and screen-prints recorded during the fatigability study.

We have acquired variable temperature optical absorption data of the films before the fatigability test, after 1858 cycles (in the course of the thermal cycling) and finally at the end of the test following 10321 cycles. Figure 3.12 summarizes these results. First, one can observe that the room temperature optical absorption spectra are virtually the same before and after 10321 thermal cycles. Even more impressive is the overlap of the thermal spin transition curves

with a spin transition temperature, which remains the same with a variation of less than 0.5 K. We only observe a slight decrease in the amplitude of the absorbance change, but this remains close to the experimental uncertainty.

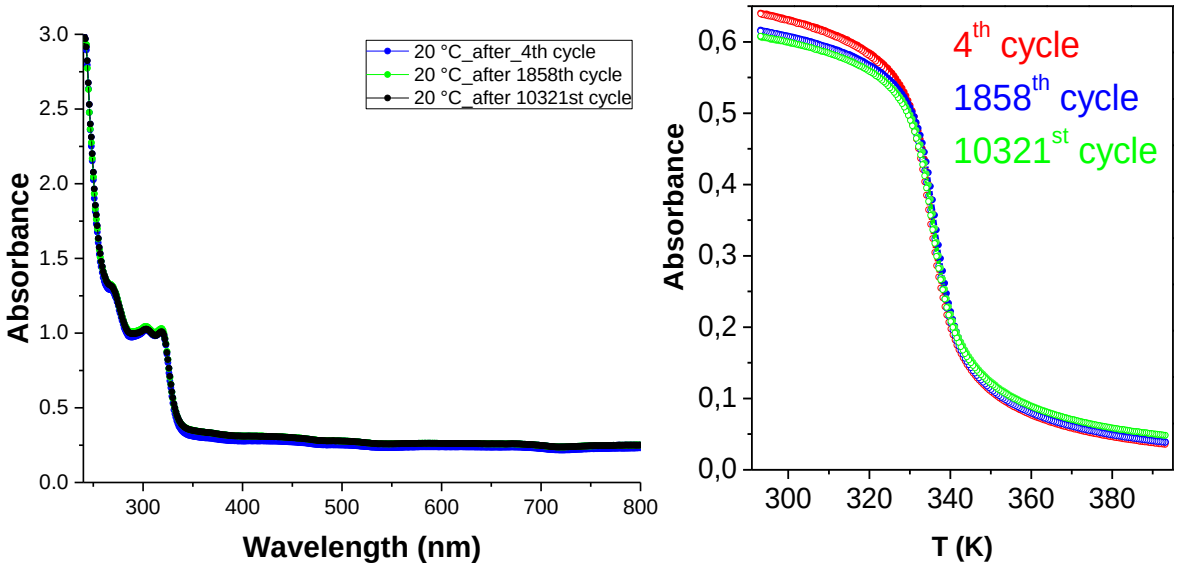

Figure 3.12: (Left panel) Absorption spectra and (Right panel) thermal spin transition curves of a $[Fe(HB(tz)_3)_2]$ film before and after 1857 and 10320 consecutive cycling.

The first fatigability test lasted over nearly two weeks because the highest heating-cooling rate we can achieve with the Peltier stage is only 20 K/min. In order to be able to accomplish a significantly higher number of thermal cycles in a reasonable lapse of time, we decide to use metallic microwires heated by Joule effect. Due to their small thermal mass, the temporal response of such microwires is very fast and the temperature distribution is spatially well confined [148]. These two important properties, together with their reliable all-electrical operation, make these wires ideal test stands. The performance of the heating platform is largely dependent on its design, the material properties and the geometry of the different components. For these reasons, the precise thermal characterization of these heating elements is a critical step. The concept of the device and the fabrication of the nanowires were carried out by Olena Kraieva and Carlos Quintero in collaboration with Christian Bergaud (LAAS–Toulouse). It was shown both experimentally and by finite element simulations that the microheaters have a very fast response time (ca. 1 µs) and they do not induce any thermal drift of the sample [149]. The fabrication of the wires was accomplished by successive photolithography, metal deposition and lift off both on glass and silicon wafers. The wafers with the wires were cut into smaller pieces that correspond to chips (typically of sizes 20×10 mm). Regarding the possible

connections of the wires, 7 wires per chip were placed with a common path (see Figure 3.13(a)) to attach it to an 8-track connector, see Figure 3.13(b) [150].

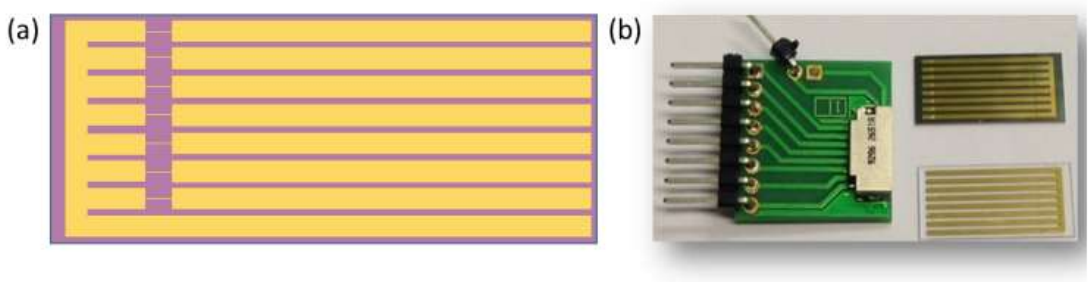

Figure 3.13: (a) The schema of a chip (20×10 mm) with 7 gold microwire heaters. (b) Photo of the 8 track connector with two chips on silicon (above) and glass (below) substrates [150].

For our experiment, a layer of ca. 175 nm of $[Fe(HB(tz)_3)_2]$ was deposited directly by thermal evaporation on the surface of the resistive heated nanowire and the post-deposition humidity treatment was carried out. This original approach allows us to heat a small sample area quickly and locally. Electrical characterizations and measurements were carried out by applying a bias current in order to guarantee always a reproducible current excitation and temperature difference due to the Joule effect. The temperature calibration of the gold nanowire was performed combining two different electrical measurements. First, the resistance of the wires at low bias current was measured as a function of the temperature (T) using an input current source-meter (Keithley 2420) and a heating stage. The resistance of the selected heating element in the chip was monitored in the temperature range of 30 to 95 °C. In a second time, the resistance of the selected heater was measured as a function of the applied electrical current while keeping the temperature of the substrate fixed at 35 °C. Assuming that the resistance variation mainly comes from the change of the temperature in the microwire, it is possible to relate the two measurements to obtain a calibration of the mean temperature of the wire as a function of the applied current.

For the fatigability test, the SCO coated wires were placed on the Peltier stage (Linkam PE 94) and the base temperature was fixed at 35 °C. A square shaped ac current oscillating between 0 and 38 mA at a frequency of ca. 1 Hz was then applied to the sample during two weeks. According to our calibration, this corresponds to successive temperature jumps between 30 and 100 °C, i.e. to a full LS - HS - LS switching cycle in 1 second. To confirm this temperature change the optical microscopy image of this wire was recorded in reflectance mode (λ = 450 nm) using a CCD camera (Andor Technology Clara – see Figure 3.14) at regular intervals (30 min every morning) and 4 successive spin transition curves were also acquired.

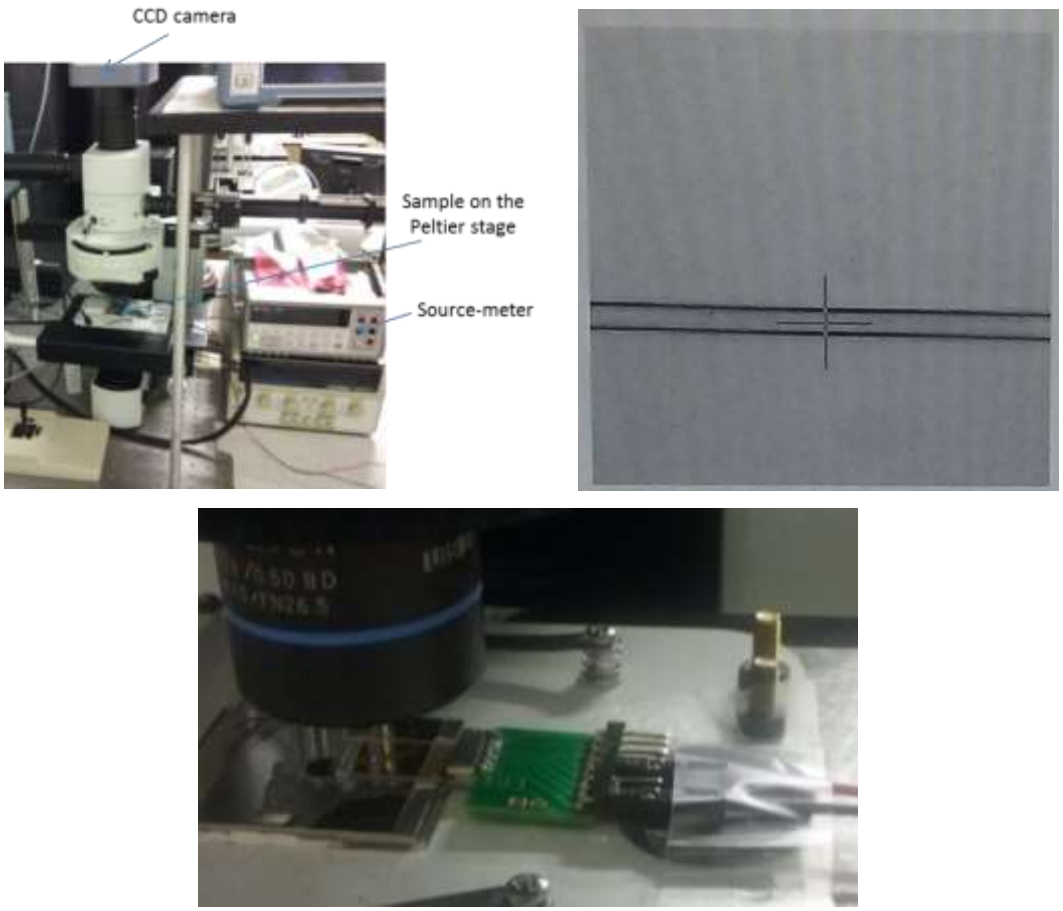

Figure 3.14: (Top, left) Photo of the experimental setup, (Top, right) Optical microscopy image of a section of a gold microwire used in our experiment. The width of the wire is 1 μm, its thickness is 300 nm and its length is 80 μm. (Bottom) Photo of the chip with the connector below the microscope objective.

Figure 3.15 depicts the recorded oscillations of the optical reflectance upon the oscillating current excitation. Unfortunately, there is a baseline drift over the two weeks long experiment. We attribute this on one hand side to the intrinsic stability of the CCD camera and on the other hand to the fact that the experiment was performed in ambient air at high temperatures and under electrical bias leading to the slow accumulation of dust on the surface. Nevertheless, the amplitude of the oscillations remain comparable denoting comparable changes of temperature. The spin transition curves after ca. 100 cycles and 1 million cycles are plotted in Figure 3.16. Remarkably, the spin transition temperature remains unchanged (within the experimental precision) and the shape of the spin transition curves is only slightly altered. We can thus conclude that films of $[Fe(HB(tz)_3)_2]$ show extremely high resilience to repeated thermal spin state switching in ambient air.

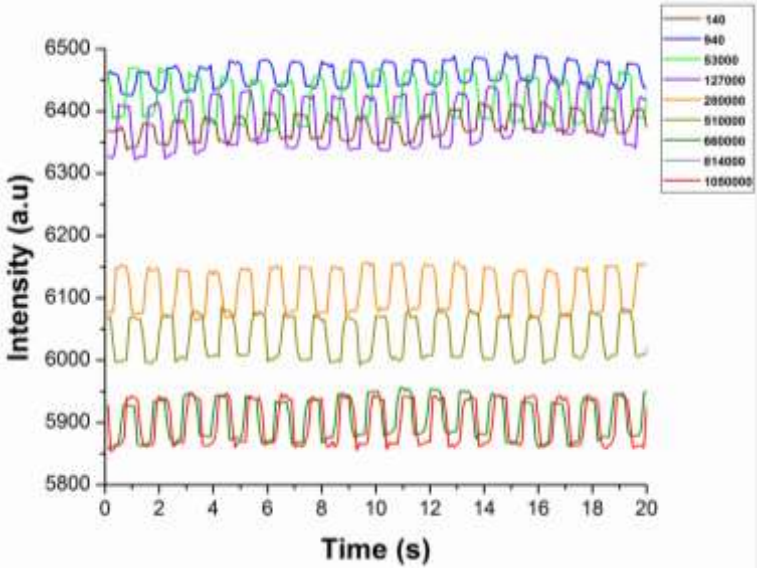

Figure 3.15: Optical reflectivity recorded during the current excitation for different width of current pulses from 0 s to 20 s.

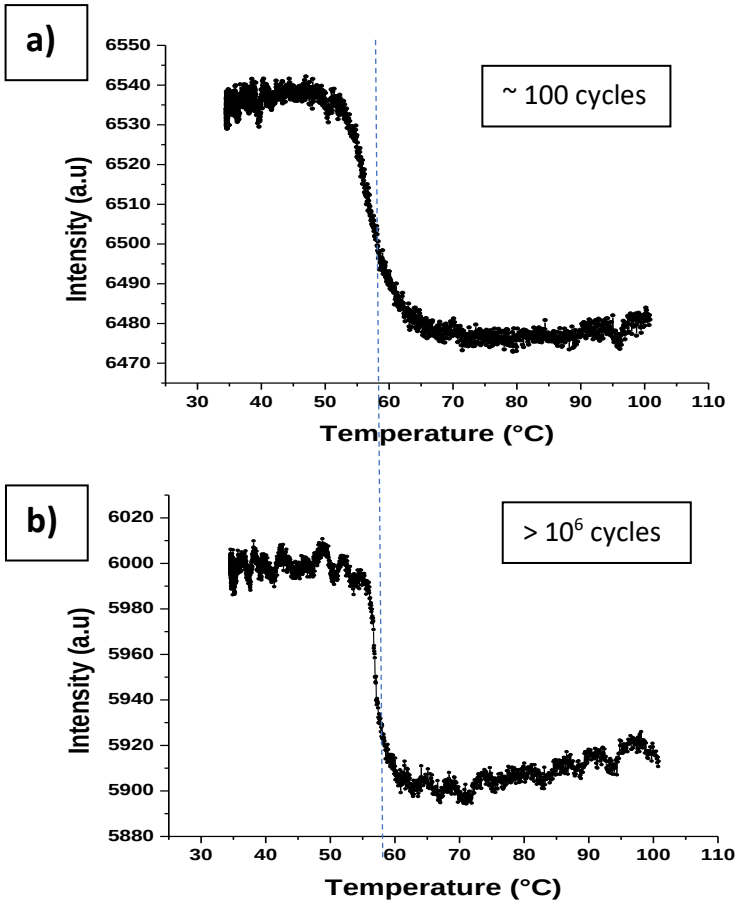

Figure 3.16: Variation of the reflectivity signal of a [Fe(HB(tz)$_3$)$_2$] film deposited on a gold microwire heater as a function of the temperature (heating mode): a) after 100 cycles and b) after 1000000 cycles.

3.2 Size reduction effects in [Fe(HB(tz)$_3$)$_2$] films

Phase transitions at the nanometric scale in functional materials [151] have attracted much attention of scientists for this last decade. In this context, the interest in the elaboration and the integration of nano-objects based on phase change molecular compounds have grown considerably thanks to their applicative potentials in memory and display devices. The phase stability of bulk materials is inexorably altered at reduced sizes due, mostly, to the increasing role of surfaces/interfaces. The most well-known example for this phenomenon is the melting point depression of metallic nanoparticles [152]. Finite size effects on solid-solid polymorphism has been less investigated, but similar to the melting phenomenon, an increase (decrease) of the transition temperature (pressure) is observed universally [153-160]. This change of the *P,T*-phase diagram is driven fundamentally by the fact that the cohesive energy of high temperature (low pressure) phases is generally lower, which implies also a lower surface energy. Higher energy polymorphs, which are unstable in the bulk material, become thus thermodynamically stabilized in small particles due to the increasing contribution of the surface energy to the total free energy of the particle. A notable exception to this trend is the melting point elevation of small particles when embedded in a solid matrix with an epitaxial confinement (Figure 3.17) [161].

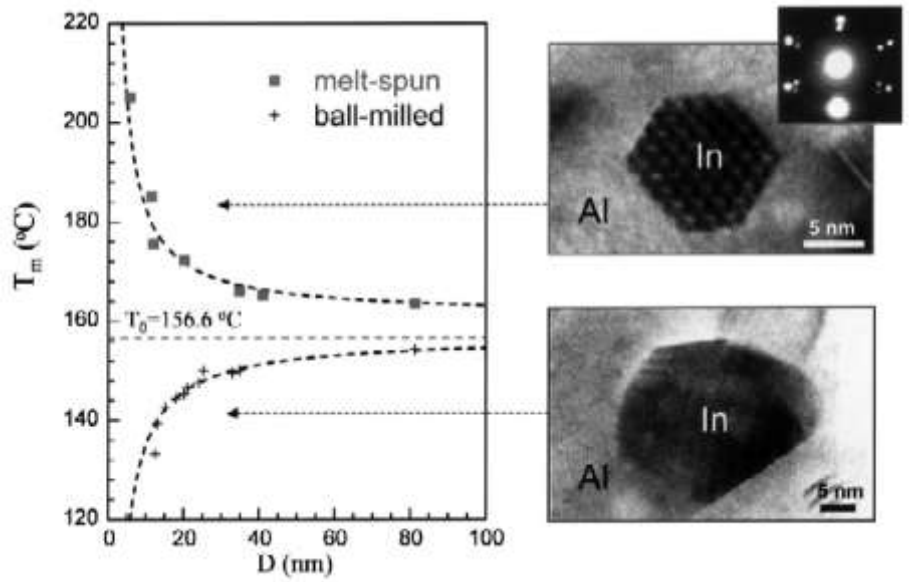

Figure 3.17: Variation of melting point with the particle size for In nanoparticles embedded in an Al matrix in two kinds of In /Al nanogranular samples prepared by means of melt-spinning and ball-milling. The remarkable different melting point variations in these two cases might be attributed to the In /Al interfacial structures. For the melt-spun sample a semi-coherent In /Al interface was formed as evidenced by the HRTEM image of the In particle and the electron diffraction pattern, and for the ball-milled sample, the In /Al interfaces are random [161].

This phenomenon is believed to result from the specific properties of the epitaxial interface, but the mechanistic details remain often elusive. As a new example for such atypical behavior, we provide evidence on the elevation of the spin transition temperature in nanocrystalline thin films of $[Fe(HB(tz)_3)_2]$ when reducing their thickness. We show that this unusual stabilization of the low temperature phase can be linked to the particular anisotropy of the structural changes associated with the LS to HS transition in $[Fe(HB(tz)_3)_2]$.

In the past decade, the investigation of nanometer-sized molecular SCO materials has generated significant interest [1, 3, 162, 163]. Understanding the complex relationships between the size, crystal structure, surface/interface properties and the SCO behavior of these various nano-objects is arduous, but will be crucial for integrating them into useful devices. The general experimental observation [164-167], supported also by various theoretical predictions [168-171], is a loss of the hysteresis properties, a downshift of the transition temperature (*i.e.* the stabilization of the HS phase) and the occurrence of incomplete transitions when the size of the objects is reduced. All these observations were satisfactorily explained on simple thermodynamical grounds, assuming that the surface energy of these systems is lower in the high spin state [172].

Unfortunately, at present the link between theory and experiment remains rather poor for different reasons. First of all, the surface energies of SCO compounds are not known as these quantities are difficult to determine in *both* spin states using conventional experimental (contact angle, calorimetry) or theoretical methods (molecular dynamics, density functional theory. In addition, to produce SCO nano-objects with different sizes it is (obviously) necessary to use different synthesis conditions, which consequently can lead to differences not only in the size of the object, but also in other parameters, such as the particle shape, composition, crystallinity, surface coating, defects and so forth. Unfortunately, these parameters remain often ill-determined for the lack of appropriate sample characterization tools. Considering this, it becomes necessary to develop series of high quality, size-controlled samples, which are comparable in terms of morphology, chemical composition, crystallinity, surface/interface properties.

In this context, thin films of $[Fe(HB(tz)_3)_2]$ prepared by thermal evaporation appear as "ideal" samples for the study of size reduction effects. As we mentioned in the previous chapter, using a very rigorous protocol (both during deposition and post-deposition) it is possible to obtain films with very high purity and tight thickness control. The post-deposition recrystallization of $[Fe(HB(tz)_3)_2]$ allows for highly oriented nanocrystalline films (orthorhombic *c*-axis normal to the surface) with smooth surfaces and robust, well-reproducible

SCO properties. Indeed, from crystallographic, Raman spectroscopic data, AFM and optical absorption, we noticed that in a thickness range of approx. 40 - 200 nm, these films appear identical in all aspects. Their similarity is most clearly attested by the fact that, at a first examination, we have noticed no significant difference between the spin transition curves of films with different thicknesses, which is a very sensitive indicator of the sample quality.

For this study, eight thin films of $[Fe(HB(tz)_3)_2]$ with thickness between 45 nm and 201 nm were prepared by high vacuum deposition on fused silica substrates. A subsequent treatment for 10 min in air with a relative humidity of approximately 80 % was further employed for the formation of stable and fully crystalline layers. The film thickness was determined from AFM data (see Figure A3.2.1 in Annexes). The films are characterized by a homogenous morphology with an arithmetic average surface roughness R_a of *ca.* 1-2 nm (see Figure 3.18 for AFM surface topography images).

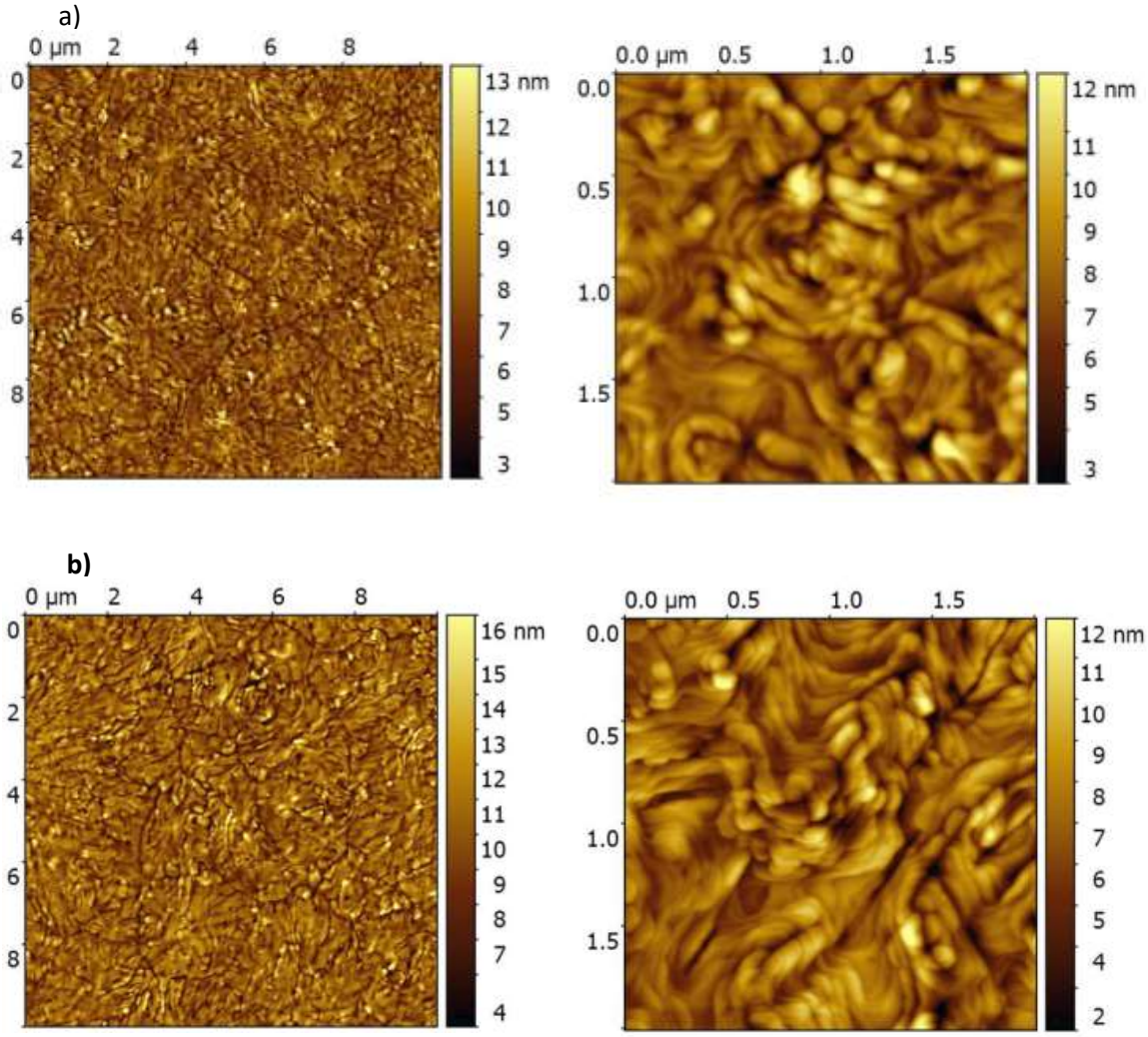

c)

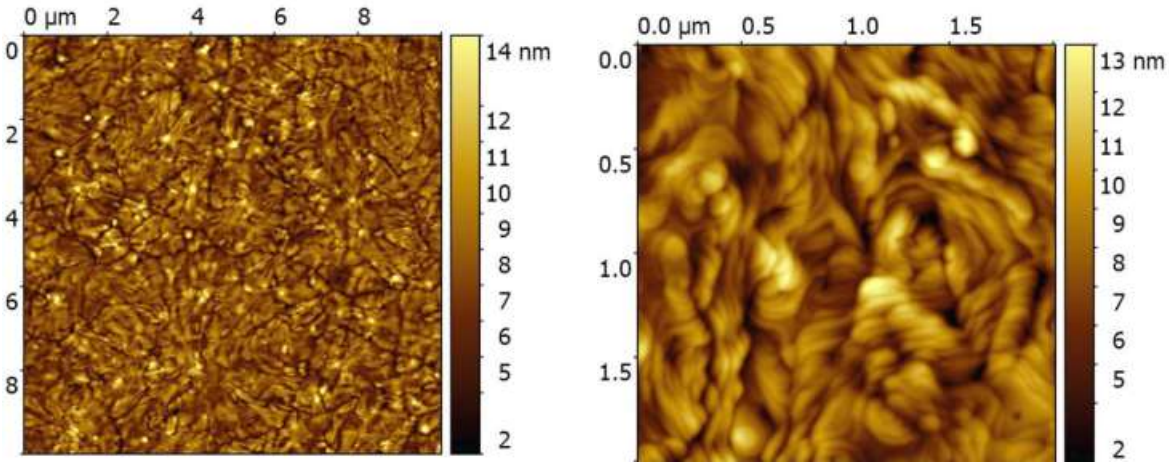
0 µm 2 4 6 8
0 2 4 6 8
14 nm 12 11 10 9 8 7 6 5 2
0.0 µm 0.5 1.0 1.5
0.0 0.5 1.0 1.5
13 nm 12 11 10 9 8 7 6 5 2

d)

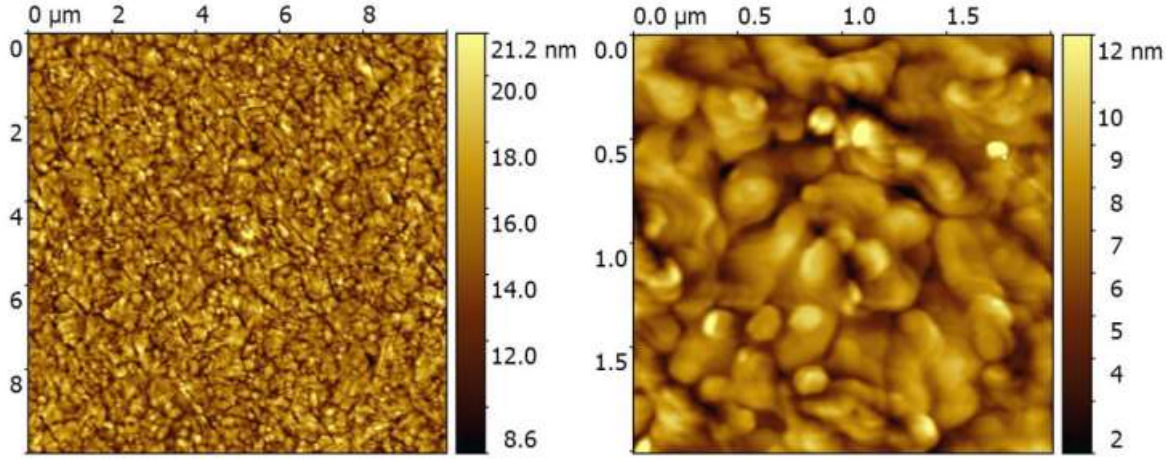
0 µm 2 4 6 8
0 2 4 6 8
21.2 nm 20.0 18.0 16.0 14.0 12.0 8.6
0.0 µm 0.5 1.0 1.5
0.0 0.5 1.0 1.5
12 nm 10 9 8 7 6 5 4 2

e)

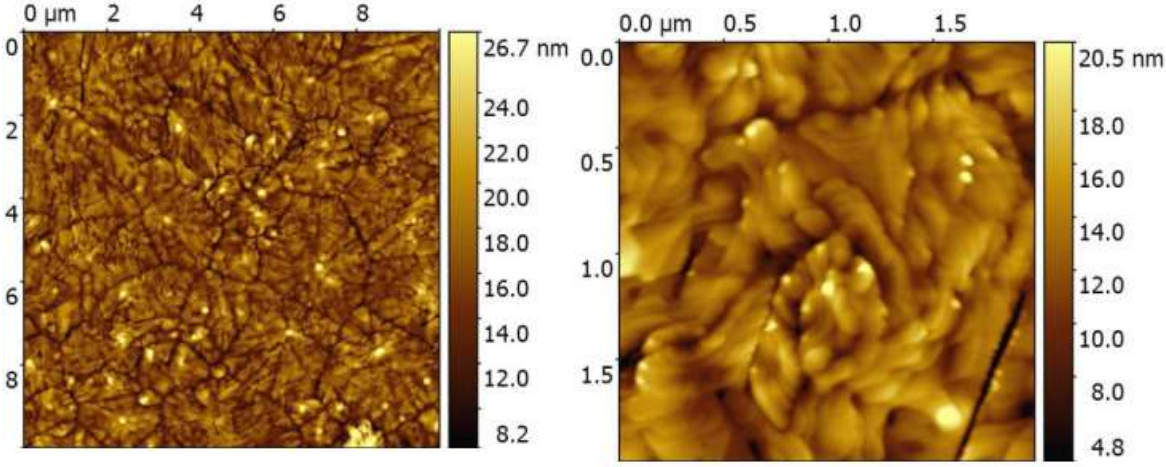
0 µm 2 4 6 8
0 2 4 6 8
26.7 nm 24.0 22.0 20.0 18.0 16.0 14.0 12.0 8.2
0.0 µm 0.5 1.0 1.5
0.0 0.5 1.0 1.5
20.5 nm 18.0 16.0 14.0 12.0 10.0 8.0 4.8

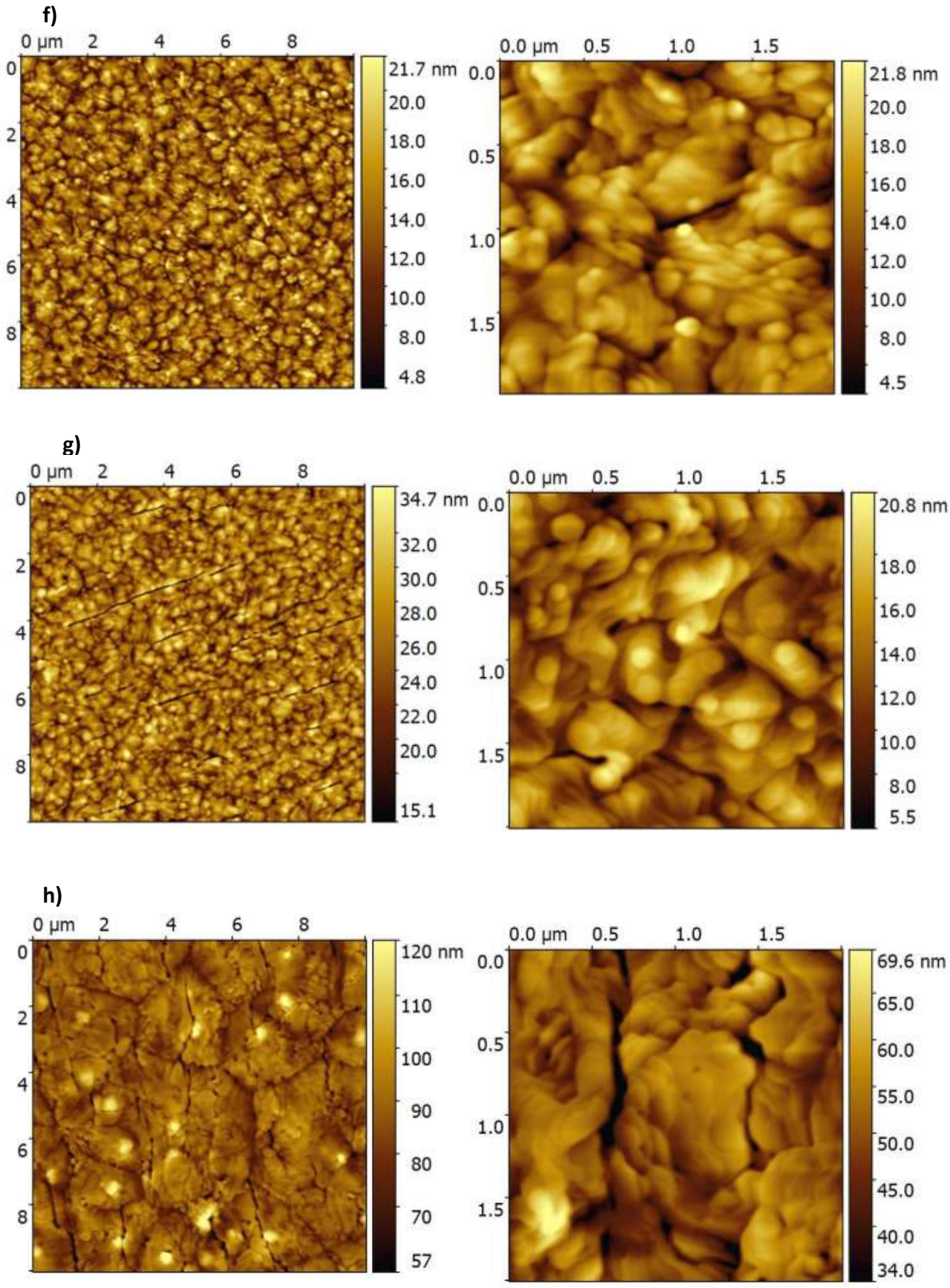

Figure 3.18: Representative AFM topography images (10×10 and 2×2 μm^2) of films of $[Fe(HB(tz)_3)_2]$ with different thicknesses: a) 45 nm; b) 55 nm; c) 72 nm; d) 92 nm; e) 100 nm; f) 112 nm; g) 155 nm and h) 201 nm.

Variable temperature optical absorption measurements were performed over four heating – cooling cycles between 293 K and 393 K with a rate of 1 K/min – with a tight control on all experimental conditions (synthesis, pre-treatment, storage and measurement), including even details such as the time laps between the film deposition and the measurement cycles. It may be worth to note that the spin transition temperatures of $[Fe(HB(tz)_3)_2]$ were shown to be strictly rate-independent between 0.1 and 1 K/min [114], *i.e.* they denote the quasi-static hysteresis.

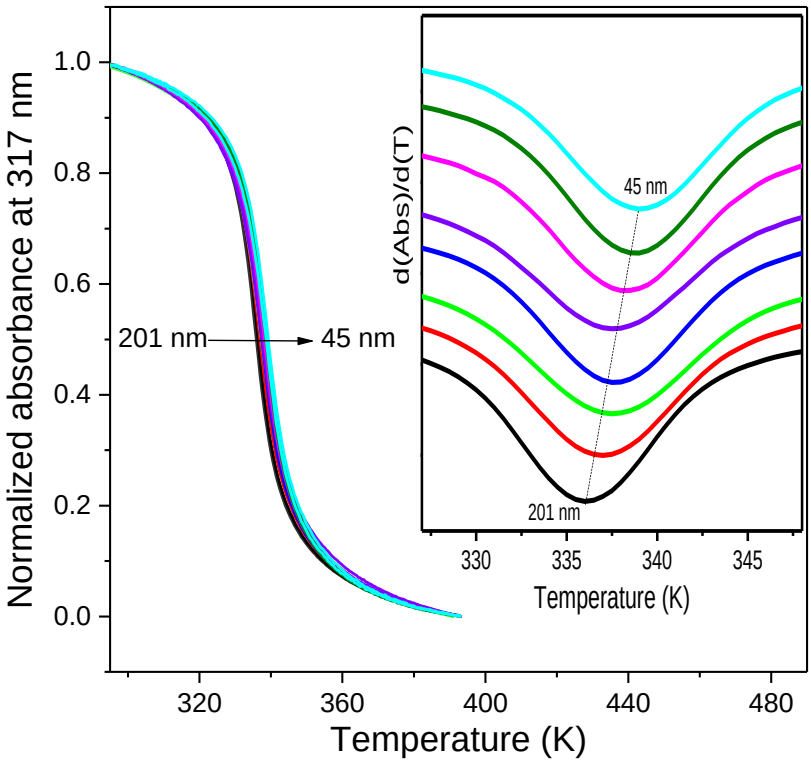

Figure 3.19: Temperature dependence of the normalized absorbance at 317 nm along the fourth heating-cooling cycle recorded at 1 K/min scan rate for eight films of $[Fe(HB(tz)_3)_2]$ with different thicknesses between 45 and 201 nm. The inset shows the derivatives of the absorbance curves in the heating mode.

The abrupt change of the absorbance around *ca.* 337-338 K with a small hysteresis of ca. 0.5 K width clearly reflects the SCO phenomenon. The SCO curves are very similar for different thicknesses: one can observe the same shape and the same small hysteresis, which is a very sensitive indicator of the sample quality. However, a closer look at the SCO curves reveals a slight, but systematic increase of the transition temperature for decreasing film thickness, which is particularly obvious in the derivative curves (see the inset of figure 3.19). The perfect linear fit on the UV absorbance vs. thickness curve (see Figure 2.11) confirms also the full crystallinity and complete spin transition in each film.

Figure 3.20a and Figure 3.20b show the thickness dependence of the spin transition temperature $T_{1/2}$ (which we approximate here as the barycenter of the hysteresis loop) and the hysteresis width, respectively. We must note that during the first heating of the sample the spin transition occurs at a slightly higher temperature than in the successive cycles (see Figure 3.21), which can be possibly attributed to the relaxation of some residual film growth stress. Then, the transition temperatures of the successive cycles become well reproducible. Hence in figure 3.20 the transition temperatures and hysteresis widths corresponding to the 2-4th thermal cycles are shown only, as these quantities cannot be defined for the first cycle. The key experimental finding here is the systematic upshift by *ca.* 3 K of $T_{1/2}$ when decreasing the film thickness from 201 to 45 nm. What deserves also attention is the fact that the hysteresis width, unlike $T_{1/2}$, remains virtually the same for different film thicknesses (*ca.* 0.5 K).

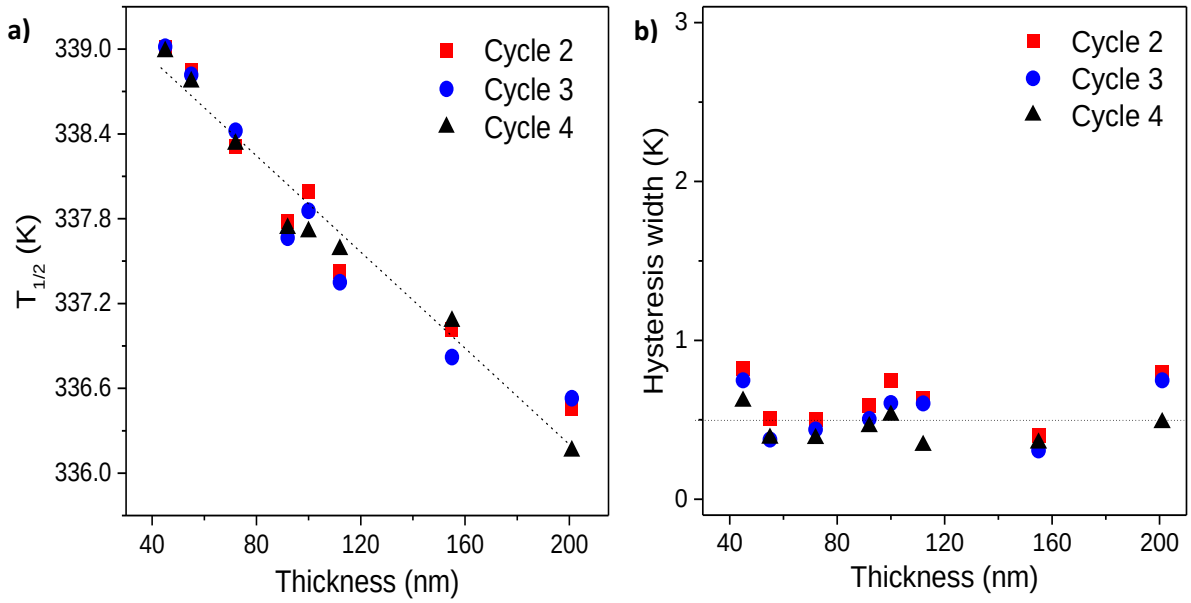

Figure 3.20: a) Spin transition temperature and b) hysteresis width as a function of the film thickness of [Fe(HB(tz)$_3$)$_2$] for the different heating-cooling cycles. (The dotted lines are guides to the eye.)

Before discussing the intrinsic film properties, one should notice that the observed decrease of $T_{1/2}$ with increasing film thickness might also occur due to the heating of the film by the UV light, which is used to probe its spin state. In order to examine this possibility we performed UV absorption measurements by placing a *ca.* 2.6 % UV transmission filter in front of the samples to expose them to reduced light intensity. The measurements done with and without the filter gave strictly the same result demonstrating the absence of any significant thermal effect (see Figure 3.22).

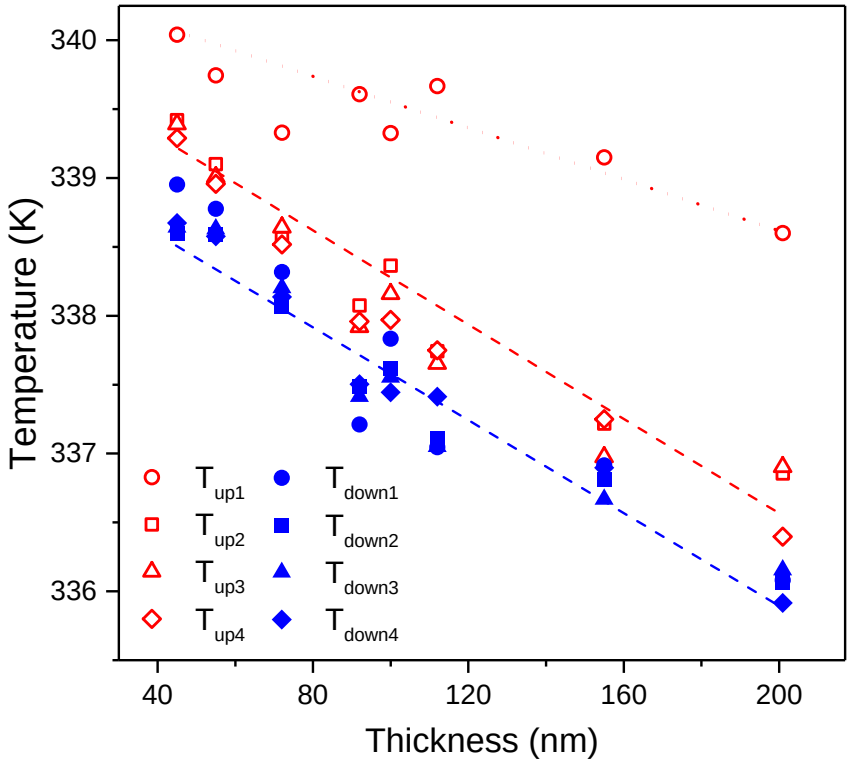

Figure 3.21: Transition temperatures on heating (T_{up}) and cooling (T_{down}) as a function of the film thickness of [Fe(HB(tz)$_3$)$_2$] for the first four heating-cooling cycles. The dashed/dotted lines are guides to the eye.

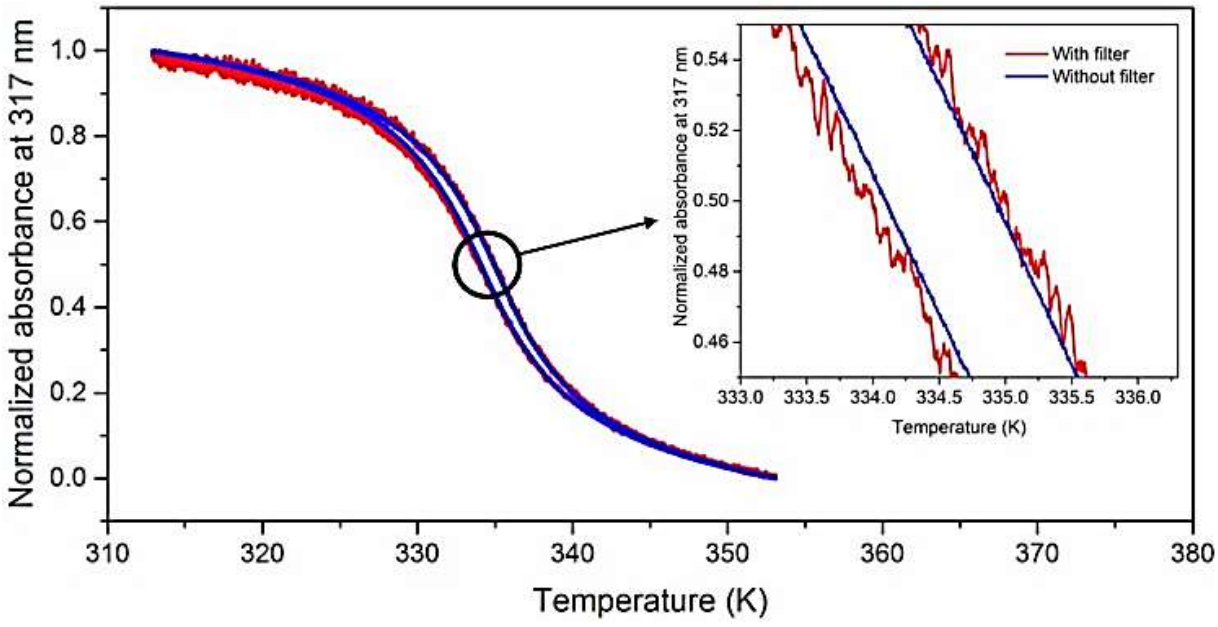

Figure 3.22: Temperature dependence of the absorbance of a 200 nm thick film of [Fe(HB(tz)$_3$)$_2$] recorded at 317 nm at a 2 K/min scan rate with and without a blocking filter (2.6 % transmission) in front of the sample.

The origin of the upshift of the transition temperature can be multiple. From a mechanical point of view, it may result from a biaxial stress in the SCO film due to its mechanical coupling with the substrate leading to a spin-state dependent elastic work. From a nano-thermodynamical point of view it may result from excess quantities due to the increasing surface-to-volume ratio at this scale. In this latter case, the relevant parameters are surface energy and stress, which can provide a driving force for phase transitions, which minimize the surface/interface energy [157, 158]. If we take into account these ingredients as well as the bulk free energy, the change in the Gibbs free energy of the film for the LS to HS transition can be expressed as:

$$\Delta G(T) = G_{HS} - G_{LS} = \Delta H - T\Delta S + \Delta\gamma_{gb}A_{gb} + \Delta\gamma_{sv}A_{sv} + \Delta\gamma_{ss}A_{ss} + \Delta W_{el} \qquad (3.1)$$

where H is the bulk enthalpy, S is the bulk entropy, γ is the surface energy density, A is the surface/interface area and W_{el} the mechanical work due to the elastic interfacial stress at the film/substrate interface. The subscripts *gb*, *sv* and *ss* stand for the different interfaces (grain boundary, solid-vapor and solid-solid, respectively). At equilibrium, $\Delta G(T_{1/2}) = 0$, we obtain:

$$T_{1/2} = T_{1/2}^{B} + \frac{\Delta\gamma_{gb}A_{gb} + \Delta\gamma_{sv}A_{sv} + \Delta\gamma_{ss}A_{ss} + \Delta W_{el}}{\Delta S} \qquad (3.2)$$

where $T_{1/2}^{B} = \frac{\Delta H}{\Delta S}$ is the bulk transition temperature of the film.

Now, let us examine one by one the role of these parameters. The biaxial stress and the resulting elastic work W_{el} was first pointed out to be at the origin of the transition temperature shift. Indeed, most thin films are under biaxial mechanical stress, whose sign (compressive or tensile) and magnitude can be thickness dependent. In our case, Mikolasek et al. determined the intrinsic film stress using a recently developed approach based on micromechanical devices and assessed a *ca.* 320 MPa value [173]. Such high tensile stresses occur frequently in annealed films as the crystallization process results usually in denser films [174]. Perhaps even more importantly, the strain associated with the SCO leads also to the variation of stress state of the film. Indeed, as it was discussed by Rat et al. [114], the LS to HS transition in $[Fe(HB(tz)_3)_2]$ leads to an important expansion of the orthorhombic (*Pbca*) unit cell volume by +4.5 %, but this strain is strongly anisotropic: −2.3 % for the *a*-axis, +1.0 % for the *b*-axis and +5.6 % for the *c*-axis. However, these phenomena (*i.e.* intrinsic and SCO induced stress) should not lead to a considerable elastic work in our case due to the very important difference between the thickness of the stiff glass substrate and the deposited film. We can thus neglect this term in our case.

From our previously discussed X-ray diffraction study the average crystalline domain size was estimated as *ca.* 45 - 50 nm for each film and it was shown that the crystalline domains were oriented with their orthorhombic *c*-axis normal to the surface (see Figure 2.15). Taking into account the similar crystallite sizes the grain boundary energy γ_{gb} should not play an important role here,[175] all the more that the grain boundaries are likely to consist of low-energy (semi)coherent interfaces. The high-energy solid-vapor and film-substrate interfaces should therefore account primarily for the size dependence of the transition temperature. For a further simplification we can assume $A_{sv} = A_{ss} = A_0$ and $(\Delta\gamma_{ss} + \Delta\gamma_{sv})/2 = \langle\Delta\gamma\rangle$. Finally, we obtain:

$$T_{1/2} = T_{1/2}^{B} + \frac{2\langle\Delta\gamma\rangle A_0}{\Delta S} = T_{1/2}^{B} + \frac{2\langle\Delta\gamma\rangle}{\Delta s}\frac{A_0}{V} = T_{1/2}^{B} + \frac{2\langle\Delta\gamma\rangle}{\Delta s}\frac{1}{h} \qquad (3.3)$$

where: Δs is the entropy density, V is the film volume, and h is the film thickness. It is important to note that the equation above (eq.3.3) does not take into account explicitly the effect of surface stress, but we shall consider that both surface energy and surface stress contribute to the shift of $T_{1/2}$ [157]. The best fit of equation 3.3 on the experimental data is shown in figure 3.23a. To further improve the fit we took into account the experimentally determined surface roughness by assuming a linear variation of the surface area with the roughness:

$$A = A_0(1 + nR_a) \qquad (3.4)$$

As shown in Figure 3.23b, considering the surface roughness of the films not only improves the fit, but also allows one to understand the apparent non-monotonous evolution of $T_{1/2}$ below and above ca. 100 nm thickness. The fit parameters, n, $\langle\Delta\gamma\rangle$, and $T_{1/2}^{B}$ are summarized in Table 3.1. The obtained bulk transition temperature (*ca.* 336 K) is reasonably close to the values reported for powder and single crystal samples (331 - 334 K) [114]. The key finding, however, is the positive value of $\langle\Delta\gamma\rangle$. This unusual *increase* of the (*00l*) surface energy (and surface stress) in the HS phase is perfectly in line with the crystallographic data, which indicates an unusual *contraction* of the (*00l*) crystal planes in the HS state, despite the overall expansion of the lattice. Interestingly, this finding not only explains the upshift of the spin transition temperature for reduced film thicknesses, but corroborates also the unexpected bending behavior of silicon microcantilevers when actuated with thin films of $[Fe(HB(tz)_3)_2]$ [176].

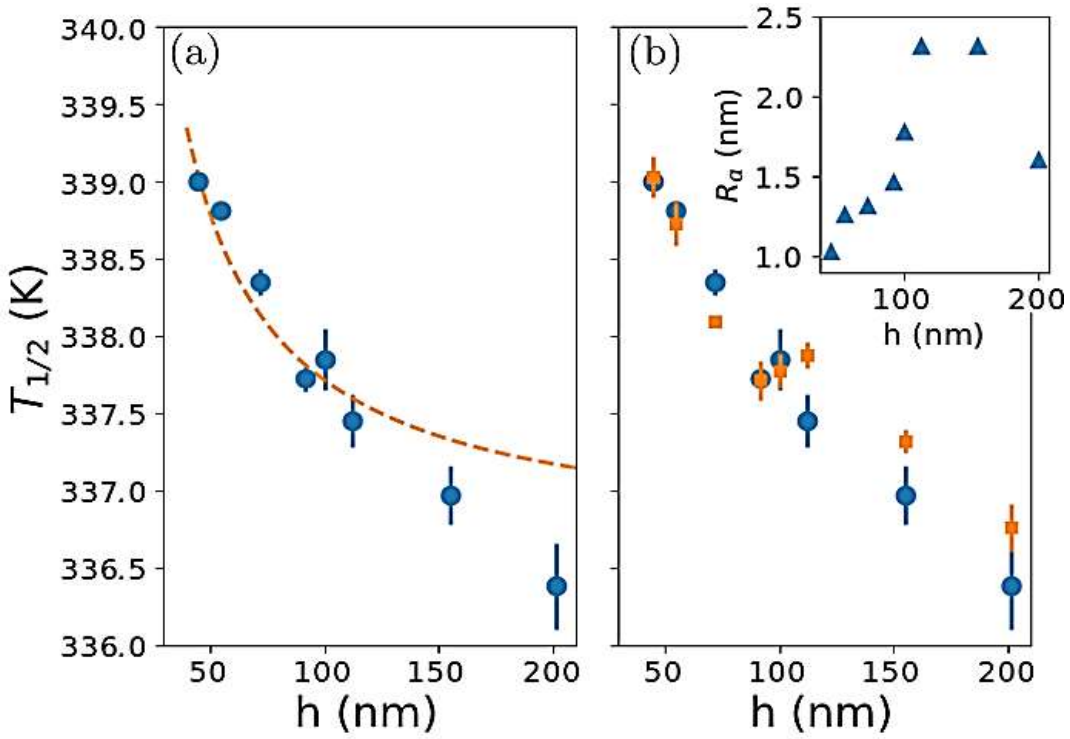

Figure 3.23: *h-T* phase diagram of oriented [Fe(HB(tz)$_3$)$_2$] thin films. Blue circles are the averaged experimental data. (a) The dashed line is the fit using equation (3.3), *i.e.* assuming the same surface area for each film. (b) The orange squares are fitted values using both equations (3.3) and (3.4), *i.e.* taking into account the experimental surface roughness. The inset in (b) shows the mean surface roughness vs. film thickness extracted from the AFM topography images.

Table 3.1. Fit parameters obtained using equations 3.3 and 3.4, with and without taking into account the surface roughness.

Fit parameters	Without roughness	With roughness
$T_{1/2}^{B}$ (K)	336.6 ± 0.3	335.9 ± 0.3
$\langle \Delta\gamma \rangle$ (mJ/m^2)	7.53 ± 0.9	5.18 ± 0.5
n (nm^{-1})	0 (fixed)	0.87 ± 0.03

Regarding the magnitude of the (*00l*) surface energy change between the two spin states (*ca.* 5 mJ/m^2), it is comparable with those reported for polymorphic thin films of organic compounds [155]. This model is seen to describe thus quite closely the effect of film thickness on the spin transition temperature of [Fe(HB(tz)$_3$)$_2$]. Nevertheless, other parameters (e.g. defects), which

remain hidden in the experimental characterization of the samples might also play a role here. From this point of view, the observed rather small shift of $T_{1/2}$ (*ca.* 3 K) and the tightly comparable shape of the SCO curves (Figure 3.21b) are very useful features, as they prove that the films are indeed very similar in all aspects, except their thickness. A higher shift of $T_{1/2}$ can be obtained simply by increasing the surface to volume ratio of the objects (*e.g.* in small SCO nanoparticles) [164], but this will also inevitably increase the uncertainty in the analysis of different sized objects.

3.3 Conclusions

In contrast to what is usually thought about SCO materials, our investigations revealed an unexpected and unprecedented robustness of the water vapor treated thin films of $[Fe(HB(tz)_3)_2]$. In particular, we have shown that (1) the SCO properties do not evolve significantly upon storage in ambient air (at least on a year scale), (2) the films exhibit no appreciable change of their SCO properties upon the elevation of temperature up to the sublimation temperature (ca. 260 °C), (3) the SCO properties remain virtually unchanged upon repeated spin state switching (at least up to one million switching cycles), and (4) the SCO properties can be maintained when encapsulating the films in between polymer (SU8) layers.

This exceptional stability and reversibility of the SCO in the films of $[Fe(HB(tz)_3)_2]$ allowed us to carry out a careful investigation of finite size effects on a series of films with different thicknesses. These measurements provided unambiguous evidence for the elevation of the spin transition temperature when reducing the film thickness. We show that this unexpected behavior is fully compatible with the nanothermodynamical theory of spin transitions by assuming an increase of the relevant surface energies when going from the low-spin to the high-spin phase (instead of the usual decrease). The particular anisotropy of the transformation strain in the oriented films appears as the origin of this behavior. This result calls for a modification of the paradigm of how the phase diagram of nanocrystalline materials (not only SCO) scales as a function of size and indicates the tight relationships among structural anisotropy, surface energy and phase stability.

Chapter 4. Combining spin crossover with luminescent properties

In this chapter, we present a novel approach for luminescence modulation by spin crossover, based on the deposition of our $[Fe(HB(tz)_3)_2]$ thin films on top of a luminescent film. We show that by an appropriate combination of materials their properties can be preserved by this straightforward method and it becomes therefore possible to modulate in a fully reversible and predictable manner the emission intensity of a luminescent film using the thin, transparent SCO top-coating. This combination of luminescence and SCO properties can be particularly interesting for micro- and nano-scale thermometry purposes in particular in combination with near-field scanning optical microscopy (NSOM) methods.

4.1 Fluorescence switches

Fabbrizzi et al. defined "Fluorescence switches as molecular systems containing a light-emitting fragment whose activity can be quenched/revived reversibly, at will, through an external parameter" [177]. Fluorescence switches are very useful notably for detection, imaging and optical storage devices. Therefore, they have applications in a large diversity of fields ranging from health to informatics via environment. The concept of fluorescence switches requires a way to controllably and reversibly modify the luminescence intensity. To obtain a modification of the luminescence activity, an external stimulus (chemical, thermal, mechanical…) is applied to the system.

The use of chemical compounds in fluorescence switches is applied in the field of medicine, analysis and detection; it is probably the most documented in the literature [178, 179]. In this case, chemical reactions [180-182] (Figure 4.1a) or intermolecular interactions [183-190] (Figure 4.1b) lead to a modification of the system, and therefore yield an increase or decrease of the luminescence.

To obtain a highly specific and reversible luminescence switching, an important and challenging chemical design is crucial and this important research work has to be done for each targeted molecule. In a similar manner, the chemical structure of the luminophore could change significantly if the luminescent material is in acid/basic medium, under oxydo/reduction conditions or even under UV/visible irradiation (Figures 4.1c and 4.1d) [191-202]. For some applications as optical or electronic materials, chemical modification is not the best choice; however, fluorescent switches can also so be activated by thermal, electrothermal or mechanical stimuli as well as by light irradiation.

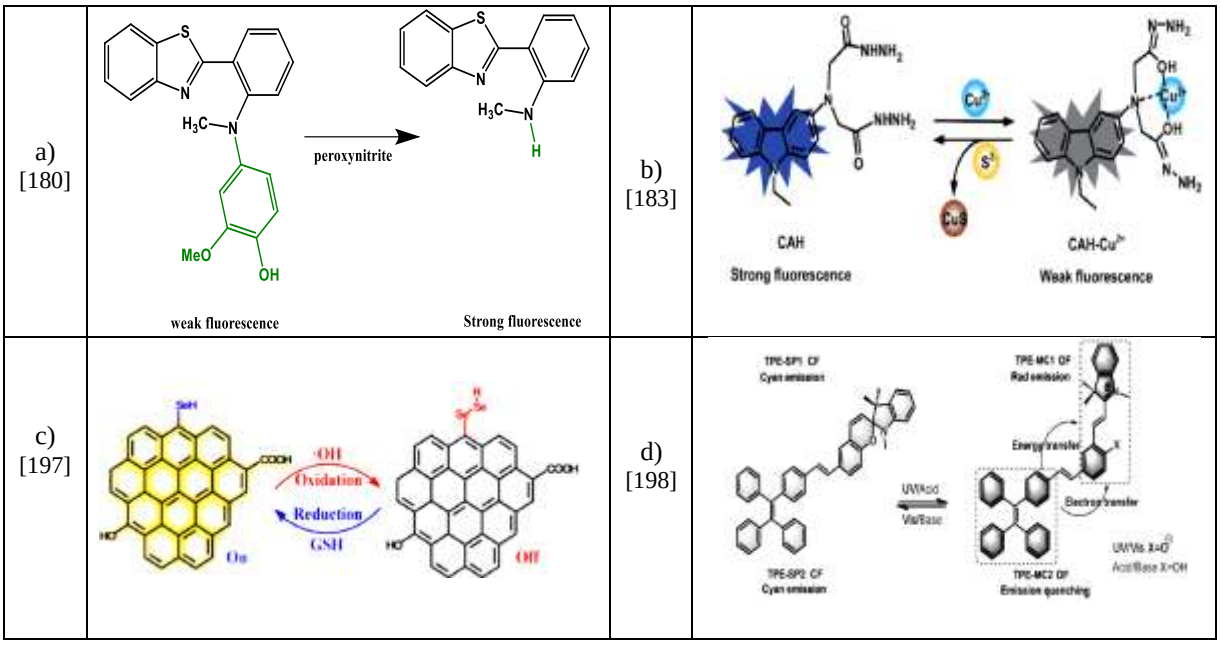

Figure 4.1: Selected examples of fluorescence switches working with (electro) chemical stimuli

Under mechanical stimuli are regrouped all technics as grinding, apply of pressure or removing the solvent by evaporation, that can be used to modify the molecular arrangement of luminophore compounds [203]. Indeed, several compounds exhibit significantly different luminescence properties depending if molecules are isolated from each other, which is the case when the compound is dissolved in a solvent, or aggregated (Figure 4.2a) [204]. In the crystalline state, the luminescent property depends also on the specific molecular arrangement, which is maintained by intermolecular interactions, such as π - π stacking, hydrogen bonding or dipole-dipole interactions. These interactions are weak and can easily be broken by grinding or by applying pressure and this results in a modification of the luminescent property [205, 206]. In a similar fashion, a phase-transition can be detected by a modification of luminescence [206, 207]. Finally, some compounds exist in distinct conformers, which can have different luminescent properties. Conformational interconversion can easily and rapidly occur in solution, whereas this interconversion is hampered in the solid state (Figure 4.2b) [208, 209]. If by mechanical stimuli the chemical structure of the compound remains unchanged, two main challenges have to be taken up. Firstly, as it was pointed out by Di et al. "*For the development of efficient and useful mechanoluminescence materials, further revealing the mechanisms that induce these phenomena to establish a design strategy of the molecules, and deeper understanding of the relationship between molecular structures and the mechano-responsive behaviors are highly desirable*" [203]. Moreover some improvements have to be done in order

to perform the modification of molecular arrangement in a faster way and in conditions compatible with a use in optical or electrical devices.

a)[204]	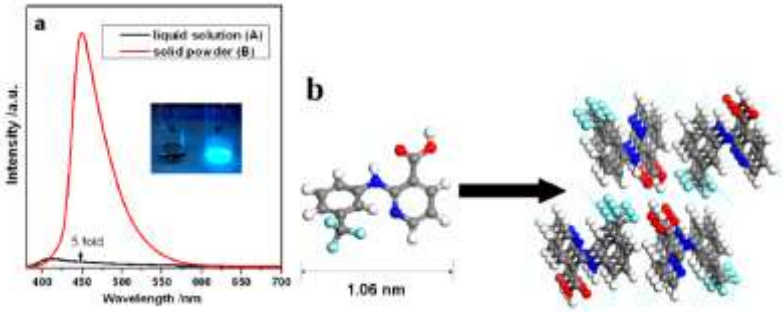
b)[208]	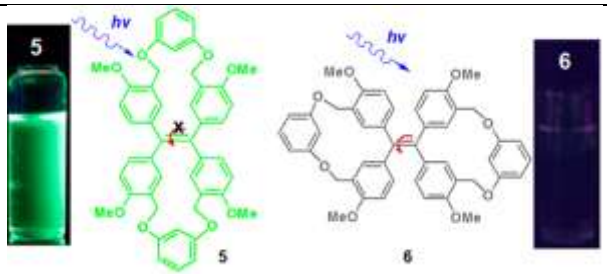
c)[210]	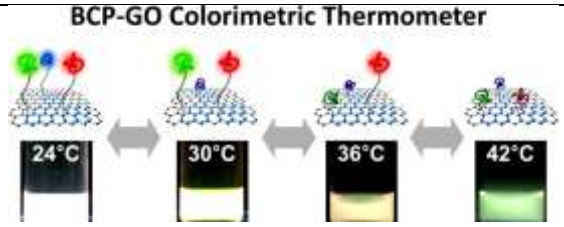
d)[211]	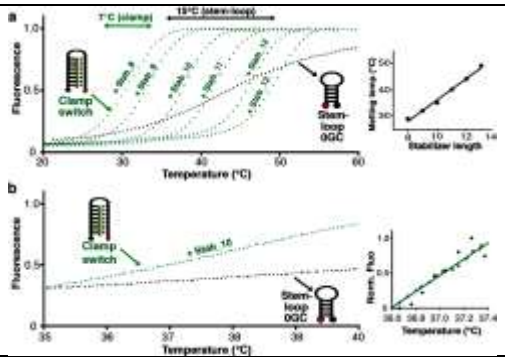
e)[212]	

Figure 4.2: Selected examples of fluorescence switches working with physical stimuli.

Luminescence switching can also be triggered by a thermal stimulus (Figure 4.2c-d). The principal causes of this modulation can be either a chemical modification or a different molecular arrangement of the system [210, 211, 213-222]. Several articles emphasize the improvement of the luminescence switching by the association of luminophore molecules with a substrate or other type of molecules. Lee et al. elegantly demonstrated that their system exhibits four different luminescence properties depending of the temperature [210]. Their material consists of a graphene oxide substrate functionalized by an association of three different luminophore molecules. The luminescence property of the material is the sum of the luminescence of each type of molecules. The luminescence is a result of a FRET (*Förster-type resonant energy transfer*) from the molecules to the graphene oxide and therefore depends of the disposition of the molecules relative to the substrate. This disposition can be modulated by a change of temperature, which was found different for each type of molecule. Then, the luminescence comes from the association of the molecules and the graphene oxide, whereas the four different luminescence characters of the material are explained by the combination of the three types of molecules. In 2016, an article of Gareau and coworkers is another example of the benefit to associate two different classes of molecules [211]. It is documented that to attach a luminophore and its quencher to the extremities of DNA stem-loops allows obtaining a thermal luminescence switching. Indeed, when the loop is closed the luminophore interacts with its quencher and no luminescence is observed whereas at higher temperatures, the loop is open and the luminescence significantly increases. Gareau and coworkers make an important improvement of the system by adding a DNA strand to the functionalized DNA stem-loops. Indeed, this allows them to get a more important intensity ratio between the open and closed forms in a small temperature range gaining therefore more precision of the measure of temperature, which is an important issue to utilize their concept as nanothermometer. Moreover, they also demonstrate that changing the size of the DNA stabilizer allows them to cover a wide range of temperatures, which was not accessible without stabilizing the DNA strand.

Recently, Lin and coworkers described an electrothermal fluorescent switching [212]. Their sophisticated device is constituted by an electrode, which is connected to an electric generator, a hybrid film, which is composed of multilayers of liquid crystal elastomers (LCE) and titanium oxide (TiO_2) successively, and a luminophore layer deposited on the top of the material (Figure 4.2e). It is important to note that a so efficient luminescence modulation cannot be achieved by electrothermal stimuli without their hybrid material LCE / TiO_2. Indeed, their luminescence switching is based on the amount of photons having the adequate wavelength to excite the luminophore. This amount of photons, received by the luminophore, is efficiently

modulated by the hybrid film composed of LCE and TiO_2. On one hand, liquid crystals can act as wavelength guides and mirrors. Moreover, on the other hand, molecular arrangements of liquid crystals are highly dependent on different parameters, such as temperature or electric field, which lead to materials having distinct optical properties. When an electric field of 35V is applied to the hybrid material, an important blueshift of the reflectance wavelength is observed, which probably results from a modification of the molecular arrangement of liquid crystals. Because of this 40 nm shift, only a slight spectral overlap is observed between the Rhodamine and the hybrid material under electrothermal stimuli, whereas a perfect overlap is observed in the absence of electrothermal stimuli. Consequently, under electrothermal stimuli, only 20% of luminescence intensity of Rhodamine is observed. Finally, Lin et al. claim that their process can be used for a large diversity of luminophores [212]. Indeed, hybrid films with reflectance wavelengths ranging from 438 to 660 nm can be prepared by adjusting the thickness of the liquid crystal elastomer and TiO_2 layers.

4.1.1 Spin crossover based luminescence switches

In this context of luminescence switching, an attractive strategy consists to fabricate a hybrid material, which combines a luminophore species with a spin-crossover (SCO) molecule. These latter are transition metal complexes, which can be reversibly switched between the low spin (LS) and the high spin (HS) states of the central metal ion. The SCO is trigged by the application of an external stimulus such as an increase / decrease of pressure or temperature, an inclusion / removal of a guest molecule in the material, light irradiation or the presence of an magnetic field. The spin transition phenomenon leads to a significant change in the chemical and physical properties of the metal complex including the modification of its magnetic susceptibility, dielectric permittivity, mass density, color, refractive index and elastic moduli [1,31, 78, 223-225]. SCO complexes have received recently increasingly interest because they offer an opportunity to fabricate switchable nanomaterials and devices [3, 196, 226-228]. When combined with a luminophore, the presence of the SCO complex allows to transform a stimulus, which has no (or moderate) effect on the luminescent property, into a stimulus, which strongly influences the emission intensity. For example, the luminescence intensity in general slowly decreases at increasing temperatures due to the thermal activation of non-radiative decay channels. However, this trend can be inversed by associating the luminophore to an SCO complex, which will strongly quench the luminescence in the low temperature (LS) state.

The combination of a luminophore with a SCO complex can lead to a luminescence modulation fundamentally by three different pathways [229]:

(i) The luminescence emission can be selectively re-absorbed by either the HS or the LS state, depending on the overlap between the emission spectrum of the luminophore and the absorbance of the complex in a given spin state. This will lead to a modulation of the luminescence intensity and, in certain cases, to spectral shifts, but the excited state lifetime of the luminophore will remain obviously unaffected. This ***emission-reabsorption mechanism*** has been proposed to be dominant in several cases.

(ii) Alternatively, the excited state energy of the luminescent molecule can be transferred to the metal complex via Förster-type dipole-dipole interactions without photon emission. Since this resonant process is also governed to a large extent by the spectral overlap between the complex and the luminophore, it will occur selectively in one or the other spin state. Consequently, the luminescence emission intensity can be drastically quenched, but in contrast to the re-absorption scenario, this will be also accompanied by the modulation of the luminescence lifetime. On the other hand, no significant spectral shifts are expected for such ***resonant energy transfer process***. To our best knowledge, there is no literature report wherein this mechanism could be unambiguously demonstrated for a luminescent SCO material.

(iii) Finally, various ***"environmental effects"*** may also lead to the modulation of the luminescence upon the SCO process. These effects include the change of the polarity and stiffness of the local environment, the modulation of intermolecular distances as well as charge transfer phenomena. Contrary to the re-absorption and energy transfer phenomena, the occurrence and manifestation of this last category of effects remains difficult to predict and interpret. The change of local environment involves in most cases not only the modulation of emission intensity, but also a change of the non-radiative decay rate and spectral shifts. The most obvious diagnostic feature of these phenomena remains, however, the feeble correlation between the luminescence modulation and the spectral overlaps. We believe that these "environmental effects" play a non-negligible role in most reported examples of luminescent SCO materials.

Previous literature reports, which associate SCO and luminescent properties in a hybrid material can be classified in four categories (see Figure 4.3 for a few examples) [229].

(i) In the first case, the SCO complex contains a luminescent ligand [230-239]. Albeit elegant, one main challenge of this "***luminescent-SCO complex strategy"*** is the possibility to lose the SCO and/or the luminescent properties, which remain rather difficult to predict for a rational design of new complexes. In addition, the high concentration of luminophores may lead to self-quenching.

(ii) The second strategy consists of ***mixing (doping)*** the SCO material with a fluorophore.[59, 64, 240-242] This can usually be achieved in a straightforward manner by adding a few percent of luminescent species to the SCO material during the synthesis of the latter. The advantage of this approach is its simplicity and efficiency. However, it is often difficult to control the homogeneity of the material and to locate the luminophore within the mixture.

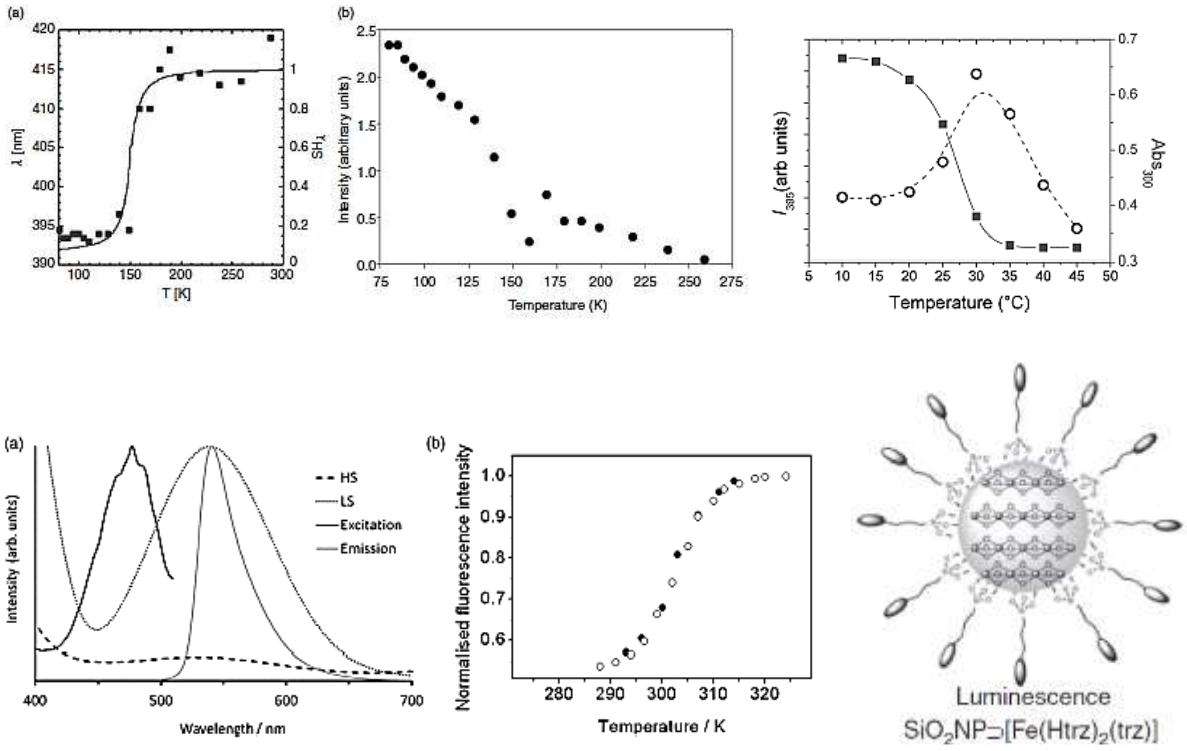

Figure 4.3: Selected examples of fluorescent-SCO switches [229]. *Top left and middle* (luminescent SCO complex approach): Temperature dependence of the luminescence wavelength and intensity for $[Fe_2(L2)_5(NCS)_4]_2.(MeOH)_4$. *Top right* (substitution approach): Temperature dependence of the luminescence (open circles) and absorption (filled squares) of an iron(II)-triazole derivative with pyrene-derivative counter-anions. *Bottom left and middle* (doping approach): Fluorescence (excitation and emission) and absorption (HS and LS) spectra of a rhodamine doped iron(II)-triazole derivative, and thermal variation of the luminescence intensity. *Bottom right* (hierarchical assembly approach): Schematic view of iron(II)-triazole nanoparticles covered by a silica shell on which organic luminophore molecules are grafted.

(iii) To overcome the latter problem one might also partially substitute different components of the SCO material (e.g. the counter-ions, the ligands or even the metal ion) by a chemically similar, but luminescent species. This way one may obtain 'co-crystals' of the SCO and the luminescent species [240]. This "***substitution approach***" can be seen also as a combination of the first two strategies. Yet, it is still not guaranteed that the substituted material will conserve intact the properties of each constituent. Indeed, the introduction of the luminescent molecule into the SCO material, even in low percentage, can lead to a significant change of the spin transition properties and, *vice-versa*, the luminescence may also be drastically altered by the SCO crystal lattice.

(iv) In a forth strategy, the luminophore and the SCO parts are juxtaposed in a spatially controlled assembly [243-249]. This "***hierarchical assembly strategy"*** was mainly applied to the synthesis of nanoparticles with a SCO core and a luminescent shell. Notably, $[Fe(Htrz)_2(trz)]BF_4$ (trz = triazolato) SCO nanoparticles were covered by a thin silica layer and luminescent molecules were then grafted on the oxide surface [246]. This way the luminophores are well localized, while they are not expected to infer substantially with the SCO properties of the core-shell particles.

4.2 Sample fabrication and properties

4.2.1 Methods

Reagents and solvents used in this study are commercially available. The bulk powder of $[Fe(HB(tz)_3)_2]$ was synthesized as described in ref [114]. The $Ir(ppy)_3$ powder was obtained from Sigma Aldrich and used without any further purification. The fused silica substrates were purchased from SCHOTT AG and cleaned with acetone and 2-propanol to remove contaminants. Multilayer films were grown by thermal evaporation in a PREVAC thermal deposition system at a base pressure of ca. 2×10^{-7} mbar. The SCO (luminescent) complex was heated until 250 °C (280 °C) in a quartz crucible and evaporated at a rate of 0.07 Å s^{-1} (0.03 Å s^{-1}). For co-deposition, the two complexes were evaporated simultaneously at a pressure of ca. 5×10^{-7} mbar. The deposition rate was 0.2 Å s^{-1} and 0.03 Å s^{-1} for the $[Fe(HB(tz)_3)_2]$ and $Ir(ppy)_3$ molecules, respectively. After deposition, the $[Fe(HB(tz)_3)_2]$ films were annealed for 10 min at room temperature in ca. 80 % relative humidity air in order to achieve a better

crystallinity. The evaporation rate and film thickness were monitored *in situ* using a quartz crystal microbalance.

The final control of the film thickness and topography was carried out using a Cypher ES microscope from Oxford Instruments in amplitude modulation mode in ambient air using OMCLAC160TS-R3 (Olympus) probes. Grazing incidence X-ray diffraction (GIXRD) experiments were carried out in a PANalytical X'Pert PRO MPD system using Cu-Kα radiation (45 kV and 40 mA) with a parallel-beam configuration. The incident beam optics consisted of a mirror with a 1/32° divergence slit. A parallel plate collimator (0.18°) and Soller slits (0.04°) were mounted on the path of the diffracted beam. An X'Celerator detector in receiving slit mode was used for X-ray collection. Temperature-dependent absorbance spectra of the films were collected at wavelengths between 200 and 800 nm using a Cary 50 (Agilent Technologies) spectrophotometer and a Linkam FTIR-600 heating/cooling stage (equipped with fused silica windows). The sample chamber was purged by dry nitrogen and spectra were acquired in the 293 - 393 K range with 1 K/min scan rate.

A Fluoromax-4 (Horiba) spectrofluorimeter equipped with a xenon lamp source and an Optistat DN-V liquid nitrogen cryostat connected to an ITC601 temperature controller (Oxford Instruments) was used to acquire fluorescence excitation and emission spectra as a function of temperature (see Figure A4.2.1 in Annexes**)**. Fluorescence spectra were corrected for the instrumental response as implemented in the software. Luminescence lifetime measurements were performed using the time-correlated single photon counting (TCSPC) technique by means of a DeltaFlex (Horiba) instrument equipped with a 303 nm (pulse duration ~1 ns) as well as with a 280 nm (pulse duration > 100 ns) electroluminescent diode. Variable temperature lifetime measurements were conducted using an Optistat DN-V cryostat. Fittings and lifetime calculations were performed using DAS6 fluorescence decay analysis software.

4.2.2 Choice of materials

We aim to stack on a transparent substrate a thin layer of luminescent molecules covered by a layer of SCO molecules in order to achieve a luminescence intensity modulation driven by the spin state switching phenomenon. Obviously, the choice of the two types of molecules is crucial. We decided to combine our high quality SCO films of $[Fe(HB(tz)_3)_2]$ with the tris[2-phenylpyridinato-C2,N]iridium(III) luminophore - $Ir(PPy)_3$ (see Figure 4.4).

Sketch of our materials	Chemical structure of SCO complex	Chemical structure of luminescent molecule
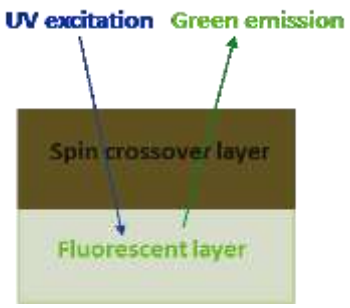	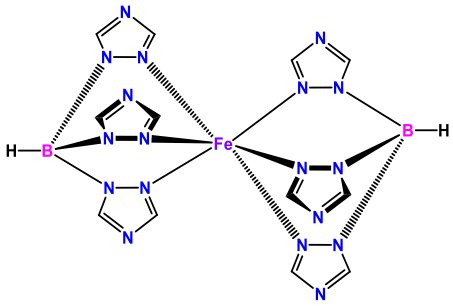	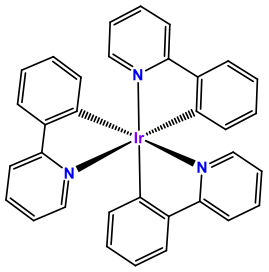

Figure 4.4: Outline of the bilayer stack and chemical structure of the iron and iridium complexes.

As we have shown in the previous chapters, high quality films of the SCO complex $[Fe(HB(tz)_3)_2]$ can be prepared by vacuum evaporation on a substrate. These films can potentially be used for optical applications since sub-micrometric layers of $[Fe(HB(tz)_3)_2]$ are largely transparent in the visible and near-infrared spectral ranges in both spin states. In addition, when using an appropriate annealing procedure they form a homogenous nano-crystalline texture with smooth surface topography, hence not only absorption, but also scattering losses are very small. On the other hand, the complex $[Fe(HB(tz)_3)_2]$ in the LS state absorbs much more UV light than in the HS state. For example, at 318 nm the absorption coefficient, related most probably to a singlet-singlet charge transfer transition between the metal center and the ligand, decreases from *ca.* 3×10^4 cm^{-1} till completely vanishing when switching the complex from the LS (^1A) to the HS (^5T) state. It is this huge difference that we would like take advantage of in modulating the intensity of the luminescence. Indeed, the complex $[Fe(HB(tz)_3)_2]$ in the LS state will strongly absorb and thus block UV irradiation. Whereas, in the HS state, it is quasi-transparent in the UV, so the main part of the irradiation will reach and excite the underneath luminophore layer. Therefore, we expect that the luminescent intensity of the material with the complex $[Fe(HB(tz)_3)_2]$ in the LS state should be substantially weaker than with **1** in HS state. Obviously, this strategy implies that UV irradiation should be used to excite the luminescence emission.

To this aim we have chosen the luminescent complex $Ir(PPy)_3$, which is probably one of the most studied molecules in the OLEDs (Organic Light-Emitting Diode) field and deep investigations have been performed in order to understand its luminescent properties [250-252].

This compound is well known to absorb light in the UV between 250 and 320 nm, which has been assigned to singlet-singlet π-π* transitions of the ligand [253]. It is well documented that its excitation under UV irradiation leads to a prominent green emission centered at 515 nm, which is attributed to the radiative decay of the triplet ^{3}MLCT (metal ligand charge transfer) state to the ground state [253]. As the SCO film is transparent in visible region, this green emission of $Ir(PPy)_3$ will not significantly be attenuated by the presence of a thin layer of $[Fe(HB(tz)_3)_2]$. Besides these favorable and very well documented luminescent properties, we shall note that compound **2** is easily available commercially and can be prepared in thin film form by vacuum evaporation.

4.3 Characterization of the luminophore films

Films of $Ir(PPy)_3$ were made by thermal evaporation under vacuum. Optical microscopy and atomic force microscopy (AFM) observations revealed the formation of homogeneous films (Figure 4.5a and 4.5b). From the AFM measurements, a film thickness of ca. 30 nm and the root-mean-square (RMS) surface roughness of ca. 0.3 nm was inferred (see Figure A4.3.1 in Annexes). Interestingly the obtained film morphology is rather different from the rod-like structures previously reported in the literature [253]. However, GIXRD measurements indicate that, contrary to those reports, the films of $Ir(PPy)_3$ made by us are amorphous (see Figure 4.5c), which is probably the main reason for the different film morphologies.

Figure 4.5d represents the UV-vis absorbance spectrum of the film of $Ir(PPy)_3$ on a fused silica substrate. We observe absorbance bands around 300 nm and 400 nm. (N.B. The strong absorption below ca. 250 nm occurs due to the substrate.) The excitation of the film in these absorption bands yields a broad luminescent emission centered at 520 nm (Figure 4.5e). The temperature dependence of this luminescence intensity turned out to be negligible in the investigated range (from 300 K to 370 K). This property is very advantageous as it allows one to investigate the influence of the thermal SCO phenomenon without any intricacy due to intrinsic luminescence thermal quenching phenomena. In a similar fashion, it appears that the luminescent lifetime of films of $Ir(PPy)_3$ is not temperature dependent either (see Figure 4.5f). The luminescence decay can be reasonably well fitted only with three exponential functions from which the average lifetime is estimated to be a few μs, which is consistent with previous literature reports.

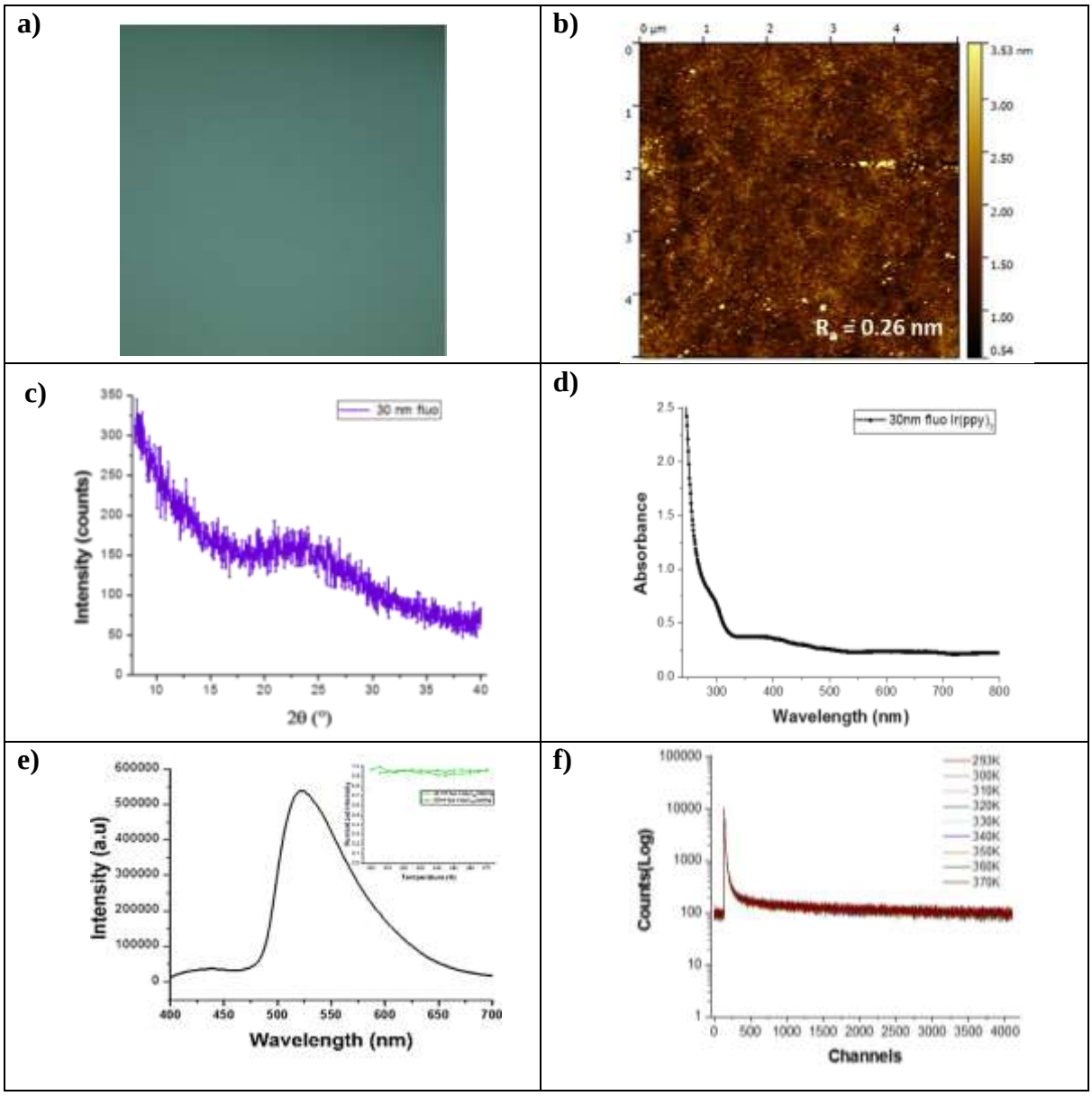

Figure 4.5: Characterization of films of $Ir(PPy)_3$. Typical optical microscopy (a) and AFM topography (b) images, (c) GIXRD pattern, (d) UV absorption spectrum (30 nm thickness – background corrected), (e) luminescence emission spectrum (excitation: 300 nm) and its temperature dependence in insert and (f) variable temperature luminescent decay curves (excitation: 286 nm, emission 520 nm) recorded over the first 800 ns of the decay.

4.4 Characterization of the bilayer films

In the next step, a 107 nm thick film of $[Fe(HB(tz)_3)_2]$ was deposited by vacuum thermal evaporation on top of the luminophore layer. Optical microscopy and AFM images (Figures 4.6a-4.6b), clearly show the change of surface morphology and reveal the formation of some islands. The RMS surface roughness of the bilayer is around 3 nm (for a bilayer thickness of 30

+ 107 nm), which is higher than typical values obtained after the evaporation of the SCO complex directly on the fused silica substrate.

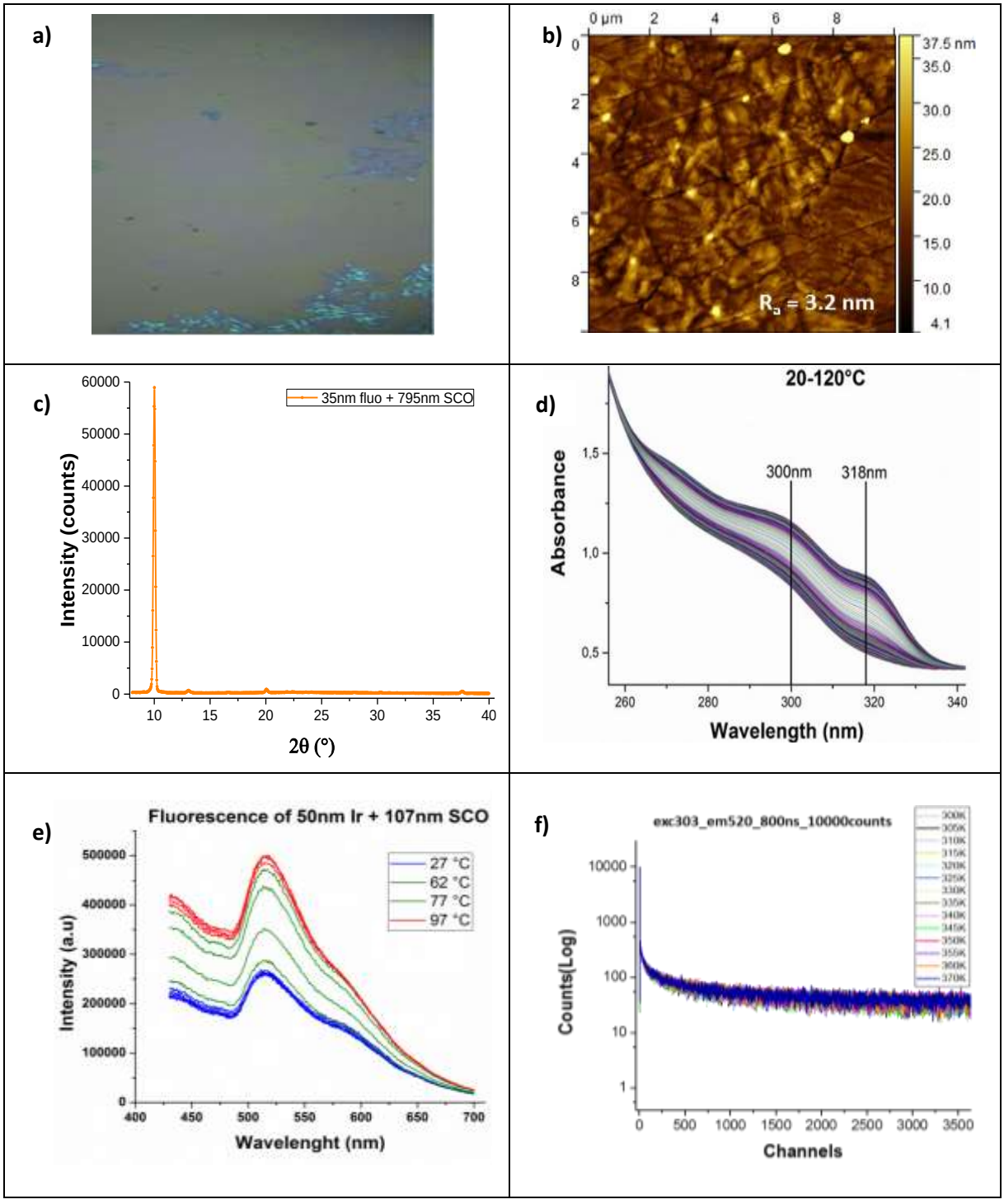

Figure 4.6: Characterization of bilayer films of $Ir(PPy)_3$ and $[Fe(HB(tz)_3)_2]$. Typical optical microscopy (a) and AFM topography (b) images, (c) GIXRD pattern, (d) variable temperature UV absorption spectra (30 + 107 nm thickness – background corrected), (e) variable temperature luminescence emission spectrum (excitation: 300 nm) and (f) variable temperature luminescence decay curves recorded over the first 800 ns of the decay.

Figure 4.6c shows a typical GIXRD trace for a bilayer film evidencing a single diffraction peak near $2\theta = 10°$. In line with our previous investigations, this diffraction pattern denotes that the films of $[Fe(HB(tz)_3)_2]$ deposited on top of the fluorescent layer are crystalline and oriented. Figure 4.6d represents the absorbance spectra of the bilayer acquired at different temperatures between 293 and 393 K. As expected, the low temperature (i.e. low spin) absorbance spectrum overlaps with that of the iridium complex around 300 nm. When heating the sample above the spin transition temperature the optical density of the SCO film decreases drastically. For example, at 300 nm the absorbance of the bilayer drops by $\Delta_{abs} = 0.33$ when going from the LS to the HS state. The highest absorbance change ($\Delta_{abs} = 0.39$) is observed at 318 nm, which corresponds to our previous observations for a complete spin transition in film of $[Fe(HB(tz)_3)_2]$ with ca. 125 nm thickness. The absorbance change as a function of temperature at this wavelength is shown in Figure 4.7. An abrupt and well reversible change of the absorbance occurs around 337 K with a small hysteresis. This thermal spin transition curve is strictly the same as it was observed for films deposited directly on glass substrates, from which we can infer that the SCO properties of $[Fe(HB(tz)_3)_2]$ are not significantly modified by the presence of the luminescent film underneath. This result corroborates our previous observations about the negligible role of the nature of the substrate on the properties of films of $[Fe(HB(tz)_3)_2]$ (see Chapters 2-3). Figure 4.6e depicts the luminescence emission spectra of the bilayer film at different temperatures. Overall, these spectra closely resemble to that of the neat fluorescent film, despite the excimer shoulder around 600 nm is somewhat more intense. Remarkably, in the bilayer the luminescence intensity changes drastically between ca. 333 and 350 K – in harsh contrast with the quasi-constant luminescent intensity of the film of $Ir(PPy)_3$ in the same temperature range. On the other hand, the luminescent lifetime of $Ir(PPy)_3$ is not significantly altered by the presence of the SCO layer and the decay curves remain virtually temperature independent (Figure 4.6f). In Figure 4.7 we compare the temperature dependences of the absorbance ($\lambda = 300$ nm) and the luminescence intensity ($\lambda_{excitation} = 300$ nm, $\lambda_{emission} = 520$ nm) of the bilayer film over two thermal cycles between 300 and 380 K. The drastic increase in the intensity of the luminescence above ca. 335 K can be unambiguously attributed to the spin transition phenomena. (*N.B.* The slight difference in SCO transition temperatures observed in absorbance and fluorescence experiments can be attributed to the different heating-cooling equipment used to control the temperature of the sample.) It may be worth to note also the good overall reproducibility of these measurements over successive heating-cooling cycles – despite a small, continuous decrease of the luminescence intensity due to a slow (hours scale) photo-bleaching phenomena.

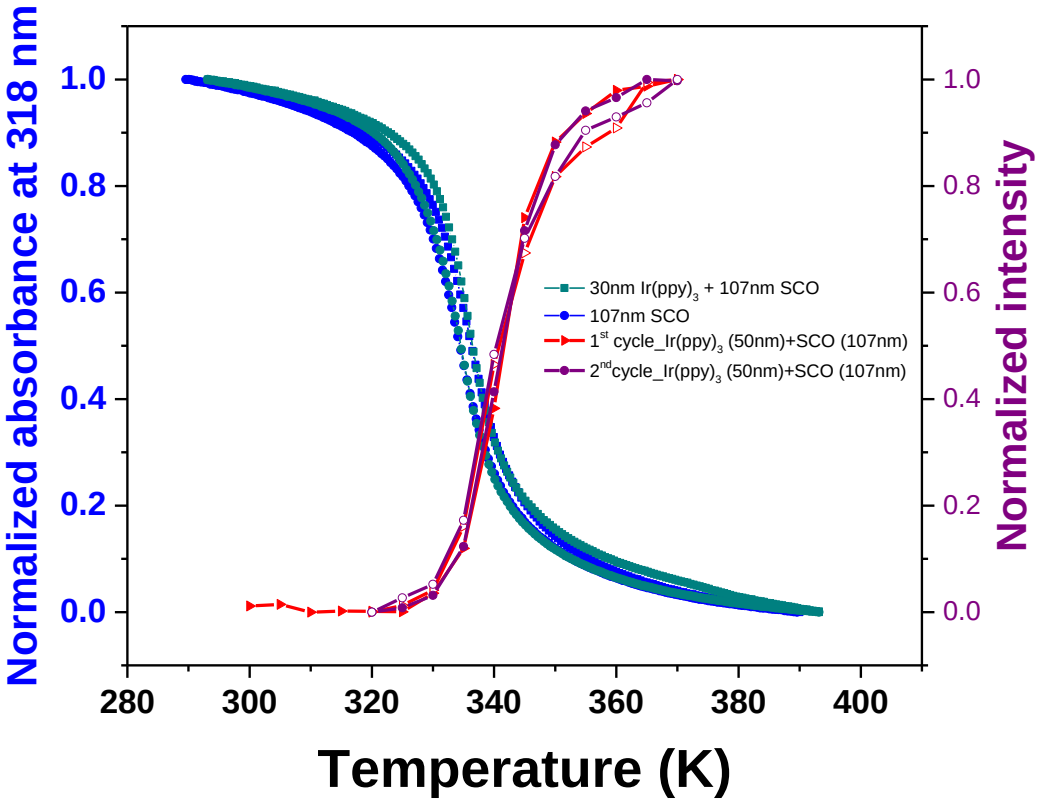

Figure 4.7: Normalized temperature dependence of the UV absorbance and the luminescence emission intensity of the bilayer film (30 + 107 nm thickness, excitation: 300 nm, emission 520 nm).

At this point, we can conclude that the intrinsic properties of each compound, luminescent and SCO, are not significantly affected by the presence of each other. Yet, we observe a reversible modulation of the luminescence intensity at the SCO, which we can attribute to the different UV absorbance properties of the iron complex in its two different spin states: either fully transmitting (HS state) or partially blocking (LS state) the light beam used for luminescence excitation. This hypothesis is supported by the fact the promotion of the iron complex from the LS to the HS state doubles the luminescence intensity of our bilayer film, while its UV transmittance (λ = 300 nm) doubles as well. In the same time, the luminescence spectral shape and lifetime remain temperature and spin-state independent, which is also fully compatible with the proposed mechanism.

In order to obtain further proof for this explanation and to verify the scalability of the luminescence modulation amplitude, we have prepared two other bilayer samples with SCO layers of ca. 200 nm and 800 nm thickness. For the thickest sample, we had to overcome a difficulty concerning the formation of a high quality crystalline film. As we have already

discussed it in detail, oriented, crystalline SCO films of $[Fe(HB(tz)_3)_2]$ are obtained by annealing the pristine evaporated film in humid air with ca. 80 % relative humidity. However, this method is not fully efficient when the thickness of the film is greater than 200 nm. To prepare the sample with 800 nm of SCO thickness (see Figure A4.4.1 in Annexes**)**, we have therefore first deposited an SCO layer of 200 nm on top of a 30 nm layer of $Ir(PPy)_3$ and we have annealed the film as usual. Then, we have put back the annealed sample in the evaporator to grow an additional 600 nm thick layer of SCO molecules. Similar to the thin films, X-ray diffraction on this thick film revealed only one significant diffraction peak near $2\theta = 10°$ (see Annexes). In other words, solvent-annealed thin films of $[Fe(HB(tz)_3)_2]$ (< 200 nm) can be used to regrow thicker films of $[Fe(HB(tz)_3)_2]$ on top of the $Ir(PPy)_3$ film, while keeping a reasonable quality in terms of crystallinity, preferential orientation, optical and SCO properties (*vide infra*).

The results obtained with the three different SCO film thickness are summarized in Figure 4.8. The spin transition curves are comparable for each sample in terms of spin transition temperatures, though slight differences in the shape of the curves can be depicted (Figure 4.8a). On the other hand, the absorbance change between the LS and HS states (ΔA_{LH}) does not scale with the film thickness (determined by AFM), which indicates that the crystallinity and thus the spin transition is not complete in the thick sample (Figure 4.8b). In response to this absorbance change, in each bilayer sample an important reversible change of the luminescence intensity is also observed around 337 K (Figure 4.8c). As expected, the extent of the luminescence modulation (I_{HS}/ I_{LS}) increases with the thickness of the SCO layer. Changes from ca. 200 % to 1300 % (with reference to the room temperature value) from thinnest to thickest film, respectively, are obtained (see Table 4.1).

The most remarkable point, as illustrated both in Table 4.1 and Figure 4.8d, is the perfect one-to-one correlation between the luminescence modulation I_{HS} / I_{LS} in the film of $Ir(PPy)_3$ and the transmittance change Tr_{HS} / Tr_{LS} in the film of $[Fe(HB(tz)_3)_2]$. In other words, the UV transmittance of the SCO films gives an accurate scale of modification of the luminescence intensity of the iridium complex. This means that one can modulate the luminescence intensity 'at will' by adjusting the thickness of the SCO layer. The results in Figure 4.8 provide an irrefutable proof of the mechanism of the luminescence modulation in the bottom layer, which occurs via the modulation of the exciting light intensity by the spin-state dependent UV absorbance of the top layer.

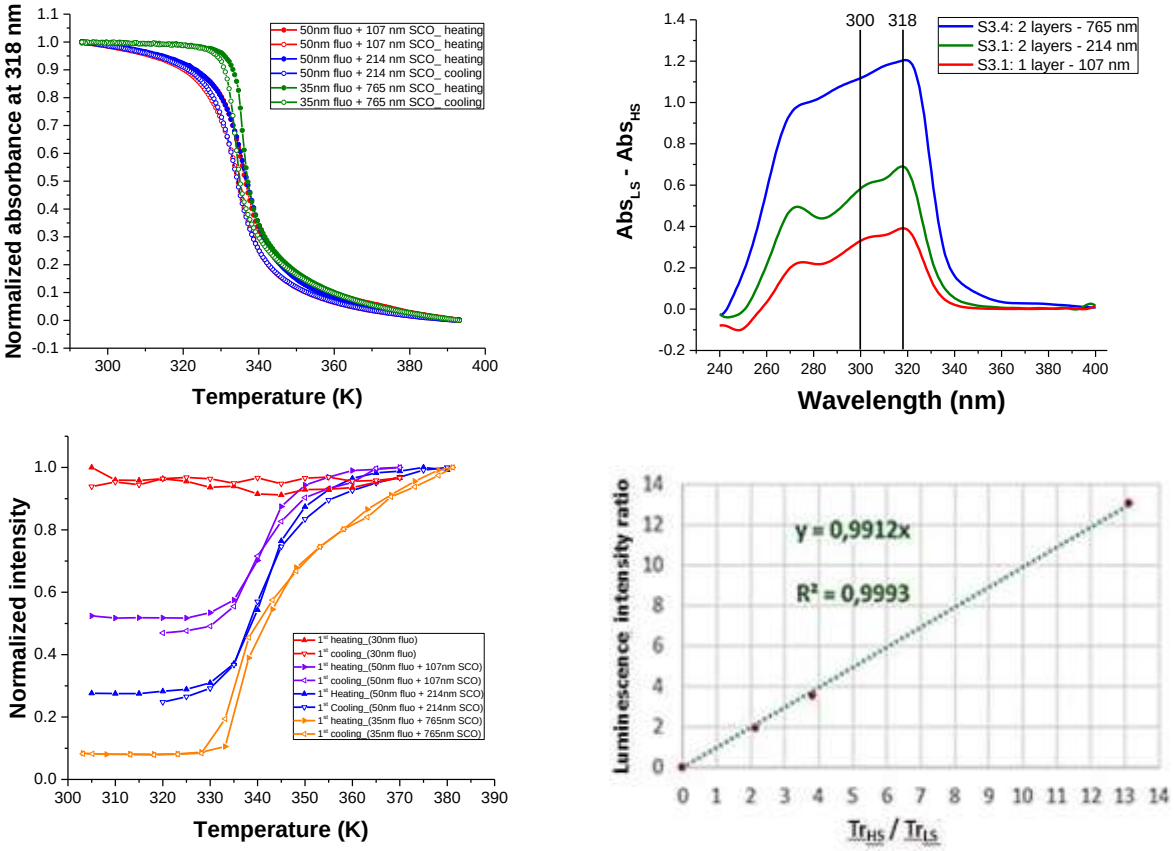

Figure 4.8: Correlation between the absorbance of $[Fe(HB(tz)_3)_2]$ and the luminescence of $Ir(PPy)_3$. (a) Normalized temperature dependence of the UV absorbance (at 318 nm) for three bilayer samples with different SCO layer thicknesses (107, 214 and 765 nm). (b) Absorbance changes associated with the SCO for different SCO film thickness. (c) Normalized temperature dependence of the luminescence intensity for different SCO film thickness. (d) Plot of the luminescence intensity ratio vs. the UV transmittance ratio between the HS and LS states.

Table 4.1. Comparison of the UV absorption and luminescent properties of bilayer films with different thickness of SCO layers

Thickness of SCO layer	**$\Delta_{Abs} = Abs_{LS} - Abs_{HS}$**		**Tr_{max}/Tr_{min} at 300 nm**	**I_{max} / I_{min}**
	at 300 nm	at 318 nm		
107 nm	0.331	0.392	2.14	1.95
214 nm	0,582	0.755	3.82	3.59
765 nm	1.118	1.204	13.05	13.12

4.5 Mixed SCO – luminescent films

We have also investigated if a closer contact between the SCO and luminescent molecules in a mixed film could allow for an efficient luminescence modulation. Indeed, a few examples in the literature demonstrate that a luminescent molecule can interact strongly and selectively with SCO complexes in either the low or the high spin state [229]. Obviously, the probability of an efficient electronic energy transfer between the triplet emitting state of the luminophore and the week singlet d-d absorption band of the LS complex is extremely low. Nevertheless, one might expect a significant amplification or quenching of the luminescence emission via 'environmental effects' related to the structural changes which accompany the SCO. In any case (i.e. electronic or structural effects), a close proximity between the two types of molecules is required.

To investigate this possibility we co-evaporated the SCO and luminescent molecules to form mixed films with ca. 12 %, 15 % and 21 % nominal luminophore content. Overall, we observed that for increasing doping levels the SCO properties of the films degrade and the luminescence modulation thus becomes negligible. Figure 4.9 summarizes the results obtained for the lowest doping (12 %), while the data obtained with the other two samples are gathered in the Annexes A4.5.

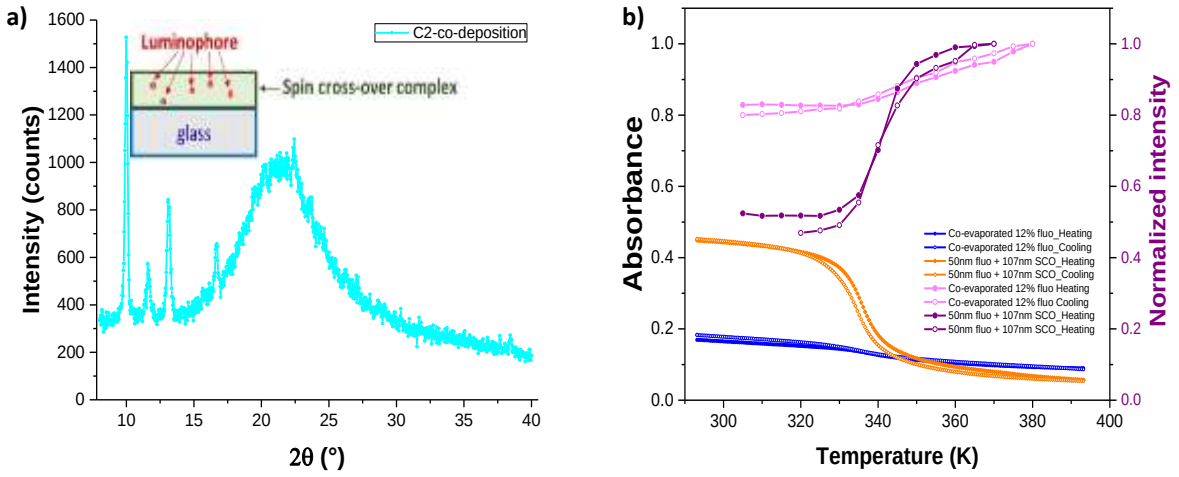

Figure 4.9: Characterization of a $[Fe(HB(tz)_3)_2]$ film doped with 12% $Ir(PPy)_3$. (a) Representative GIXRD pattern. The inset shows the outline of the sample. (b) Temperature dependence of the UV absorbance and luminescence intensity on heating and cooling.

As shown in Figure 4.9a the X-ray diffraction spectrum of the doped film can be ascribed to an amorphous / semi-crystalline film without any particular texture. This means that the presence

of the luminophore molecules within the deposit inhibit the recrystallization of the SCO film. Consequently, the spin transition curves obtained from variable temperature absorbance measurements on the mixed films (Figure 4.9b) are very different from what we generally observe for the pure films of $[Fe(HB(tz)_3)_2]$. In particular, the absorbance change associated with the SCO is very low ($\Delta A = 0.057$); it is approximately ten times smaller than what is expected for a pure SCO film with the same thickness. As it can be expected, we observe thus only a very weak effect of the spin transition on the luminescence emission intensity ratio ($I_{HS} / I_{LS} = 1.2$) (Figure 4.9b).

4.6 Conclusions

In this chapter, we outlined an efficient approach to fabricate hybrid materials, which combine luminescent and spin crossover molecules in a bilayer film stack. Crucially, we have shown that the intrinsic properties of the two layers were not affected by the presence of the other. Yet, the luminescence intensity reversibly increased when the spin crossover molecules were switched from the LS to the HS state in the uppermost layer. We found a strict one-to-one correlation between the luminescence modulation (I_{HS}/I_{LS}) and the UV transmittance change with the spin transition (Tr_{HS}/Tr_{LS}). In the same time, neither the spectral shape neither the decay time of the luminescence emission were altered. These results prove that the origin of the luminescence modulation is a direct result of the different attenuation of the exciting UV light in the two spin states. These results also show that luminescence can be a very sensitive indicator of the thermally induced spin transition, which could be exploited for micro- and nanoscale thermal sensing and imaging applications – in particular when combined with near-field scanning optical microscopy.

Chapter 5. Investigation of SCO thin films using AFM

An important objective of this thesis work was the development of efficient methodologies for the high spatial resolution investigation of the SCO phenomenon in thin films by means of scanning probe microscopic (SPM) approaches. Indeed, as it was discussed in Chapter 1, conventional experimental approaches used to characterize bulk SCO materials (magnetometry, X-ray diffraction, calorimetry, Mössbauer, electronic and vibrational spectroscopies), are often not well adapted to investigate nanoscale SCO objects, generally due to the low amount of matter, and new technics are needed to characterize them. In particular, there is a need for high spatial resolution microscopy tools as well as for high sensitivity methods able to detect molecular spin-state changes in very small amounts of matter, ideally in a single, isolated nano-object. Beyond their high resolution and/or high sensitivity, these new experimental approaches can provide also information on material properties, which are either difficult to access by conventional methods or not so relevant at other size ranges.

Far-field optical microscopy techniques have already been employed with success to monitor the spin state changes in a single nanometric object. For example, single SCO nanoparticles were studied using fluorescence [67], Raman [79] and differential interference contrast [254] microscopy. On the other hand, nanometric thin films of SCO complexes were analyzed by different refractive index sensing methods (see Chapter 1.2.2). In order to surmount the rather limited spatial resolution of far-field optical methods one may use electron or X-ray beams, which can provide structural and spectroscopic information with high spatial resolution. In the case of relatively fragile molecular SCO materials care must be taken, however, due to the invasive nature of these techniques: sample heating and radiation damage are in fact frequently encountered. These problems have been largely alleviated in a work, which used aperture-based time-resolved electron microscopy to follow the spin transition in individual nanoparticles [255].

Another possible approach, which we explored in this thesis work, is based on SPM. Although SPMs have been already used to study phase transitions in different materials, SPM studies on spin crossover materials are very scarce (see section 1.2.2). Actually mostly scanning tunneling microscopy (STM) has been used in this field, but STM is more relevant in the context of single molecule studies and not readily applicable for the study of insulating SCO films, which are the scope of our work. Atomic force microscopy (AFM) and near-field scanning optical microscopy (NSOM) techniques have been previously explored in our team to this aim (thesis of Edna Hernandez). Among the different detection channels provided by the AFM and

the NSOM, quantitative mechanical detection turned out to be the most promising approach and we focused thus our efforts mostly on AFM nano-mechanical measurements. In the beginning of this chapter, we will thus summarize our current knowledge about the mechanical properties of SCO materials. Then, a brief introduction to selected AFM measurement techniques will be presented with particular emphasis on AFM mechanical modes. In the second part of the chapter we present a preliminary investigation of films of the SCO complex $[Fe(H_2B(pz)_2)_2(phen)]$ at room temperature using different AFM instruments and detection modes. Then we turn our attention to films of $Fe(HB(tz)_3)_2$ and we discuss different approaches for variable temperature investigation of the spin state change using the so-called bimodal (AMFM) approach.

5.1 Mechanical properties of SCO materials

The knowledge of the elastic constants of SCO materials and their spin-state dependence is of primary interest because mechanical properties play an important role in the spin-transition behavior of SCO solids. In particular, cooperative phenomena and phase stability can be rationalized only by taking into account the volume difference between the HS and LS states and the concomitant elastic interactions between the SCO molecules [256]. Furthermore, the recently proposed use of SCO materials in actuator devices [104,257]requires also obviously a detailed knowledge of their mechanical properties, such as the Young's modulus, Poisson's number and the mechanical strain. Finally yet importantly, the observed fatigue of various SCO materials on repeated spin state switching was also associated in many cases with mechanical effects (e.g. self-grinding and other mechanical failures).

As was mentioned in Chapter 1, the HS to LS transition involves a drastic decrease of the metal-ligand bond lengths (approximately 10 % for Fe^{II}-N bonds) [116]. This is reflected by an overall upshift of the Raman and FTIR vibrational frequencies - in particular those associated with the metal-ligand stretching modes. Overall, in the low spin state the SCO molecules occupy thus a smaller volume; have a higher mass density and higher stiffness with respect to the high spin state. In the past, the mechanical properties of SCO materials were often discussed on the basis of the Debye model, which assumes a simplified phonon spectrum based on a single parameter, the Debye temperature Θ_D. The values of Θ_D were determined for iron complexes by ^{57}Fe Mössbauer spectroscopy [258] and revealed typically an increase of Θ_D on the order of 5-10 % when going from the HS to the LS state - in line with expected stiffening of the lattice.

If we take into account the central role of mechanics in the SCO phenomenon it is rather surprising to realize that the elastic constants of spin-transition materials have been determined only in a few occasions - and usually in only one spin state. The main cause of this lack of information is that the SCO materials are commonly obtained as nanoparticles, powders or microscopic crystals, which makes difficult the extraction of their mechanical properties using conventional characterization methods at the macroscopic scale. In addition, the extraction of such properties at different temperatures is not obvious and instrumental challenges need to be overcome in order to obtain reliable data. The methods, which have been used to this aim include high pressure X-ray diffraction (HPXRD) [259,260], Brillouin spectroscopy [261], AFM force spectroscopy [126], nuclear inelastic scattering (NIS) [262] and micromechanical measurements using MEMS cantilevers [176]. The reported HS values of bulk and Young's moduli fall typically in the range between 1 - 10 GPa with increasing values in the LS state (up to 50 % increase). Table 5.1 summarizes the available experimental data. Of particular interest for us are the elastic constants of the $[Fe(HB(tz)_3)_2]$ complex, which have been determined in the HS and LS states, both for bulk and thin film samples [173]. It is important to stress that the reported values are 'effective' elastic moduli as they refer to averaged values along different crystallographic axes. Nevertheless, from HPXRD measurements some information about the anisotropy of the elastic properties could be inferred, with the orthorhombic b-axis being the stiffest and the a-axis the softest direction [173].

Table 5.1 Comparison of reported effective (isotropically averaged) elastic moduli of different SCO complexes (*B*: bulk modulus, *E*: Young's modulus, *v*: Poisson's number) [173].

Compound	Elastic moduli (GPa)	Method	Sample
$Fe(phen)_2(NCS)_2$	B_{HS} = 9.3, B_{LS} = 12.2	HPXRD [259]	Single crystal
$Fe(btz)_2(NCS)_2$	B_{HS} = 8.3, B_{LS} = 11.2	HPXRD [259]	Single crystal
$Fe(dpp)_2(NCS)_2$.py	B_{HS} = 10.6	HPXRD [260]	Single crystal
[{Fe(bpp)$(NCS)_2$}(4,4'-bpy)].2MeOH	B = 6.2	HPXRD [263]	Single crystal
[Fe(TPA)(TCC)]SbF6	B_{LS} = 10.8	HPXRD [264]	Single crystal
$[Fe(3\text{-}MeOsalEen)_2]PF_6$	B_{HS} = 4.3	HPXRD [265]	Single crystal
$[Fe(hptrz)_3](OTs)_2$	E_{HS} = 1.3, E_{LS} = 1.7	AFM [126]	Film
$[Fe(ptz)_6](BF_4)_2$	B_{HS} = 4.8 E_{HS} = 4.5 v_{HS} = 0.34	Brillouin spectra [261]	Single crystal
[Fe(pyrazine)$(Ni(CN)_4)$]	E_{HS} = 10.4, E_{LS} = 13.5	NIS [258]	Crystalline powder
$[Fe(H_2B(pz)_2(phen)]$	E_{HS} = 4.7, E_{LS} = 5.2 E_{HS} = 6.9	NIS [262] MEMS [266]	Crystalline powder Amorphous film
$\{Fe(3\text{-}CNpy)[Au(CN)_2]_2\}\cdot 2/3H_2O$	E_{LS} = 7.5	Cantilever bending [257]	Single crystal
$[Fe(HB(tz)_3)_2]$	E_{HS} = 7.1, E_{LS} = 10.9 B_{LS} = 11.5 v_{LS} = 0.34	NIS [173] HPXRD [173]	Crystalline powder Single crystal
	E_{HS} = 9.9, E_{LS} = 12.0	MEMS [173]	Crystalline film

5.2 AFM operating modes for mechanical property analysis

The quantitative imaging of mechanical properties using an AFM represents a big challenge due to the problems to quantify tip-sample interactions and the contact geometry. In the course of this thesis, we used different AFM techniques to extract mechanical properties of SCO thin films. In this section, a description of these modes will be presented. They are divided into two major categories: *dynamic AFM* (often called "tapping mode") and *force curves*. (N.B. It may be worth to mention here that several other AFM techniques have been developed for mechanical measurements, mostly high frequency 'ultrasonic' methods such as the force-modulation or the contact-resonance techniques. However, these are more relevant for the investigation of stiff surfaces and are not included therefore in this discussion.)

5.2.1 Tapping mode and its variants

All the techniques which are based on dynamic (or AC) AFM modes have the capability to perform fast and 'gentle' measurements, minimizing the effects of friction. In the most frequently used AC-AFM configuration (Figure 5.1), the tip/cantilever ensemble is vibrated by a piezoelectric transducer around its resonance frequency, while the sample is raster scanned in the *xy* directions using piezo actuators and the deflection of the cantilever is detected by a laser beam deflection method. We can differentiate operation modes depending on which parameter of the sinusoidal oscillation (amplitude A, frequency f or the phase φ) is used to control the feedback loop.

a) Amplitude modulation

Due to the frequently occurring intermitted contact between tip and sample at the lowest point of the oscillation, the amplitude modulation (AM) mode has often been denoted as "tapping mode". Over the years, the use of the term "tapping mode" has then evolved into a synonym for the amplitude modulation (AM) mode in many publications, disregarding whether the tip is actually making intermitted contact or not.

In AM-AFM mode, the probe is externally vibrated at a constant frequency near its resonance and a feedback loop acts on the tip-sample distance (i.e. on the z piezo) in order to keep the amplitude of the oscillation constant around a user specified set-point value. In other words, the average normal tip-sample interaction force remains constant. During the *xy* scan, the experimental observables are the surface topography (Δz), the oscillation amplitude (i.e. the error signal) and the phase of the oscillation. The phase shift (Δφ) will depend on the viscoelastic properties of the sample surface. Phase imaging is sensitive to surface stiffness and

adhesion between the tip and sample. It allows thus chemical mapping of surfaces based on these material properties. For a damped, driven harmonic oscillator, the phase angle φ of a cantilever oscillation can be calculated as a function of the driving frequency ω as follows [267]

$$\tan(\phi) = \frac{\omega\omega_0 / Q}{\left(\omega_0^2 - \omega^2\right)} \tag{5.1}$$

where: ω_0 is the resonant frequency and Q is the quality factor of the cantilever. This factor characterizes the damping of the oscillator and can be calculated as $Q = \frac{\omega_0}{\Delta\omega}$, where $\Delta\omega$ is the half-power bandwidth.

From equation (5.1), the probe phase angle is 90° at the resonance frequency. When the cantilever is far from the sample, there is no interaction between the tip and the sample. Thus, the probe phase angle is 90° when the driving frequency is chosen as the cantilever resonance frequency. As the probe approaches the sample surface, the attractive forces acting on the probe decrease the resonance frequency. Hence, the probe driving frequency becomes larger than the probe resonance frequency and therefore, the probe phase angle is $\varphi > 90^0$ .When the tip is further approaching the sample the probe works in a repulsive force region, the resonant frequency becomes larger than the driving frequency and the probe phase angle is $\varphi < 90^0$. In other terms, attractive forces make the cantilever "softer", reducing the cantilever resonant frequency. In contrast, repulsive forces make the cantilever "stiffer", increasing its resonant frequency. Therefore it is possible to obtain qualitative information regarding the adhesive/repulsive forces and the viscoelastic properties [268,269].

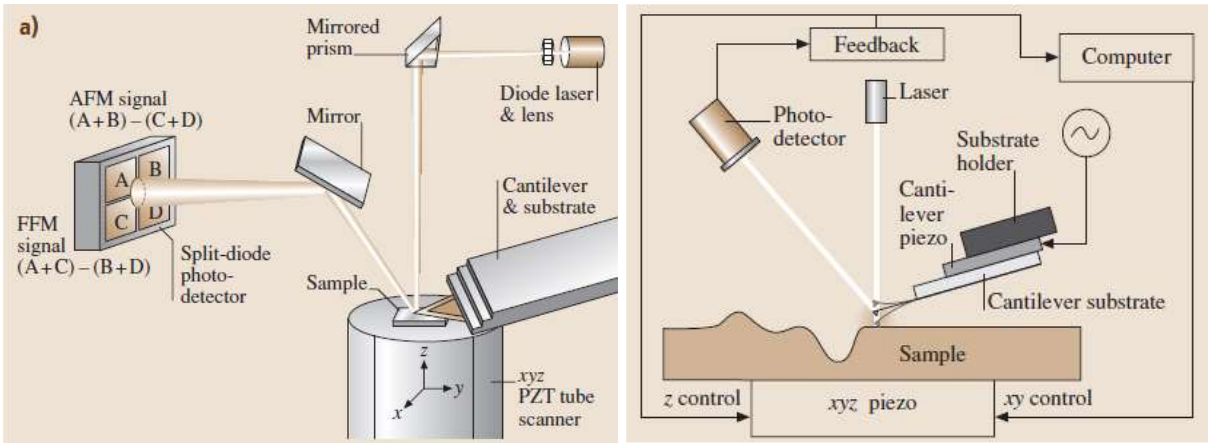

Figure 5.1: (a) The most frequent design of an AFM and (b) schematic picture of the AC mode.

b) Frequency modulation

In the FM-AFM mode, the cantilever is vibrated always at its resonance frequency by adjusting continuously the cantilever excitation frequency such that φ = 90°. In addition, the oscillation amplitude is also kept constant by adjusting the drive amplitude with a second feedback loop. The shift of the resonance frequency is the main control parameter in FM-AFM: it is used as the set-point signal for the *z* piezoelectric actuator. The topography of the sample is then obtained by adjusting the tip-sample distance to keep the resonance frequency constant. The record of the drive amplitude over the course of a scan provides a second image where variations in the drive amplitude are proportional to the energy dissipated by non-conservative tip-sample interactions (viscoelasticity, friction, …) [270]. The drive signal image (similar to the phase image in AM-AFM) provides thus a compositional map, because, unlike the frequency shift, the drive signal is free to vary during the course of a scan according to the composition of the sample. A particular interest of FM-AFM is that it provides a way to access short-range tip-sample interactions and, in certain cases, atomic resolution can be thus reached.

c) Phase modulation

Compared with the FM-AFM where the scan is performed at the resonant frequency by adjusting the drive frequency, in the case of PM-AFM, the scan is performed by adjusting the phase difference. The phase-modulation technique is capable to measure conservative and dissipative tip-sample forces without any jumps caused by instabilities. This feature is an important advantage compared to the conventional AM-AFM mode [271]. The dissipation channel is given by the amplitude signal. Using the amplitude image, we can thus observe a contrast due to the differences in the viscoelastic properties of the sample.

d) Loss tangent mode

Notable progress has been made in quantifying phase imaging in terms of the tip – sample energy dissipation [272-274] or conservation [275]. Even with these advances, obtaining quantitative material or chemical properties of the surface remains problematic. Loss tangent imaging is a recently introduced quantitative technique [276], that recasts the interpretation of phase imaging into one term that includes both the dissipated (E'') and the stored (E') energy of the tip sample interaction. The loss tangent is a well-characterized quantitative material property, which is defined as tan(δ) = E”/E’.

For many materials (polymers, etc.), the loss tangent is a very sensitive probe of phase transitions. When measured on bulk samples with traditional dynamical mechanical analysis

(DMA) techniques, tan δ typically ranges from less than 0.001 for metals and ceramics to more than 1 for elastomers and biological materials (Figure 5.2). For most materials, $tan\ \delta < 3$.

The loss tangent measurement in AFM is achieved in two pass (Figure 5.2). In the first pass, the topography, amplitude and phase images are recorded in standard AM-AFM mode with care taken to conduct the measurement in the 'repulsive regime'. In the second pass, the tip moves at a preset height Δz = 50-100 nm above the surface (the so-called 'lift' or 'nap'), where the resonant frequency (ω_{free}) and the reference amplitude (A_{free}) are measured by operating the cantilever in phase locked loop ($\varphi = 90°$). Then the loss tangent is obtained as:

$$\tan(\delta) = \frac{\sin\varphi_1 - \frac{\omega}{\omega_{free}}\frac{A_1}{A_{free}}}{Q\frac{A_1}{A_{free}}\left(1-\frac{\omega^2}{\omega_{free}^2}\right) - \cos\varphi_1} \tag{5.2}$$

The quality factor Q and the resonance frequency ω are extracted from a frequency sweep (tune). ω_{free} and A_{free} are determined during the second scan, while A_1 and φ_1 are measured during the first scan. AFM loss tangent measurements provide a simple means to access a well-defined material property at the nanoscale, but remain controversial as several potential artefacts may occur. Air damping effects are effectively reduced thanks to the second scan, while capillary effects can be largely decreased by purging the AFM sample chamber with an inert gas at elevated temperatures (e.g. 100 °C). Yet, many other sources of error can arise, which need to be considered case-by-case (e.g. sample plasticity, attractive forces, etc.)..

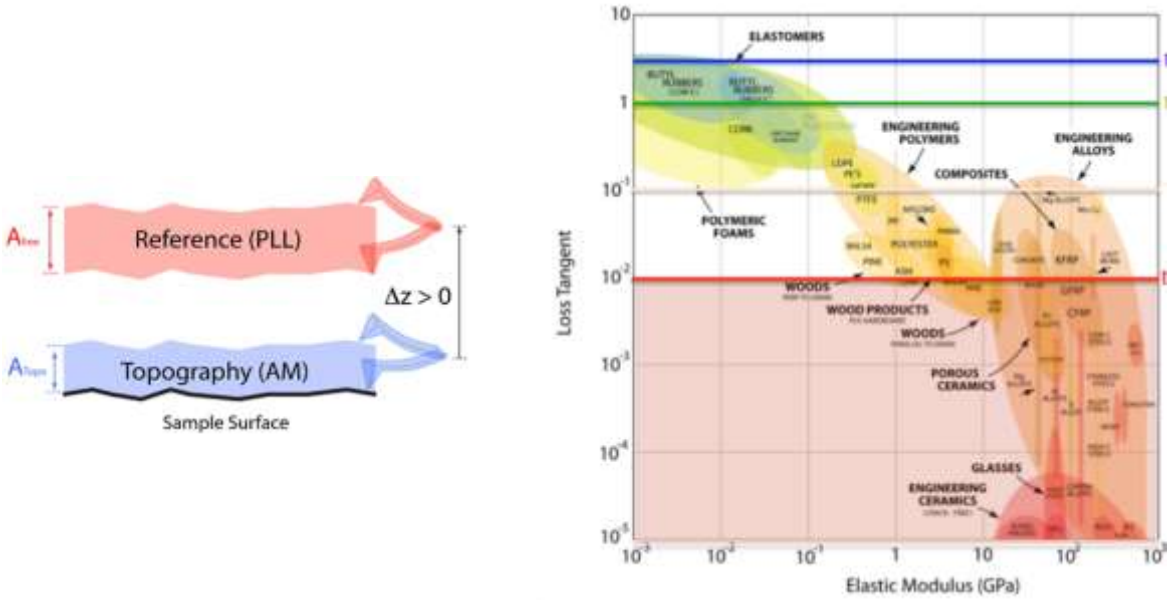

Figure 5.2: (left) Schematic representation of the two-pass loss tangent measurement method, (right) loss tangent vs. elastic modulus for some common materials [276, 277].

5.2.2 Multi-frequency methods

Multi-frequency AFM is based on the simultaneous excitation and detection of more than one eigenmodes of the AFM cantilever, typically the first and the second modes, although other combination of eigenmodes could be used. The observables of the first mode are primarily used to generate the topography of the surface, while the observables of the second mode in combination with those of the first mode are used to generate maps of mechanical/viscoelastic properties such as the Young's modulus, dissipation, indentation depth, peak force or viscous coefficients[278]. A distinctive feature of bimodal force microscopy is the capability to obtain quantitative information with fast scan rates.

Three main factors singularize bimodal AFM operation [279]: (i) the coupling between excited modes induced by the nonlinear tip-surface force, (ii) the doubling of the number of observables to record information on material properties and (iii) the lack of feedback restrictions for the additional excited mode. The eigenmodes of a cantilever have different force constants, quality factors and resonant frequencies; consequently they do not offer the same sensitivity to detect material properties. Depending on the type of feedback applied to a given excited mode (amplitude, frequency or open loops) different bimodal configurations can be obtained. Table 5.2 shows a classification of the most common bimodal AFM approaches with the feedback technique (amplitude modulated or frequency modulated) for each flexural mode and the properties that can be measured quantitatively.

Table 5.2: Bimodal AFM configurations

Mode name	Feedback mode 1	Feedback mode 2	Material Property
Bimodal AM	AM	open	Loss tangent
AM-FM	AM	FM	Loss tangent, stiffness, Young's modulus
Bimodal FM	FM	open	Dissipation, stiffness, Young's modulus

Figure 5.3 illustrates the fundamental principles of operation of the AM-FM mode. Two function generators emit signals, which are used concomitantly to excite the cantilever. This results in the simultaneous excitation of two different vibrational modes of the cantilever. The first and the second flexural resonances are generally applied. The lower cantilever resonance runs in amplitude-modulation mode. A lock-in amplifier measures the amplitude and phase at a fixed frequency. The loss tangent is determined from these signals. The AFM also applies the amplitude for feedback control, fine-tuning the tip-sample distance to maintain the amplitude

at the set-point value. Such as in tapping mode, topography data can be obtained from this signal. At the same time, the amplitude and phase are measured by a second lock-in amplifier in the frequency modulation mode (higher resonance mode). The amplitude is maintained constant by an automatic gain control (AGC) circuit through the adjustment of drive amplitude. The phase is kept at 90º by a phase-locked loop (PLL) by adjusting the drive frequency. The output drive voltage signal provides information about dissipative forces, while the output resonance frequency delineates the elastic interaction between the sample and tip. Higher frequency indicates greater modulus or stiffness. Simply put, a stiffer sample shifts the second resonance to a higher value while a softer sample shifts it to a lower value.

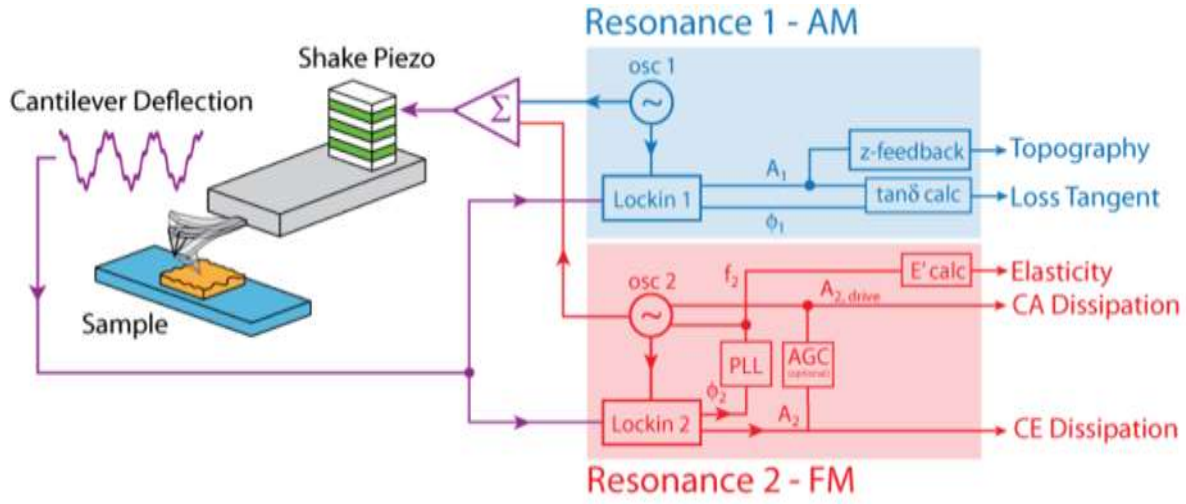

Figure 5.3: Schematic representation of the AM-FM mode, where two separated excitation signals are sent to the tip (blue and red) [280].

Using a contact mechanics model, the elastic modulus can be quantified. For the particular case of a Hertz indenter (see section 5.2.3), Garcia et al. has shown that

$$E_{eff} = \frac{\Delta f_2}{f_{0,2}} \frac{k_2}{r_c} \tag{5.3}$$

with:

$$\frac{1}{E_{eff}} = \frac{1-\nu_t^2}{E_t} + \frac{1-\nu_s^2}{E_s} \tag{5.4}$$

where ν is the Poisson's ratio and E is the Young's modulus. The subscripts *eff*, *t* and *s* refer to effective, tip and sample properties, respectively. If $E_t >> E_s$ one obtains $E_{ff} \approx E_s$. Equation 5.3 means that the sample modulus can be calculated from the resonance frequency shift of the second mode Δf_2 (with respect to the resonance frequency of the free cantilever $f_{0,2}$) if the force

constant of the second mode (k_2) and the tip contact radius (r_c) are known. In practice, using a reference sample of known modulus, one does not need to determine the model parameters such as the radius of the tip. Here, one assumes that a single calibration constant (C_2) relates the frequency shift of the second mode to the elastic modulus:

$$E_{eff} = C_2 \Delta f_2 \tag{5.5}$$

Highly accurate results are obtained when the moduli of the reference and test samples are similar. In addition, during the AMFM scan maps of sample indentation, dissipation, and loss tangent are collected for further analysis.

5.2.3 Force curves based methods

Nanoindentation testing is a method of measuring the mechanical properties of a material such as hardness and Young's modulus on the microscopic scale [281].This method consists of applying pressure to the sample using a hard tip with known mechanical properties. The applied pressure is determined as a function of the indented depth or the residual indentation area. In the AFM nanoindentation, the force applied by the tip can be in the range of few *pN* for softer samples (e.g. cells) to μN for harder samples (e.g. silicon wafers). In an effort to combine AFM force spectroscopy and imaging with nanometric resolution different methods have been developed by the AFM manufacturers, such as 'force volume mapping', 'quantitative imaging' and 'peak force tapping'. The primary difference between these methods is the way the probe is moved along the sample surface (Figure 5.4). In any case, the key issue is to achieve reasonable imaging time while obtaining proper and detailed spectral data from each pixel.

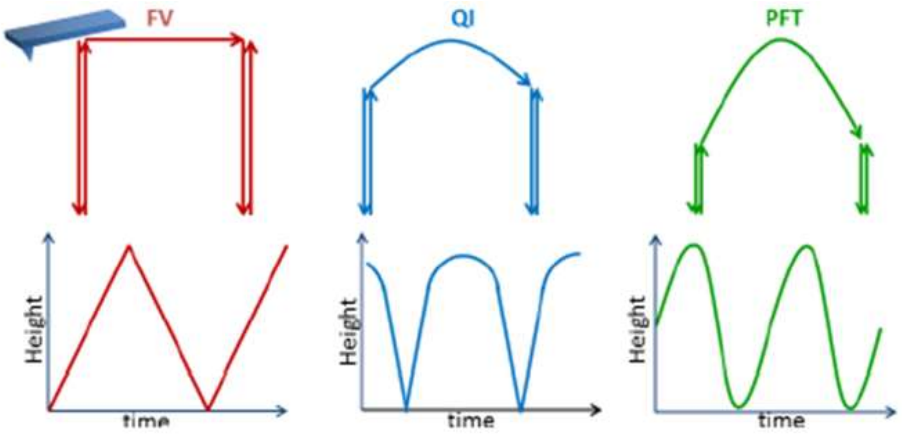

Figure 5.4: Schematic representation of the tip movement in force-volume mapping (FV), quantitative imaging (QI) and peak force tapping (PFT). The arrows show the tip movement.

a) Force-distance curves

Force spectroscopy allows a quantitative determination of different physical and mechanical properties such as the Young's modulus, adhesion and dissipated energy. Figure 5.5 depicts a typical force-distance curve obtained with an AFM. The different interactions between the tip and the sample are marked with numbers (1-5). As the cantilever approaches the surface, initially the forces are too small to give a measurable deflection of the cantilever, and the cantilever remains in its free position (1). At a certain tip-sample distance, attractive forces (usually Van der Waals or and capillary forces) overcome the cantilever spring constant and the tip jumps into contact with the surface (2). Once the tip is in contact with the sample, it remains on the surface as the separation between the base of the cantilever and the sample decreases further, causing a deflection of the cantilever and an increase in the repulsive contact force (3). As the cantilever is retracted from the surface, often the tip remains in contact with the surface due to some adhesion and the cantilever is deflected downwards (4), until the tip is suddenly released from the surface (5). For measurements in air, such as the one shown in Figure 5.5, there is usually adhesion from capillary forces between the tip and sample.

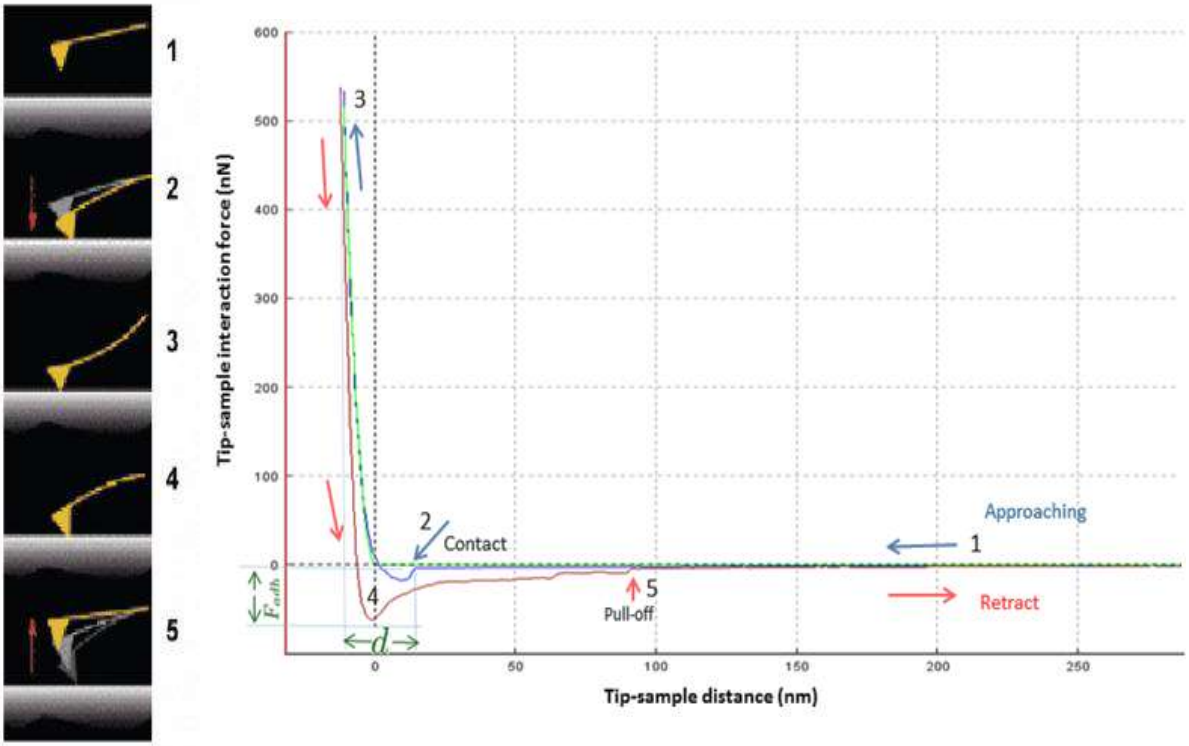

Figure 5.5: Force-distance curve of a $[Fe(H_2B(pz)_2)_2(phen)]$ film obtained with an AFM. The Young's modulus is obtained from the linear fit of the repulsive region (between 3 and 4), while the work of adhesion is calculated from the hysteresis area between the 'approach' and 'retract' curves.

b) Force – distance calibration

The deflection of the cantilever spring is directly proportional to the tip-sample interaction force, but two measurements are required to convert the photodetector signal into a quantitative value of force.

The first step is to calibrate the cantilever deflection (D), measured as a photodetector voltage, by determining the deflection sensitivity (S), which has units of nm/V. The value of S depends on the type of the cantilever, but also on the optical path of the AFM laser beam deflection system and will be slightly different each time the cantilever is mounted. The deflection sensitivity can be determined from a force-distance curve between a cantilever tip and a hard, non-deformable substrate (silicon or sapphire). This is a measurement of the deflection of the tip in nanometers for a given movement of the detection laser on the photodetector. The repulsive contact region, where the deflection rises steeply upwards, is linear for a hard surface and tip. Therefore, the factor for converting volts into nanometers is obtained by a simple linear fit. This calibration process can damage the tip and it should be performed thus at the end of an experiment. It should be noted that the deflection sensitivity calibration is a major source of error in force spectroscopy.

Once the deflection of the cantilever is known as a distance, DS, the tip position can be calculated from the z piezo position as follows:

$$d = z - DS \tag{5.6}$$

Yet, the spring constant, *k*, is needed to convert the cantilever deflection into a force *F*, using Hooke's law:

$$F = kDS \tag{5.7}$$

Uncertainty in cantilever spring constants is also a critical issue. Several methods have been developed to obtain the spring constant (*k*) [282-288]. Two of the most common calibration methods, the thermal tuning and the Sader's method are equally reliable and offer similar uncertainty in the calibrated spring constants, about 5% [285]. For thermal tuning, the thermal resonance curve is fitted to a Lorentz function, which allows calculation of the spring constant. This method has the advantage that it can be conducted in-situ with software analysis. The normal spring constant of a rectangular AFM cantilever can be also determined using the Sader equation [283]:

$$k_z = 0.1906\rho b^2 L Q_f \omega_f^2 \Gamma_i^f(\omega_f) \tag{5.8}$$

where L and b are the length and width of the cantilever, respectively. ρ is the density of the fluid, ω_f and Q_f are the resonant frequency and quality factor of the fundamental resonance peak, respectively. Γ_i^f is the imaginary part of the hydrodynamic function, which is discussed in more details in Sader's publications [289]. A key issue with the Sader method is that the cantilever geometry is not always accurately known and its experimental determination is fastidious.

c) Tip-sample interaction

The contact mechanics between the sample and the AFM probe is a critical issue – not only for force spectroscopy, but for all AFM based mechanical measurements. The usual starting point to describe the tip sample interaction is the Hertz model, which describes the contact stress when two curved surfaces come into contact. This model gives the contact stress as a function of the applied force, the radii of curvature of the surfaces and the elastic moduli of the materials. The main assumptions behind this approach are:

- The deformations are small and the behavior of the bodies is fully elastic.
- The surfaces are smooth, continuous, homogenous and non-conforming (small contact).
- There is no friction and no adhesion forces. Only normal forces operate.

With these assumptions, Hertz has shown that in the case of a sphere (i.e. the tip) in contact with a plane (Figure 5.6) the force between the tip and the sample is:

$$F_{ts} = \frac{4}{3} E^* \sqrt{R(d-d_0)^3} \tag{5.9}$$

where E^* is the effective Young's modulus defined by eq. 5.4, R is the tip radius and d-d_0 is the indentation depth (with the contact point d_0). In order to determine the Young's modulus of the sample from a force-distance curve one needs to know the Poisson's ratio of the sample (if not known, it is usually assumed to have a value between 0.2 and 0.4) and, more crucially, the tip radius. In practice, the latter can be determined using a polystyrene calibration sample with known values of E (2.7 GPa) and v (0.35). When the adhesion is not negligible, one may use instead the Dejarguin, Müller, Toporov (DMT) model (Figure 5.6), wherein the tip-sample interaction force takes also into account the adhesion force (F_{adh}) extracted from the force spectrum:

$$F_{ts} = \frac{4}{3} E^* \sqrt{R(d-d_0)^3} + F_{adh} \tag{5.10}$$

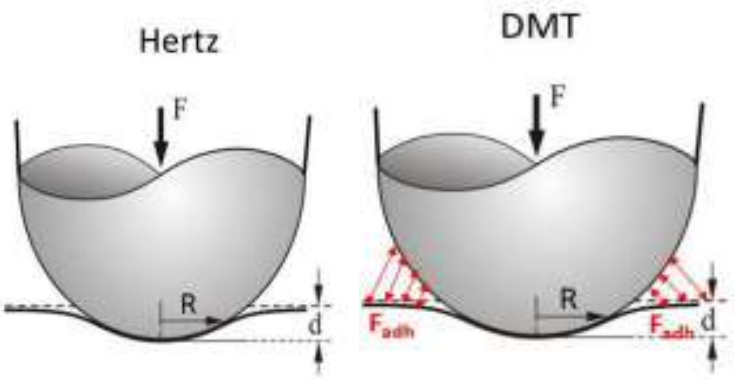

Figure 5.6: Hertz and DMT models of the mechanics of a spherical tip in contact with a flat surface

5.3 A comparative investigation of AFM based quantitative mechanical measurement techniques

Variable temperature quantitative AFM mechanical imaging of samples with unknown elastic properties (SCO thin films in our case) is very challenging. To test the performance of different AFM mechanical modes we have used in a first time a thin film of the SCO compound $[Fe(H_2B(pz)_2)_2(phen)]$ (pz=pyrazolyl, phen=1,10-phenantroline). We have chosen this compound for our experiments because it can be conveniently deposited by thermal evaporation, and has the advantage of giving smooth, homogeneous films with low roughness [82,83]. In addition, at the time when we started this work it was the only SCO film with known Young's modulus (see Table 5.1). This complex appeared therefore as a good candidate for AFM mechanical tests.

5.3.1 Generalities on the sample $[Fe(H_2B(pz)_2)_2(phen)]$

The SCO complex $[Fe(H_2B(pz)_2)_2(phen)]$ has been reported first by Real and coworkers [290] in 1997, while the successful film deposition was achieved by Naggert et al. in 2011 [82]. The microcrystalline powder displays a rather abrupt, cooperative, first-order thermal spin transition around 163 K with a narrow hysteresis (2 K), while the vacuum-deposited, amorphous films exhibit a very gradual thermal spin crossover between ca. 100 K (LS state) and 200 K (HS state) (see Figure 5.7). Both the powder and film samples exhibit light-induced excited spin-state switching. For our work, the bulk, powder of $[Fe(H_2B(pz)_2)_2(phen)]$ was synthesized by Sylvain Rat (LCC-CNRS) and thin films of were grown by thermal evaporation at 160 °C at a base pressure of ca 10^{-8} mbar by Isabelle Séguy (LAAS-CNRS). The films were deposited onto fused silica substrates, which were before cleaned with acetone and isopropanol to remove

contaminants. The control of the film thickness was carried out by AFM in tapping mode in ambient air using a Bruker Icon AFM instrument and MPP11120 (Bruker) probes. The films are homogeneous, continuous and smooth (see Figure 5.8), and the thickness obtained is consistent with the desired nominal thickness.

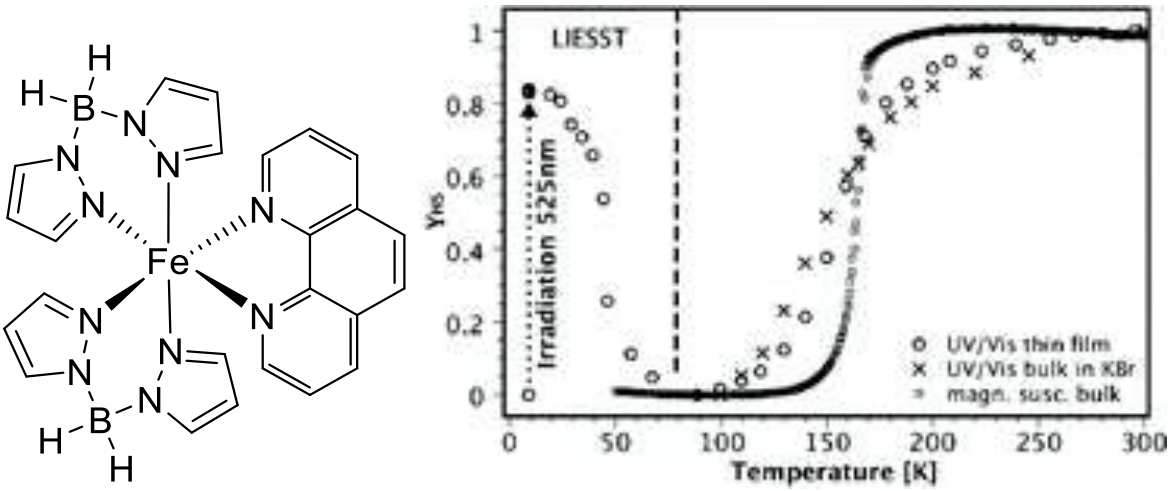

Figure 5.7: Molecular structure and spin crossover properties of the compound $[Fe(H_2B(pz)_2)_2(phen)]$. The thermal spin crossover is shown both for the bulk powder and for a thin film sample [82, 83].

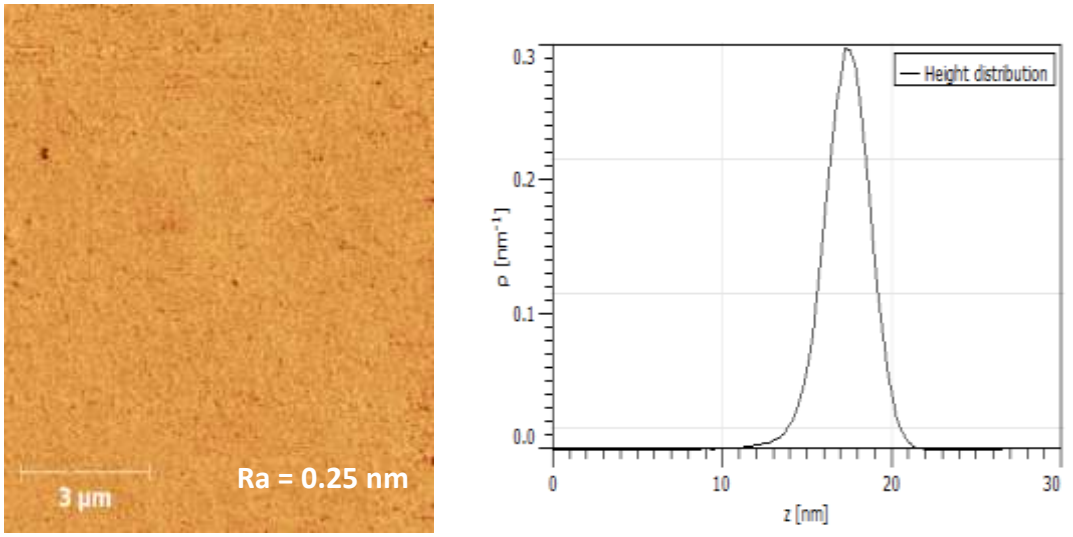

Figure 5.8: AFM image and corresponding height histogram of a thin film of $[Fe(H_2B(pz)_2)_2(phen)]$ with nominal thickness of 200 nm (image size 10 x 10 μm^2).

5.3.2 AFM mechanical measurements

All measurements presented in this section were performed in ambient air at room temperature (i.e. in the HS state) on a thin film of ca. 200 nm thickness of the SCO compound $[Fe(H_2B(pz)_2)_2(phen)]$ - unless otherwise stated. Our aim was to compare three different

mechanical modes implemented on three different AFM instruments: bimodal AM-FM mode with a CYPHER-ES AFM from Oxford Instruments, Peak-Force Tapping Quantitative Nanomechanical Measurements (PFT-QNM) mode on a Dimension Icon AFM from Bruker and Quantitative Imaging (QI) mode with a NanoWizard3 AFM from JPK Instruments. In each case, to determine the tip radius, a polystyrene calibration sample (Bruker PSFILM, with E = 2.7 GPa and Poisson's ratio = 0.35) was used in conjunction with the Hertz model (AMFM and QI) or the DMT model (PFT) as implemented in the software of each AFM instrument.

Measurements in AM-FM mode were performed using Si probes (OMCLAC160TS-R3, Olympus). These probes are characterized by a nominal resonance frequency of 300 kHz, a spring constant of 26 N/m and a tip radius of 7 nm. Figure 5.9a shows an example of sample topography and Young's modulus maps of the film recorded at room temperature. We observe a very smooth surface: the arithmetic mean surface roughness, Ra, is only 0.24 nm. We note also that the average value of the Young's modulus (2.54 ± 0.09 GPa) is of the same order of magnitude, yet significantly smaller than the value (6.9 ± 0.1 GPa) obtained by Manrique et al. [266] on the same film by means of MEMS micromechanical measurements. Our AFM instruments do not allow us low temperature imaging of the films in the LS state. Nevertheless, to test the temperature dependent behavior of the mechanical properties we heated the sample to 333 K using the heating stage of the Cypher microscope. In the case of thermomechanical property studies an obvious problem is related to the fact that the mechanical properties of the probe (spring constant, resonant frequency, etc.) change also with the temperature. Therefore, these parameters were recalibrated at each temperature change. The AMFM data obtained at 333 K are shown in figure 5.9b. While the sample topography remained virtually the same, we observe a decrease of the Young's modulus from ca. 2.54 GPa to 1.2 GPa – in agreement with its expected softening upon heating. Then, to verify the reversibility of the measurements we cooled back the sample to room temperature. As shown in Figure 5.9c the initial room-temperature value of the Young's modulus is recovered after a full thermal cycle within the experimental uncertainty (2.49 vs. 2.54 GPa), providing evidence that the observed changes are not linked to sample degradation or instrumental drift. For multiple scans, however, the wearing of the tip becomes a critical issue. For example, studies of the wear of different tips have been made by Vahdat et al. [291] in tapping mode and the authors showed that the radius of a silicon tip doubled after only nine scans. We observed similar phenomena in our experiments. Hence, before each measurement, a further calibration on polystyrene was necessary to control the tip radius. This protocol is not only very time consuming, but makes extremely difficult to conduct longer series of measurements as a function of the temperature.

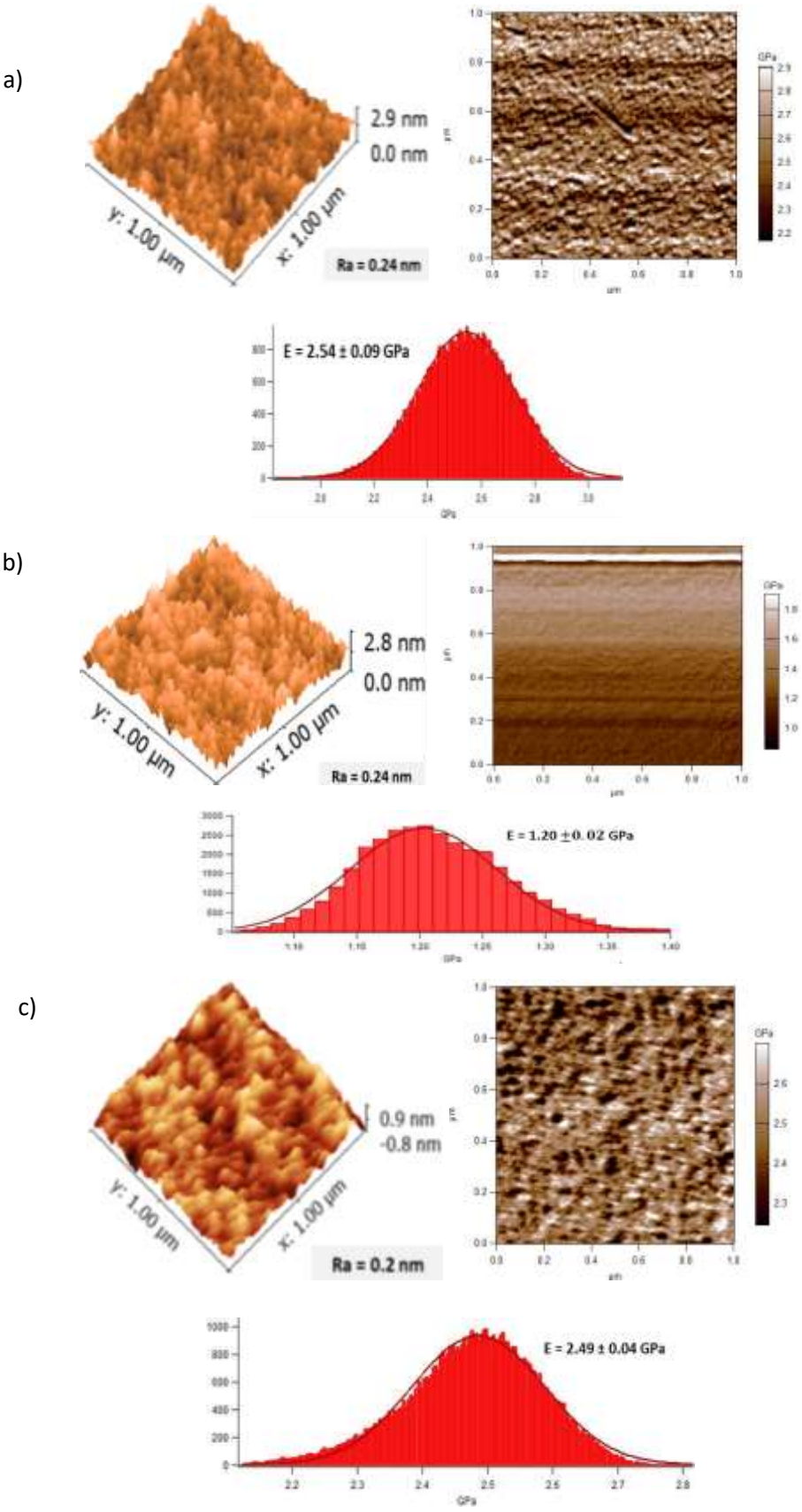

Figure 5.9: AM-FM topography and Young's modulus images and associated Young's modulus histogram for a 200 nm $[Fe(H_2B(pz)_2)_2(phen)]$ thin film acquired successively at 298 K (a), 333 K (b) and again at 298 K (c). The scan rate was 1.5 Hz.

Measurements in PFT-QNM mode were performed using reflective (Al-coated) RTESPA probes (Bruker) with a nominal resonant frequency of 300 kHz, a spring constant of 40 N/m and a tip radius of 8 nm. AFM images (scan size 500 nm × 18 nm) were recorded at a scan rate of 0.6 Hz at 2 kHz modulation. The peak force set-point (24.4 nN) was chosen to achieve small sample indentations within the elastic limit. The deflection sensitivity of the photodetector was obtained on a silicon wafer and the spring constant of the cantilever was determined by thermal tuning (k = 20.03 N/m). The tip radius determined using the polystyrene calibration sample was 9.5 nm. The images acquired at room temperature for different channels (Young's modulus, adhesion, deformation and topography) are presented in figure 5.10 together with the associated histograms.

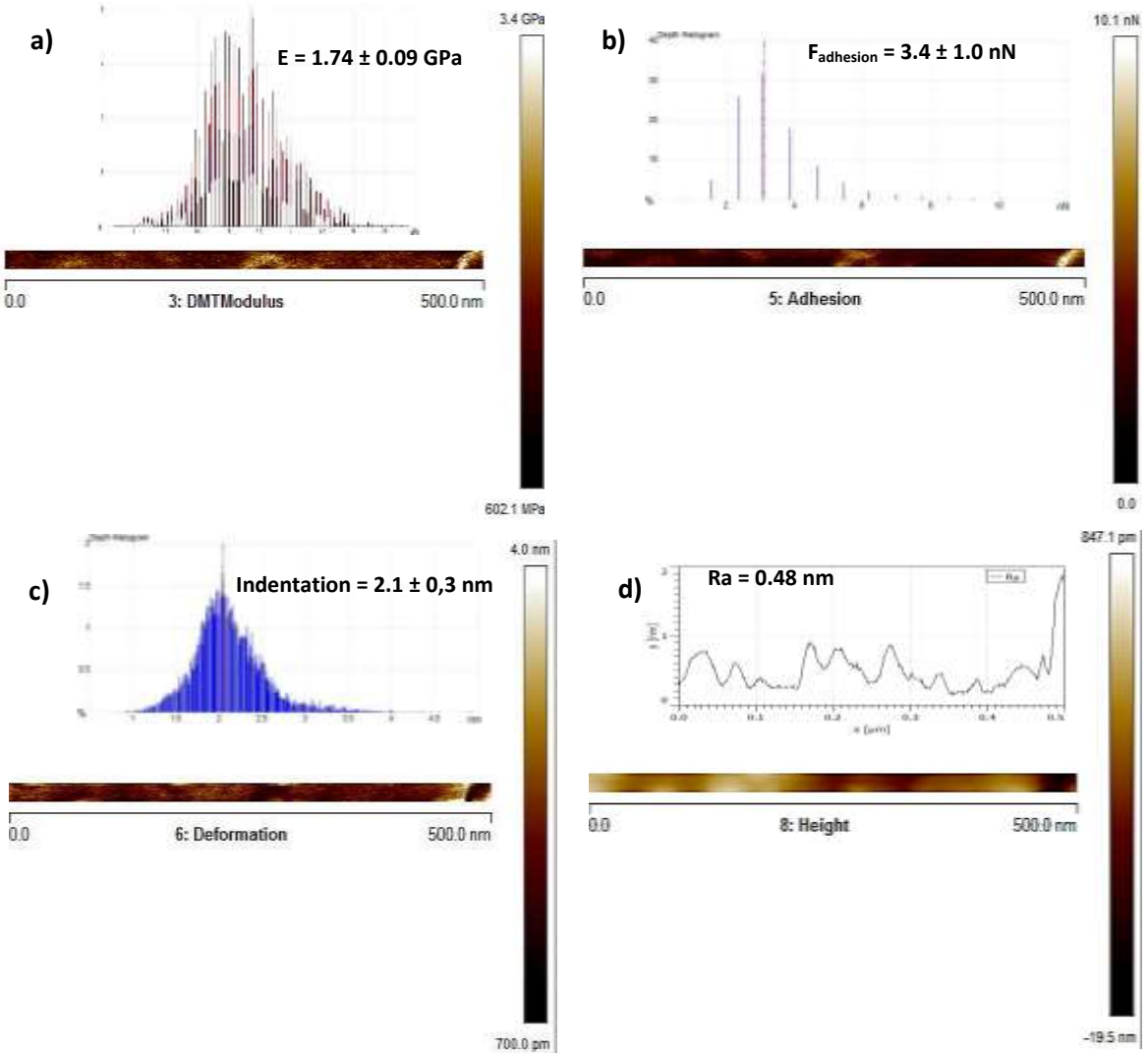

Figure 5.10: PFT-QNM images and histograms for a thin film of ca. 200 nm thickness of [Fe($H_2B(pz)_2)_2$(phen)]. a) Young's modulus, b) Adhesion, c) Deformation and d) Topography.

From the histogram of Young's moduli (Figure 5.11) one can deduce an average value of ca. 1.75 ± 0.09 GPa. The average indentation depth was 2.1 ± 0.3 nm, the sample roughness Ra = 0.48 nm and the average adhesion force F_{adh} = 3.4 ± 1.1 nN. From this latter value, one can estimate an average surface energy of ca. 10-20 mJ/m^2 [https://tel.archives-ouvertes.fr/tel-00669475/].

For measurements in QI mode, we used OMCLAC160TS-R3 (Olympus) probes. Force-distance curves were saved for posterior analysis using the JPK software, SPM Data Processing. Figure 5.11 shows a typical force spectrum while the images recorded in the QI mode are presented in the Annexes A.5.3.2.1. By assuming a Poisson's ratio of 0.3, from the QI data we extracted a Young's modulus value of 2.70 ± 0.02 GPa.

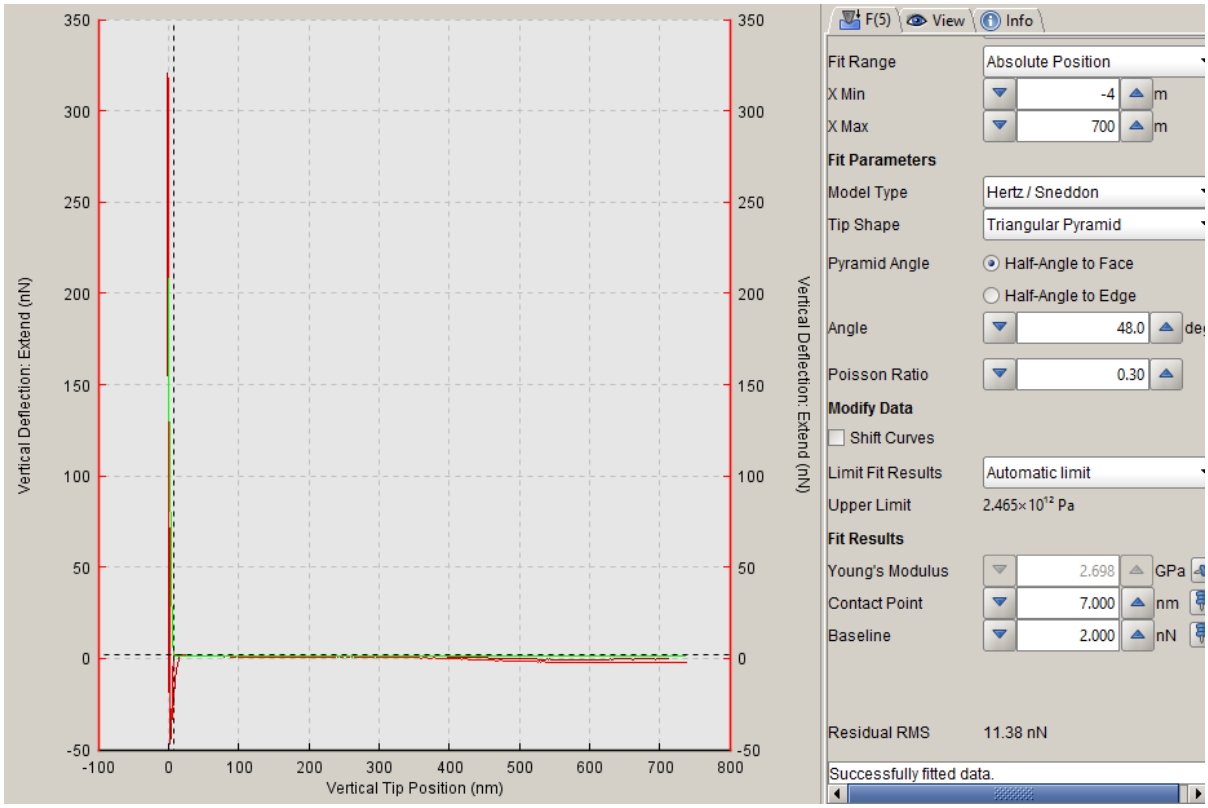

Figure 5.11: Force-distance curve of a 200 nm thick film of [Fe(H_2B(pz)$_2$)$_2$(phen)] obtained in QI mode

The summary of the AFM mechanical data obtained with different AFM instruments is presented in the Table 5.3. Overall, we can conclude that: (i) using different AFM techniques we have obtained very similar values for the Young's modulus of our sample (ca. 2.0 ± 0.5 GPa); (ii) the values obtained are smaller than the MEMS data **(**6.9 GPa), but in the same range; (iii) we can follow the effect of an external stimuli (i.e. temperature) on the Young's modulus; (iv) with careful calibration a precision of nearly 0.1 GPa can be reached along a measurement series; (v) the repetability is, however, less good: up to 1 GPa variation is observed from one

series to another. Overall, the wear of the tip and the sample during successive scans as well as the occurrence of unwanted thermal effects remain very difficult to handle because the different measurement parameters (cantilever stiffness, tip radius, etc.) must be continuously verified. In particular, the regular control of the tip radius on an external reference sample (i.e. the polystyrene) appears practically not feasible. For this reason, we have developed novel measurement strategies, which will be described in the next sections.

Table 5.3: Summary of AFM mechanical data on a $[Fe(H_2B(pz)_2)_2(phen)]$ film

T (°C)	Young's modulus (GPa)	Tip radius (start) (nm)	Tip radius (end) (nm)	AFM Instrument
23	2.54	4.1	7.0	Cypher
60	1.2			
23	2.49			
23	2.7	8.3	4.1	NanoWizard
23	1.94	25.0	16.0	Cypher
23	1.7	9.5	2.5	Dimension Icon
23	1.39	8.8	5.3	Cypher
60	0.55			
23	1.18			

5.4 Nanomechanical investigation of the spin transition in $Fe(HB(tz)_3)_2]$ films

The work described in this section has been carried out on the $[Fe(HB(tz)_3)_2]$ thin films described in the previous chapters of the thesis. This sample is particularly well adapted to AFM thermomechanical studies as (i) it is extremely robust on repeated thermal cycling in air, (ii) its spin transition temperature (ca. 335 K) is easily accessible for most AFM instruments and (iii) its elastic moduli have been determined in both spin states using different characterization methods (see Table 5.1) [173]. As for the AFM methodology, we decided to focus on the AMFM mode implemented in the Cypher-ES (Oxford Instruments), due to the advantage of having the heater/cooler stage incorporated in the body of the AFM microscope as well as due to the high speed and good quantitative performance of the AMFM technique (see section 5.3).

5.4.1 AMFM scans at constant heating/cooling rates

At the beginning of our work, we wanted to control the performance of the AFM heater/cooler stage and verify possible issues, which may arise due to the heat exchange between the sample and the AFM probe. Indeed, Hernandez et al. [127] has shown that the presence of a cold AFM probe above a hot sample stage in ambient air can lead to a local

temperature decrease of as much as 20 K – primarily due to heat exchange by convection. To investigate these issues first we used a single crystal of the compound $[Fe(HB(tz)_3)_2]$ synthesized in its solvent-free form as described by Rat et al. [114]. These crystals exhibit an extremely abrupt first-order spin transition centered around 333 K, associated with a narrow (1 K wide) thermal hysteresis loop. The crystal was placed on the top of the AFM stainless steel disk sample holder and we performed a heating-cooling cycle between 330 – 340 K at a rate of 0.6 K/min – *without* the AFM probe. During the thermal cycle, optical reflectivity images were recorded at 0.100 Hz capture rate using the CMOS camera integrated in the Cypher AFM. From the color change of the crystal (see Figure A5.4.1 in Annexes) we identified the spin transition temperatures $T_{1/2\uparrow}$ = 333.7 K and $T_{1/2\downarrow}$ = 332.7 K upon heating and cooling, respectively. The values obtained are in close agreement with those reported by Ridier et al. [292] using a Linkam Scientific heating/cooling stage and optical microscopy (between 332 and 335 K – varying slightly from crystal to crystal) - confirming thus the excellent temperature accuracy of the heating-cooling stage of our AFM.

In the next step, we performed tests on a nanocrystalline $[Fe(HB(tz)_3)_2]$ film of 100 nm thickness, which was grown on a quartz substrate using the conditions described in Chapter 2. The aim of these experiments was to detect the spin transition *in-situ* while acquiring AFM data. (In other words, contrary to the previous experiment on the crystals, here the AFM probe was mounted in the probe holder and engaged on the surface of the sample upon heating and cooling.) First, an AMFM scan was carried out at a constant temperature (331 K) in the LS state just below the spin transition temperature using an OMCLAC160TS-R3 (Olympus) probe. Then, in order to detect the spin transition in the film we carried out a second AMFM scan at a scan rate of 1.2 Hz while heating the sample from 331 K to 341 K at a constant rate of 3 K/min. The scan size was 2 μm × 2 μm with 256 × 256 lines. Therefore, every 0.25 μm in the image (i.e. 32 lines) corresponds to a temperature interval of 1 K. After the end of the heating, another image was acquired at a constant temperature (341 K) in the HS state to stabilize the system. Finally, an AMFM scan was also recorded in the cooling mode between 341 K and 331 K. Figure 5.12 shows selected AFM images (topography, phase of the AM mode, Young's modulus and dissipation channels) recorded in the heating and cooling modes. One can observe that around a specific temperature, the AFM images become extremely noisy and the probe is not able to track the surface during approx. 5-10 sec. However, when this 'critical' temperature region is passed the AFM imaging of the surface continues as before. We can obviously attribute this phenomenon to the spin transition in the film. As discussed in chapter 1, the first-order spin transition in $[Fe(HB(tz)_3)_2]$ crystals is accompanied with a discontinuous increase of

the unit cell volume. We believe that this spontaneous strain at the SCO leads to a loss of the AFM tracking – as if one would 'shake' the sample during the AFM scan. Once the compound is in the new phase, the image becomes again stable.

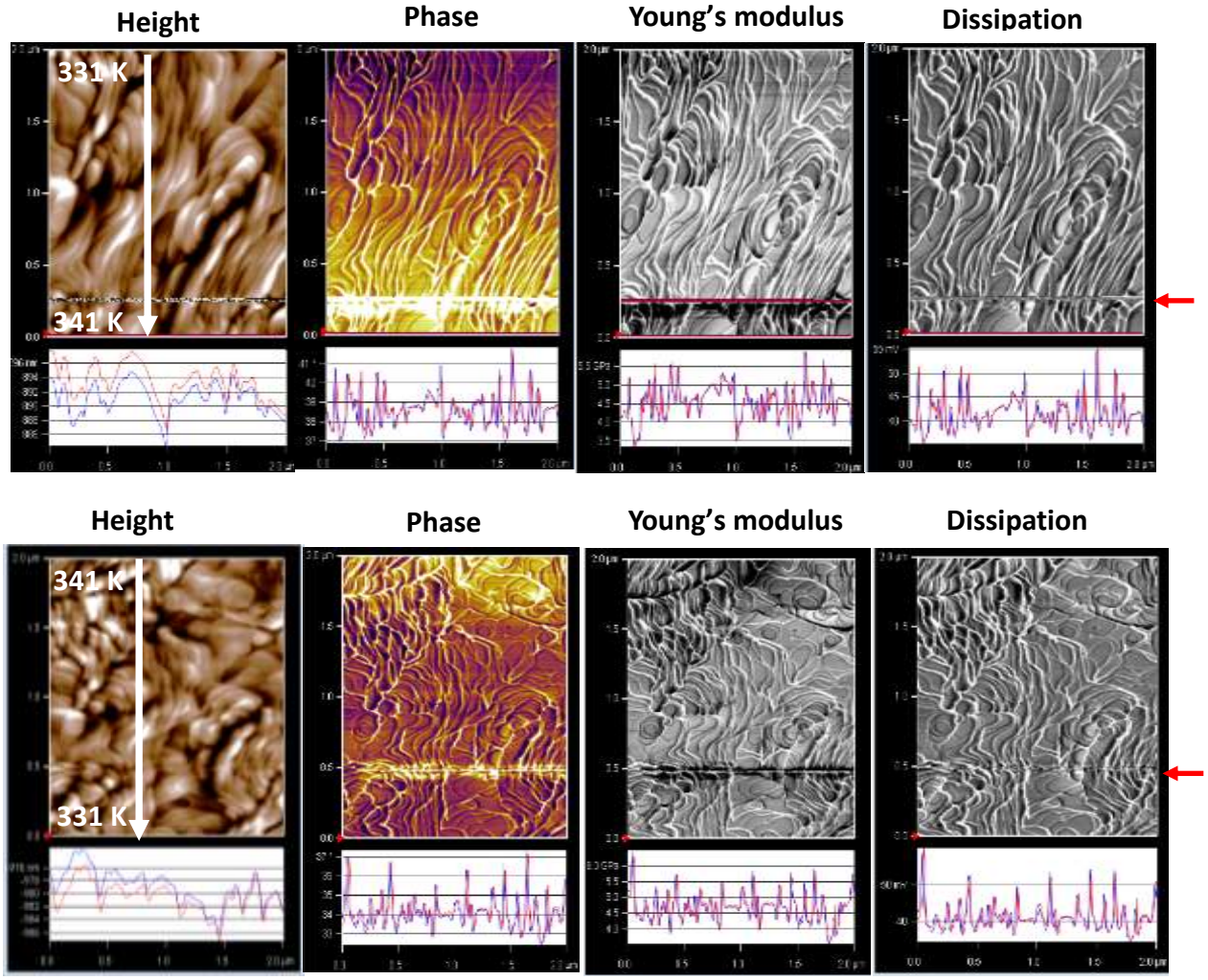

Figure 5.12: Height, phase, Young's modulus and dissipation images of a 100 nm thick $[Fe(HB(tz)_3)_2]$ film obtained in AMFM mode upon heating (upper panel) and cooling (lower panel) the sample between 331 K to 341 K at a rate of 3 K/min. The white arrows indicate the scan direction with the corresponding temperatures. Red arrows point to the scan lines where the surface tracking was temporarily lost.

The spin transition is particularly clear when plotting the different AMFM observables as a function of the temperature. For example, Figure 5.13 shows the temperature dependence of the effective Young's modulus, the phase of the AM signal and the dissipation. Sharp peaks are observed around $T_{1/2\uparrow}$ = 340.2 K and $T_{1/2\downarrow}$ = 333.8 K upon heating and cooling, respectively. Obviously, these peaks have no physical meaning, but they allow us to detect accurately the occurrence of the spin transition. For comparison, Figure 5.13d shows the derivative of the spin transition curve of the same sample obtained from variable temperature UV absorbance

measurements. Several interesting observations can be made at this point by comparing the local AFM measurement with the ensemble averaging UV data. First, the equilibrium temperature, which can be defined roughly as the barycenter of the hysteresis, is nearly the same in the two experiments (ca. 336-337 K). This confirms that the local temperature of the sample during the AFM scan is not much different from the temperature of the heating-cooling stage. We attribute this good performance to the compact design of the environmental chamber of the Cypher-ES, which allow us efficiently thermalize not only the sample, but also the probe and the surrounding atmosphere.

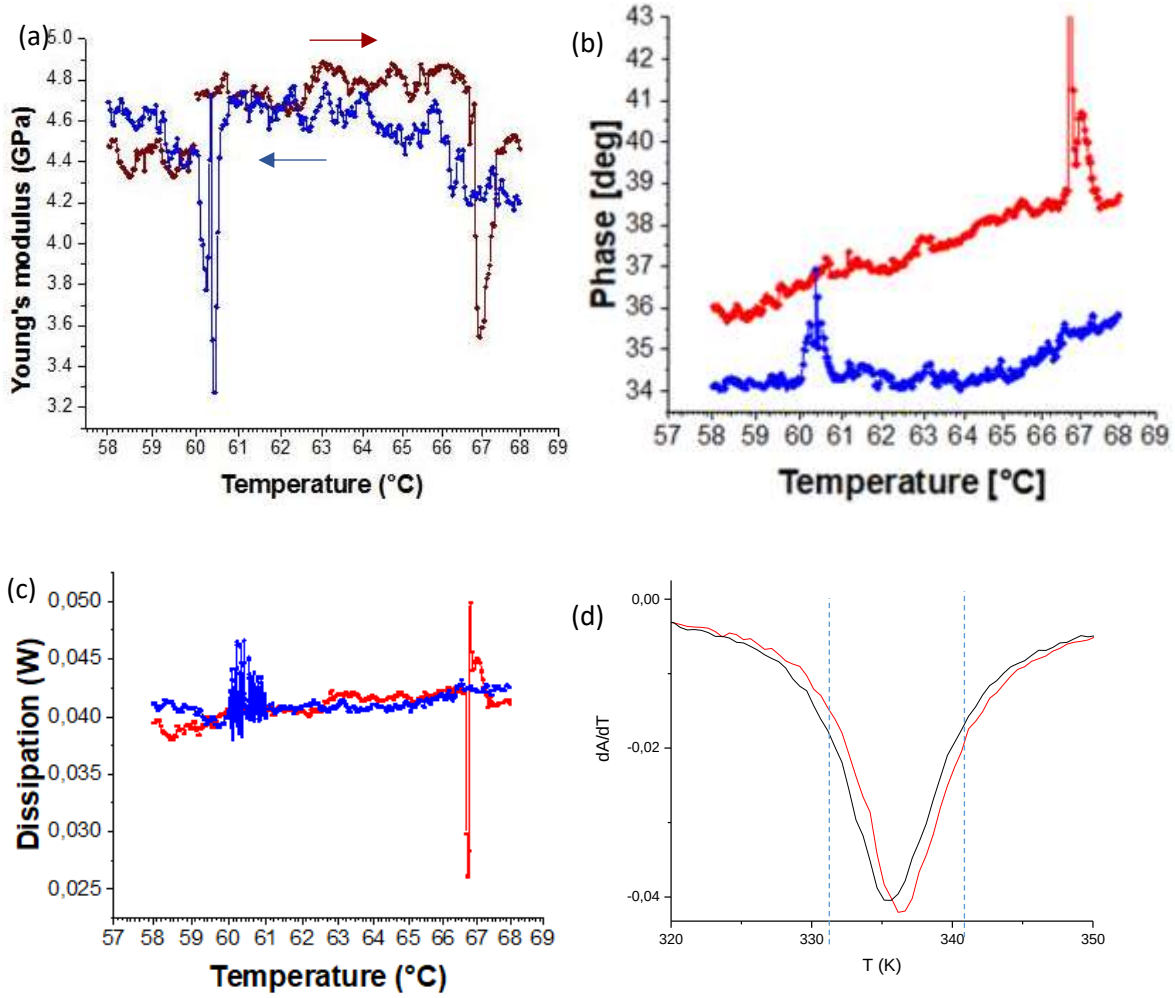

Figure 5.13: (a) Young's modulus, (b) phase and (c) dissipation data for a 100 nm thick $[Fe(HB(tz)_3)_2]$ film as a function of temperature upon heating (red color) and cooling (blue color). These data were extracted from the AFM images shown in Figure 5.12. (d) Derivative of the spin transition curve of the film obtained from UV absorbance measurements. The dashed lines indicate the temperature limits of the AFM scan.

That said, there are also obvious differences between the AFM and UV absorbance data. Notably, the hysteresis width is much larger in the case of the AFM results (ca. 6-7 K vs. 0.5-1

K). We believe that this large hysteresis is just apparent and actually does not correspond to the quasi-static hysteresis loop. In other words, most likely it just indicates the limits of the sample thermalization in our AFM experiment. In fact, due to the presence of the AFM probe, upon cooling (heating) the local temperature below the probe decreases (increases) slower than the mean temperature of the stage and this leads to an apparent broadening of the hysteresis width.

Another interesting observation is that the spin transition spans over a much smaller temperature range in the AFM experiment ($\Delta T \approx 0.5$ - 1 K) when compared to the UV absorbance measurement ($\Delta T \approx$ 15-20 K). We can interpret this result by considering that in the AFM we detect the SCO only in a few hundreds of nanocrystals and, more importantly, only during the nucleation and growth period. On the contrary, in the UV-absorbance measurement, we average the properties of hundreds of millions of nanocrystals and we probe any spin state change likewise whether it occurs by nucleation and growth or not. These AFM results tell us therefore that the spin transition in the nanocrystals occurs in a very abrupt manner, similar to the bulk single crystals. In addition, they indicate that the relatively broad span of the spin transition curves of the films cannot be accounted solely for ensemble averaging effects, but also for a combination of different spin transition mechanisms (abrupt and gradual).

Overall, these *in-situ* AFM measurements revealed to be very useful in determining the temperature(s) at which the spin transition occurs during the AFM imaging and brought into light a few interesting aspects of the SCO at the nanoscale. On the other hand, it should be noted that the mean values of the Young's modulus in the two spin states (within the hysteresis region) are very similar, ca. 4.5 – 4.6 GPa (Figure 5.13). These values are significantly smaller than the Young's modulus of $[Fe(HB(tz)_3)_2]$ obtained by other methods (see Table 5.1). Our AFM measurement fails thus to give an accurate value for the Young's modulus and it does not allow us to detect the softening of the film in the HS phase. We attribute these discrepancies to the low quantitative accuracy of the *in-situ* measurements. A further plausible issue is the presence of humidity adsorbed on the sample surface, which may hamper the accurate assessment of the elastic moduli.

5.4.2 Isothermal AMFM scans

To progress towards our initial aim we have decided to carry out a series of AMFM measurements at fixed temperatures. First, we performed topography analysis at different temperatures in order to verify if any reversible and/or irreversible changes occur in the surface topography between the HS and LS states as it was reported for some other SCO materials (see

section 1.2.2). AFM images sizes of 10 µm × 10 µm and 2 µm × 2 µm were recorded with 256 × 256 lines resolution between 293 K and 373 K. Figure 5.14 shows representative topography images acquired over a heating – cooling cycle.

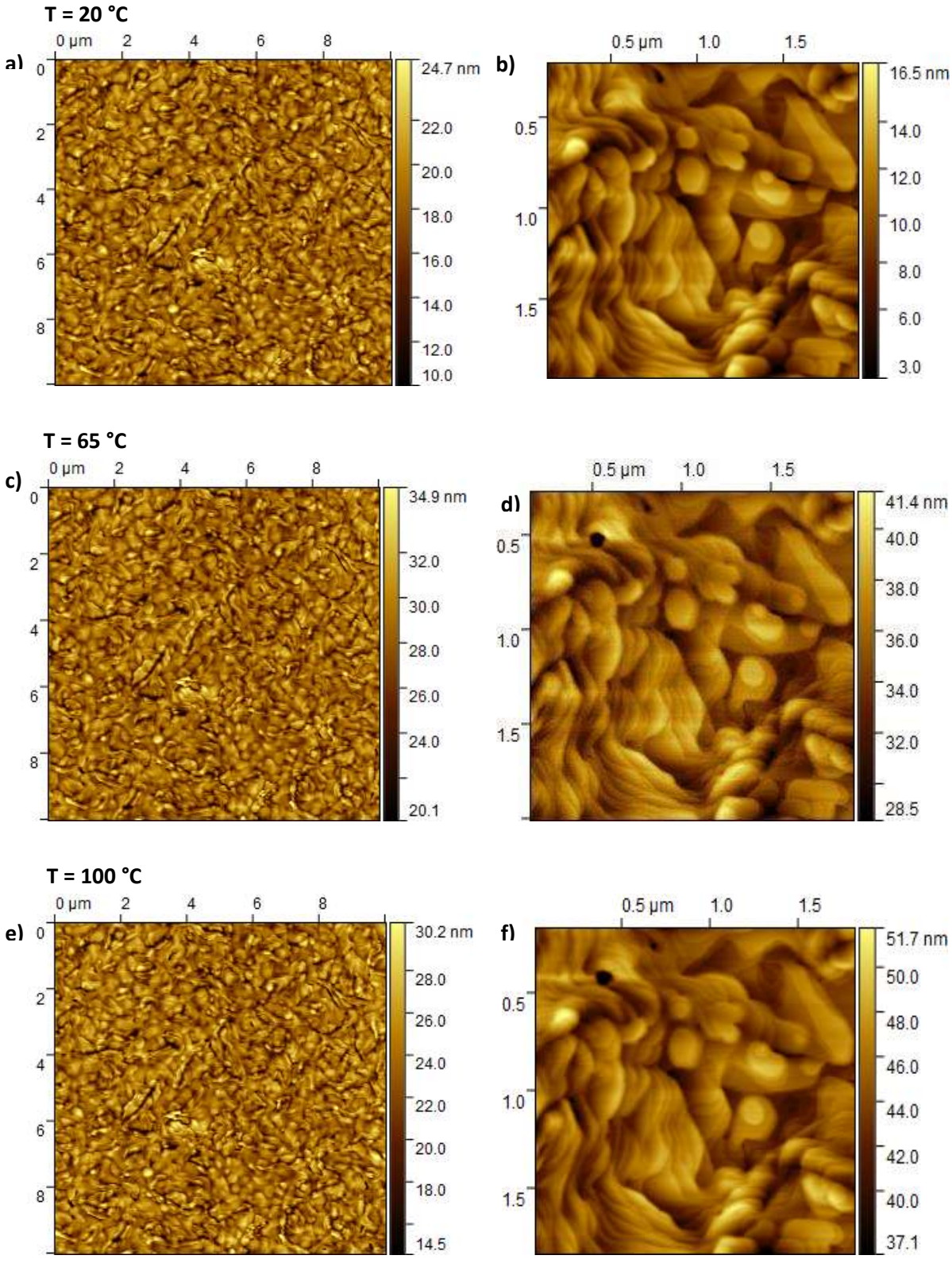

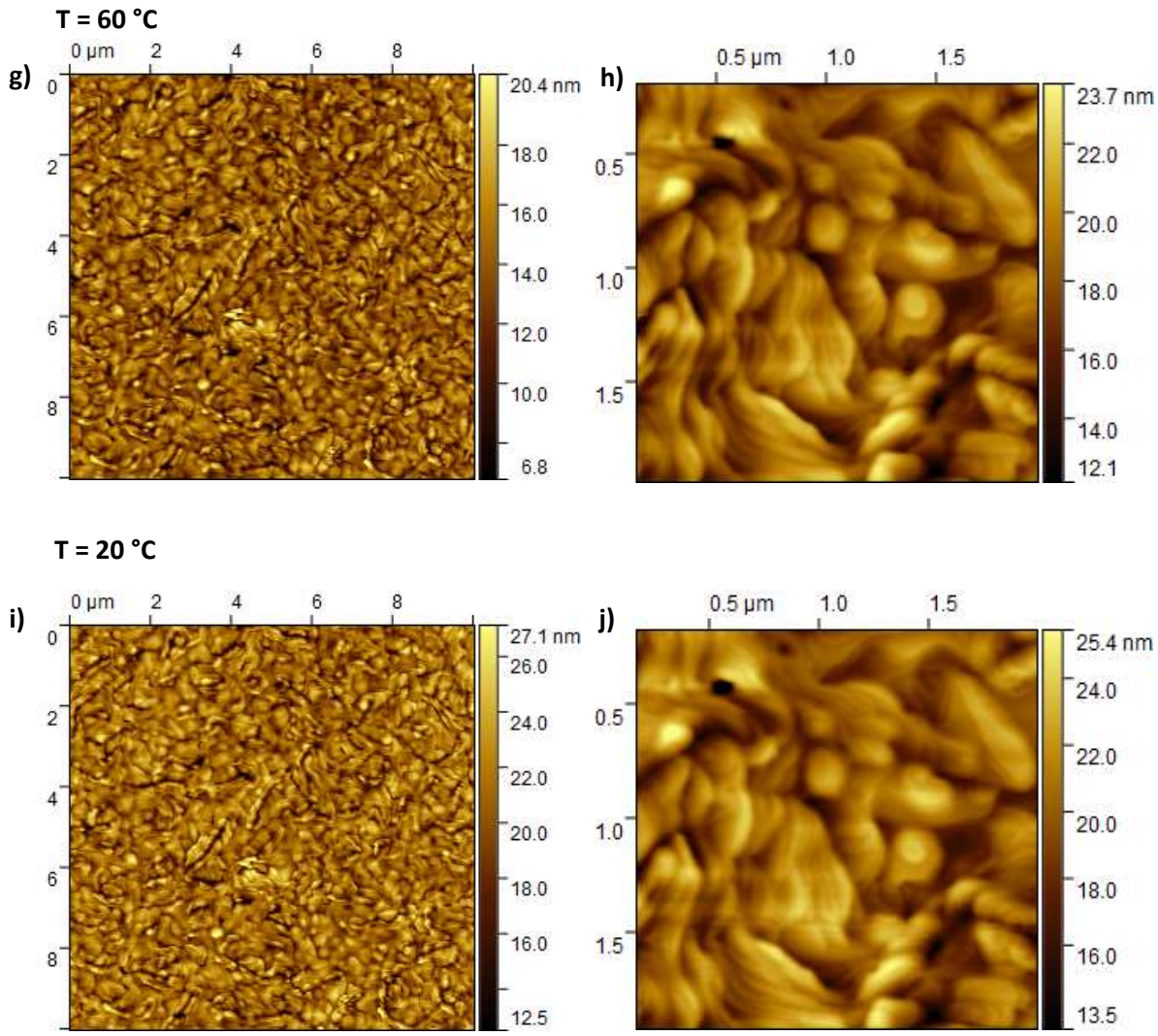

Figure 5.14: AFM topography images of a 100 nm thick film of $[Fe(HB(tz)_3)_2]$ acquired at different temperatures over a heating - cooling cycle.

Thanks to the closed loop operation of the AFM, the images recorded at different temperatures correspond closely to the same area. Remarkably, the images in the HS and LS states as well as at the beginning and at the end of the thermal cycle are virtually indistinguishable. In other words, the thermal spin transition in the films of $[Fe(HB(tz)_3)_2]$ does not lead to important changes of the surface topography. This finding constitutes probably a part of the explanation for the outstanding reproducibility of the spin transition in these films (cf. section 3.1). Yet, upon a close inspection, we noticed a few minor differences in topography between the start and the end of the experiment (e.g. the disappearance or modification of small 'terraces'). This slight variation is also reflected by Figure 5.15a-b, which displays the mean arithmetic surface roughness R_a as a function of the temperature for two successive heating – cooling cycles. Indeed a slight, but systematic increase of Ra is detected in these experiments, but the variation

remains close to the experimental uncertainty and therefore further experiments have not been conducted.

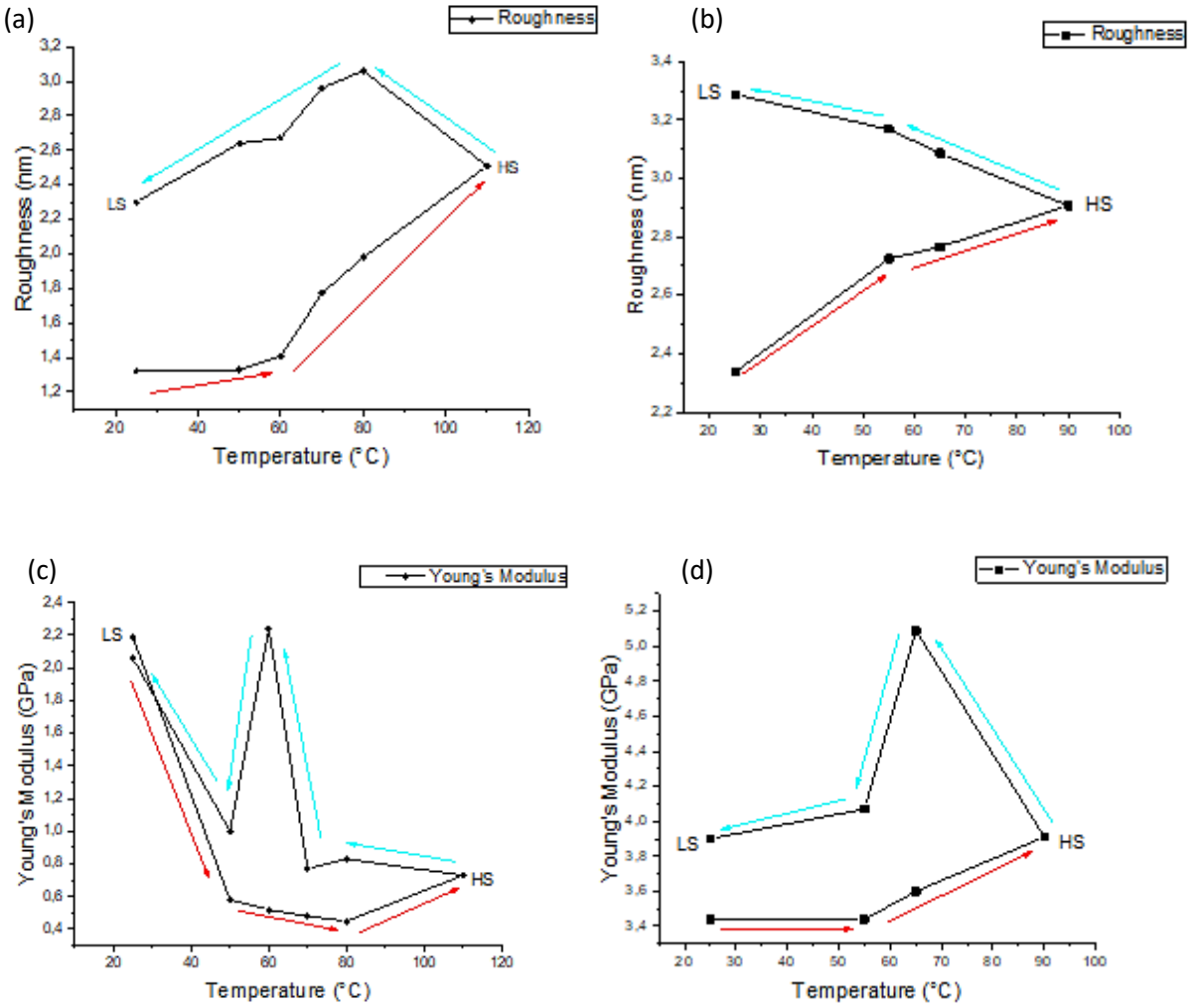

Figure 5.15: Temperature dependence of the surface roughness (a-b) and the Young's modulus (c-d) of a 100 nm thick film of $[Fe(HB(tz)_3)_2]$ obtained from AMFM measurements upon two successive heating – cooling cycles.

While the surface topography appeared very stable and reproducible, the Young's modulus values extracted from these experiments display a rather erratic behaviour, with variations between 0.5 and 5 GPa – irrespective of the spin state of the film (Figure 5.15c-d). Despite several trials, we could not obtain more 'reasonable' mechanical data in these experimental conditions. We have therefore decided to implement a new experimental strategy wherein we scan together with the $[Fe(HB(tz)_3)_2]$ film a 'reference' sample with known thermomechanical properties. As for the reference sample, we have chosen the epoxy-based photoresist SU-8, which is well known for its good thermal, mechanical and chemical stability. Its final properties depend, however, on the processing conditions [293]. Following standard processing, the elastic

modulus of SU-8 is typically around 3.5 GPa, which decreases monotonously to a value of ca. 2.5 GPa when rising the temperature to 100 °C [294]. As shown in Figure 5.16, this temperature dependence slightly diminishes at increasing frequencies.

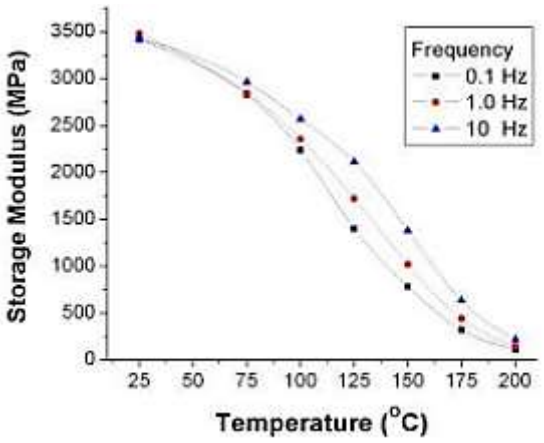

Figure 5.16: Temperature dependence of the elastic modulus of SU-8 at different frequencies [294].

In our experiments, we have carried out variable temperature measurements using the SU-8 as a calibration sample. A film of SU-8 (ca. 800 nm thickness) was spin-coated on the silicon substrate, but only a half of the substrate was coated by SU-8 while a blue polyester cleanroom tape covered the other half. The interest of this tape is that it removes without residue. After the UV crosslinking and post-baking of SU-8, the blue scotch was removed and we now masked the SU-8 coated part of the substrate. In the final step, a thin film of ca. 100 nm thickness of $[Fe(HB(tz)_3)_2]$ was deposited by thermal evaporation followed by standard recrystallization in humid air. This way we obtained a substrate half of which was covered by SU-8 and the other half with the SCO sample. AFM measurements were then carried out such a way that each scan comprises part of both materials.

AFM analysis of the films was performed between 303 K and 373 K using a Cypher-ES AFM (Oxford Instruments) and reflective Al-coated Si probes (HQ:NSC15/Al BS, MikroMasch). These probes are characterized by a nominal resonance frequency of 325 kHz, a spring constant of 40 N/m and a tip radius of 8 nm. AFM images (typically 14 μm × 3.5 μm, 512 pixels × 128 pixels) were recorded at a scan rate of 1.95 Hz in AMFM mode. The initial tip radius was determined using the Hertz model implemented in the software and a polystyrene calibration sample (Bruker PSFILM). The average Young's modulus of the SU-8 calibration sample at room temperature is E = 3.8 GPa which is in good agreement with the value reported in the literature [294]. As an important new feature of this experiment, at the beginning we purged the AFM chamber with dry nitrogen gas while heating the sample to 100 °C in order to remove moisture and dehydrate the sample surface as much as possible. Another important

novelty of our analysis is that the SU-8 and the SCO films were scanned together in each image, and the tip radius was adjusted *in-situ* at the beginning of each scan until we obtained the expected value of the Young's modulus of SU-8 at a given temperature (taken from Figure 5.16). Figure 5.17 shows the Young's modulus maps of the two films at selected temperatures.

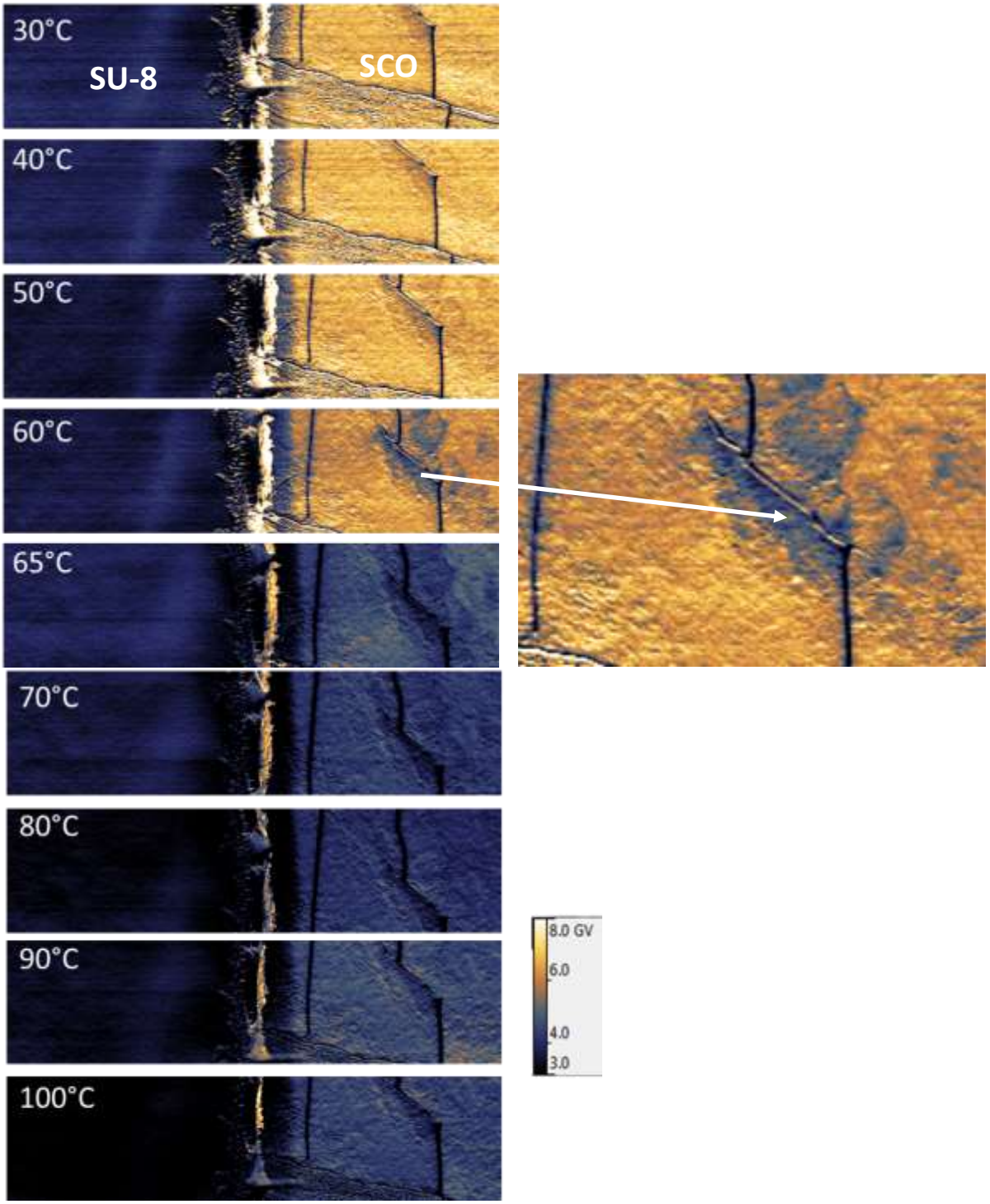

Figure 5.17: Young's modulus maps (in GPa) of the SU-8 and $[Fe(HB(tz)_3)_2]$ films at selected temperatures. The image size is 14 µm × 3.5 µm. The zoom at 60 °C shows the co-existence of the LS (gold color) and HS (blue color) states.

The most important finding here is that for temperatures above ca. 330 K a very substantial decrease of the Young's modulus occurs in the SCO film, reflected by a sudden change of contrast between the SCO film and the reference sample. Figure 5.18 shows the average value of the Young's modulus extracted from the AFM images shown in Figure 5.17. The raw data has been further treated by assuming a linear variation of the Young's modulus of SU-8 from 3.5 GPa (at 303 K) to 2.7 GPa (at 373 K) as depicted in Figure 5.16 [294]. Below and above 333 K, the mean Young's modulus value corresponds to the pure LS and HS states and has values of ca. 6 GPa and 4 GPa, respectively. This pronounced drop of the Young's modulus when going from the LS to the HS state is in good agreement with previous results obtained for $[Fe(HB(tz)_3)_2]$ using nuclear inelastic scattering (E_{LS} = 11 GPa, E_{HS} = 7 GPa) and MEMS micromechanical measurements (E_{LS} = 12 GPa, E_{HS} = 10 GPa, see Table 5.1). On the other hand, the absolute values are systematically smaller in our AFM measurements. Of course, measurement uncertainties are important for each method (at least ~GPa). In addition, due to the specific orientation of our films we actually measure by AFM the Young's modulus corresponding the c-axis of the orthorhombic structure, while the other methods average the stiffness along the different crystallographic axes (with different weighs), and provide therefore an 'effective value'. Nevertheless, we believe that the reduced Young's modulus values seen by AFM reflect also some physical phenomena specific to the surface of the samples. Notably, despite the dehydration of the films we expect the presence of different adsorbates on the surface (e.g. water molecules). In addition, the topmost molecular layers - which are actually indented – are probably disordered. All these factors contribute likely to a decrease of the Young's modulus observed by AFM.

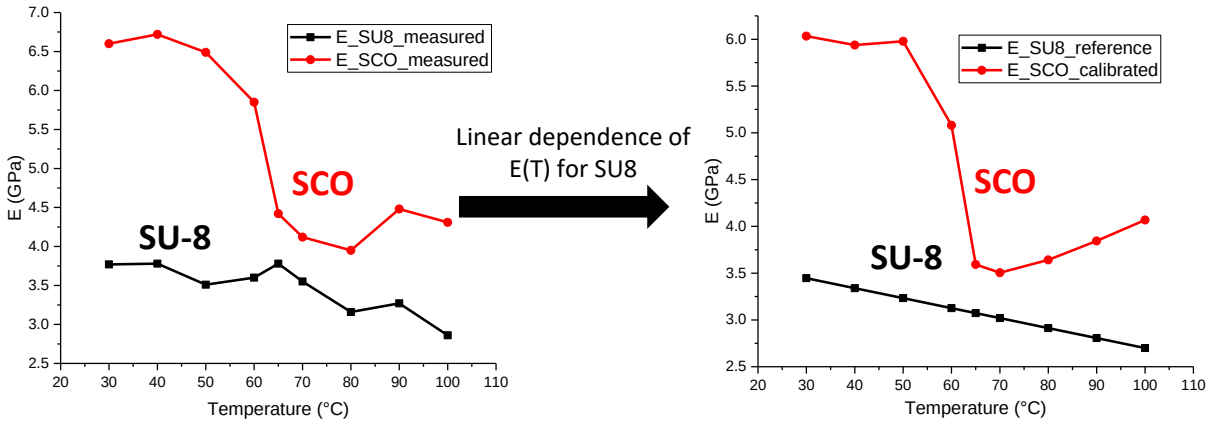

Figure 5.18: Temperature dependence of the average Young's modulus of $[Fe(HB(tz)_3)_2]$ obtained from the AMFM images shown in Figure 5.17. Data were further treated by assuming a linear variation of the Young's modulus of SU-8 from 3.5 GPa (at 303 K) to 2.7 GPa (at 373 K) as depicted in Figure 5.16.

We have also tried to extract information about the dissipation behavior of our film. To this aim we extracted the average loss tangent values both for the SU-8 and the [Fe(HB(tz)$_3$)$_2$] films. As shown in Figure 5.19 the raw loss tangent data shows a (nearly) monotonous increase for both compounds, which corresponds to classical thermoelastic damping observed for most materials at increasing temperatures. Figure 5.19 depicts also the temperature dependence of the loss tangent *difference* between the SCO and SU-8 films. Remarkably, a loss peak is observed in this plot near the spin transition temperature (ca. 338 K). As it was discussed by Pérez-Saez et al. [295], first order phase transitions in a variety of materials (ferroelectric, ferroelastic, …) are accompanied by internal friction peaks, which arise from different mechanisms. It is thought that the most important contribution comes from the viscous displacements of phase boundaries (domain walls) during the phase transition. As such, the loss peak observed in Figure 5.19 for our [Fe(HB(tz)$_3$)$_2$] film is an indication of the formation and movement of phase boundaries in our film. Indeed, a closer inspection of the Young's modulus map recorded in the course of the spin transition at 333 K (see zoom in Figure 5.17) reveals that nucleation of the HS phase occurs primarily around cracks in the film and then the growth of these germs leads to phase separation at a size scale, which is significantly larger (μm scale) than the size of the nanocrystals (ca. 50 nm). This unprecedented observation indicates that the nanocrystals are strongly 'glued' together at the grain boundaries allowing for an efficient transmission of the mechanical strain induced by the spin transition.

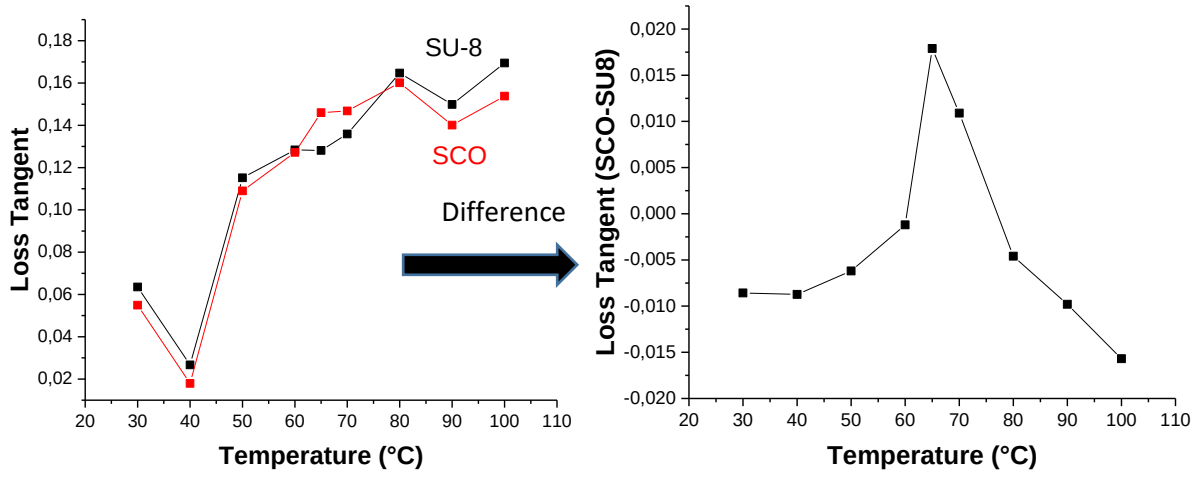

Figure 5.19: Temperature dependence of the average loss tangent of [Fe(HB(tz)$_3$)$_2$] and SU-8, as well as their difference, obtained from the AMFM images shown in Figure 5.17.

An interesting comparison can be made here with the MEMS micromechanical analysis of [Fe(HB(tz)$_3$)$_2$] films reported by Manrique et al. [176]. Figure 5.20 shows the temperature

dependence of the MEMS resonance frequency and Q-factor upon heating and cooling. The dynamical mechanical behavior of the MEMS cantilever is shown before as well as after the deposition of the [Fe(HB(tz)$_3$)$_2$] film (ca. 140 nm thickness) on top of the micromechanical device. Similar to our AFM experiments a reversible drop of the resonance frequency was detected around the spin transition temperature when going from the LS to the HS state, which can be traced back in both experiments to the decrease of the Young's modulus of the film. On the other hand, a damping peak in the Q factor around the phase transition has been also observed and can be readily correlated with the loss tangent behavior in the AFM experiments.

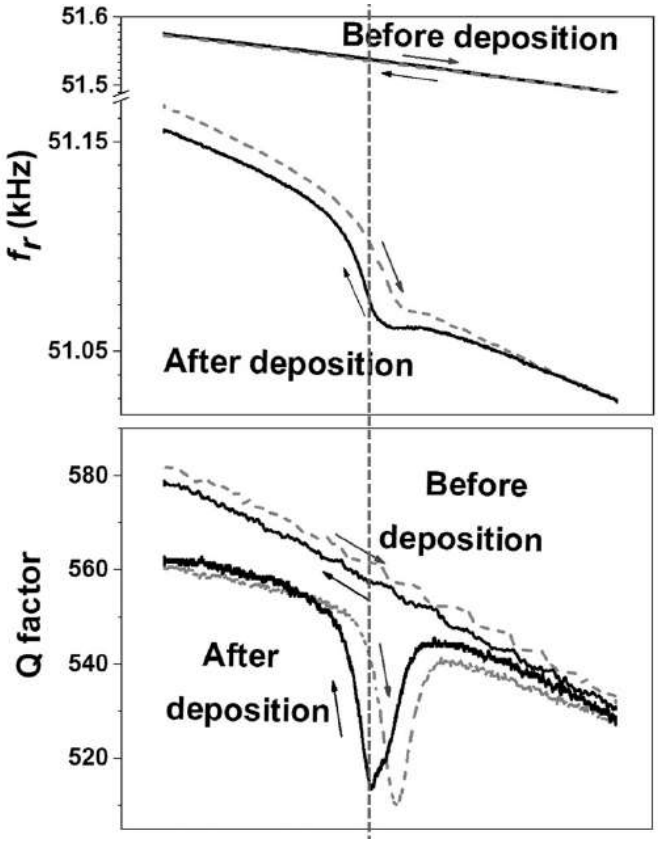

Figure 5.20: Temperature dependence of the resonance frequency and quality factor of a MEMS microcantilever before and after its coating with a 140 nm thick layer of [Fe(HB(tz)$_3$)$_2$] [176]. The spin transition temperature is depicted by the vertical dashed line.

5.5 Conclusions

We have explored the use of atomic force microscopy for the high spatial resolution investigation of the spin transition phenomenon in thin, nanocrystalline films of [Fe(HB(tz)$_3$)$_2$]. Based on previous works in the team, we have focused on quantitative nanomechanical investigations using the AFM. We have shown that the different measurement methods and

instruments provided by AFM manufacturers give similar results in terms of elastic modulus values and measurement precision/repeatability. For its high speed imaging capability, we have used in most of our work the bimodal AMFM technique implemented in the Cypher-ES (Oxford Instruments). Using this method, we have been able to detect *in-situ* the spin transition in the films of $[Fe(HB(tz)_3)_2]$ and, using an original method for tracking and correcting the tip radius changes, we were able to evidence also a substantial decrease of the Young's modulus (by ca. 50 %) when going from the LS to the HS phase. On the other hand, we observed no significant topography change due to the spin transition. Our nanomechanical measurements correlate well with previous micromechanical MEMS measurements and allow, in addition, the nanoscale imaging of the SCO. Indeed, from these AFM data, several important findings about the mechanism of the spin transition in the films could be inferred. Notably, we observed nucleation and growth phenomena at size scales much larger than the crystallite size, indicating an efficient mechanical coupling through the grain boundaries. In addition, we evidenced a considerable difference in the abruptness of the spin transition detected by AFM in comparison with ensemble averaging methods. We suggested that this is an indication of the co-existence of gradual spin conversion and nucleation-growth mechanisms in the films. Further work will be necessary to clarify different aspects of the variable temperature AMFM measurements. In particular, it will be necessary to assess carefully the temperature dependence of mechanical properties of SU-8 in our hands. Nevertheless, these results open up an interesting scope for the nanoscale investigation of mechanical couplings in SCO materials, with particular relevance for SCO – polymer composite actuator materials.

General conclusions and perspectives

Nanoscale spin-crossover materials capable of undergoing reversible switching between two electronic configurations with markedly different physical properties are excellent candidates for various technological applications. In particular, they can serve as active materials for storing and processing information in photonic, mechanical, electronic and spintronic devices as well as for transducing different forms of energy in sensors and actuators.

Despite the considerable progress, which has been achieved in the past decade in the synthesis, characterization and theoretical modelling of spin crossover nanomaterials, there remains several crucial steps to be accomplished before one can turn towards real technological applications. In particular, it will be necessary to produce robust nanoscale materials, which display spin crossover at technologically relevant temperatures and with the desired functionalities (hysteresis or gradual transition, colored or transparent, conducting or insulator, …). An important effort is therefore still needed for the development of methods for the growth of high quality spin crossover nano-objects. These new nanomaterials call also for novel characterization methods, in addition to those traditionally used in the spin crossover field (magnetometry, X-ray diffraction, calorimetry, Mössbauer, electronic and vibrational spectroscopies, …). In particular, there is still a need for high spatial resolution microscopy tools as well as for high sensitivity methods able to detect molecular spin-state changes in very small amounts of matter, ideally in a single, isolated nano-object. Beyond their high resolution and/or high sensitivity, these new experimental approaches can provide also information on material properties, which are either difficult to access by "traditional" methods or not so relevant at other size ranges. For the same reason, new theoretical approaches have been developed focusing on the increasingly dominant role of surfaces/interfaces in determining the properties of these reduced sized objects. Yet, the confrontation of these models with experiments as well as the use of high resolution, sensitive experimental methods are seriously hampered by the lack of high quality, robust spin crossover nano-objects.

This thesis work has allowed for some advances in these different directions. First of all, we succeeded in growing unprecedented high quality, robust, reproducible thin films of the $[Fe(HB(tz)_3)_2]$ complex, which display spin transition just above room temperature. This spin transition turned out to be stable in ambient air on a year scale (at least), on thermal stress (up to ca. 260 °C) and on repeated switching between the two spin states (more than 1 million cycles). One key reason behind these amazing properties is the intrinsic stability of this compound in crystalline state. The understanding of this structural stability and resilience will

be clearly one important future perspectives of this thesis work. Another reason for the stability of the films is that we could establish, by a detailed and rigorous analysis of the film growth process, a fabrication protocol producing very reproducible, smooth, fully crystalline and oriented deposits. To this aim, we used - for the first time in the spin crossover field - vacuum thermal evaporation combined with solvent vapor annealing. We have shown that different solvents with hydrogen bonding ability can afford for the recrystallization of the initially amorphous films. Among these solvents, water turned out to be the most efficient and we used therefor humidity treatment in the rest of our work.

Indeed, thanks to the high quality of the humidity treated films we were able to provide key experimental data for assessing the validity of the nanothermodynamical model of spin crossover nanomaterials. In particular, we could evidence a clear upshift of the spin transition temperature when reducing the film thickness, which we correlated with the increase of the surface energy in the high spin state. This, somewhat unexpected result, was then rationalized taking into account the strong anisotropy of the spin transition in this sample.

We have also embarked in the investigation of our films using different scanning probe microscopy approaches. In a first time we prepared luminescent bilayers films, combining the well-known luminophore $Ir(PPy)_3$ with $[Fe(HB(tz)_3)_2]$, with the aim of providing a strong optical contrast between the high spin and the low spin states, which could be exploited by near-field optical scanning microscopy. Up to now, we were not able to exploit these bilayer in NSOM experiments (this remains therefore an important perspective), but we could demonstrate an effective and well-predictable luminescence switching of $Ir(PPy)_3$ by more than one order of magnitude due to the spin transition in $[Fe(HB(tz)_3)_2]$. A further step will consist in the nanopatterning of the films by means of e-beam lithography and lift-off – taking advantage of their very low solubility of most common solvents. In another approach, following a fastidious optimization process, we have successfully exploited the atomic force microscope to achieve high spatial resolution imaging of the spin transition through quantitative nano-mechanical measurements. In particular, the double-frequency, combined amplitude-modulation and frequency-modulation (AMFM) imaging method turned out to be very sensitive to the stiffness change, which accompanies the spin transition. From the shift of the second mode frequency we could clearly infer the spin transition and we were even able to extract the associated change of the Young's modulus. On the other hand, contrary to other AFM observations on spin crossover films, we observed no discernible change of the surface topography between the high spin and low spin forms. It may be worth to mention that we have also embarked in the investigation of electrical properties of our films using conductive AFM,

but the very high resistivity of the films makes these measurements difficult. Further work in this direction may be possible using a few monolayer thickness films.

A very important perspective of our research is the development of proof of concept devices using the appealing properties of our [$Fe(HB(tz)_3)_2$] films. Actually, during this thesis work colleagues from the LAAS-CNRS and LCC-CNRS have already explored the possibility of integrating these films into crossbar type electronic junctions as well as into microelectromechanical systems (MEMS). The first results along these directions turned out to be extremely promising, revealing both resistance switching and actuating properties at the device level, and encourage us to continue working on these prototypes. In addition, we have also started to work towards the integration of these spin crossover films into photonic waveguides in collaboration between the LAAS and the LCC. The aim here is to exploit the spectacular change of the refractive index, which accompanies the spin transition. Of particular interest would be spatial light modulator and photonic integrated circuit applications requiring low loss and transparency in the visible spectral range and/or high speed of index switching.

Bibliography

[1] A. Bousseksou, G. Molnar, L. Salmon, W. Nicolazzi, *Chem. Soc. Rev.*, 40 (2011) 3313-3335.
[2] K. Senthil Kumar, M. Ruben, Coordination Chemistry Reviews, 346 (2017) 176-205.
[3] G. Molnár, S. Rat, L. Salmon, W. Nicolazzi, A. Bousseksou, Adv. Mater, 30 (2018) 17003862.
[4] L. Cambi, A. Gagnasso, Atti. Accad. Naz. Lincei, 13 (1931) 809–813
[5] L. Cambi, L. Malatesta, Berichte der deutschen chemischen Gesellschaft (A and B Series), 70 (1937) 2067-2078.
[6] J.S. Griffith, Proceedings of the Royal Society of London. Series A. Mathematical and Physical Sciences, 235 (1956) 23-36.
[7] J. W.A. Baker, H.M. Bobonich, Inorganic Chemistry, 3 (1964) 1184-1188.
[8] A.H. Ewald, I.G. Ross, A.H. White, R.L. Martin, Proceedings of the Royal Society of London Series a-Mathematical and Physical Sciences, 280 (1964) 235-257.
[9] P. Gütlich, H.A. Goodwin, Topics in Current Chemistry. Spin Crossover in Transition Metal Compounds, Springer-Verlag, Berlin, 2004.
[10] H.A. Bethe, Annals of Physics, 3 (1929) 133-206.
[11] A. Hauser, Ligand field theoretical considerations, in: Spin Crossover in Transition Metal Compounds I, 2004, pp. 49-58.
[12] Y. Tanabe, S. Sugano, Journal of the Physical Society of Japan, 9 (1954) 753-766.
[13] Y. Tanabe, S. Sugano, Journal of the Physical Society of Japan, 9 (1954) 766-779.
[14] P. Gutlich, Structure and Bonding, 44 (1981) 83-195.
[15] L.F. Lindoy, S.E. Livingstone, Coordination Chemistry Reviews, 2 (1967) 173-193.
[16] S.K. Kulshreshtha, R.M. Iyer, Chemical Physics Letters, 108 (1984) 501-504.
[17] S.K. Kulshreshtha, R.M. Iyer, E. Konig, G. Ritter, Chemical Physics Letters, 110 (1984) 201-204.
[18] M. Sorai, S. Seki, J. Phys. Chem. Solids, 35 (1974) 555-570.
[19] A. Bousseksou, J.J. McGarvey, F. Varret, J.A. Real, J.P. Tuchagues, A.C. Dennis, M.L. Boillot, Chemical Physics Letters, 318 (2000) 409-416.
[20] P. Gütlich, A.B. Gaspar, Y. Garcia, *Beilstein J. Org. Chem.*, 9 (2013) 342-391.
[21] T. Mahfoud, G. Molnar, S. Bonhommeau, S. Cobo, L. Salmon, P. Demont, H. Tokoro, S.I. Ohkoshi, K. Boukheddaden, A. Bousseksou, *Journal of the American Chemical Society*, 131 (2009) 15049-15054.
[22] E. König, K. Madeja, Inorg. Chem., 6 (1967) 48-55.
[23] S. Ohnishi, S. Sugano, Journal of Physics C: Solid State Physics, 14 (1981) 39.
[24] H. Spiering, E. Meissner, H. Koppen, E.W. Muller, P. Gutlich, Chemical Physics, 68 (1982) 65-71.
[25] E. Konig, G. Ritter, Solid State Communications, 18 (1976) 279-282.
[26] V.V. Zelentsov, Sov. Sci. Rev B. Chem, 81 (1981) 543.
[27] J.A. Real, H. Bolvin, A. Bousseksou, A. Dworkin, O. Kahn, F. Varret, J. Zarembowitch, Journal of the American Chemical Society, 114 (1992) 4650-4658.
[28] A. Bousseksou, J. Nasser, J. Linares, K. Boukheddaden, F. Varret, *J. Phys. I*, 2 (1992) 1381-1403.
[29] A. Bousseksou, F. Varret, J. Nasser, Journal De Physique I, 3 (1993) 1463-1473.
[30] P. Gutlich, H.A. Goodwin, Spin crossover - An overall perspective, in: Spin Crossover in Transition Metal Compounds I, 2004, pp. 1-47.
[31] M.A. Halcrow, Chemical Society Reviews, 40 (2011) 4119-4142.
[32] A.B. Gaspar, G. Molnár, A. Rotaru, H.J. Shepherd, Comptes Rendus Chimie, (2018).
[33] F. Varret, A. Bleuzen, K. Boukheddaden, A. Bousseksou, E. Codjovi, C. Enachescu, A. Goujon, J. Linares, N. Menendez, M. Verdaguer, Pure and Applied Chemistry, 74 (2002) 2159-2168.
[34] P. Gutlich, A.B. Gaspar, V. Ksenofontov, Y. Garcia, *J. Phys. Condens. Matter*, 16 (2004) S1087-S1108.
[35] V. Ksenofontov, A.B. Gaspar, G. Levchenko, B. Fitzsimmons, P. Gutlich, Journal of Physical Chemistry B, 108 (2004) 7723-7727.

[36] J.J. McGravey, I. Lawthers, Journal of the Chemical Society, Chemical Communications, (1982) 906-907.
[37] S. Decurtins, P. Gutlich, C.P. Kohler, H. Spiering, A. Hauser, *Chemical Physics Letters*, 105 (1984) 1-4.
[38] A. Hauser, Chemical Physics Letters, 124 (1986) 543-548.
[39] A. Hauser, Journal of Chemical Physics, 94 (1991) 2741-2748.
[40] C. Brady, J.J. McGarvey, J.K. McCusker, H. Toftlund, D.N. Hendrickson, Time-resolved relaxation studies of spin crossover systems in solution, in: Spin Crossover in Transition Metal Compounds Iii, 2004, pp. 1-22.
[41] A. Hauser, Comments on Inorganic Chemistry, 17 (1995) 17-40.
[42] S. Hayami, Z.Z. Gu, M. Shiro, Y. Einaga, A. Fujishima, O. Sato, Journal of the American Chemical Society, 122 (2000) 7126-7127.
[43] J. Zarembowitch, New Journal of Chemistry, 16 (1992) 255-267.
[44] C. Roux, J. Zarembowitch, B. Gallois, T. Granier, R. Claude, Inorganic Chemistry, 33 (1994) 2273-2279.
[45] J. Zarembowitch, C. Roux, M.L. Boillot, R. Claude, J.P. Itie, A. Polian, M. Bolte, Molecular Crystals and Liquid Crystals Science and Technology Section a-Molecular Crystals and Liquid Crystals, 234 (1993) 247-254.
[46] M.L. Boillot, A. Sour, P. Delhaes, C. Mingotaud, H. Soyer, Coordination Chemistry Reviews, 192 (1999) 47-59.
[47] M.L. Boillot, J. Zarembowitch, A. Sour, Ligand-driven light-induced spin change (LD-LISC): a promising photomagnetic effect, in: Spin Crossover in Transition Metal Compounds Ii, 2004, pp. 261-276.
[48] V. Ksenofontov, G. Levchenko, H. Spiering, P. Gutlich, J.F. Letard, Y. Bouhedja, O. Kahn, Chemical Physics Letters, 294 (1998) 545-553.
[49] E. Breuning, M. Ruben, J.-M. Lehn, F. Renz, Y. Garcia, V. Ksenofontov, P. Gütlich, E. Wegelius, K. Rissanen, Angewandte Chemie (International Edition), 39 (2000) 2377 and 2504-2507.
[50] P. Gütlich, Y. Garcia, H.A. Goodwin, Chemical Society Reviews, 29 (2000) 419-427.
[51] O. Sato, Accounts of Chemical Research, 36 (2003) 692-700.
[52] S. Bonhommeau, T. Guillon, L.M.L. Daku, P. Demont, J.S. Costa, J.F. Letard, G. Molnar, A. Bousseksou, *Angewandte Chemie-International Edition*, 45 (2006) 1625-1629.
[53] A. Bousseksou, G. Molnar, P. Demont, J. Menegotto, *Journal of Materials Chemistry*, 13 (2003) 2069-2071.
[54] F. Varret, K. Boukheddaden, E. Codjovi, A. Goujon, Hyperfine Interactions, 165 (2005) 37-47.
[55] M. Cavallini, I. Bergenti, S. Milita, G. Ruani, I. Salitros, Z.R. Qu, R. Chandrasekar, M. Ruben, *Angewandte Chemie-International Edition*, 47 (2008) 8596-8600.
[56] O. Kahn, J. Kröber, C. Jay, Advanced Materials, 4 (1992) 718-728.
[57] J. Linares, E. Codjovi, Y. Garcia, *Sensors*, 12 (2012) 4479-4492.
[58] S. Shi, G. Schmerber, J. Arabski, J.B. Beaufrand, D.J. Kim, S. Boukari, M. Bowen, N.T. Kemp, N. Viart, G. Rogez, E. Beaurepaire, H. Aubriet, J. Petersen, C. Becker, D. Ruch, *Applied Physics Letters*, 95 (2009) 043303.
[59] M. Matsuda, H. Isozaki, H. Tajima, Chemistry Letters, 37 (2008) 374-375.
[60] J. Daen, Journal of Colloid and Interface Science, 22 (1966) 309.
[61] H. Soyer, C. Mingotaud, M.L. Boillot, P. Delhaes, Langmuir, 14 (1998) 5890-5895.
[62] A. Bousseksou, C. Vieu, J.-F. Letard, P. Demont, J.P. Tuchagues, L. Malaqin, J. Menegotto, L. Salmon, Molecular memory and method for making same, in: CNRS (Ed.), France, 2009.
[63] M. Matsuda, H. Tajima, *Chemistry Letters*, 36 (2007) 700-701.
[64] M. Matsuda, H. Isozaki, H. Tajima, Thin Solid Films, 517 (2008) 1465-1467.
[65] A. Tissot, J.-F. Bardeau, E. Riviere, F. Brisset, M.-L. Boillot, Dalton Transactions, 39 (2010) 7806-7812.
[66] G. Felix, K. Abdul-Kader, T. Mahfoud, I.y.A. Gural'skiy, W. Nicolazzi, L. Salmon, G. Molnar, A. Bousseksou, Journal of the American Chemical Society, 133 (2011) 15342-15345.

[67] C.M. Quintero, I.y.A. Gural'skiy, L. Salmon, G. Molnar, C. Bergaud, A. Bousseksou, Journal of Materials Chemistry, 22 (2012) 3745-3751.
[68] R.D. Deegan, O. Bakajin, T.F. Dupont, G. Huber, S.R. Nagel, T.A. Witten, Nature, 389 (1997) 827.
[69] Y. Galyametdinov, V. Ksenofontov, A. Prosvirin, I. Ovchinnikov, G. Ivanova, P. Gutlich, W. Haase, Angewandte Chemie-International Edition, 40 (2001) 4269-4271.
[70] M. Seredyuk, A.B. Gaspar, V. Ksenofontov, S. Reiman, Y. Galyametdinov, W. Haase, E. Rentschler, P. Gutlich, Chemistry of Materials, 18 (2006) 2513-2519.
[71] K. Kuroiwa, T. Shibata, S. Sasaki, M. Ohba, A. Takahara, T. Kunitake, N. Kimizuka, Journal of Polymer Science Part a-Polymer Chemistry, 44 (2006) 5192-5202.
[72] A. Nakamoto, Y. Ono, N. Kojima, D. Matsumura, T. Yokoyama, Chemistry Letters, 32 (2003) 476-476.
[73] K. Hajime, J. Taketomo, S. Hideharu, O. Atsushi, E. Masaya, K. Norimichi, Chemistry Letters, 40 (2011) 888-889.
[74] S. Cobo, G. Molnar, J.A. Real, A. Bousseksou, Angewandte Chemie-International Edition, 45 (2006) 5786-5789.
[75] G. Agusti, S. Cobo, A.B. Gaspar, G. Molnar, N.O. Moussa, P.A. Szilagyi, V. Palfi, C. Vieu, M.C. Munoz, J.A. Real, A. Bousseksou, Chemistry of Materials, 20 (2008) 6721-6732.
[76] C. Bartual-Murgui, L. Salmon, A. Akou, C. Thibault, G. Molnar, T. Mahfoud, Z. Sekkat, J. Antonio Real, A. Bousseksou, New Journal of Chemistry, 35 (2011) 2089-2094.
[77] C. Bartual-Murgui, A. Akou, L. Salmon, G. Molnar, C. Thibault, J.A. Real, A. Bousseksou, *Small*, 7 (2011) 3385-3391.
[78] T. Mallah, M. Cavallini, Comptes Rendus Chimie, (2018) 1-17.
[79] G. Molnar, S. Cobo, J.A. Real, F. Carcenac, E. Daran, C. Vien, A. Bousseksou, Advanced Materials, 19 (2007) 2163-+.
[80] T. Mahfoud, G. Molnar, S. Cobo, L. Salmon, C. Thibault, C. Vieu, P. Demont, A. Bousseksou, *Applied Physics Letters*, 99 (2011) 053307.
[81] V. Davesne, M. Gruber, M. Studniarek, W.H. Doh, S. Zafeiratos, L. Joly, F. Sirotti, M.G. Silly, A.B. Gaspar, J.A. Real, G. Schmerber, M. Bowen, W. Weber, S. Boukari, V. Da Costa, J. Arabski, W. Wulfhekel, E. Beaurepaire, Journal of Chemical Physics, 142 (2015).
[82] H. Naggert, A. Bannwarth, S. Chemnitz, T. von Hofe, E. Quandt, F. Tuczek, Dalton Transactions, 40 (2011) 6364-6366.
[83] T. Palamarciuc, J.C. Oberg, F. El Hallak, C.F. Hirjibehedin, M. Serri, S. Heutz, J.-F. Letard, P. Rosa, Journal of Materials Chemistry, 22 (2012) 9690-9695.
[84] H. Naggert, J. Rudnik, L. Kipgen, M. Bernien, F. Nickel, L.M. Arruda, W. Kuch, C. Näther, F. Tuczek, Journal of Materials Chemistry C, 3 (2015) 7870-7877.
[85] S. Ossinger, H. Naggert, L. Kipgen, T. Jasper-Toennies, A. Rai, J. Rudnik, F. Nickel, L.M. Arruda, M. Bernien, W. Kuch, R. Berndt, F. Tuczek, The Journal of Physical Chemistry C, 121 (2017) 1210-1219.
[86] E.C. Ellingsworth, B. Turner, G. Szulczewski, Rsc Advances, 3 (2013) 3745-3754.
[87] M. Bernien, D. Wiedemann, C.F. Hermanns, A. Krüger, D. Rolf, W. Kroener, P. Müller, A. Grohmann, W. Kuch, The Journal of Physical Chemistry Letters, (2012) 3431-3434.
[88] S. Gueddida, M. Gruber, T. Miyamachi, E. Beaurepaire, W. Wulfhekel, M. Alouani, The Journal of Physical Chemistry Letters, 7 (2016) 900-904.
[89] M. Gruber, V. Davesne, M. Bowen, S. Boukari, E. Beaurepaire, W. Wulfhekel, T. Miyamachi, Physical Review B, 89 (2014) 195415.
[90] K. Bairagi, O. Iasco, A. Bellec, A. Kartsev, D. Li, J. Lagoute, C. Chacon, Y. Girard, S. Rousset, F. Miserque, Y.J. Dappe, A. Smogunov, C. Barreteau, M.-L. Boillot, T. Mallah, V. Repain, Nature Communications, 7 (2016) 12212.
[91] T. Miyamachi, M. Gruber, V. Davesne, M. Bowen, S. Boukari, L. Joly, F. Scheurer, G. Rogez, T.K. Yamada, P. Ohresser, E. Beaurepaire, W. Wulfhekel, Nat Commun, 3 (2012) 938.
[92] A. Pronschinske, Y.F. Chen, G.F. Lewis, D.A. Shultz, A. Calzolari, M.B. Nardelli, D.B. Dougherty, Nano Letters, 13 (2013) 1429-1434.

[93] T.G. Gopakumar, F. Matino, H. Naggert, A. Bannwarth, F. Tuczek, R. Berndt, Angewandte Chemie-International Edition, 51 (2012) 6262-6266.
[94] M. Sense Jan van der, L. Peter, Journal of Physics: Condensed Matter, 22 (2010) 133001.
[95] E. Ludwig, H. Naggert, M. Kalläne, S. Rohlf, E. Kröger, A. Bannwarth, A. Quer, K. Rossnagel, L. Kipp, F. Tuczek, Angewandte Chemie International Edition, 53 (2014) 3019-3023.
[96] M. Bernien, H. Naggert, L.M. Arruda, L. Kipgen, F. Nickel, J. Miguel, C.F. Hermanns, A. Krueger, D. Krueger, E. Schierle, E. Weschke, F. Tuczek, W. Kuch, Acs Nano, 9 (2015) 8960-8966.
[97] A. Pronschinske, R.C. Bruce, G. Lewis, Y. Chen, A. Calzolari, M. Buongiorno-Nardelli, D.A. Shultz, W. You, D.B. Dougherty, Chemical Communications, 49 (2013) 10446-10452.
[98] T.G. Gopakumar, M. Bernien, H. Naggert, F. Matino, C.F. Hermanns, A. Bannwarth, S. Muehlenberend, A. Krueger, D. Krueger, F. Nickel, W. Walter, R. Berndt, W. Kuch, F. Tuczek, Chemistry-a European Journal, 19 (2013) 15702-15709.
[99] X. Zhang, T. Palamarciuc, P. Rosa, J.F. Letard, B. Doudin, Z.Z. Zhang, J. Wang, P.A. Dowben, Journal of Physical Chemistry C, 116 (2012) 23291-23296.
[100] B. Warner, J.C. Oberg, T.G. Gill, F. El Hallak, C.F. Hirjibehedin, M. Serri, S. Heutz, M.A. Arrio, P. Sainctavit, M. Mannini, G. Poneti, R. Sessoli, P. Rosa, Journal of Physical Chemistry Letters, 4 (2013) 1546-1552.
[101] S. Beniwal, X. Zhang, S. Mu, A. Naim, P. Rosa, G. Chastanet, J.F. Letard, J. Liu, G.E. Sterbinsky, D.A. Arena, P.A. Dowben, A. Enders, Journal of Physics-Condensed Matter, 28 (2016) 206002.
[102] M. Gruber, T. Miyamachi, V. Davesne, M. Bowen, S. Boukari, W. Wulfhekel, M. Alouani, E. Beaurepaire, The Journal of Chemical Physics, 146 (2017) 092312.
[103] W. Kuch, M. Bernien, J. Phys.: Condens. Matter, 29 (2017) 023001.
[104] M.D. Manrique-Juarez, S. Rat, F. Mathieu, D. Saya, I. Séguy, T. Leïchlé, L. Nicu, L. Salmon, G. Molnár, A. Bousseksou, Applied Physics Letters, 109 (2016) 061903.
[105] C. Lefter, S. Rat, J.S. Costa, M.D. Manrique-Juárez, C.M. Quintero, L. Salmon, I. Séguy, T. Leichle, L. Nicu, P. Demont, A. Rotaru, G. Molnár, A. Bousseksou, Advanced Materials, 28 (2016) 7508-7514.
[106] X. Zhang, T. Palamarciuc, J.-F. Letard, P. Rosa, E.V. Lozada, F. Torres, L.G. Rosa, B. Doudin, P.A. Dowben, Chemical Communications, 50 (2014) 2255-2257.
[107] K. Abdul-Kader, M. Lopes, C. Bartual-Murgui, O. Kraieva, E.M. Hernández, L. Salmon, W. Nicolazzi, F. Carcenac, C. Thibault, G. Molnár, A. Bousseksou, Nanoscale, 5 (2013) 5288-5293.
[108] L. Salmon, G. Molnar, S. Cobo, P. Oulie, M. Etienne, T. Mahfoud, P. Demont, A. Eguchi, H. Watanabe, K. Tanakae, A. Bousseksou, *New Journal of Chemistry*, 33 (2009) 1283-1289.
[109] S. Trofimenko, Journal of the American Chemical Society, 89 (1967) 6288-6294.
[110] C. Janiak, Journal of the Chemical Society, Chemical Communications, (1994) 545-547.
[111] C. Janiak, T.G. Scharmann, T. Brauniger, J. Holubova, M. Nadvornik, Zeitschrift Fur Anorganische Und Allgemeine Chemie, 624 (1998) 769-774.
[112] C. Janiak, T.G. Scharmann, J.C. Green, R.P.G. Parkin, M.J. Kolm, E. Riedel, W. Mickler, J. Elguero, R.M. Claramunt, D. Sanz, Chemistry-a European Journal, 2 (1996) 992-1000.
[113] P.J. van Koningsbruggen, J.S. Miller, Solid State Sciences, 10 (2008) 1804-1806.
[114] S. Rat, K. Ridier, L. Vendier, G. Molnar, L. Salmon, A. Bousseksou, Crystengcomm, 19 (2017) 3271-3280.
[115] E. Konig, Structure and Bonding, 76 (1991) 51-152.
[116] P. Gutlich, A. Hauser, H. Spiering, *Angewandte Chemie-International Edition*, 33 (1994) 2024-2054.
[117] B. Gallois, J.A. Real, C. Hauw, J. Zarembowitch, Inorganic Chemistry, 29 (1990) 1152-1158.
[118] M. Atzori, L. Poggini, L. Squillantini, B. Cortigiani, M. Gonidec, P. Bencok, R. Sessoli, M. Mannini, Journal of Materials Chemistry C, 6 (2018) 8885-8889.
[119] W. Morscheidt, J. Jeftic, E. Codjovi, J. Linares, A. Bousseksou, H. Constant-Machado, F. Varret, Measurement Science & Technology, 9 (1998) 1311-1315.
[120] I.y.A. Gural'skiy, C. Quintero, K. Abdul-Kader, M. Lopes, C. Bartual-Murgui, L. Salmon, G. Molnár, A. Bousseksou, P. Zhao, D. Astruc, Journal of Nanophotonics, 6 (2012) 063517-063513.

[121] A. Akou, I.y.A. Gural'skiy, L. Salmon, C. Bartual-Murgui, C. Thibault, C. Vieu, G. Molnar, A. Bousseksou, Journal of Materials Chemistry, 22 (2012) 3752-3757.
[122] J.A. Wolny, V. Schünemann, Z. Németh, G. Vankó, Comptes Rendus Chimie, (2018).
[123] M. Lopes, C.M. Quintero, E.M. Hernandez, V. Velazquez, C. Bartual-Murgui, W. Nicolazzi, L. Salmon, G. Molnar, A. Bousseksou, Nanoscale, 5 (2013) 7762-7767.
[124] O. Kraieva, C.M. Quintero, I. Suleimanov, E.M. Hernandez, D. Lagrange, L. Salmon, W. Nicolazzi, G. Molnár, C. Bergaud, A. Bousseksou, Small, 12 (2016) 6325-6331.
[125] M. Manrique-Juárez, I. Suleimanov, E. Hernández, L. Salmon, G. Molnár, A. Bousseksou, Materials, 9 (2016) 537.
[126] E.M. Hernández, C.M. Quintero, O. Kraieva, C. Thibault, C. Bergaud, L. Salmon, G. Molnár, A. Bousseksou, Advanced Materials, 26 (2014) 2889-2893.
[127] E.M. Hernández, S. Zheng, H.J. Shepherd, D.S. Yufit, K. Ridier, S. Bedoui, W. Nicolazzi, V. Velázquez, S. Bonnet, G. Molnár, A. Bousseksou, The Journal of Physical Chemistry C, 120 (2016) 27608-27617.
[128] C. Jin, B.C. Olsen, E.J. Luber, J.M. Buriak, Chemistry of Materials, 29 (2017) 176-188.
[129] J.I. Langford, A.J.C. Wilson, Journal of Applied Crystallography, 11 (1978) 102-113.
[130] I. Suleimanov, J.S. Costa, G. Molnar, L. Salmon, A. Bousseksou, Chemical Communications, 50 (2014) 13015-13018.
[131] J. Zhang, D. Posselt, A. Sepe, X. Shen, J. Perlich, D.-M. Smilgies, C.M. Papadakis, Macromolecular Rapid Communications, 34 (2013) 1289-1295.
[132] X. Gu, I. Gunkel, A. Hexemer, W. Gu, T.P. Russell, Advanced Materials, 26 (2014) 273-281.
[133] X. Gu, I. Gunkel, A. Hexemer, T.P. Russell, Macromolecules, 49 (2016) 3373-3381.
[134] S. Nam, J. Jang, H. Cha, J. Hwang, T.K. An, S. Park, C.E. Park, Journal of Materials Chemistry, 22 (2012) 5543-5549.
[135] Y. Zheng, S. Li, D. Zheng, J. Yu, Organic Electronics, 15 (2014) 2647-2653.
[136] G. De Luca, A. Liscio, P. Maccagnani, F. Nolde, V. Palermo, K. Müllen, P. Samorì, Advanced Functional Materials, 17 (2007) 3791-3798.
[137] L. Wan, S. Ji, C.-C. Liu, G.S.W. Craig, P.F. Nealey, Soft Matter, 12 (2016) 2914-2922.
[138] A.O.F. Jones, Y.H. Geerts, J. Karpinska, A.R. Kennedy, R. Resel, C. Röthel, C. Ruzié, O. Werzer, M. Sferrazza, ACS Applied Materials & Interfaces, 7 (2015) 1868-1873.
[139] H.M.A. Ehmann, A. Zimmer, E. Roblegg, O. Werzer, Crystal Growth & Design, 14 (2014) 1386-1391.
[140] H.M.A. Ehmann, R. Baumgartner, B. Kunert, A. Zimmer, E. Roblegg, O. Werzer, The Journal of Physical Chemistry C, 118 (2014) 12855-12861.
[141] F. Borgatti, P. Torelli, M. Brucale, D. Gentili, G. Panaccione, C. Castan Guerrero, B. Schäfer, M. Ruben, M. Cavallini, Langmuir, 34 (2018) 3604-3609.
[142] Y. Marcus, Chemical Society Reviews, 22 (1993) 409-416.
[143] S. Nam, D.S. Chung, J. Jang, S.H. Kim, C. Yang, S.K. Kwon, C.E. Park, Journal of the Electrochemical Society, 157 (2010) H90-H93.
[144] I.y.A. Gural'skiy, C.M. Quintero, J.S. Costa, P. Demont, G. Molnar, L. Salmon, H.J. Shepherd, A. Bousseksou, Journal of Materials Chemistry C, 2 (2014) 2949-2955.
[145] V. Nagy, I. Suleimanov, G. Molnár, L. Salmon, A. Bousseksou, L. Csóka, Journal of Materials Chemistry C, 3 (2015) 7897-7905.
[146] C. Lefter, R. Tan, S. Tricard, J. Dugay, G. Molnár, L. Salmon, J. Carrey, A. Rotaru, A. Bousseksou, Polyhedron, 102 (2015) 434-440.
[147] A. Grosjean, N. Daro, S. Pechev, L. Moulet, C. Etrillard, G. Chastanet, P. Guionneau, European Journal of Inorganic Chemistry, (2016) 1961-1966.
[148] A.F. Hebard, W.M. Steverson, Journal of Applied Physics, 49 (1978) 5250-5255.
[149] C.M. Quintero, O. Kraieva, F. Carcenac, D. Lagrange, N.A. Yaremchuk, G. Molnár, C. Bergaud, Microelectronics Journal, 46 (2015) 1167-1174.
[150] O. Kraieva, New approaches for high spatial and temporal resolution nanothermometry : development of hot wire nano heater devices and investigation of thermosensitive materials with

fluorescent and spin crossover properties, in: École Doctorale Sciences de la Matière (Toulouse) Université Toulouse III-Paul Sabatier, 2015, pp. 179.
[151] A. Saxena, G. Aeppli, MRS Bulletin, 34 (2009) 804-813.
[152] P.R. Couchman, W.A. Jesser, Nature, 269 (1977) 481.
[153] S.H. Tolbert, A.P. Alivisatos, Science, 265 (1994) 373-376.
[154] J.M. McHale, A. Auroux, A.J. Perrotta, A. Navrotsky, Science, 277 (1997) 788-791.
[155] L.F. Drummy, D.C. Martin, Advanced Materials, 17 (2005) 903-907.
[156] S.M. Clark, S.G. Prilliman, C.K. Erdonmez, A.P. Alivisatos, Nanotechnology, 16 (2005) 2813.
[157] C.C. Yang, S. Li, J. Armellin, The Journal of Physical Chemistry C, 111 (2007) 17512-17515.
[158] S. Sood, P. Gouma, Journal of the American Ceramic Society, 96 (2013) 351-354.
[159] H. Zhang, J. F. Banfield, Journal of Materials Chemistry, 8 (1998) 2073-2076.
[160] V. Swamy, A. Kuznetsov, L.S. Dubrovinsky, R.A. Caruso, D.G. Shchukin, B.C. Muddle, Physical Review B, 71 (2005) 184302.
[161] K. Lu, Z.H. Jin, Current Opinion in Solid State and Materials Science, 5 (2001) 39-44.
[162] M.A. Halcrow, *Spin-Crossover Materials. Properties and Applications.*, John Wiley & Sons, Ltd., 2013.
[163] K.S. Kumar, M. Ruben, Coordination Chemistry Reviews, 346 (2017) 176-205.
[164] F. Volatron, L. Catala, E. Riviere, A. Gloter, O. Stephan, T. Mallah, *Inorg. Chem.*, 47 (2008) 6584-6586.
[165] T. Forestier, A. Kaiba, S. Pechev, D. Denux, P. Guionneau, C. Etrillard, N. Daro, E. Freysz, J.-F. Létard, Chemistry – A European Journal, 15 (2009) 6122-6130.
[166] I. Boldog, A.B. Gaspar, V. Martinez, P. Pardo-Ibanez, V. Ksenofontov, A. Bhattacharjee, P. Gutlich, J.A. Real, Angewandte Chemie-International Edition, 47 (2008) 6433-6437.
[167] A. Rotaru, F. Varret, A. Gindulescu, J. Linares, A. Stancu, J. Létard, T. Forestier, C. Etrillard, *Eur. Phys. J. B* 84 (2011) 439-449.
[168] T. Kawamoto, S. Abe, *Chem. Comm.*, (2005) 3933-3935.
[169] A. Muraoka, K. Boukheddaden, J. Linares, F. Varret, *Phys. Rev. B*, 84 (2011) 054119.
[170] G. Felix, W. Nicolazzi, M. Mikolasek, G. Molnar, A. Bousseksou, Physical Chemistry Chemical Physics, 16 (2014) 7358-7367.
[171] L. Stoleriu, P. Chakraborty, A. Hauser, A. Stancu, C. Enachescu, Physical Review B, 84 (2011).
[172] G. Felix, W. Nicolazzi, L. Salmon, G. Molnar, M. Perrier, G. Maurin, J. Larionova, J. Long, Y. Guari, A. Bousseksou, *Phys. Rev. Lett.*, 110 (2013) 235701.
[173] M. Mikolasek, M.D. Manrique-Juarez, H.J. Shepherd, K. Ridier, S. Rat, V. Shalabaeva, A.-C. Bas, I.E. Collings, F. Mathieu, J. Cacheux, T. Leichle, L. Nicu, W. Nicolazzi, L. Salmon, G. Molnár, A. Bousseksou, Journal of the American Chemical Society, 140 (2018) 8970-8979.
[174] W.D. Nix, B.M. Clemens, Journal of Materials Research, 14 (1999) 3467-3473.
[175] Y.F. Zhu, J.S. Lian, Q. Jiang, The Journal of Physical Chemistry C, 113 (2009) 16896-16900.
[176] M.D. Manrique-Juarez, F. Mathieu, V. Shalabaeva, J. Cacheux, S. Rat, L. Nicu, T. Leichle, L. Salmon, G. Molnar, A. Bousseksou, Angewandte Chemie-International Edition, 56 (2017) 8074-8078.
[177] V. Amendola, M. Di Casa, L. Fabbrizzi, M. Licchelli, C. Mangano, P. Pallavicini, A. Poggi, Journal of inclusion phenomena and macrocyclic chemistry, 41 (2001) 13-18.
[178] A.P. de Silva, D.B. Fox, T.S. Moody, S.M. Weir, Trends in biotechnology, 19 (2001) 29-34.
[179] U. Pischel, Chimia (Aarau), 68 (2014) 505-511.
[180] X. Li, R.R. Tao, L.J. Hong, J. Cheng, Q. Jiang, Y.M. Lu, M.H. Liao, W.F. Ye, N.N. Lu, F. Han, Y.Z. Hu, Y.H. Hu, J Am Chem Soc, 137 (2015) 12296-12303.
[181] H.A. Anila, F. Ali, S. Kushwaha, N. Taye, S. Chattopadhyay, A. Das, Analytical Chemistry, 88 (2016) 12161-12168.
[182] Z. Sheng, L. Chen, Analytical and Bioanalytical Chemistry, 409 (2017) 6081-6090.
[183] L. Yang, J. Wang, L. Yang, C. Zhang, R. Zhang, Z. Zhang, B. Liu, C. Jiang, RSC Advances, 6 (2016) 56384-56391.
[184] T.Z. Cservenyi, A.J. Van Riesen, F.D. Berger, A. Desoky, R.A. Manderville, ACS Chemical Biology, 11 (2016) 2576-2582.

[185] Y. Cheng, J. Wu, C. Guo, X.-G. Li, B. Ding, Y. Li, Journal of Materials Chemistry B, 5 (2017) 2524-2535.
[186] M. Shakir, A. Abbasi, Inorganica Chimica Acta, 465 (2017) 14-25.
[187] X. Yue, W. Zhu, S. Ma, S. Yu, Y. Zhang, J. Wang, Y. Wang, D. Zhang, J. Wang, Journal of Agricultural and Food Chemistry, 64 (2016) 706-713.
[188] T. Liu, N. Li, J.X. Dong, H.Q. Luo, N.B. Li, Sensors and Actuators B: Chemical, 231 (2016) 147-153.
[189] T.-B. Wei, J.-F. Chen, X.-B. Cheng, H. Li, Q. Lin, H. Yao, Y.-M. Zhang, RSC Advances, 6 (2016) 65898-65901.
[190] H. Agarwalla, P.S. Mahajan, D. Sahu, N. Taye, B. Ganguly, S.B. Mhaske, S. Chattopadhyay, A. Das, Inorganic Chemistry, 55 (2016) 12052-12060.
[191] R.S. Chouhan, J.H. Niazi, A. Qureshi, Sensors and Actuators B: Chemical, 196 (2014) 381-387.
[192] J. Garcia-Amorós, S. Swaminathan, S. Sortino, F.M. Raymo, Chemistry – A European Journal, 20 (2014) 10276-10284.
[193] G. Chang, L. Yang, S. Liu, R. Lin, J. You, Polymer Chemistry, 6 (2015) 697-702.
[194] X.L. Ho, P.-J. Chen, W.-Y. Woon, J.D. White, Chemical Physics Letters, 686 (2017) 212-217.
[195] Z. Li, R. Liang, W. Liu, D. Yan, M. Wei, Nanoscale, 7 (2015) 16737-16743.
[196] J. Kumar, M.J. Sarma, P. Phukan, D.K. Das, Journal of Fluorescence, 25 (2015) 1431-1435.
[197] S. Yang, J. Sun, P. He, X. Deng, Z. Wang, C. Hu, G. Ding, X. Xie, Chemistry of Materials, 27 (2015) 2004-2011.
[198] Q. Qi, J. Qian, S. Ma, B. Xu, S.X.-A. Zhang, W. Tian, Chemistry – A European Journal, 21 (2015) 1149-1155.
[199] X. Su, Y. Wang, X. Fang, Y.-M. Zhang, T. Zhang, M. Li, Y. Liu, T. Lin, S.X.-A. Zhang, Chemistry – An Asian Journal, 11 (2016) 3205-3212.
[200] X. Lian, T. Miao, X. Xu, C. Zhang, B. Yan, Biosensors and Bioelectronics, 97 (2017) 299-304.
[201] C.A. Choi, J.E. Lee, Z.A.I. Mazrad, I. In, J.H. Jeong, S.Y. Park, Journal of Industrial and Engineering Chemistry, 63 (2018) 208-219.
[202] M. Villabona, M. Benet, S. Mena, R.O. Al-Kaysi, J. Hernando, G. Guirado, The Journal of Organic Chemistry, 83 (2018) 9166-9177.
[203] B.-H. Di, Y.-L. Chen, Chinese Chemical Letters, 29 (2018) 245-251.
[204] Y. Zhao, H. Lin, M. Chen, D. Yan, Industrial & Engineering Chemistry Research, 53 (2014) 3140-3147.
[205] Q. Kong, W. Zhuang, G. Li, Y. Xu, Q. Jiang, Y. Wang, New Journal of Chemistry, 41 (2017) 13784-13791.
[206] X. Su, Y. Ji, W. Pan, S. Chen, Y.-M. Zhang, T. Lin, L. Liu, M. Li, Y. Liu, S.X.-A. Zhang, Journal of Materials Chemistry C, 6 (2018) 6940-6948.
[207] Y. Sagara, N. Tamaoki, RSC Advances, 7 (2017) 47056-47062.
[208] J.-B. Xiong, Y.-X. Yuan, L. Wang, J.-P. Sun, W.-G. Qiao, H.-C. Zhang, M. Duan, H. Han, S. Zhang, Y.-S. Zheng, Organic Letters, 20 (2018) 373-376.
[209] X. Liu, A. Li, W. Xu, Z. Ma, X. Jia, Physical Chemistry Chemical Physics, 20 (2018) 13249-13254.
[210] J. Lee, H. Yang, C.H. Park, H.-H. Cho, H. Yun, B.J. Kim, Chemistry of Materials, 28 (2016) 3446-3453.
[211] D. Gareau, A. Desrosiers, A. Vallée-Bélisle, Nano Letters, 16 (2016) 3976-3981.
[212] C. Lin, Y. Jiang, C.-a. Tao, X. Yin, Y. Lan, C. Wang, S. Wang, X. Liu, G. Li, ACS Applied Materials & Interfaces, 9 (2017) 11770-11779.
[213] L. He, X. Yang, K. Wang, Q. Wang, F. Zhao, J. Huang, J. Liu, Chemical Communications, 50 (2014) 7803-7805.
[214] P. Srujana, T.P. Radhakrishnan, Angewandte Chemie International Edition, 54 (2015) 7270-7274.
[215] T. Aotake, M. Suzuki, K. Tahara, D. Kuzuhara, N. Aratani, N. Tamai, H. Yamada Chemistry – A European Journal, 21 (2015) 4966-4974.
[216] Y. Zhan, P. Yang, G. Li, Y. Zhang, Y. Bao, New Journal of Chemistry, 41 (2017) 263-270.
[217] J. Cui, J.E. Kwon, H.-J. Kim, D.R. Whang, S.Y. Park, ACS Applied Materials & Interfaces, 9 (2017) 2883-2890.

[218] I. Gallardo, G. Guirado, J. Hernando, S. Morais, G. Prats, Chemical Science, 7 (2016) 1819-1825.
[219] N. Sala, G. Prats, M. Villabona, I. Gallardo, T. Hamdan, R.O. Al-Kaysi, J. Hernando, G. Guirado, Dyes and Pigments, 153 (2018) 160-171.
[220] P.S. Hariharan, G. Parthasarathy, A. Kundu, S. Karthikeyan, Y. Sagara, D. Moon, S.P. Anthony, Crystal Growth & Design, 18 (2018) 3971-3979.
[221] D. Kim, J.E. Kwon, S.Y. Park, Advanced Functional Materials, 28 (2018) 1706213.
[222] K.C. Naeem, V.C. Nair, Molecular Systems Design & Engineering, 3 (2018) 142-149.
[223] M.A. Halcrow, Chemical Communications, 49 (2013) 10890-10892.
[224] M.-L. Boillot, B. Weber, Comptes Rendus Chimie, (2018).
[225] H.J. Shepherd, G. Molnar, W. Nicolazzi, L. Salmon, A. Bousseksou, European Journal of Inorganic Chemistry, (2013) 653-661.
[226] G. Molnar, L. Salmon, W. Nicolazzi, F. Terki, A. Bousseksou, Journal of Materials Chemistry C, 2 (2014) 1360-1366.
[227] M. Attwood, S.S. Turner, Coordination Chemistry Reviews, 353 (2017) 247-277.
[228] H. Li, H. Peng, Current Opinion in Colloid & Interface Science, 35 (2018) 9-16.
[229] H.J. Shepherd, C.M. Quintero, G. Molnár, L. Salmon, A. Bousseksou, Luminescent Spin-Crossover Materials, in: M.A. Halcrow (Ed.) Spin-Crossover Materials, John Wiley & Sons, Ltd., 2013, pp. 347-373.
[230] C. Piguet, E. Rivaraminten, G. Hopfgartner, J.C.G. Bunzli, Helvetica Chimica Acta, 78 (1995) 1651-1672.
[231] C.-F. Wang, R.-F. Li, X.-Y. Chen, R.-J. Wei, L.-S. Zheng, J. Tao, Angewandte Chemie-International Edition, 54 (2015) 1574-1577.
[232] C. Lochenie, K.G. Wagner, M. Karg, B. Weber, Journal of Materials Chemistry C, 3 (2015) 7925-7935.
[233] C.-F. Wang, M.-J. Sun, Q.-J. Guo, Z.-X. Cao, L.-S. Zheng, J. Tao, Chemical Communications, 52 (2016) 14322-14325.
[234] M. Estrader, J. Salinas Uber, L.A. Barrios, J. Garcia, P. Lloyd-Williams, O. Roubeau, S.J. Teat, G. Aromí, Angewandte Chemie International Edition, 56 (2017) 15622-15627.
[235] K.S. Kumar, I. Šalitroš, E. Moreno-Pineda, M. Ruben, Dalton Transactions, 46 (2017) 9765-9768.
[236] B. Schafer, T. Bauer, I. Faus, J.A. Wolny, F. Dahms, O. Fuhr, S. Lebedkin, H.-C. Wille, K. Schlage, K. Chevalier, F. Rupp, R. Diller, V. Schunemann, M.M. Kappes, M. Ruben, Dalton Transactions, 46 (2017) 2289-2302
[237] J.L. Wang, Q. Liu, Y.S. Meng, X. Liu, H. Zheng, Q. Shi, C.Y. Duan, T. Liu, Chemical Science, 9 (2018) 2892-2897.
[238] C. Lochenie, K. Schötz, F. Panzer, H. Kurz, B. Maier, F. Puchtler, S. Agarwal, A. Köhler, B. Weber, Journal of the American Chemical Society, 140 (2018) 700-709.
[239] H. Kurz, C. Lochenie, K.G. Wagner, S. Schneider, M. Karg, B. Weber, Chemistry-a European Journal, 24 (2018) 5100-5111.
[240] C.A. Tovee, C.A. Kilner, J.A. Thomas, M.A. Halcrow, Crystengcomm, 11 (2009) 2069-2077.
[241] M. Matsuda, K. Kiyoshima, R. Uchida, N. Kinoshita, H. Tajima, Thin Solid Films, 531 (2013) 451-453.
[242] L.J.K. Cook, M.A. Halcrow, Polyhedron, 87 (2015) 91-97.
[243] C.M. Quintero, G. Félix, I. Suleimanov, J. Sánchez Costa, G. Molnár, L. Salmon, W. Nicolazzi, A. Bousseksou, Beilstein Journal of Nanotechnology, 5 (2014) 2230-2239.
[244] J. Manuel Herrera, S. Titos-Padilla, S.J.A. Pope, I. Berlanga, F. Zamora, J. Jose Delgado, K.V. Kamenev, X. Wang, A. Prescimone, E.K. Brechin, E. Colacio, Journal of Materials Chemistry C, 3 (2015) 7819-7829.
[245] I. Suleimanov, O. Kraieva, G. Molnar, L. Salmon, A. Bousseksou, Chemical Communications, 51 (2015) 15098-15101.
[246] I. Suleimanov, O. Kraieva, J. Sánchez Costa, I.O. Fritsky, G. Molnár, L. Salmon, A. Bousseksou, Journal of Materials Chemistry C, 3 (2015) 5026-5032.
[247] O. Kraieva, I. Suleimanov, G. Molnár, L. Salmon, A. Bousseksou, Magnetochemistry, 2 (2016) 1-8.

[248] I. Suleimanov, G. Molnár, L. Salmon, A. Bousseksou, European Journal of Inorganic Chemistry, 2017 (2017) 3446-3451.
[249] Y.H. Luo, J.W. Wang, W. Wang, X.T. He, D.L. Hong, C. Chen, T. Xu, Q.Y. Shao, B.W. Sun, Acs Applied Materials & Interfaces, 10 (2018) 16666-16673.
[250] C. Adachi, M.A. Baldo, S.R. Forrest, M.E. Thompson, Applied Physics Letters, 77 (2000) 904-906.
[251] Y. Kawamura, J. Brooks, J.J. Brown, H. Sasabe, C. Adachi, Physical Review Letters, 96 (2006) 017404.
[252] T. Tsuboi, N. Aljaroudi, Optical Materials, 30 (2008) 1375-1381.
[253] E.B. Namdas, A. Ruseckas, I.D.W. Samuel, S.-C. Lo, P.L. Burn, The Journal of Physical Chemistry B, 108 (2004) 1570-1577.
[254] C. Arnaud, T. Forestier, N. Daro, E. Freysz, J.F. Letard, G. Pauliat, G. Roosen, Chemical Physics Letters, 470 (2009) 131-135.
[255] R.M. van der Veen, O.H. Kwon, A. Tissot, A. Hauser, A.H. Zewail, Nature Chemistry, 5 (2013) 395-402.
[256] H. Spiering, K. Boukheddaden, J. Linares, F. Varret, Physical Review B, 70 (2004).
[257] H.J. Shepherd, I.y.A. Gural'skiy, C.M. Quintero, S. Tricard, L. Salmon, G. Molnar, A. Bousseksou, Nature Communications, 4 (2013).
[258] G. Felix, M. Mikolasek, H. Peng, W. Nicolazzi, G. Molnar, A.I. Chumakov, L. Salmon, A. Bousseksou, Physical Review B, 91 (2015) 024422.
[259] T. Granier, B. Gallois, J. Gaultier, J.A. Real, J. Zarembowitch, Inorganic Chemistry, 32 (1993) 5305-5312.
[260] H.J. Shepherd, T. Palamarciuc, P. Rosa, P. Guionneau, G. Molnar, J.-F. Letard, A. Bousseksou, Angewandte Chemie-International Edition, 51 (2012) 3910-3914.
[261] J. Jung, F. Bruchhäuser, R. Feile, H. Spiering, P. Gütlich, Zeitschrift für Physik B Condensed Matter, 100 (1996) 517-522.
[262] S. Rat, M. Mikolasek, J.S. Costa, A.I. Chumakov, W. Nicolazzi, G. Molnar, L. Salmon, A. Bousseksou, Chemical Physics Letters, 653 (2016) 131-136.
[263] H.J. Shepherd, P. Rosa, L. Vendier, N. Casati, J.-F. Letard, A. Bousseksou, P. Guionneau, G. Molnar, *Phys. Chem. Chem. Phys.*, 14 (2012) 5265-5271.
[264] A. Tissot, H.J. Shepherd, L. Toupet, E. Collet, J. Sainton, G. Molnar, P. Guionneau, M.L. Boillot, *Eur. J. Inorg. Chem.*, (2013) 1001-1008.
[265] J. Laisney, H.J. Shepherd, L. Rechignat, G. Molnár, E. Rivière, M.L. Boillot, Physical Chemistry Chemical Physics, 20 (2018) 15951-15959.
[266] M.D. Manrique-Juarez, S. Rat, L. Mazenq, F. Mathieu, I. Séguy, T. Leïchlé, L. Nicu, L. Salmon, G. Molnár, A. Bousseksou, Spin crossover materials for MEMS actuation: Film integration and characterization, in: 2017 19th International Conference on Solid-State Sensors, Actuators and Microsystems (TRANSDUCERS), 2017, pp. 1300-1303.
[267] B. Voigtländer, Amplitude Modulation (AM) Mode in Dynamic Atomic Force Microscopy, in: B. Voigtländer (Ed.) Scanning Probe Microscopy: Atomic Force Microscopy and Scanning Tunneling Microscopy, Springer Berlin Heidelberg, Berlin, Heidelberg, 2015, pp. 187-204.
[268] F.Z. Fang, Z.W. Xu, S. Dong, Measurement Science and Technology, 19 (2008) 055501.
[269] B. Bharat, Q. Jun, Nanotechnology, 14 (2003) 886.
[270] D. Martinez-Martin, C. Carrasco, M. Hernando-Perez, P.J. de Pablo, J. Gomez-Herrero, R. Perez, M.G. Mateu, J.L. Carrascosa, D. Kiracofe, J. Melcher, A. Raman, PLOS ONE, 7 (2012) e30204.
[271] H. Hölscher, M. Y., W.C. C., W.H. K., Journal of Applied Physics, 103 (2008) 064317.
[272] J.P. Cleveland, B. Anczykowski, A.E. Schmid, V.B. Elings, Applied Physics Letters, 72 (1998) 2613-2615.
[273] C.J. Gómez, R. Garcia, Ultramicroscopy, 110 (2010) 626-633.
[274] N.F. Martínez, R. García, Nanotechnology, 17 (2006) S167-S172.
[275] Á.S. Paulo, R. García, Physical Review B, 66 (2002) 041406.
[276] R. Proksch, D.G. Yablon, Applied Physics Letters, 100 (2012) 073106.

[277] R. Proksch, M. Kocun, D. Hurley, M. Viani, A. Labuda, W. Meinhold, J. Bemis, Journal of Applied Physics, 119 (2016) 134901.
[278] R. Garcia, R. Proksch, European Polymer Journal, 49 (2013) 1897-1906.
[279] J.R. Lozano, R. Garcia, Physical Review Letters, 100 (2008) 076102.
[280] D. Hurley, M. Kocun, I. Revenko, B. Ohler, R. Proksch, Fast, quantitative AFM nano-mechanical measurements using AM-FM Viscoelastic Mapping Mode, in: Microscopy and Analysis, John Wiley & Sons, Ltd, , 2015, pp. 9-13.
[281] W.C. Oliver, G.M. Pharr, Journal of Materials Research, 7 (1992) 1564-1583.
[282] J.L. Hutter, J. Bechhoefer, Review of Scientific Instruments, 64 (1993) 1868-1873.
[283] J.E. Sader, J.W.M. Chon, P. Mulvaney, Review of Scientific Instruments, 70 (1999) 3967-3969.
[284] C.T. Gibson, D.A. Smith, C.J. Roberts, Nanotechnology, 16 (2005) 234-238.
[285] B. Ohler, Review of Scientific Instruments, 78 (2007) 063701-063705.
[286] J.E. Sader, J.A. Sanelli, B.D. Adamson, J.P. Monty, X. Wei, S.A. Crawford, J.R. Friend, I. Marusic, P. Mulvaney, E.J. Bieske, Review of Scientific Instruments, 83 (2012) 103705.
[287] J.E. Sader, R. Borgani, C.T. Gibson, D.B. Haviland, M.J. Higgins, J.I. Kilpatrick, J. Lu, P. Mulvaney, C.J. Shearer, A.D. Slattery, P.-A. Thorén, J. Tran, H. Zhang, H. Zhang, T. Zheng, Review of Scientific Instruments, 87 (2016) 093711.
[288] M.L.B. Palacio, B. Bhushan, Critical Reviews in Solid State and Materials Sciences, 35 (2010) 73-104.
[289] J.E. Sader, Journal of Applied Physics, 84 (1998) 64-76.
[290] J.A. Real, M.C. Munoz, J. Faus, X. Solans, Inorganic Chemistry, 36 (1997) 3008-3013.
[291] V. Vahdat, D.S. Grierson, K.T. Turner, R.W. Carpick, ACS Nano, 7 (2013) 3221-3235.
[292] K. Ridier, S. Rat, L. Salmon, W. Nicolazzi, G. Molnar, A. Bousseksou, Physical Chemistry Chemical Physics, (2018).
[293] F. Ru, J.F. Richard, Journal of Micromechanics and Microengineering, 13 (2003) 80.
[294] S. Chung, S. Park, Journal of Mechanical Science and Technology, 27 (2013) 2701-2707.
[295] R.B. Pérez-Sáez, V. Recarte, M.L. Nó, J. San Juan, Physical Review B, 57 (1998) 5684-5692.

Annexes

A2. Elaboration of thin films of $[Fe(HB(tz)_3)_2]$

A2.1 Pristine thermally evaporated thin films

Figure A2.1: Photo of the setup used for variable temperature optical absorption measurements.

A2.2 Crystallization by solvent vapour annealing

Figure A2.2.1: a) Scheme of the setup used in our study for humidity treatment; b) Photo of the setup used for humidity treatment

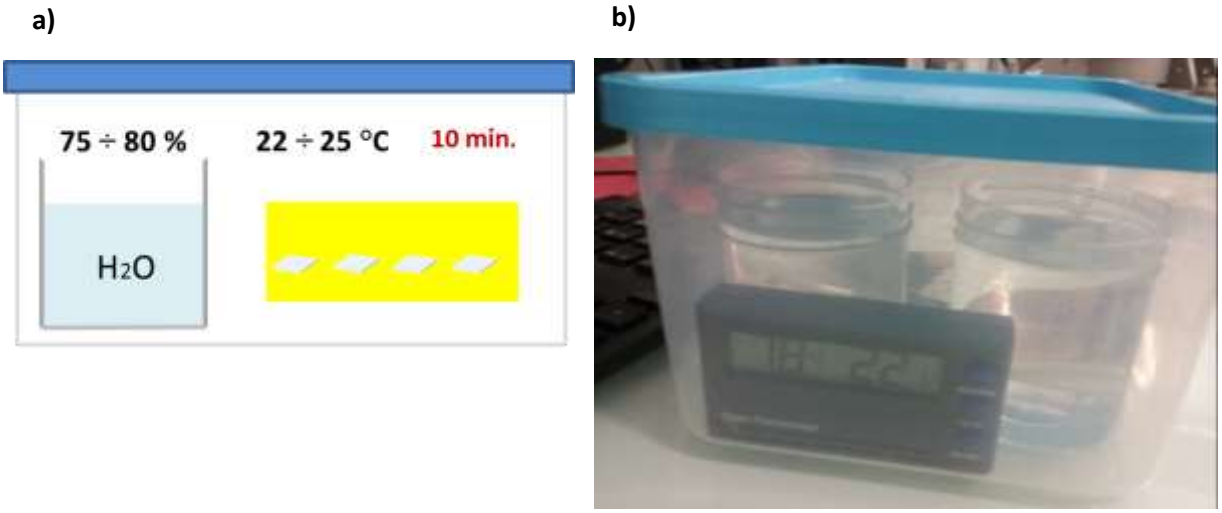

Figure A2.2.2: Selected AFM images of crystalline films obtained by solvent vapour annealing: (a)-(b) two different zones of 90 nm film; (c) 90 nm film after 3 months of storage in ambient air; (d) 150 nm film with roughness 2.5 nm; (e) film thickness evaluation.

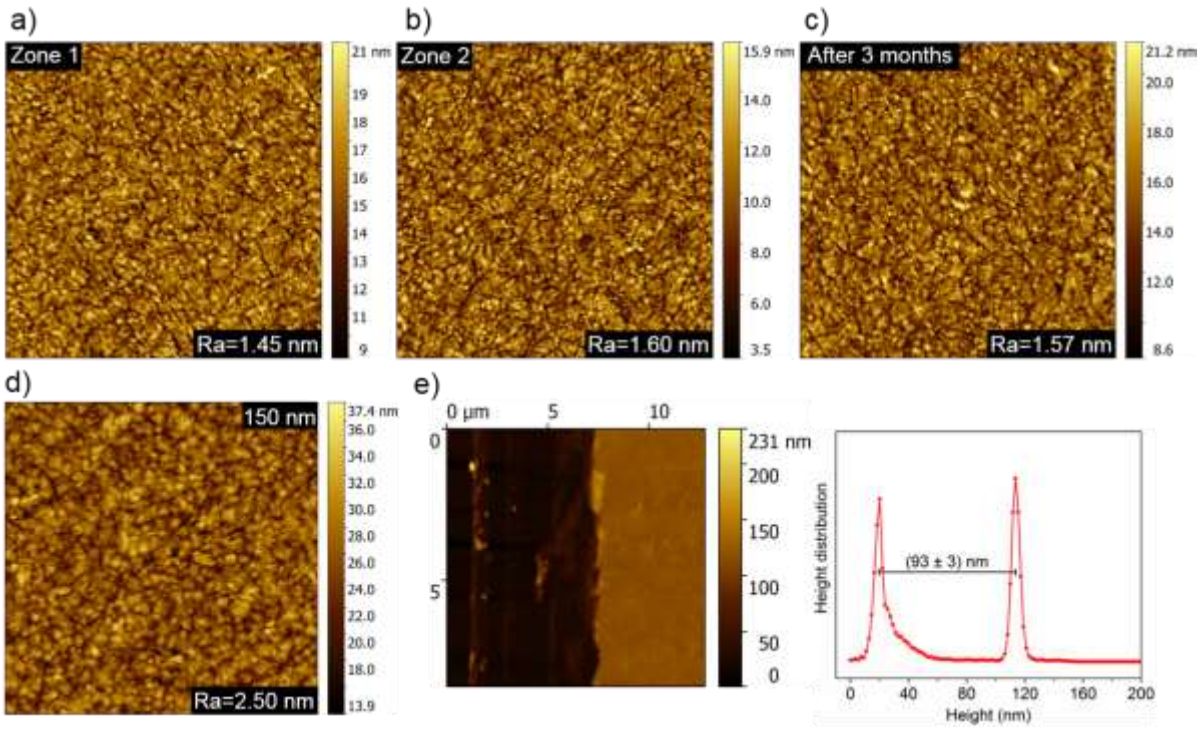

Figure A2.2.3: Temperature dependent magnetic measurements for a crystalline film of *ca.* 200 nm thickness, deposited on a paper substrate and rolled-on to increase the quantity of matter analysed. Measurements were done at 2 K/min heating-cooling rate.

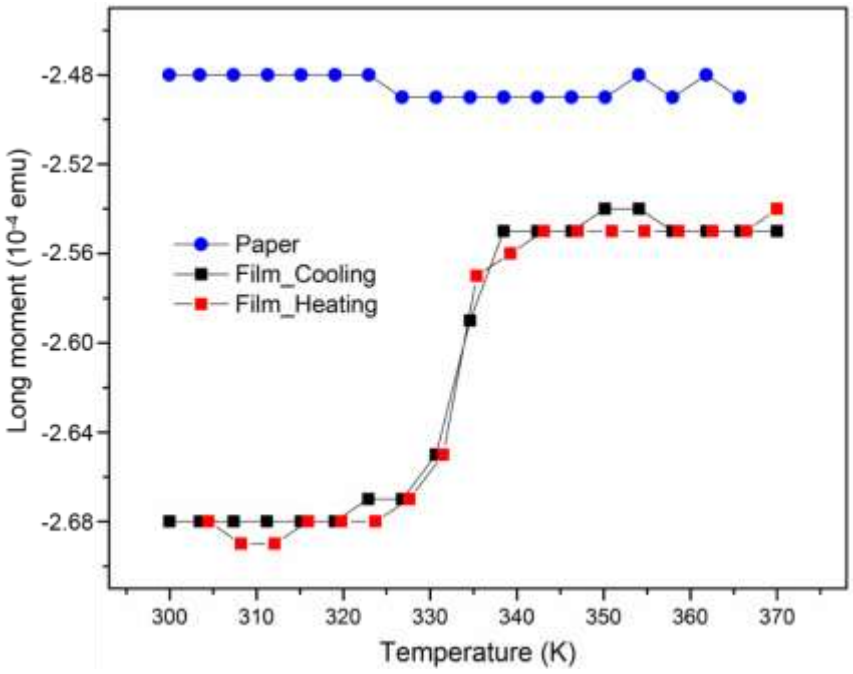

Figure A2.2.4: Thermal variation of Raman spectrum of a 194 nm crystalline film on heating.

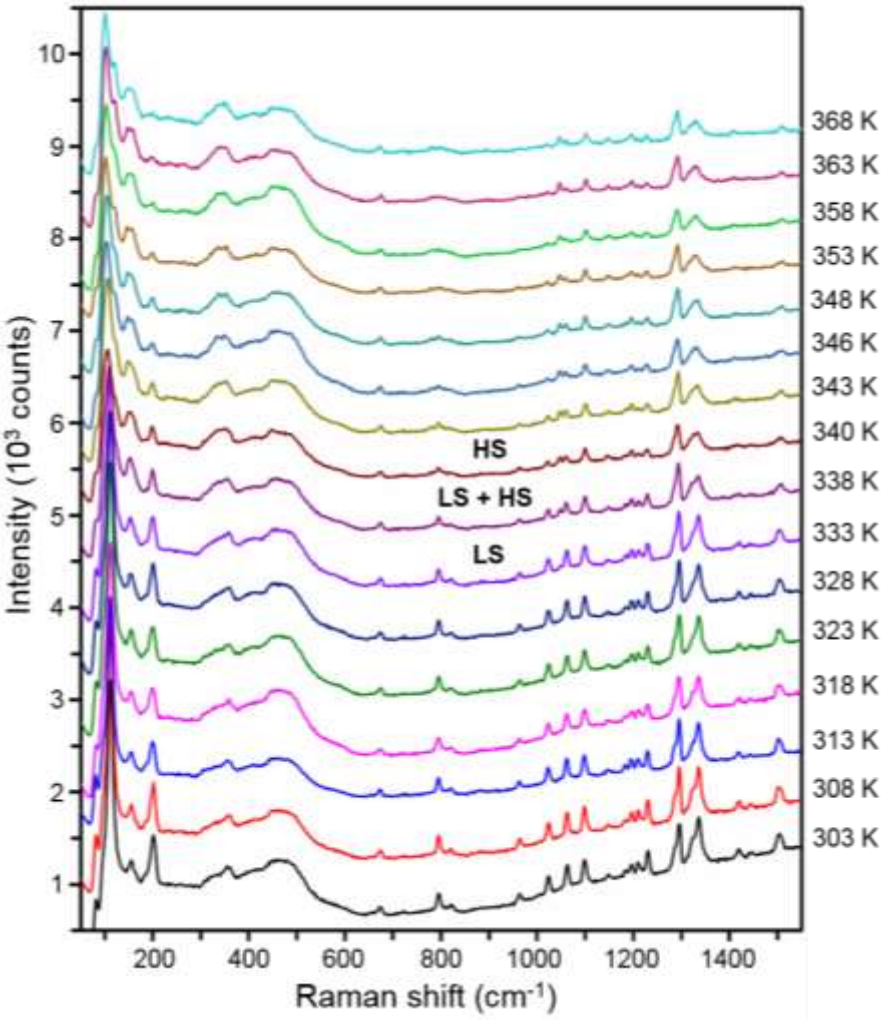

Figure A2.2.5: Photo of the setup used for *in-situ* absorbance measurements [Linkam RH95 humidity controller connected to a Cary 50 (Agilent Technologies) spectrophotometer].

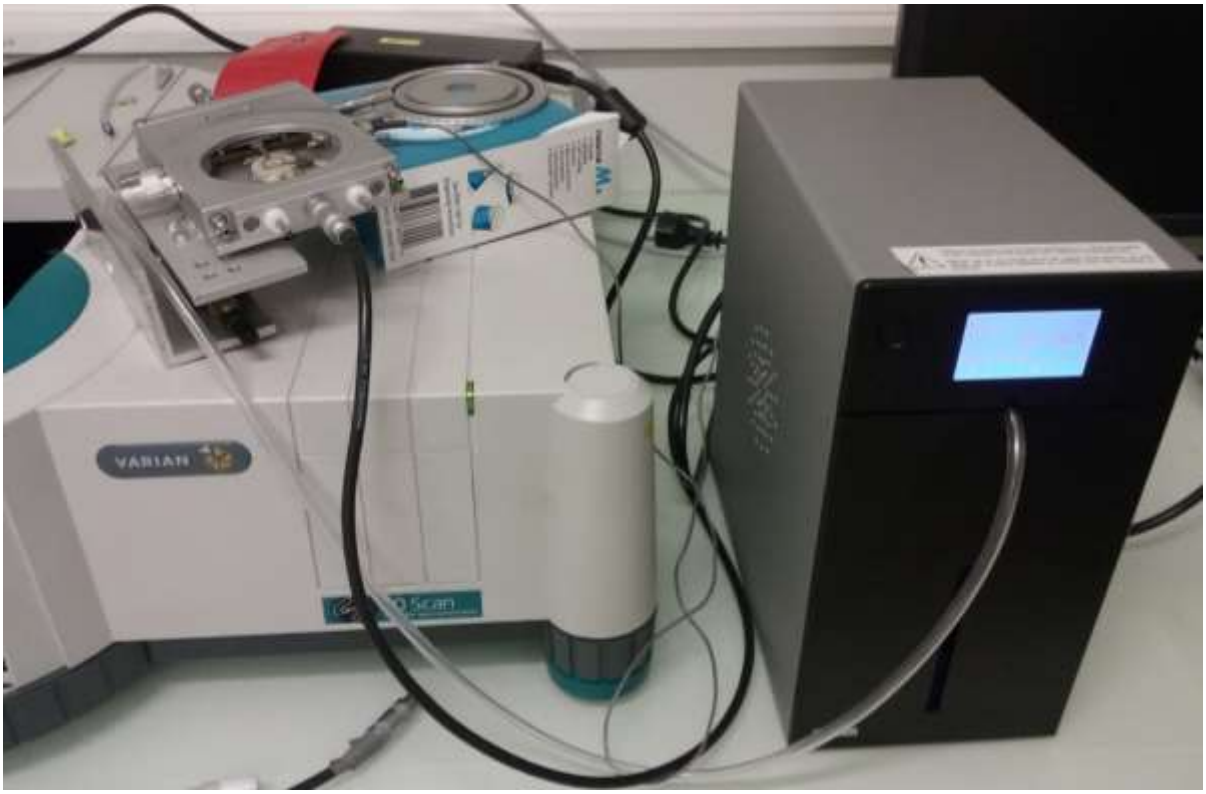

Figure A2.2.6: Absorbance change at 318 nm of a $[Fe(HB(tz)_3)_2]$ thin film as a function of time (black curve) for increasing and decreasing values of relative humidity (red curve) at a fixed temperature of 298 K

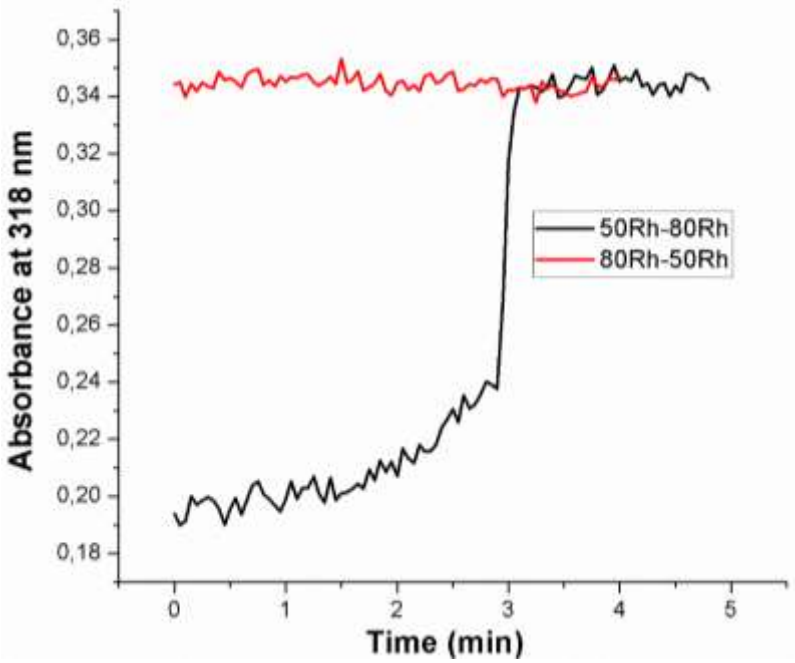

Deposition of thin layers using different techniques

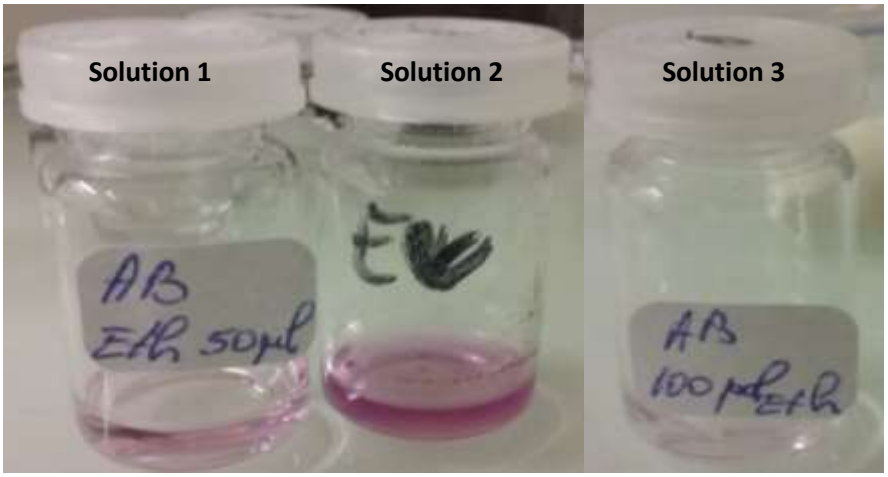

Solution 1 were prepared mixing together 4.5 mg of $[Fe(HB(tz)_3)_2]$ powder and 50 µl of ethanol. The resulting solution was sonicated during 5 minutes. Then 5 drops of distilled water were added for solubilization.

Solution 2 were prepared mixing together 20 mg of $[Fe(HB(tz)_3)_2]$ powder and 50 µl of ethanol. The resulting solution was sonicated during 5 minutes. Then 5 drops of distilled water were added for solubilization.

Solution 3 were prepared mixing together 4.5 mg of $[Fe(HB(tz)_3)_2]$ powder and 100 µl of ethanol. The resulting solution was sonicated during 5 minutes. Then 5 drops of distilled water were added for solubilization.

Spin coating method

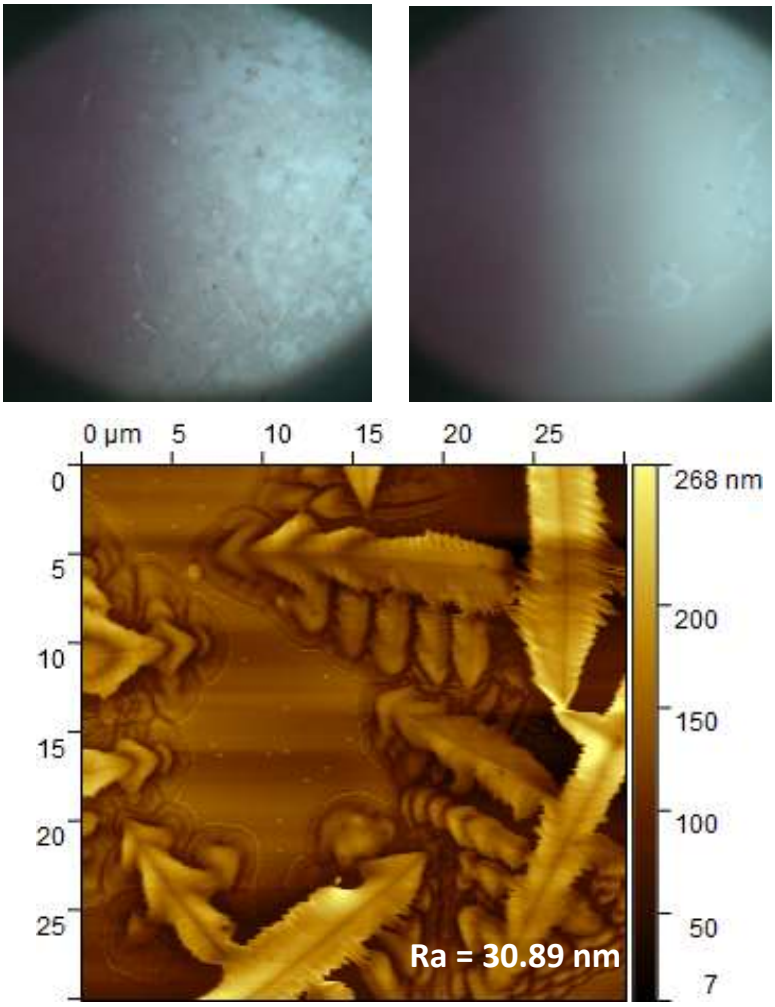

Concentrated solution (1 drop of 10µl *solution)*

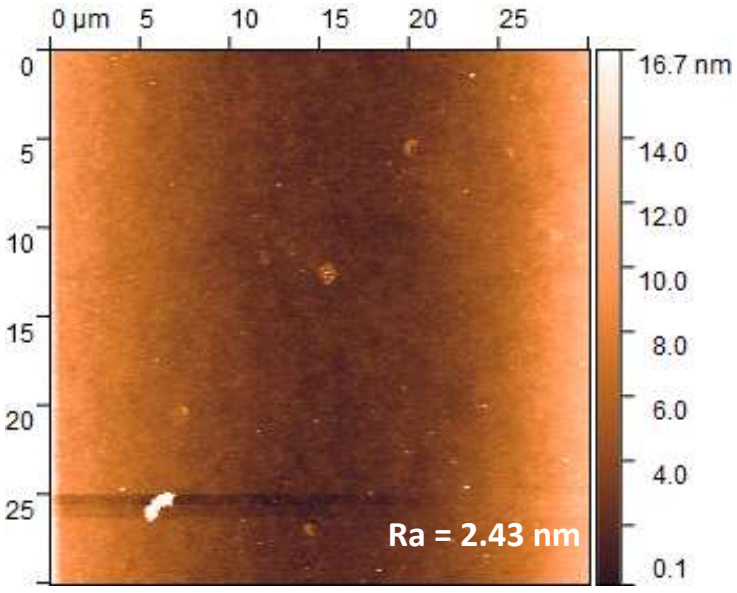

Diluted solution (1 drop of 10µl *solution)*

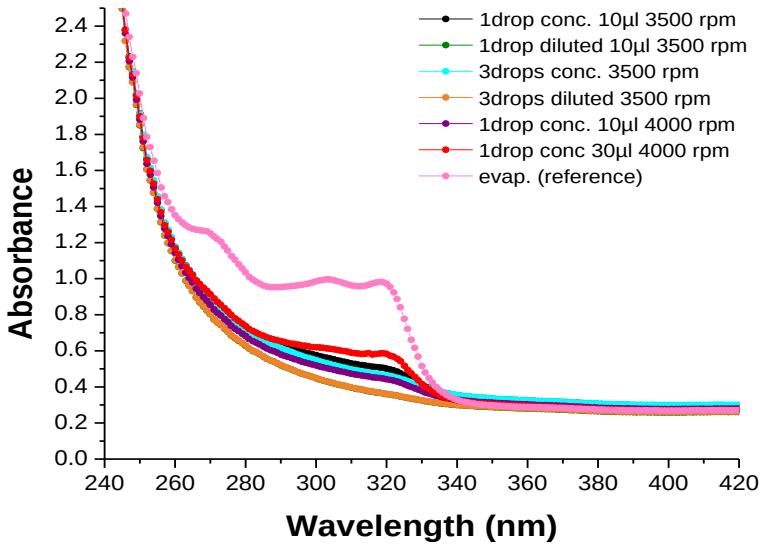

Drop casting method

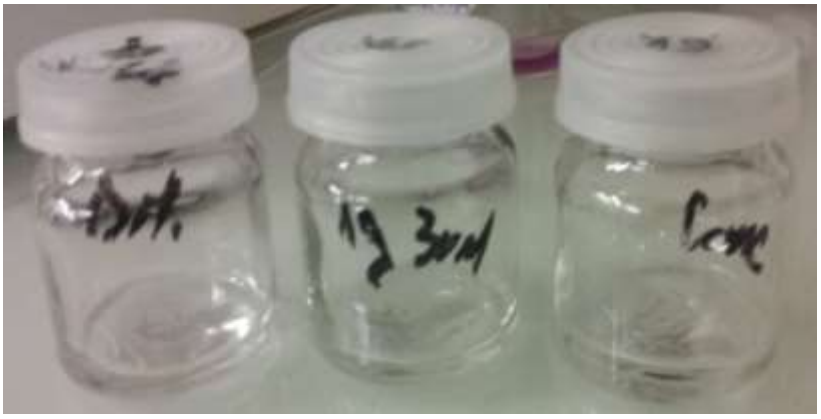

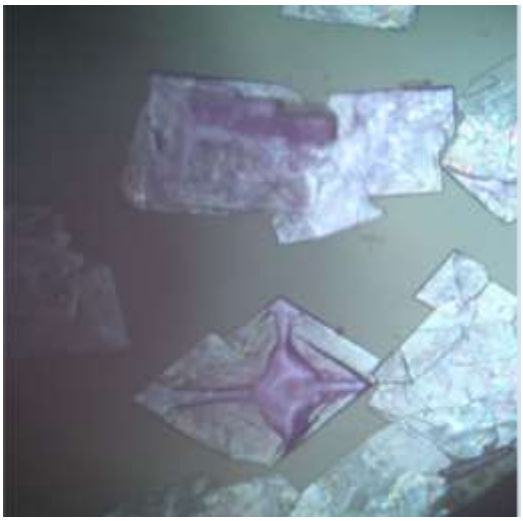

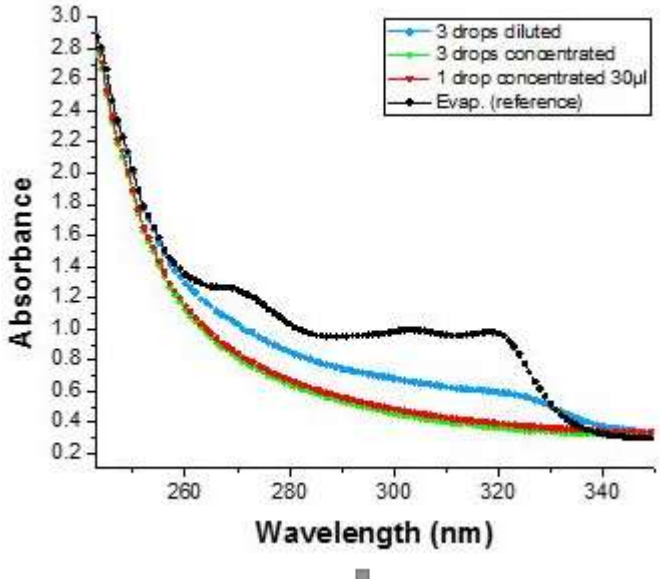

Solution crystallization method

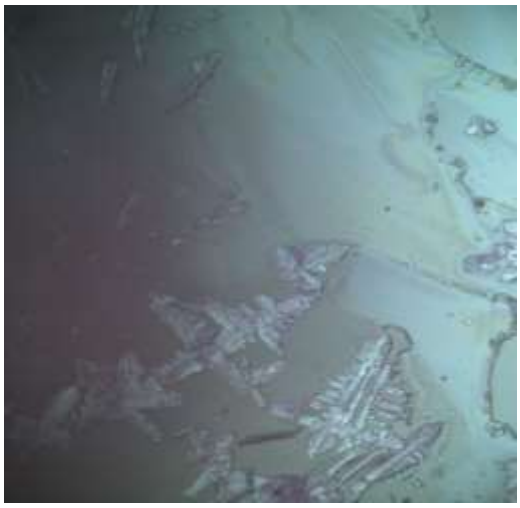

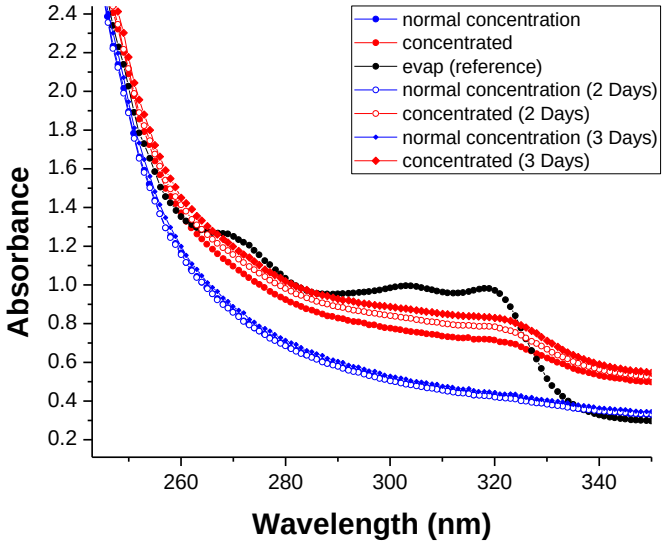
normal concentration
concentrated
evap (reference)
normal concentration (2 Days)
concentrated (2 Days)
normal concentration (3 Days)
concentrated (3 Days)
Absorbance
Wavelength (nm)
2.4
2.2
2.0
1.8
1.6
1.4
1.2
1.0
0.8
0.6
0.4
0.2
260
280
300
320
340

A3. Spin transition properties of $[Fe(HB(tz)_3)_2]$

A3.1 SCO and its stability

A3.1.1 Thermal stability

Figure A3.1.1: Temperature dependence of the absorbance at 317 nm along four heating-cooling cycles recorded at 1 K/min scan rate for film of $[Fe(HB(tz)_3)_2]$ with *ca*.125 nm thickness.

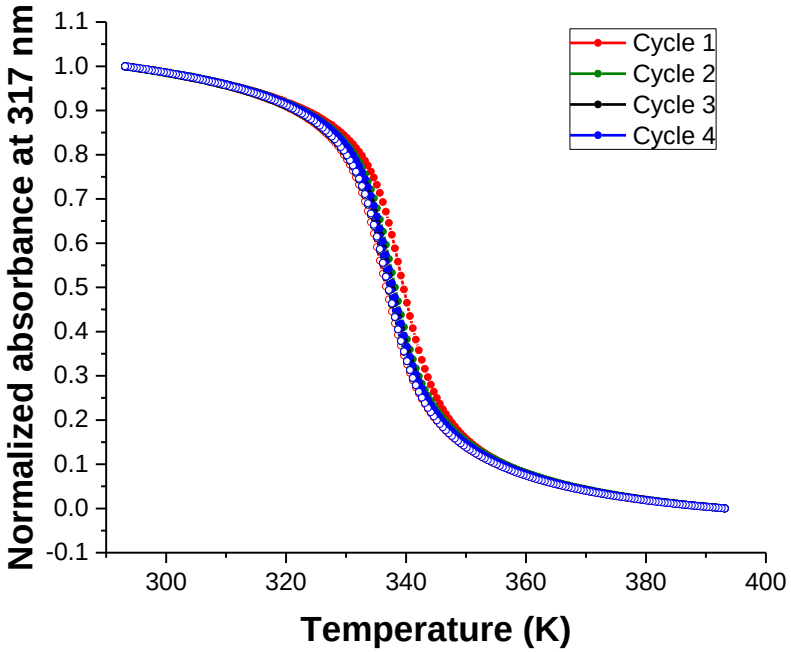

A3.1.2 Long term environmental stability

Figure A3.1.2.1: Absorbance spectra of different crystalline thin films acquired at 293 K after several months of storage in ambient air

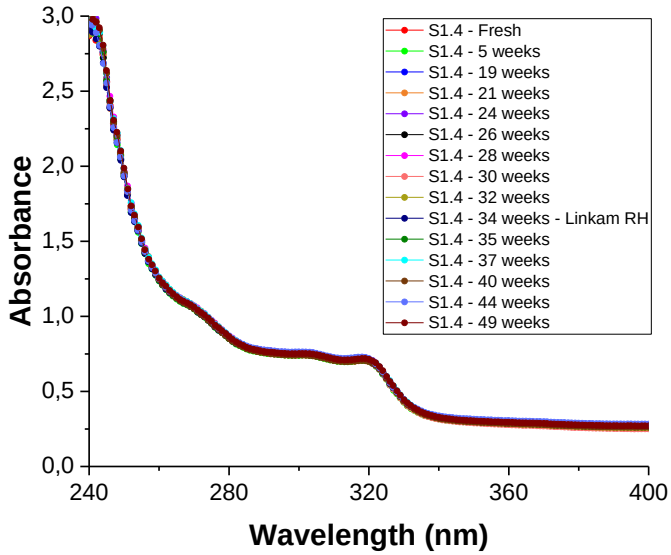

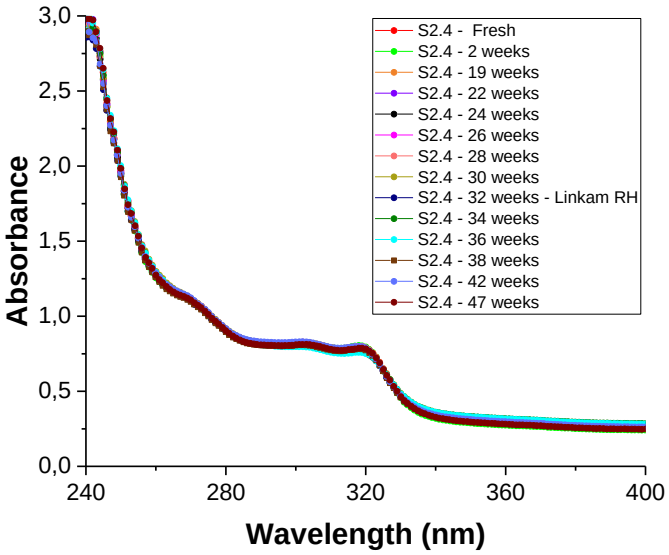

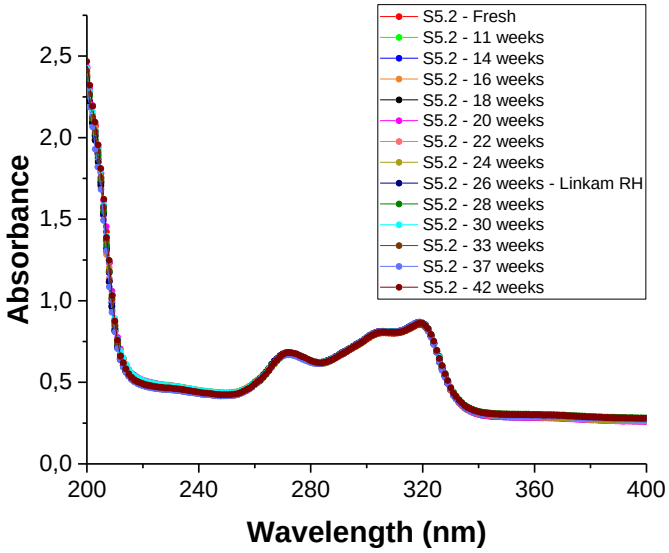
S5.2 - Fresh
S5.2 - 11 weeks
S5.2 - 14 weeks
S5.2 - 16 weeks
S5.2 - 18 weeks
S5.2 - 20 weeks
S5.2 - 22 weeks
S5.2 - 24 weeks
S5.2 - 26 weeks - Linkam RH
S5.2 - 28 weeks
S5.2 - 30 weeks
S5.2 - 33 weeks
S5.2 - 37 weeks
S5.2 - 42 weeks
Absorbance
2,5
2,0
1,5
1,0
0,5
0,0
200
240
280
320
360
400
Wavelength (nm)

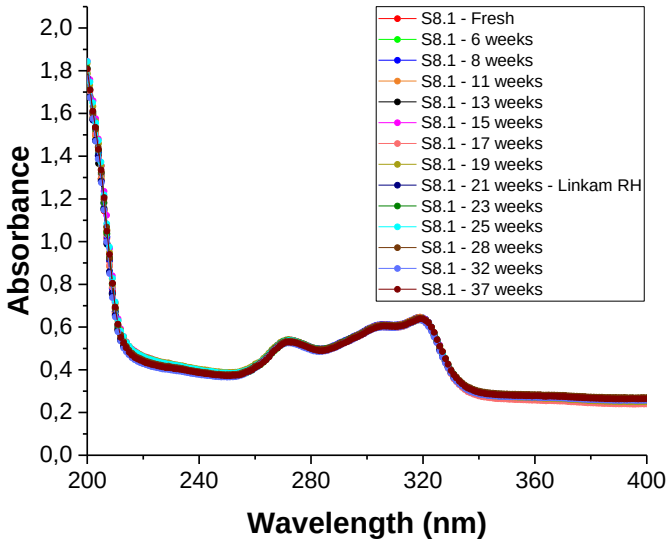
S8.1 - Fresh
S8.1 - 6 weeks
S8.1 - 8 weeks
S8.1 - 11 weeks
S8.1 - 13 weeks
S8.1 - 15 weeks
S8.1 - 17 weeks
S8.1 - 19 weeks
S8.1 - 21 weeks - Linkam RH
S8.1 - 23 weeks
S8.1 - 25 weeks
S8.1 - 28 weeks
S8.1 - 32 weeks
S8.1 - 37 weeks
Absorbance
2,0
1,8
1,6
1,4
1,2
1,0
0,8
0,6
0,4
0,2
0,0
200
240
280
320
360
400
Wavelength (nm)

A3.2 Size effect of $[Fe(HB(tz)_3)_2]$ films

Figure A3.2.1: AFM film thickness analysis.

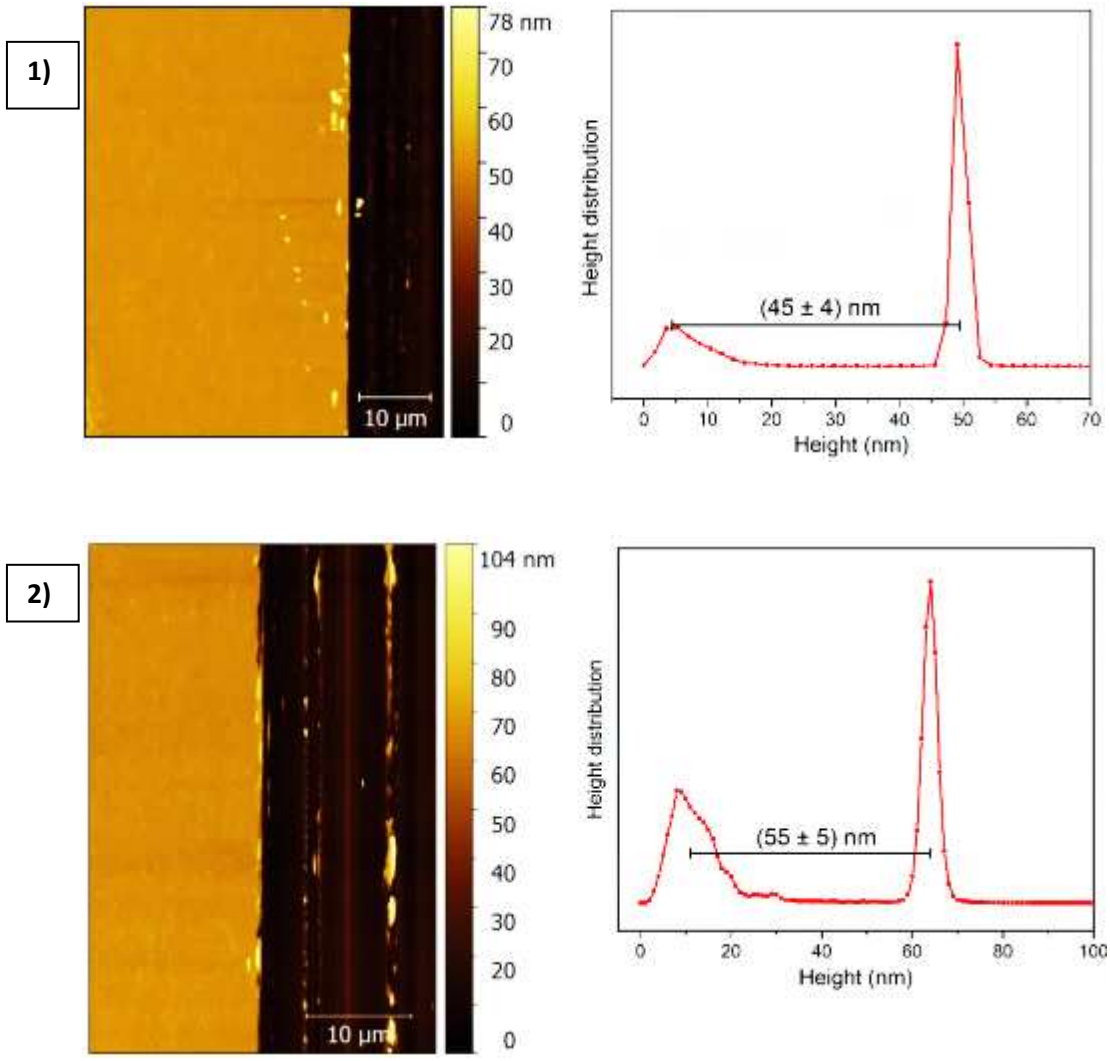

3)

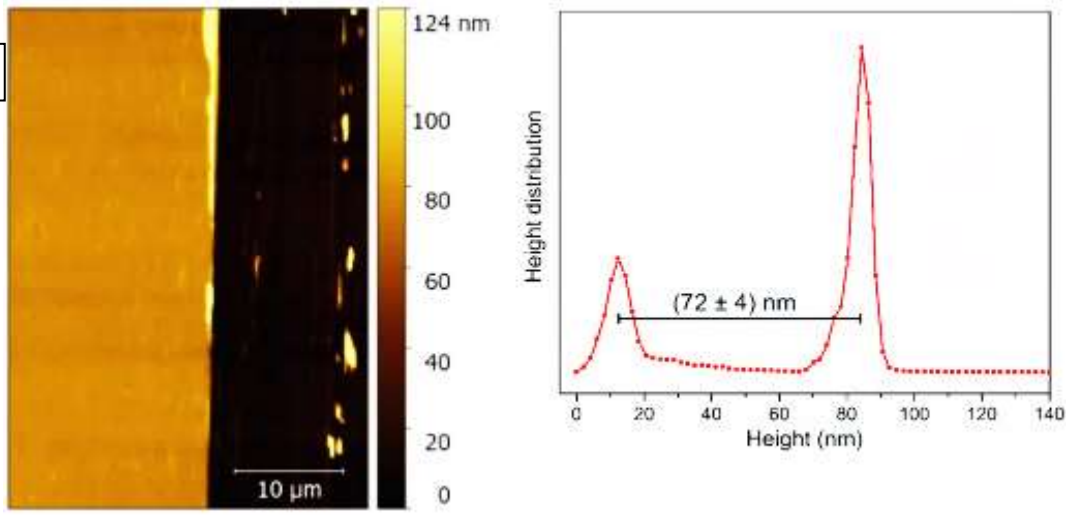
124 nm
100
80
60
40
20
0
10 µm
Height distribution
(72 ± 4) nm
0
20
40
60
80
100
120
140
Height (nm)

4)

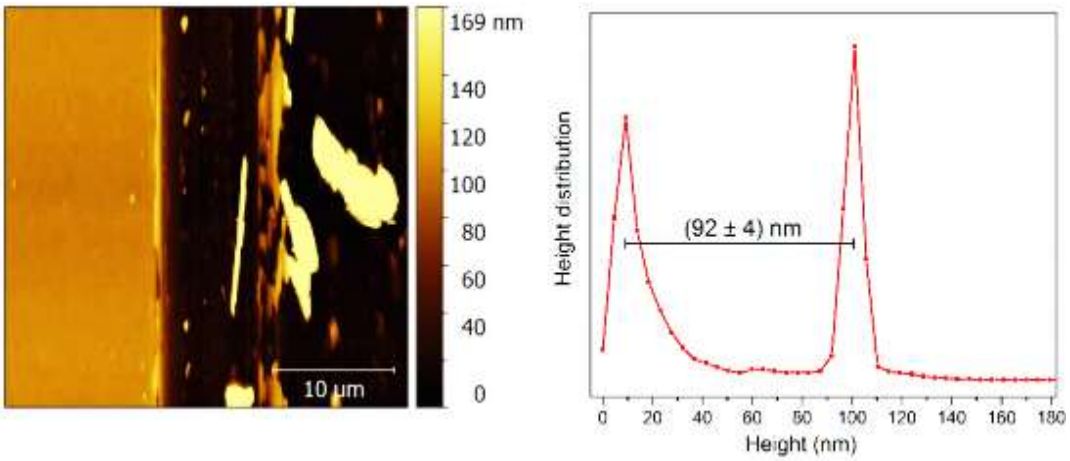
169 nm
140
120
100
80
60
40
0
10 µm
Height distribution
(92 ± 4) nm
0
20
40
60
80
100
120
140
160
180
Height (nm)

5)

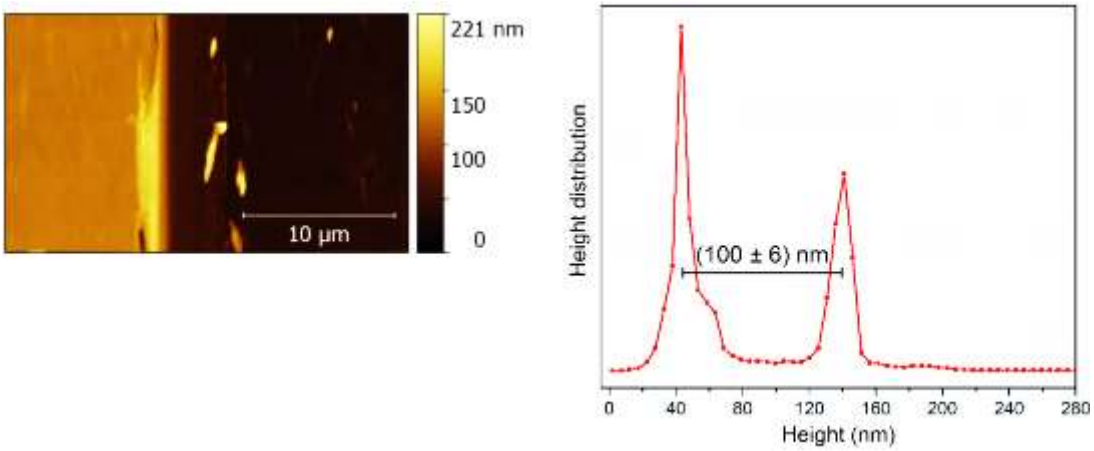
221 nm
150
100
0
10 µm
Height distribution
(100 ± 6) nm
0
40
80
120
160
200
240
280
Height (nm)

6)

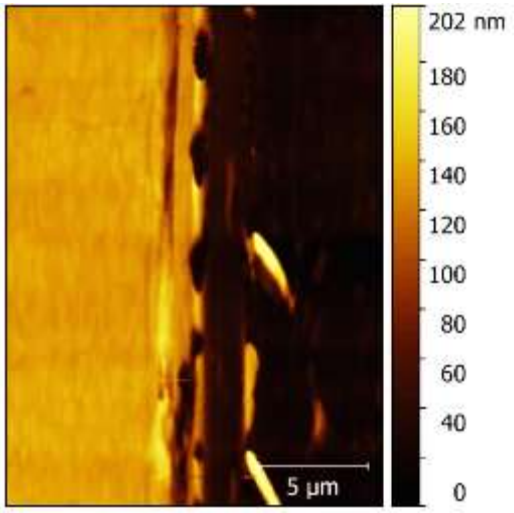
202 nm
180
160
140
120
100
80
60
40
0
5 µm

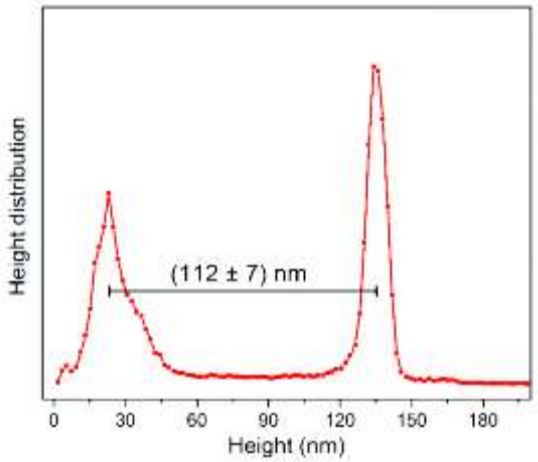
Height distribution
(112 ± 7) nm
0
30
60
90
120
150
180
Height (nm)

7)

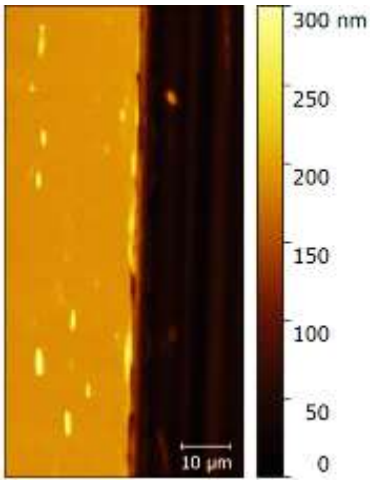
300 nm
250
200
150
100
50
0
10 µm

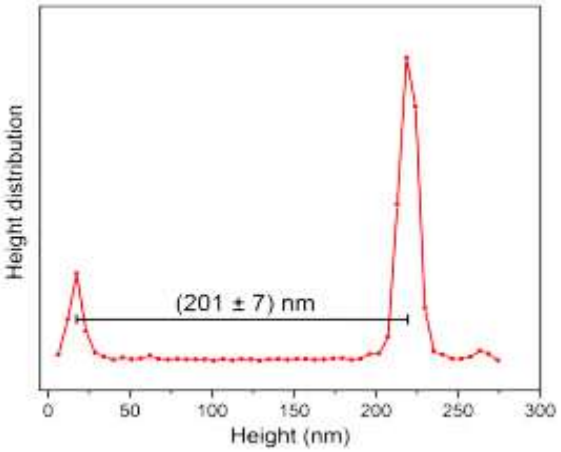
Height distribution
(201 ± 7) nm
0
50
100
150
200
250
300
Height (nm)

8)

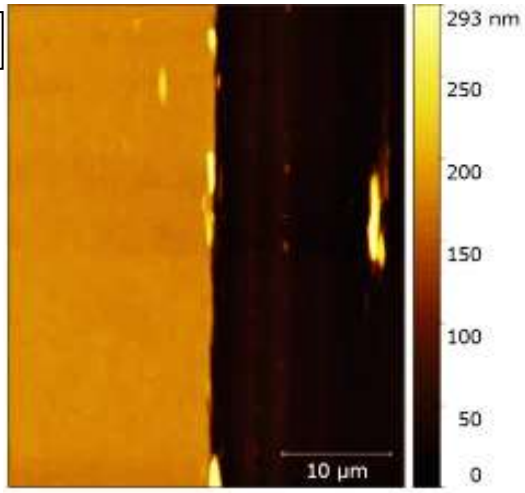
293 nm
250
200
150
100
50
0
10 µm

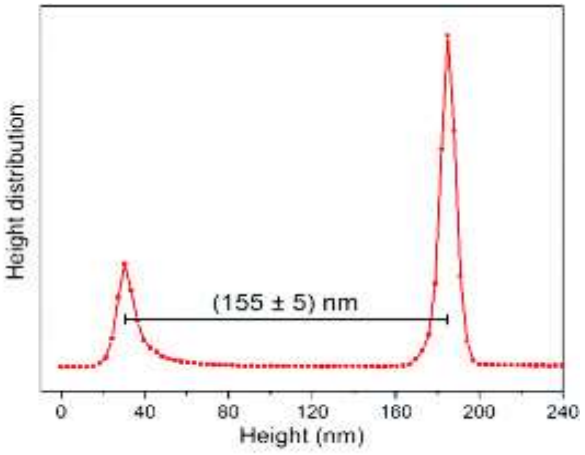
Height distribution
(155 ± 5) nm
0
40
80
120
160
200
240
Height (nm)

A4. Combining spin crossover with luminescent properties

A4.2 Sample fabrication and properties

Figure A4.2.1: Photo of the setup used to acquire fluorescence excitation and emission spectra as a function of temperature **[**Fluoromax-4 (Horiba) spectrofluorimeter equipped with a xenon lamp source and an Optistat DN-V liquid nitrogen cryostat connected to an ITC601 temperature controller (Oxford Instruments)].

A4.3 Characterization of the luminophore films

Figure A4.3.1: (Top side) AFM image of ca.30 nm film with roughness 0.27 nm; (Bottom side) Film thickness evaluation

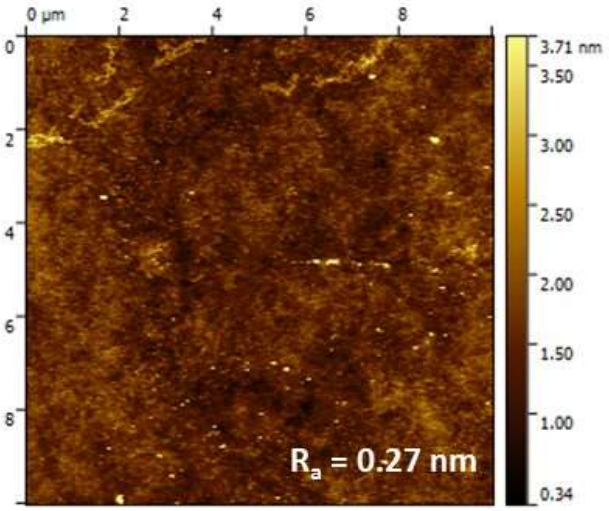

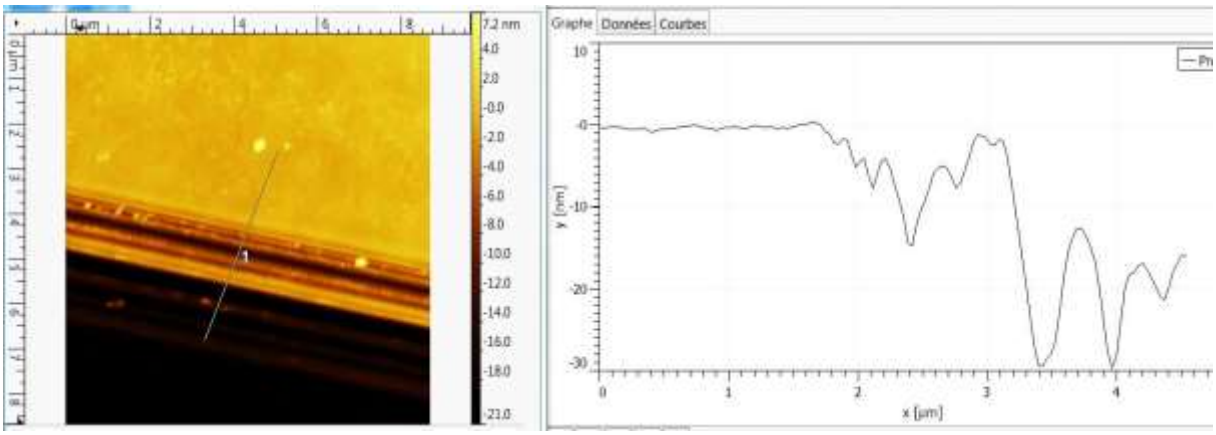

A4.4 Characterization of the bilayer films

Figure A4.4.1: (Top side) AFM image of ca.800 nm film and (Bottom side) AFM film thickness analysis of the bilayer sample with SCO layers of ca.800 nm.

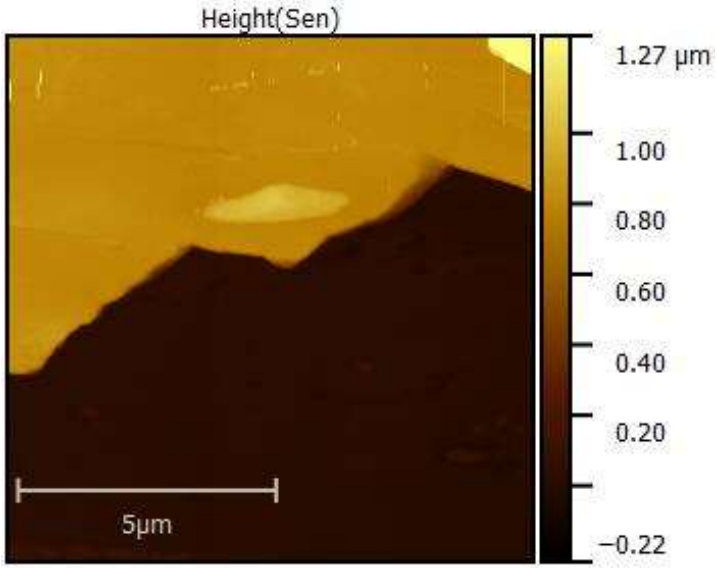

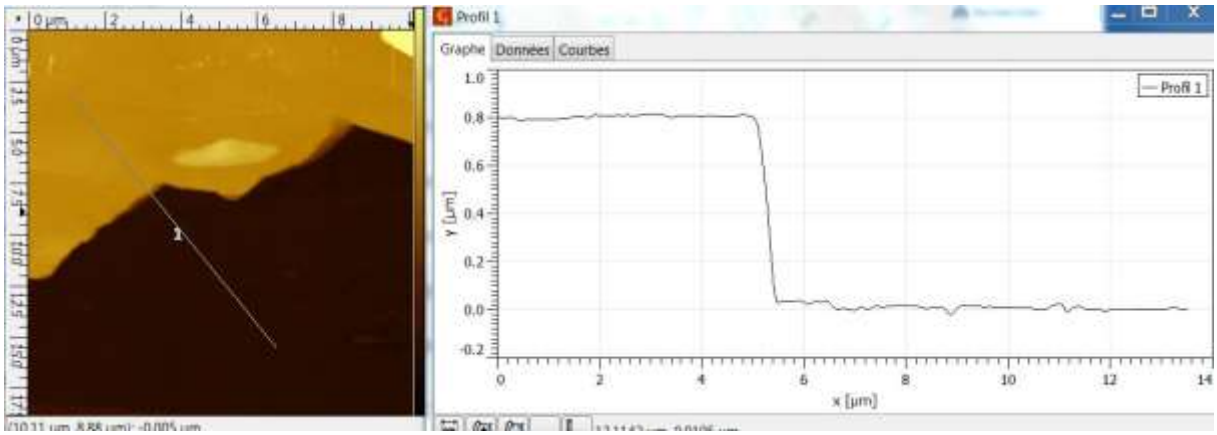

Film thickness evaluation of the co-evaporated S31 sample. From quartz balance: ~ 264 nm (50 nm fluo+107 nm SCO+107 nm SCO)

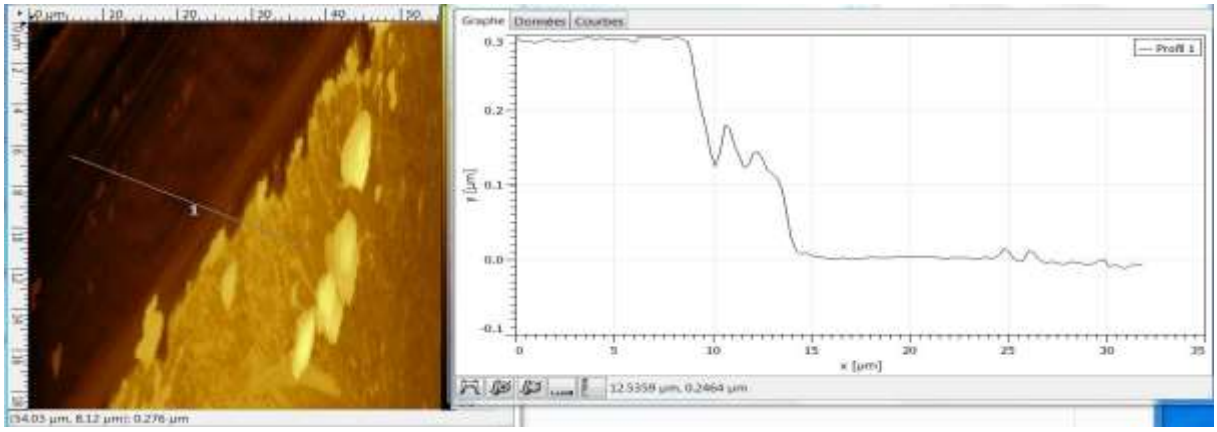

A4.5 Mixed SCO – luminescent films

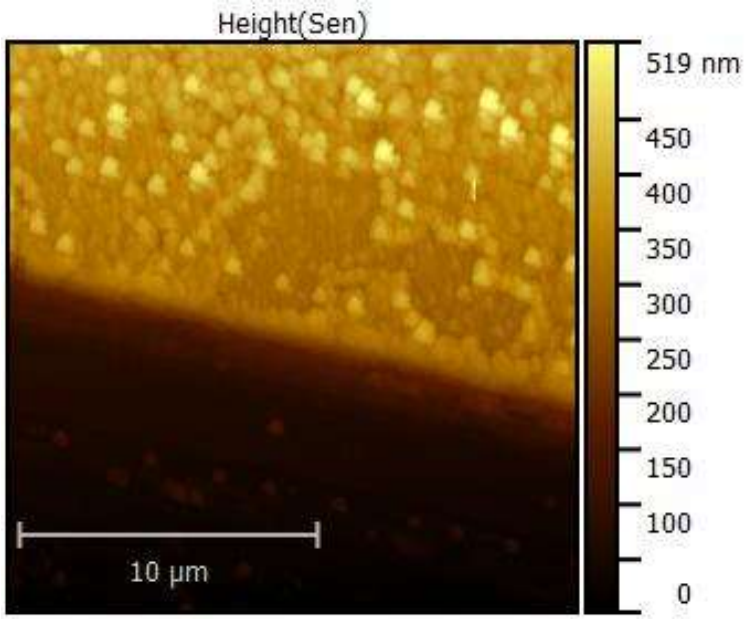

Film thickness evaluation of the co-evaporated C_2 sample **(**ca. 15 % nominal luminophore content). From quartz balance: ~ 223 nm (195 nm SCO + 28 nm fluo)

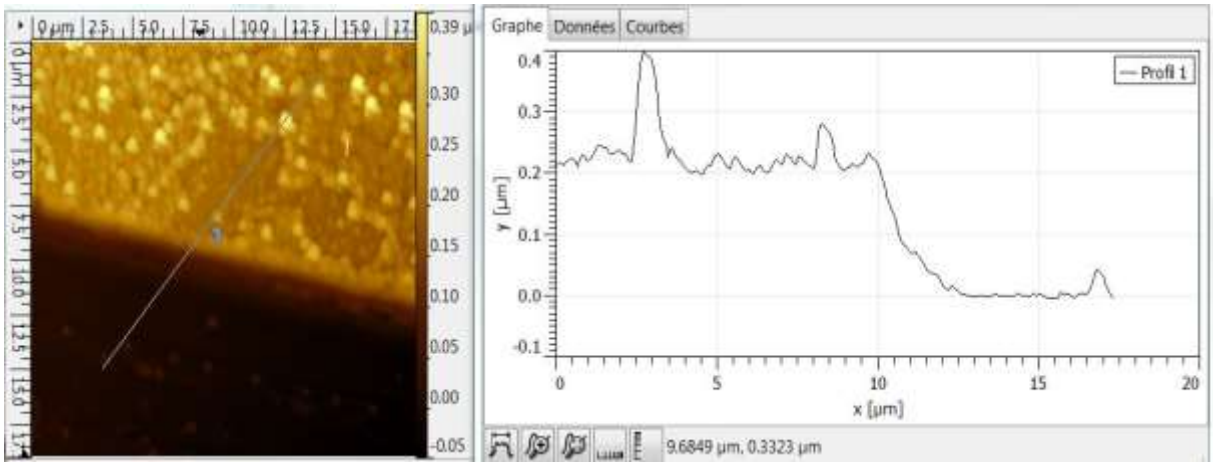

Film thickness evaluation of the co-evaporated SCO_1 sample (with ca. 15 % nominal luminophore content). From quartz balance: ~ 150 nm (136.5 nm SCO + 13.5 nm fluo).

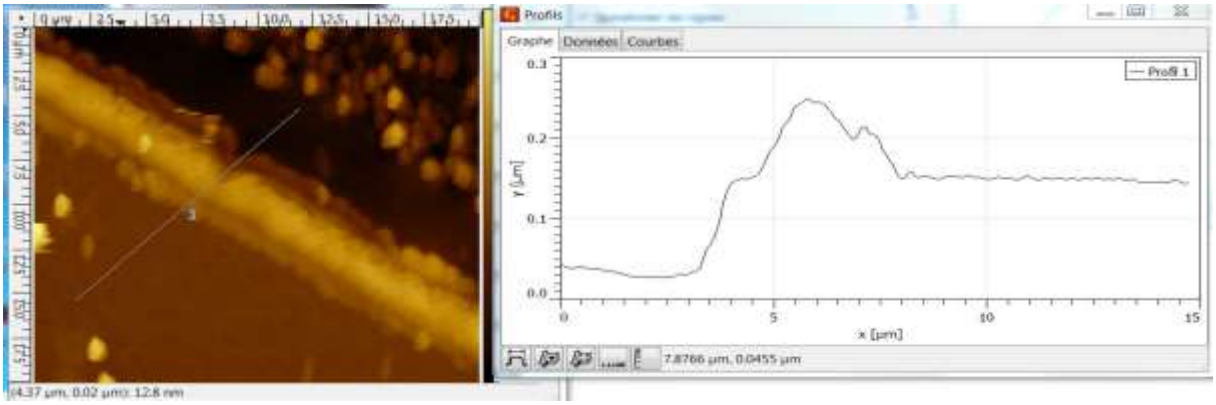

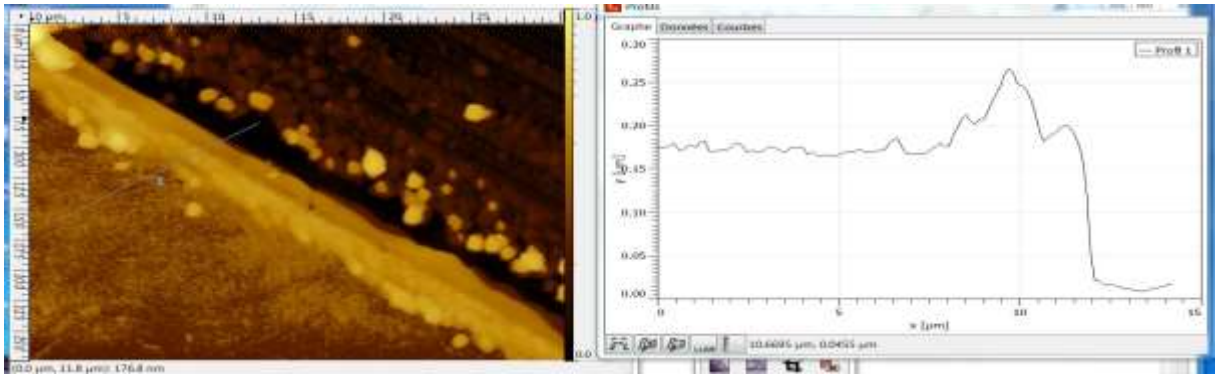

Figure A4.5.1: Temperature dependence of the luminescence intensity on heating and cooling (co-evaporated the SCO and luminescent molecules with ca. 15 % and 21 % nominal luminophore content).

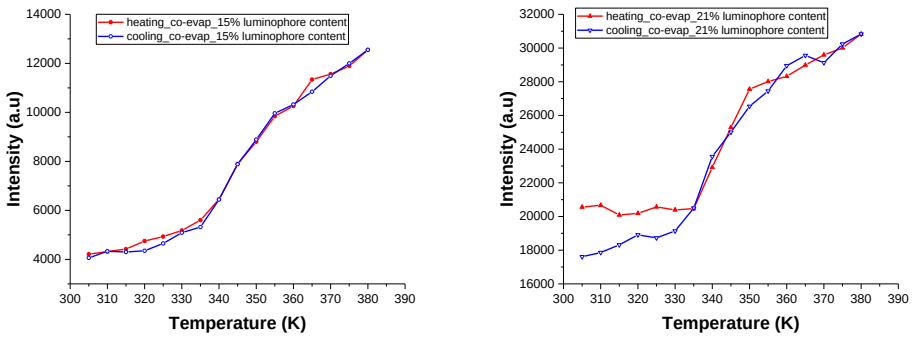

A5. Investigation of SCO thin films using AFM

Figure A.5.3.2.1: AFM images acquired in QI mode of [Fe(H_2B(pz)$_2$)$_2$(phen)] thin film. a) Adhesion map; b) Baseline map; c) Slope map and d) Setpoint map.

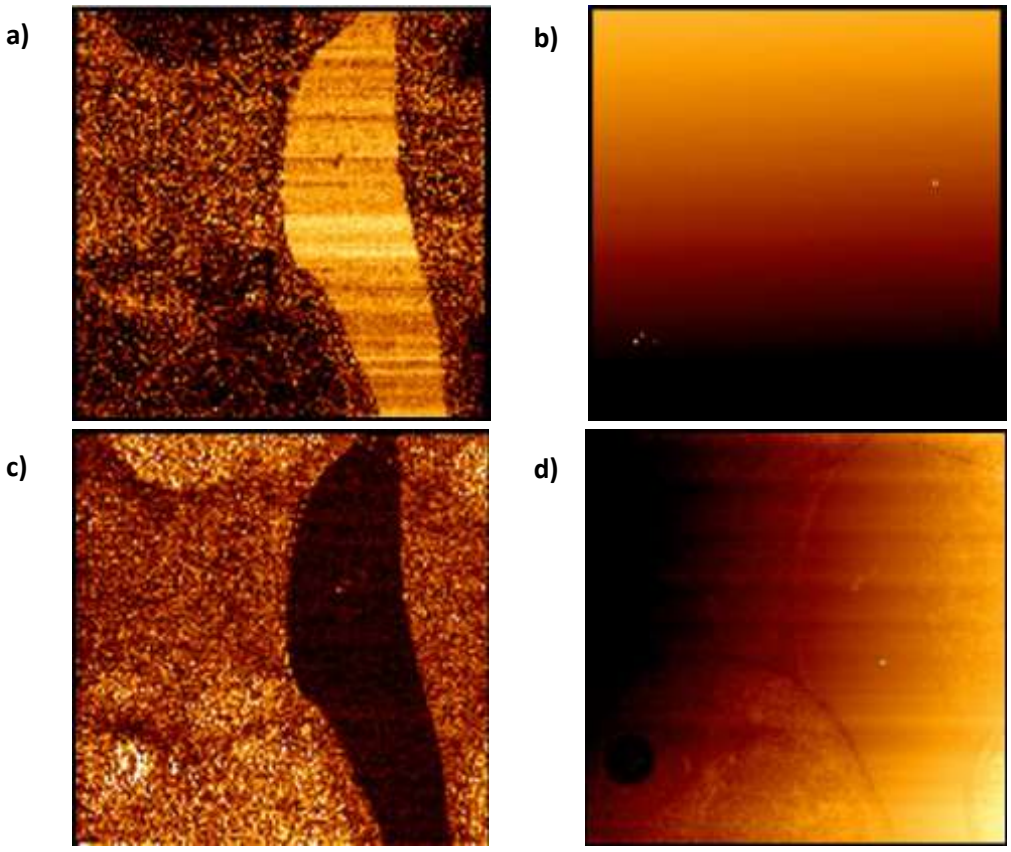

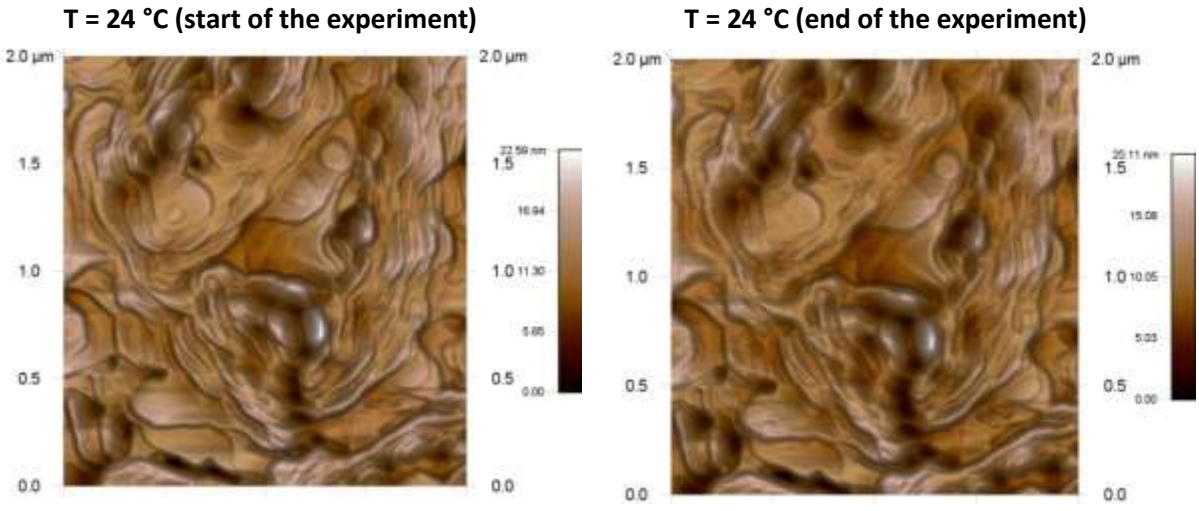

5.4 Nanomechanical investigation of the spin transition in $Fe(HB(tz)_3)_2$] films

Figure A5.4.1: Color change of the crystal

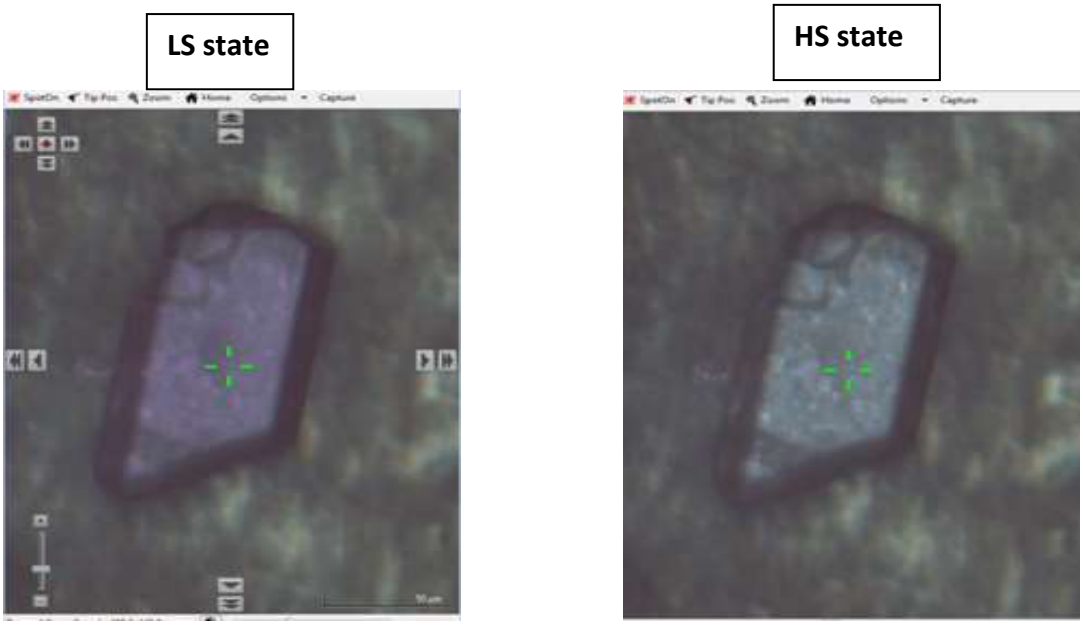

Etude de la croissance et des propriétés physiques des couches minces moléculaires du composé $Fe(HB(tz)_3)_2$ à transition de spin

Les progrès récents réalisés pour la synthèse à l'échelle nanométrique et dans l'organisation de matériaux à transition de spin ont permis l'élaboration d'une variété de nano-objets moléculaires (nanoparticules, films minces, nano-motifs, assemblages à l'échelle nanométrique, etc.) présentant des propriétés remarquables. Ces nouveaux matériaux de tailles nanométriques offrent la possibilité intéressante d'exploiter leurs propriétés commutables à l'échelle nanométrique et ouvrent la voie à l'intégration et à la mise en application du phénomène de transition de spin dans diverses applications (capteurs, actionneurs, dispositifs pour le traitement de l'information et de stockage). Malgré les progrès considérables accomplis, il reste de nombreux défis à relever. Notamment, il apparaît crucial d'élargir considérablement le portefeuille de complexes à transition de spin montrant des propriétés de commutation robustes proches de la température ambiante. La transformation de ces composés en nanomatériaux de haute qualité nécessite également des études scientifiques approfondies sur la science des matériaux ainsi qu'une compréhension fondamentale du rôle des propriétés de surface / interface sur la fonctionnalité souhaitée. Il serait particulièrement important de préciser si la robustesse du phénomène peut répondre aux exigences strictes pour une application "réelle". Dans ce contexte, ce travail de thèse décrit la croissance et les propriétés physiques de couches minces de tailles nanométriques du composé $Fe(HB(tz)_3)_2$ (tz = 1,2,4-triazol-1-yl). Notamment, nous décrivons le dépôt sous vide de ce composé par évaporation thermique et montrons qu'un simple processus de recuit par vapeur de solvant permet d'obtenir des films minces nanométriques de haute qualité présentant une transition de spin proche de la température ambiante. Nous révélons également une résilience sur de nombreux cycles de commutation (> million) de la transition de spin dans ces films qui montrent également une bonne stabilité thermique, environnementale et une excellente processabilité. Cette stabilité exceptionnelle nous a permis (1) de mener une étude minutieuse des effets de taille sur les propriétés de transition, ainsi que (2) de mettre en œuvre une imagerie quantitative des films par microscopie à force atomique avec un accent particulier sur l'analyse des propriétés mécaniques (module de Young, tangente de perte, etc.). En vue d'études plus approfondies en optique en champ proche à haute résolution spatiale, nous avons également mis au point des films hybrides luminescents à transition de spin consistant en une combinaison de molécules $Fe(HB(tz)_3)_2$ et de $Ir(ppy)_3$ (ppy = 2-phénylpyridine) et démontré la modulation de la luminescence par le composé à transition de spin.

Mots-clés: Transition de spin, couches minces, luminescence, microscopie à force atomique

Investigation of the film growth and physical properties of thin molecular layers of the spin crossover compound $Fe(HB(tz)_3)_2$

The recent progress in the nanoscale synthesis and organization of molecular spin crossover (SCO) materials allowed the elaboration of a variety of molecular nano-objects (nanoparticles, thin films, nanopatterns, nanoscale assemblies, etc.) exhibiting SCO properties. These new nanometer-sized materials offer the appealing possibility to exploit their switchable properties at the nanometric scale and open the way for the integration and implementation of SCO in various applications (sensors, actuators, information processing and storage devices). Despite the considerable progress accomplished, numerous challenges remain to be addressed. Notably, it appears crucial to enlarge considerably the portfolio of SCO complexes displaying robust, near room temperature switching properties. Turning these compounds into high quality nanomaterials calls also for rigorous material science studies along with fundamental understanding of the role of surface/interface properties on the desired functionality. Of particular importance would be to clarify if the robustness of the SCO phenomenon can meet the stringent requirements for 'real world' applications. In this context, this thesis work describes the growth and physical properties of nanometric thin films of the SCO compound $Fe(HB(tz)_3)_2$ (tz = 1,2,4-triazol-1-yl). Notably we describe the vacuum deposition of this compound by thermal evaporation and we show that a straightforward solvent vapor annealing process allows for obtaining high quality, nanometric thin films exhibiting SCO near room temperature. We reveal also an unprecedented and unexpected reversibility of the SCO in these films over numerous switching cycles (> million) as well as its thermal, environmental and processing stability. This exceptional stability of the SCO allowed us (1) to carry out a careful investigation of finite size effects for different film thicknesses as well as (2) to implement quantitative atomic force microscopy imaging of the films with particular emphasis on the analysis of mechanical properties (Young's modulus, loss tangent, etc.). In view of high spatial resolution near-field optical studies, we also developed hybrid luminescent – SCO films consisting of a combination of $Fe(HB(tz)_3)_2$ and $Ir(ppy)_3$ (ppy = 2-phenylpyridine) molecules and demonstrated the luminescence modulation by the SCO.

Keywords: Spin crossover, thin films, luminescence, atomic force microscopy